Development of Analytically Reduced Chemistries (ARC) and applications in Large Eddy Simulations (LES) of turbulent combustion

Anne Felden

THÈSE

En vue de l'obtention du

DOCTORAT DE L'UNIVERSITÉ DE TOULOUSE

Délivré par :

Institut National Polytechnique de Toulouse (INP Toulouse)

Discipline ou spécialité :

Dynamique des fluides

Présentée et soutenue par :

Mme ANNE FELDEN

le vendredi 30 juin 2017

Titre :

Development of Analytically Reduced Chemistries (ARC) and applications in Large Eddy Simulations (LES) of turbulent combustion

---

Ecole doctorale :

Mécanique, Energétique, Génie civil, Procédés (MEGeP)

Unité de recherche :

Centre Européen de Recherche et Formation Avancées en Calcul Scientifique (CERFACS)

Directeur(s) de Thèse :

MME BENEDICTE CUENOT

MME ELEONORE RIBER

Rapporteurs :

Mme PASCALE DOMINGO, CORIA

M. NASSER DARABIHA, ECOLE CENTRALE DE PARIS

Membre(s) du jury :

M. FRÉDÉRIC GRISCH, CORIA, Président

M. HAI WANG, STANFORD UNIVERSITY, Membre

Mme BENEDICTE CUENOT, CERFACS, Membre

Mme PERRINE PEPIOT, CORNELL UNIVERSITY EU, Membre

Contents

Acknowledgements

I would like to express my sincere thanks to P. Domingo and N. Darabiha, for agreeing to read and carefully review this manuscript. I would also like to thank all jury members for participating in my PhD defense on june 30th. I am very grateful that they chose to challenge me with their always interesting remarks and questions over planning their well-deserved summer break !

Je remercie ensuite naturellement mes deux encadrantes, Bénédicte Cuenot et Eleonore Riber, qui m'ont fourni un environnement de travail idéal, à mi-chemin entre sérieux et décontraction, me permettant de ne pas (trop) paniquer ! Ces années ont été très riches en expériences, des multiples conférences à l'été passé en Californie, en passant par de fructueuses collaborations internationales: merci pour ces nombreuses opportunités que j'ai saisies du mieux possible. Bien entendu, mes remerciements vont aussi à l'ensemble des séniors de l'équipe Combustion, qui sont toujours disponibles et pleins de conseils avisés ! En parlant de conseils avisés, comment ne pas remercier mes bouées de sauvetage: Isa, Gérard, Fabrice et tous les membres présents ou passés de l'équipe CSG qui s'est toujours révelée disponible et redoutablement efficace pour pallier a mon manque inné d'esprit "informatique" (mais j'y travaille !). Mais les problèmes quotidiens du thésard ne se limitent pas à la partie informatique malheureusement, et il est difficile de ne pas remercier Marie, Michèle, Chantal et Nicole pour leur aide précieuse et parfois trop discrète, ainsi que toute l'administration.

Il y a également, en dehors du CERFACS, d'autres personnes qui m'ont fait beaucoup progresser dans ma réfléxion et mon cheminement scientifique. A ce titre, je tiens à adresser un énorme Merci à Perrine Pepiot, pour sa disponibilité, sa gentillesse, son efficacité dans la résolution de tous les problèmes YARCeux que je n'ai eu de cesse de lui soumettre... et l'inspiration qu'elle n'a manqué d'être tout au long de cette thèse. Mes pensées se tournent aussi vers Carmen Jimenez, qui a été mon mentor des premiers instants et m'a initiée a la chimie de la combustion. Merci également à Fabienne Bessac de m'avoir fait confiance trois années durant et de m'avoir fait découvrir la facète enseignement de notre travail de chercheur !

Il me faut également remercier du fond du coeur mon grand-père, personnage d'une importance cruciale dans mes choix de carrière, aussi généreux et attentionné qu'il peut être exécrable, pour avoir attisé et nourri toute mon enfance ma curiosité scientifique en usant de toutes les ressources de la Capitale. J'ai eu beaucoup de chance.

Je finirai par remercier toutes les personnes qui ont rendu la vie plus douce au cours de ces dernières années -voire de toutes mes années, en m'acceptant telle que je suis: parfois un peu "soupe au lait", sans doute hyper sensible et bien souvent un peu trop directe. Il va de soi que ces traits de caractère ne se sont très certainement pas adoucis au cours de ces derniers mois ! Merci donc à ma mère et à mon père d'adoption d'être absolument disponibles et de bons conseils dans TOUTES les situations... De m'avoir gavée de films, de musique et de voyages, de m'avoir suivie dans mes choix, et surtout d'être toujours tellement positifs, curieux et facile a vivre. Ce sont là des qualités que j'envie ! Vous êtes et resterez mes piliers dans la tempête. You're wonderful individuals. Merci aussi à Lucas d'avoir été mon petit serviteur des derniers instants ;), à Pauline qui ne lira jamais cette thèse sauf peut-être pour en corriger les fautes d'orthographes des quelques rares parties francophones :), à Romain pour nos passions communes (et pour ne jamais manquer d'être l'incarnation de l'adage "malheureux doit trouver plus malheureux que lui" mouhahaha), à toutes les copines de la danse qui ont été un rappel quasi quotidien que la vie continue en dehors du labo, à toute la Spicy bande pour leur bonne humeur, et enfin bien sûr à mes fidèles compagnons, Titeuf et Gimli, qui ont accepté gracieusement que je redirige la quasi totalité de mon attention sur mon Mac cette dernière année, bien qu'il soit certain qu'ils ne liront jamais le fruit de ce dur sacrifice, ni aucun autre document d'aucune sorte d'ailleurs (quoique ... ?).

"(...) And the first lesson of all was the basic trust that he could learn. It is shocking to find how many people do not believe they can learn, and how many more believe learning to be difficult."

Dune, Frank Herbert (1920-1986)

"Nobody's perfect !!"

Osgood E Fielding III, Some Like It Hot, Billy Wilder (1959)

À Daddy & Françoise.

Nomenclature

Roman characters

Symbol	Definition
Δh_f^0	Formation enthalpy
Δ_x	Mesh size
κ	Flame curvature
$\mathbf{F}$	Matrix of rate-of-production sensitivities
$\mathbf{J}$	Jacobian matrix
$\mathbf{S}$	Matrix of concentration sensitivities
$\mathcal{D}_{k,i}$	Binary diffusion coefficient of species k and i
$\mathcal{E}$	Efficiency function
$\mathcal{F}$	Thickening factor
$\mathcal{P}$	Products
$\mathcal{Q}$	Net progress rate of the reaction
$\mathcal{R}$	Reactants
ε	Dissipation rate
A	Pre-exponential constant/species
a	Strain rate
c	Normalized progress variable
C_p	Constant pressure heat capacity
C_v	Constant volume heat capacity
D	Molar diffusivity
D_{th}	Thermal diffusivity
E	Total energy
E_a	Activation energy
h	enthalpy
h_{tot}	Total enthalpy
J	Species diffusion flux
k	Reaction rate coefficient
K_p	Pressure equilibrium constant

l_t	Integral length scale
N_e	Number of elements
N_r	Number of reactions
N_s	Number of species
P	Pressure
q	Heat flux
R	Perfect gases universal constant
r_{AB}	DRG coefficient
S_a	Flame absolute speed
S_c	Flame consumption speed
S_d	Flame displacement speed
S_T	Turbulent flamme speed
s_l^0	Laminar flame speed
T	Temperature
u, v, w	Velocity components
V	Diffusion velocity
W	Molar mass
X	Molar fraction
Y	Mass fraction
Y_c	Progress variable
Y_z	Mixture fraction

Non-dimensional numbers

Symbol	**Definition**
Da	Damkhöler number
Ka	Karlovitz number
Le	Lewis number
Pr	Prandtl number
Re	Reynolds number
Sc_k	Schmidt number of species k

Superscript

Symbol	**Definition**
c	Correction
ext	Extinction

sgs	Subgrid-scale contribution
t	Turbulent contribution

Greek characters

Symbol	Definition
χ	Scalar dissipation rate
δ_r	Reactive layer thickness
$\delta_{i,j}$	Kronecker symbol
δ_l^0	Flame thickness
$\dot{\omega}_k$	Reaction rate of species k
$\dot{\omega}_T$	Heat release rate
η_k	Kolmogorov length scale
κ	Flame stretch
λ	Thermal conductivity
μ	Dynamic viscosity
ν	Kinematic viscosity
ν''_{kj}	Products stoichiometric coefficient
ν'_{kj}	Reactants stoichiometric coefficient
$\nu_{tot,kj}$	Global stoichiometric coefficient
ϕ	Equivalence ratio
ρ	Density
Σ	Flame surface density
τ	Time-scale
$\tau_{i,j}$	Viscous stress tensor

Subscripts

Symbol	Definition
0	Initial state
b	Burnt gas state/backward
c	Chemical
F	Fuel
f	Fresh gas state/forward
fl	Flame
i	i-th component/species
j	j-th component/reaction

K	Kolmogorov
k	k-th species
O	Oxidizer
st	Stoichiometric
v	Viscous

Acronyms

Symbol	**Definition**
AV	Artificial Viscosity
CFD	Computational Fluid Dynamics
DNS	Direct Numerical Simulation
DRG	Directed Relation Graph
DTFLES	Dynamically Thickened Flame model for LES
DZ	Dilution Zone
FPI	Flame Prolongation of Intrinsic Low Dimensional Manifold
ILDM	Intrinsic Low Dimensional Manifold
IRZ	Inner Recirculation Zone
LES	Large Eddy Simulation
LHS	Left Hand Side
LW	Lax-Wendroff
NSCBC	Navier-Stokes Characteristic Boundary Condition
OPR	Overall Pressure Ratio
ORZ	Outer Recirculation Zone
PDF	Probability Density Function
PEA	Pre-Exponential Adjustment
PIV	Stereo Particle Image Velocimetry
PLIF	Planar Laser-Induced Fluorescence
PVC	Precessing vortex core
PZ	Primary Zone
RANS	Reynolds Averaged Navier-Stokes
RHS	Right Hand Side
sgs	Sub-Grid Scale
TFLES	TF model for LES
TTGC	Two-step Taylor-Galerkin version C

Chapter 1

Introduction

Contents

1.1 Motivations

The emergence of new energy sources over the last century, such as natural gas, nuclear energy and renewable energies, is on the verge of significantly decreasing the need for fossil fuels in the industrial sector as well as in the tertiary sector. Nonetheless, its need in the transport sector continues to increase, due to both a lack of viable substitute source and increasing population. In 2014, this sector alone accounted for about 65% of the total oil consumption [1]. The predicted trends for the next century is towards an increase of this fossil energy demand, especially in the aeronautic sector, where the number of passengers worldwide is expected to double in the next twenty years, see Fig. 1.1.

Unfortunately, combustion of fossil fuels releases pollutant species such as oxides of carbon (CO, CO_2), oxides of nitrogen (NO_x), oxides of sulfur (SO_x) and soot, which are a major worldwide concern due to their now recognized contribution to global warming and air quality deterioration. Indeed, warming of the climate system over the last century is unequivocal (see Fig. 1.2), and the observed changes, ranging from the diminishing of ice to the increase of weather-related disasters such as cyclones and floods, are alarming. A non exhaustive list of the main effects of the various aforementioned pollutant sources can be summarized as follows [2]:

- Acid rain: designates any form of precipitation (rain, snow, fog) with an acidic Ph, typically about 4.3 (natural rain has a Ph of about 5.6). Such precipitations result from the interaction of SO_x and NO_x with rain droplets and other chemicals in the atmosphere, forming sulfuric and nitric acids, which then mix to water. Acid rains can harm plants and wildlife, by modifying the Ph of lakes and soils. Furthermore, acidic particles may also react in the atmosphere and form larger particles that can be harmful to human health.

[1] International Energy Agency : https://www.iea.org
[2] Environmental Protection Agency: http://www.epa.gov/air/topics/comeap.html

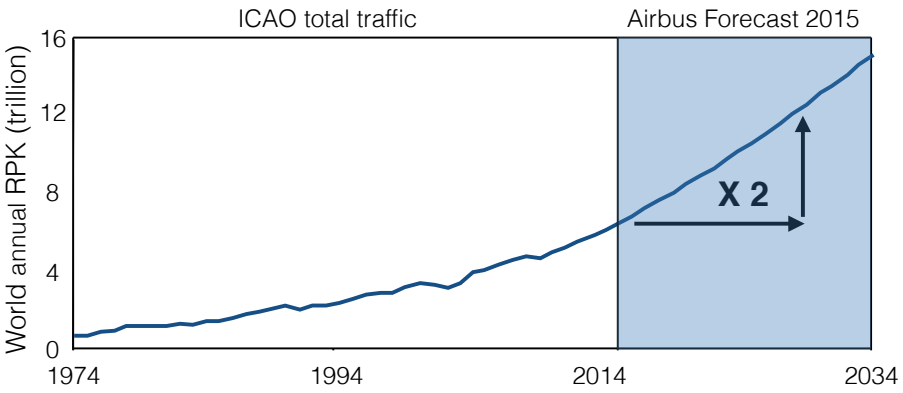

Figure 1.1: Global market forecast 2015-2034 (Adapted from an Airbus Technical report, 2015).

- Photochemical smog (tropospheric ozone): is caused by complex atmospheric reactions involving the irradiation of NO_x as well as the chemistry of light hydrocarbons such as CO to increase the ozone layer. Ozone can cause or worsen a variety of lung and respiratory diseases.
- Global warming: is caused by the release of greenhouse gases that prevents the solar radiation to reverberate into space. As a consequence, they promote warming of the Earth's surface. Major greenhouse gases include carbon dioxide (CO_2), methane (CH_4) and nitrous oxides (N_2O). However, it should be noted that transportation only accounts for 14% of the human global greenhouse gas emissions according to the IPCC [3].
- Visibility impairment, contrails: are a direct consequence of particulate matter such as soot in the atmosphere.

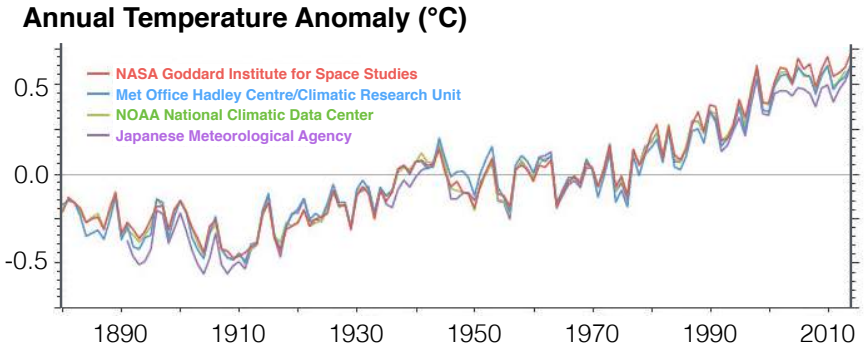

Figure 1.2: Temperature anomaly -changes when compared to a base period of 1951-1980, throughout the years (Adapted from http://earthobservatory.nasa.gov)

In this context, numerous emission regulation and recommendations have been issued by concerned institutions from the aeronautic sector, such as the ICAO [4] or the European ACARE [5]. ACARE, through the *Strategic Research and Innovation Agenda for Aviation* (SRIA), provides guidelines to meet the Flightpath 2050 goal concerning CO_2 and NO_x emissions as well as condensation trails and cirrus clouds. SRIA sets short and long terms targets to be able to reach a 75% reduction in CO_2 emissions per passenger per kilometer and a 90% reduction in NO_x emissions in 40 years, see Fig.1.3.

This awareness has motivated considerable actions from engine manufacturers towards the development of a new fuel-efficient generation of aeroengine combustors with low emissions. These new technologies mainly rely on a high overall pressure ratio (OPR) in order to increase the engine thermal efficiency (Lefebvre, 1998). However, this is accompanied by an increase of the combustor temperature which, as illustrated in Fig. 1.4, enhances NO_x

[3] Intergovernmental Panel on Climate Change, 2014 report on Climate Change
[4] International Civil Aviation Organization : http://www.icao.int
[5] Advisory Council for Aviation Research and innovation in Europe : http://www.acare4europe.com/

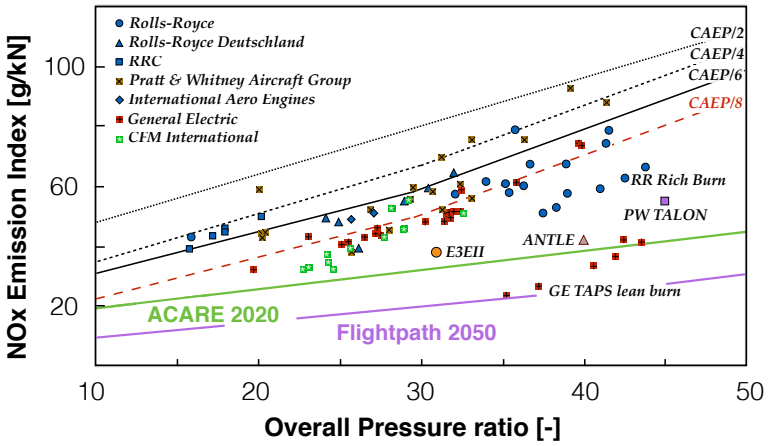

Figure 1.3: NO_x stringency standards

production. Indeed, the simultaneous improvement of efficiency and minimization of harmful emissions results in somewhat contradictory design trends. The trade-off suggest lean combustion technologies (i.e. with large excess of air) to minimize temperature, as well as NO_x production and the formation of soot and other unburnt hydrocarbons. However, the design of aeronautical combustion chambers is further complicated by constraining safety and operability specifications: thermo-acoustic stability, engine relight and efficient cooling of the core elements are only a few of the multiple requirements. The intricacies of the combustion process in modern aero-engines prevent a direct control of all the parameters, and promotes further research. In parallel, due to a competitive market, engine manufacturers require a reduction of both development and experimental costs of new technologies.

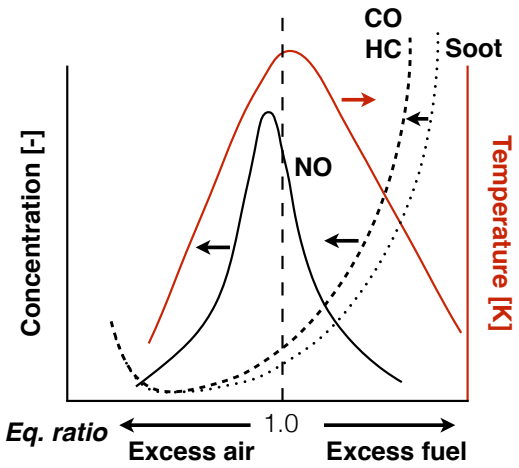

Figure 1.4: Typical evolution of CO and NO emissions with equivalence ratio

The advent of numerical simulation tools such as reacting Reynolds-Averaged Navier Stokes (RANS) and Large Eddy Simulation (LES) (Veynante & Poinsot, 1997; Poinsot & Veynante, 2005), coupled to the continuously increasing available computational power, now provides a way to tackle these issues with high accuracy for a reasonable cost. Numerical simulations of complex devices, that include the description of turbulent reacting flows, are becoming affordable at a design stage (Gicquel *et al.*, 2012). However, the capability to predict pollutant emissions relies heavily upon the fidelity of the chemistry description, and insights must be provided on both the dynamic of the fluid and the chemistry of the flame, as well as on their possible interactions. If the interaction between combustion and turbulence is well understood and described today from a thermodynamics point of view, the impact of detailed chemistry in real systems is far from straightforward.

1.2 Challenges of chemistry description in turbulent combustion

The following discussion provides a non exhaustive list of challenges faced when performing numerical simulations of complex devices featuring turbulent reacting flows.

1.2.1 Chemical processes of combustion

Comprehensive flame chemistry in computational fluid dynamics (CFD) is a rather new field of research, owing to the complexity of the process. Combustion of real fuels involves up to hundreds of different chemical compounds through complex and highly non-linear mechanisms, making it difficult to study both theoretically and experimentally. For a long time, the lack of sufficiently reliable kinetic information prevented any sort of detailed analysis. However, the progress made during the second half of the 20^{th} century regarding fundamental measurements and quantum chemistry calculations led to an improved understanding of the underlying physics, allowing the development of accurate and comprehensive detailed kinetic mechanisms.

Fig. 1.5 (a) displays the size of several detailed and moderately reduced chemical mechanisms, for various hydrocarbons, compiled over the last two decades. It can be seen that the number of species and reactions to consider in order to describe all types of combustion process increases exponentially with the size of the molecule considered. Obviously, if no simplifications are made, the computational time required to run even the simplest 0D simulation (auto-ignition, extinction) becomes rapidly prohibitive. Recent mechanisms proposed by the LLNL [6] contain over 1000 species, the largest one involving 3012 species amongst 8820 reactions (Herbinet *et al.*, 2008) !

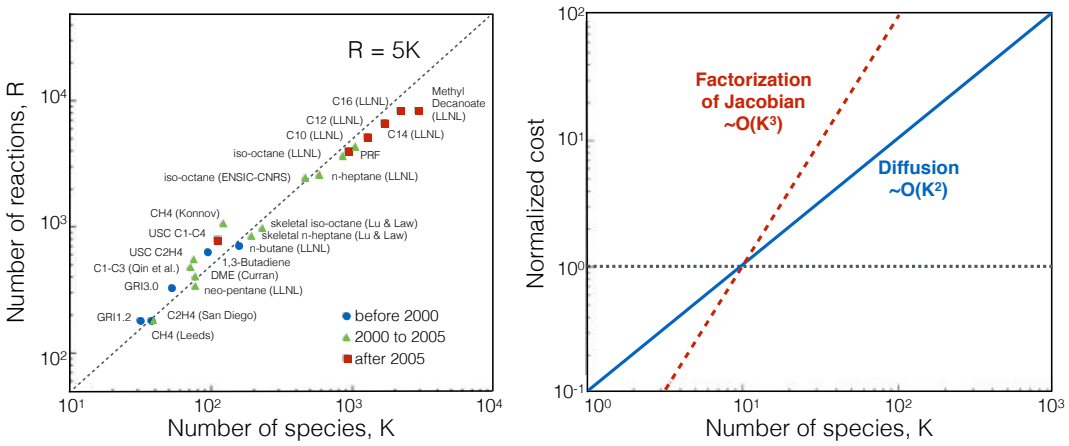

Figure 1.5: a) Exponential increase of mechanism size throughout the years for various hydrocarbons, and b) asymptotic analysis of CFD computational cost, which is a function of the complexity of the molecule through the number of species to consider. From (Lu & Law, 2009)

Quantitatively, it can be shown that the cost C of a numerical simulation scales with the number of species K as $C = C_0 + \alpha(100K + 10K^2 + K^3)$, where diffusion processes (quadratic dependency) and operations on the Jacobian (cubic dependency) quickly become the dominant terms in this formulation for realistic fuels. This is illustrated on Fig. 1.5 (b), where the cost induced by diffusion and Jacobian operations are relatively high compared to that induced by the evaluation of the chemical rates (black dotted curve). For this reason, explicit solvers are often preferred in LES, so that no costly Jacobian factorizations are necessary. Furthermore, simplification of transport processes are also frequently performed, to avoid the tedious evaluation of binary diffusion coefficients. With such an approach, the cost of a simulation reduces to the linear relation $C = C_0 + \gamma K$. In this relation, the factor γ is a direct function of the number of time steps (Lu & Law, 2009), which raises the issue of stiffness that may lead to prohibitively small time steps.

Stiffness is inherent to any chemical process, as the conversion from reactants to products, including the modeling of chain branching dominated by radicals to the slow formation of pollutants, spans a very large range

[6] Lawrence Livermore National Laboratory

of time scales, see Fig. 1.6. This is all the more true when considering realistic fuels, because longer alkanes involve many highly reactive C_3-C_5 radicals with very small associated time scales. Stiffness then adds considerably to the computational cost of combustion chemistry, and complicates the coupling between chemistry and turbulence.

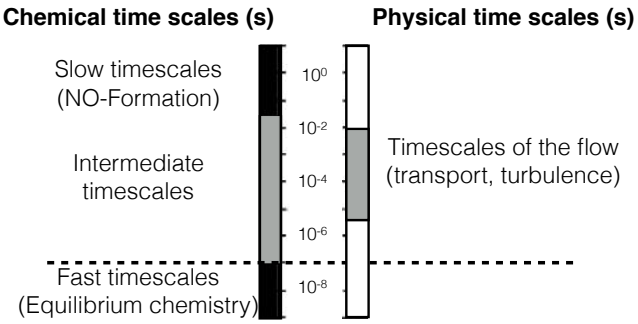

Figure 1.6: Characteristic time-scales in turbulent reactive flows

To cope with these difficulties, employing some sort of *reduced or simplified* chemistry in numerical simulations appears as the only viable approach. However, this implies neglecting or reorganizing some of the available chemical pathways, and as such, restrictions upon the operating range will always apply and should be kept in mind. This phenomenon is illustrated in Fig. 1.7 (a), where the explosion limits (i.e. the region delimiting favorable/unfavorable temperature and pressure conditions to observe ignition) of a mixture of hydrogen and air are represented, in a pressure VS temperature diagram. Two inflections of the curve can be observed, each finding an explanation in the subtle competition of the chemical pathways. If a set of reactions are removed for a particularly low operating pressure (say, the degenerative chain branching reaction $H_2O_2+M = OH+OH+M$), the mechanism might give very erroneous results for higher operating pressure. Another well known manifestation of these effects is the Negative Temperature Coefficient (NTC) region observed in the auto-ignition of heavy hydrocarbons. As illustrated in Fig. 1.7 (b) for iso-octane, discarding the so-called low-chemistry pathways (dotted line) leads to an over-prediction of auto-ignition timing for initial mixtures with low temperatures.

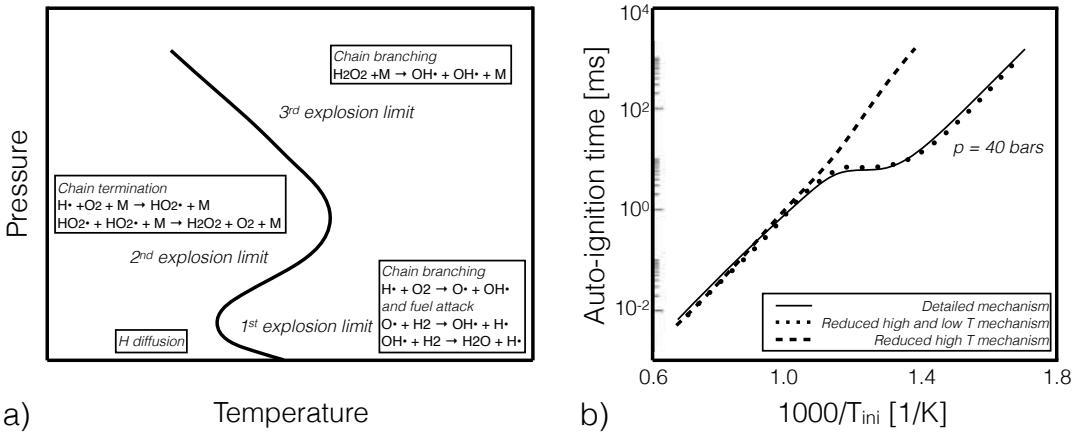

Figure 1.7: a) Explosion limits of homogeneous hydrogen-air mixtures and b) auto-ignition of iso-octane mixtures at 40 bars exhibiting the NTC behavior, from Pepiot (2008)

1.2.2 Real fuel description

Adding to the aforementioned complexity of chemistry modeling in CFD, transportation fuels are in fact complex blends of a large number of hydrocarbons, the exact composition of which is very difficult to determine and varies depending from their origin and time of production. Average fuel properties are known at best (Edwards, 2002), and a large scatter can be observed from different fuel batches, as illustrated on Fig. 1.8 showing the volumetric content of aromatics found in various aviation fuel (JP-8) mixtures. Therefore, the question of fuel characterization is raised, on top of the question of the fidelity of the fuel description.

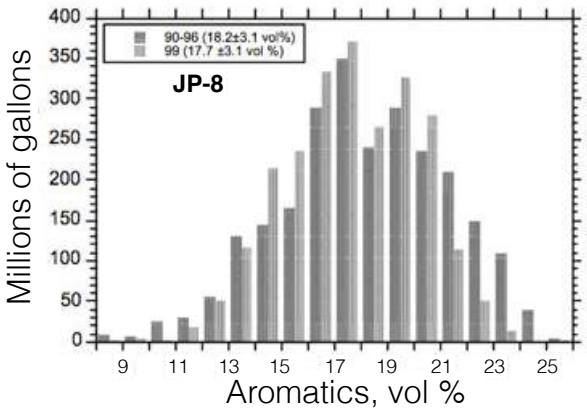

Figure 1.8: Variation of aromatics content of JP-8 fuel, from the Petroleum Quality Information System of the Defense Energy Support Center.

Real fuel emulation is traditionally achieved through the definition of *surrogates*, which are mixtures of one or more components selected in order to match specified chemical (average molecular weight, H/C ratio, sooting tendencies, ...) and/or physical (density, viscosity, ...) features (Edwards & Maurice, 2001; Dagaut & Cathonnet, 2006). Many surrogate formulations have been proposed in the literature, usually based upon experimental studies (Guéret *et al.*, 1991; Dooley *et al.*, 2010, 2012; Xu *et al.*, 2017*b*). In a simple approach, reaction mechanisms for surrogates have been compiled from the reaction mechanisms of each component. However, the multiplication and interactions of the various pathways can become problematic when trying to reduce the surrogate chemistry to make it affordable for turbulent simulations. Furthermore, this approach requires to take particular attention to the retained kinetic pathways, in order to avoid counter effects associated with the non-linearity of competitive chemistry routes.

1.2.3 Transport-related phenomena

Chemical species diffuse into each other at very different velocities and as a consequence, reaction fronts are prone to a variety of diffusion-related effects. At the same time slowly diffusing species are more affected by convection effects induced by the unsteady interactions with the turbulent flow. As a result, strain, curvature and other differential-diffusion related effects impact the flame structure (Haworth *et al.*, 1992; Echekki & Chen, 1996; Savard & Blanquart, 2015); and can ultimately have a direct impact on pollutant formation. For example, a few experimental and numerical studies related to soot formation can be found, suggesting that soot formation is enhanced by preferential diffusion (Malik *et al.*, 2011; Franzelli *et al.*, 2016).

A classical assumption in order to reduce the complexity and computational cost associated with diffusion in turbulent simulations, is to postulate that heat and species diffusivities are equal (unity Lewis assumption). However, the inclusion of a real-fuel description, as discussed in the previous paragraph, usually requires the use of more accurate transport models.

1.2.4 Spray combustion

In many practical combustion devices, the fuel is injected as a liquid. Spray combustion, through the various injector and combustor designs and technologies, diversify the local length and time scales of the flow. As a result, various combustion regimes and flame structures may be observed. In particular, partially-premixed combustion covers a wide range of equivalence ratio, as freshly evaporated rich pockets mix while burning with the surrounding oxidant. Such non-homogeneities in composition space are susceptible to lead to non-negligible spatial and temporal variations of heat release rate, flame speed, intermediate species mass fraction, etc. The flammability limits could also broaden due to the temperature stratification, a side-effect that should be reproduced by the reaction mechanism. Eventually, all of these effects could impact the formation of pollutants. An illustration of these effects can be found in Jiménez *et al.* (2002) in the context of direct-injection engines, where it was shown that global NO levels present a strong sensibility to the length scale of the non-homogeneities.

The main spray-related problem arises from the fact that the range of timescales of the flow is considerably broaden, and that models must be provided for all the processes of injection such as, for example, atomization and evaporation. In relation with the multi-component aspect of real fuels that was discussed in Section 1.2.2, it is noted that evaporation also plays a crucial role on the resulting gaseous chemistry which should be considered in the chemistry description. Indeed, the chemical pathways of all single fuel components should be retained since, following a realistic evaporation process, inhomogeneities in the fuel composition can be observed in the gaseous phase (Cuoci *et al.*, 2005; Stagni *et al.*, 2016). This can become a major issue when trying to reduce a multi-component surrogate chemistry description.

1.3 Overview of chemistry description in LES

1.3.1 Tabulation methods

In practice, chemical kinetics in LES is today often taken into account through pre-tabulated laminar flame solutions computed with detailed chemistry. As discussed by Peters (1984), this method, adapted from attractive manifold approaches (Maas & Pope, 1992) very popular in RANS (Norris & Pope, 1995; Saxena & Pope, 1999), assumes that thermo-chemical evolutions in the composition/temperature space (phase space) can be parameterized by a reduced set of variables. Usually, these include the mixture fraction, characterizing the degree of fuel and oxidizer mixing, and the progress variable, monitoring the progress of reaction towards chemical equilibrium. All other quantities (mass fractions, temperature, thermochemical properties) are assumed unique functions of these variables and retrieved by interpolation from the database.

This approach drastically reduces the number of transport equations to be solved, and is thus very computationally efficient. Recent techniques falling into that category include the flame-generated manifold (FGM) (Oijen *et al.*, 2001), the Flame Prolongation of ILDM (FPI) (Gicquel *et al.*, 2000) or the Flamelet Progress Variable (FPV) (Pierce & Moin, 2004). Each method has been successfully employed to perform the LES of complex geometries, by considering various turbulence-chemistry interaction models: subgrid-scale PDF (Mahesh *et al.*, 2006; Galpin *et al.*, 2008; Ihme & Pitsch, 2008*b*; Avdić *et al.*, 2017), filtering procedures (Auzillon *et al.*, 2013; Philip *et al.*, 2015), artificially thickened flame front (Kuenne *et al.*, 2011; Philip *et al.*, 2015; Avdić *et al.*, 2013; Franzelli *et al.*, 2015*b*) and sometimes even, no model (Bekdemir *et al.*, 2013).

Obviously, simulations using tabulations are very much dependent upon the type of canonical configurations chosen to build the look-up table. The FPI and FGM models, in their original formulation, are based upon premixed canonical configurations, when the FPV model relies upon diffusion flamelets. Fiorina *et al.* (2005) and Vreman *et al.* (2008) have both investigated the impact of employing look-up tables constructed from premixed canonical flames on the prediction of diffusion and partially-premixed canonical test cases, and concluded that both approaches have distinct applicability ranges. Recent studies have addressed this issue. They include tabulation based upon premixed and non-premixed flamelet (Knudsen *et al.*, 2015), or based upon hybrid flamelet trajectories (Nguyen *et al.*, 2010; Franzelli *et al.*, 2013*a*), for which additional parametrization variables must be introduced; for instance, to identify the local combustion regime (Knudsen & Pitsch, 2009). Other techniques exist, relying upon arbitrary trajectories in the phase space. Increasing the number of controlling parameters (to more than 3), however, can eventually lead to excessive memory requirements and Input/Output cost in numerical simulations. Additionally, the usual definitions of the progress variable and/or mixture fraction might fail in providing a correct framework to retrieve all necessary quantities, typically, for multi-component mixtures (Niu *et al.*, 2013).

Another disadvantage of the tabulated approach is that the interactions between the flame and the flow are oversimplified. If this was not a problem in the RANS framework, it is more problematic in the context of LES. Taking into account complex phenomena like preferential diffusion, dilution, heat losses or slow pollutant chemistry requires additional modeling efforts that can be far from trivial. Very often, additional parametrization variables are introduced, for which transport equations must be solved (Fiorina *et al.*, 2004; Ihme & Pitsch, 2008*a*; Mueller & Pitsch, 2012, 2013), resulting in additional unclosed terms.

1.3.2 Global reaction mechanisms

Another classical approach consists in using globally-fitted chemical mechanisms, as introduced by Westbrook & Dryer (1981). In such methods, 5 to 10 major species interact in no more than one to four global reactions, the parameters of which are optimized against a set of flame characteristics over a specified parameter range. This method yields good results on global flame parameters such as temperature and burnt gas state, and is very CPU efficient due to the few considered variables. Also, the interactions between the flame and the flow are considered. For all these reasons, LES studies using global schemes are numerous (Selle *et al.*, 2004; Fureby, 2012; Jones & Tyliszczack, 2010; Franzelli *et al.*, 2015*b*), with, again, various turbulence-chemistry interaction models. This type of approach has been very much employed at CERFACS over the past decade, with usually, a thickened chemistry-turbulent interaction model (TFLES of Colin *et al.* (2000); Legier *et al.* (2000)).

The main disadvantage of this technique is that, by reducing the number of reacting steps, a very narrow range of operating conditions (usually, lean conditions) is covered. However, specific treatment can be employed in order to broaden the range of validity. Franzelli *et al.* (2010), for example, developed a systematic methodology to derive equivalence ratio varying two-step mechanisms, enabling them to be accurate under both poor and rich conditions. In addition, with this approach, the direct description of pollutant chemistry or complex, multi-component fuels is impossible because the necessary intermediate species are not included. A possible remedy to these drawbacks is to employ so-called "hybrid" techniques, relying upon the definition of a progress variable compatible with that of a tabulation technique so as to retrieve missing information (soot precursors, intermediate species, NO_x) from a look-up table (Lecocq *et al.*, 2014; Cuenot *et al.*, 2014; Jaravel, 2016). However, the drawbacks associated with tabulation are retrieved. Furthermore, the coupling between computed variables and tabulated variables requires additional modeling assumptions.

1.3.3 Physically based reduced reaction mechanisms

It is evident that both approaches introduced so far suffer from several drawbacks, the least of all being the very narrow resulting range of operability and the necessity to adapt the chemistry description to each simulation through, sometimes, daunting implementations of additional models. Additionally, these models should be carefully selected in accordance with the configuration under investigation. Indeed, inherent to these common approaches, is the need to know or guess *a-priori* the leading order phenomenon of the specific case; which could obviously lead to some erroneous conclusions under unexpected circumstances. Furthermore, for all the reasons discussed in Section 1.2, oversimplifying the interactions between the flame and the flow (unity Lewis assumption, for instance) and reorienting or removing kinetic pathways can be detrimental to the accurate prediction of pollutants. In this context, and since the available computational resources continue to increase, there is a need for methods and tools to perform a more physically-oriented reduction of detailed reaction mechanisms, in order to make the numerical simulation of reactive flow both computationally affordable and comprehensively accurate. Of tremendous importance, is the preservation of the most important kinetic pathways.

Discussed for example by Goussis & Mass (2011), a promising approach consists in performing an analytical reduction of kinetic mechanisms. The idea is based on the mathematical analysis of the timescales and species fluxes in a reaction mechanism. Typically, between 10 to 30 species and up to 500 reactions are retained in the final kinetic scheme, and most of the stiffness is eradicated. Due to their higher associated computational expense however, up until recently, such chemistry descriptions -labelled Analytically Reduced Chemistry in what follows or ARC- have mainly been restricted to small hydrocarbons and to premixed gaseous configurations. Table 1.1 summarizes LES which have included an analytical (or in some cases a detailed) description of the chemistry, in a relatively complex flow and/or geometrical configuration, since 2000. Though non-exhaustive, Table 1.1 provides a good overview of the current state-of-the art.

An inspection of Table 1.1 calls for several comments. First of all, as previously said, it is obvious that the use of comprehensive reaction schemes have been mainly performed in gaseous configurations, burning methane or hydrogen. For the latter, a detailed reaction scheme still is worth using, since the transport of 10-15 species suffices to reproduce a wide range of combustion phenomena (auto-ignition, premixed/non-premixed flames, detonations, ...). Second, many amongst these studies have considered the relatively canonical configuration of a jet issuing in a co-flow, to study auto-ignition. On the contrary, studies of swirling (confined or unconfined) burner are only a handful, and as of today, no studies have directly considered non-premixed realistic gaseous burners (as can be seen in Fig. 6 of Bulat *et al.* (2013), the Siemens SGT-100 burner has sufficiently long residence

Fuel type	Mechanism's specifics	Application's specifics	Refs.
hydrogen (H_2)	13 species, 28 reactions (Yetter *et al.*, 1991)	Auto-ignition of a gaseous jet (Markides & Mastorakos, 2005)	(Jones *et al.*, 2007) (Jones & Navarro-Martinez, 2008)
	9 species, 19 reactions (Jachimowski, 1992)	supersonic coflowing jet (Jarrett *et al.*, 1988)	(Moule *et al.*, 2014)
	9 species, 21 reactions (Mueller *et al.*, 1999)	Auto-ignition of a gaseous jet (Markides & Mastorakos, 2005)	(Tyliszczak, 2015)
methane (CH_4)	48 species, 300 reactions (Meyer, 2001)	Sandia Flames D (Barlow, 1996)	(Navarro-Martinez *et al.*, 2005)
	48 species, 300 reactions (Meyer, 2001) H_2/CH_4 mixture	Sydney bluff-body flame HM1 (Dally *et al.*, 1998)	(Navarro-Martinez & Kronenburg, 2007)
	44 species, 256 reactions (Lindstedt & Meyer, 2002)	Lifted flame (Cabra, 2004)	(Navarro-Martinez & Kronenburg, 2009)
	16 species, 25 reactions (Smooke & Giovangigli, 1991)	Forced ignition (Ahmed *et al.*, 2007)	(Triantafyllidis *et al.*, 2009)
	19 species, 15 reactions (Sung *et al.*, 2001)	Sandia Flames D-F (Barlow, 1996)	(Jones & Prasad, 2010)
	19 species, 15 reactions (Sung *et al.*, 2001) *(?)*	Sandia Flames D & F (Barlow, 1996)	(Garmory & Mastorakos, 2011)
	19 species, 15 reactions (Sung *et al.*, 2001)	Unconfined premixed gaseous burner (Schneider *et al.*, 2005)	(Jones *et al.*, 2012)
	8 species, 4 reactions (Peters, 1985) 8 species, 4 reactions (Seshadri & Peters, 1989) 13 species, 73 reactions (Lu & Law, 2008*a*)	PRECCINSTA burner (Meier *et al.*, 2007)	(Franzelli *et al.*, 2013*b*)
	19 species, 15 reactions (Sung *et al.*, 2001)	Industrial gaseous burner: Siemens SGT-100, 3 bars (Stopper *et al.*, 2009)	(Bulat *et al.*, 2013, 2014)
	22 species (Jaravel *et al.*, 2016)	Auto-igniting flame (Cabra *et al.*, 2005)	(Schulz *et al.*, 2017)
	22 species (Jaravel *et al.*, 2016)	Industrial gaseous burner: Siemens SGT-100, 3 bars (Stopper *et al.*, 2009)	(Jaravel *et al.*, 2016)
	9 species, 15 reactions (Sung *et al.*, 2001)	Extinction in swirling non-premixed flames (Cavaliere *et al.*, 2013)	(Zhang & Mastorakos, 2016)
ethylene (C_2H_4)	Various ARC see Section 4.3	Industrial gaseous burner (Geigle *et al.*, 2013)	This work see Chapter 7
ethanol (C_2H_5OH)	57 species, 383 reactions (Marinov, 1999)	Swirling spray flames	(Giusti & Mastorakos, 2016)
n-heptane (C_7H_{16})	22 species, 18 reactions (Liu *et al.*, 2004)	Auto-ignition of a gaseous jet (Markides & Mastorakos, 2005)	(Jones & Navarro-Martinez, 2009)
	22 species, 18 reactions (Liu *et al.*, 2004)	Spray auto-ignition constant volume vessel (Idicheria & Pickett, 2005)	(Gallot-Lavallee & Jones, 2016)
Kerosene	Jet-A2 POSF10325 surrogate Various ARC see Section 4.4	NASA-LDI (spray) (Cai *et al.*, 2005)	(Felden *et al.*, 2016) & this work, see Chapter 8
	$nC_{12}H_{26}$ surrogate 27 species, 452 reactions (Jaravel, 2016)	LEMCOTEC: Spray injection system (Guin & Orain, 2016)	(Jaravel, 2016)
	$nC_{12}H_{26}$ surrogate 24-species (You *et al.*, 2009; Franzelli *et al.*, 2016)	MERCATO	(Franzelli *et al.*, 2016)

Table 1.1: Summary of LES with analytical chemistry in complex flows since 2000

times to allow almost complete premixing before combustion). Studies interested with two-phase flow burners, adding a new layer of complexity, are also very sparse in the literature, and only two references (Jaravel, 2016; Franzelli *et al.*, 2016) could be found.

1.3.4 Turbulent combustion modeling with ARC

From the listed publications of Table 1.1, it is noted that mainly three frameworks have been considered so far to implement Analytically Reduced Chemistries (ARC) in LES codes, namely, the Conditional Moment Closure (CMC-LES), the transported subgrid PDF (PDF-LES) and the Analytically Reduced Chemistry with a thickened flame approach (ARC-TFLES). They all make use of different assumptions, and are thus not entirely equivalent. A rapid review of the main characteristics of the first two are presented hereafter, while the last one will be detailed in Section 6.2.2 of this PhD. thesis.

1.3.4.a CMC-LES

Similar to tabulated approaches, the idea behind CMC lies in the observation that the variation of almost any quantity of interest (species mass fraction, temperature, ..) can be related to that of one specific quantity. In non-premixed systems, this specific quantity is traditionally the mixture fraction (Y_z). Indeed, as illustrated in Fig. 1.9 depicting a scatter plot of temperature versus Y_z, any process inducing a fluctuation about any $Y_z = z$ translates into limited and predictable fluctuations in temperature. This is the evidence of a strong correlation between the mixture fraction and species mass fraction, temperature, etc. - at least in non-premixed systems. This correlation is best highlighted when looking at *conditional* averages: in Fig. 1.9, we see that the scatter of data in the T-Y_z plane is in fact well approximated by the line $< T|_z >$, representing the average of temperature conditional on Y_z values. The conditional expectation is here expressed in terms of the joint PDF of T and Y_z: $< T|_z > P(z) = \int T^* P(T^*, z) dT^*$. This mean is also referred to as a conditional first order moment in statistics. There exists an infinity of moments, providing information about the shape of the distribution of a scatter of data (second order moments are variances, third order moments are skewness, etc.).

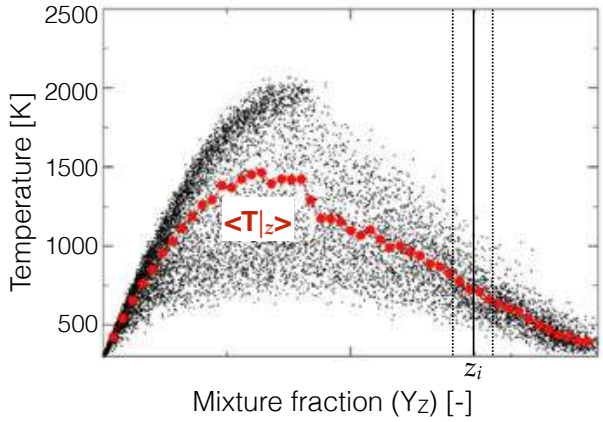

Figure 1.9: Illustration of the CMC concept.

Bilger (1993) makes use of the aforementioned observations to express species mass fractions Y and energy as the sum of a conditioned mean and a fluctuation. In case of a species k: $Y_k =< Y_k|_{z(\mathbf{x},t)} > + y(\mathbf{x}, t)$, where $< y(\mathbf{x}, t)|_{z(\mathbf{x},t)} >= 0$. Differentiating with respect to time and using the chain rule before substituting the results into the classical transport equations for Y_z and Y_k, which we write as (equal diffusivities D have been assumed),:

$$\rho \frac{\partial Y_z}{\partial t} + \rho \mathbf{v}.\nabla Y_z - \nabla \cdot (\rho D \nabla Y_z) = 0 \tag{1.1}$$

$$\rho \frac{\partial Y_k}{\partial t} + \rho \mathbf{v}.\nabla Y_k - \nabla \cdot (\rho D \nabla Y_k) = \rho W_k \tag{1.2}$$

leads to an equation for the conditional species $Q_k =< Y_k|_z >$ (Klimenko & Bilger, 1999):

$$\frac{\partial Q_k}{\partial t} + < \mathbf{v}|_z > .\nabla Q_k - < N|_z > \frac{\partial^2 Q_k}{\partial z^2} = < W_k|_z > + e_{Q_k} + e_Y \tag{1.3}$$

where $N = D(\nabla z)^2$. Note that the original definitions are here presented, where the conditional fluctuations of density are neglected. Expressions for e_{Q_k} and e_Y require closure assumptions. Usually:

$$e_{Q_k} = 0 \tag{1.4}$$

stemming from a high Reynolds numbers assumption, and:

$$e_Y = \frac{-div(\rho_z < \mathbf{v}'' y|_z > P(z))}{\rho_z P(z)} \tag{1.5}$$

where $\mathbf{v}'' = \mathbf{v} - < \mathbf{v}|_z >$ and $\rho_z =< \rho|_z >$; this is referred to as the *primary closure hypothesis*. The same treatment is applied to the energy variable, often chosen to be the enthalpy h, so that an equation for $Q_h =< h|_z >$ reads:

$$\frac{\partial Q_h}{\partial t} + < \mathbf{v}|_z > .\nabla Q_h + \frac{div(< \mathbf{v}'' h''|_{z''} > \rho_z P(z''))}{\rho_z P(z'')} =< N|_z > \frac{\partial^2 Q_h}{\partial z'^2} + < \frac{1}{\rho}\frac{\partial p}{\partial t} > - < W_R|_{z'} > \tag{1.6}$$

where W_R is the heat loss rate per unit mass due to radiation.

In parallel, Klimenko (1990) derived the same set of equations, but from a probability standpoint, by investigating the joint PDF of Y_z and Y_k (or h), defined as P(z,y_k)=$< \Psi >$ where $\Psi = \delta(z^* - z)\delta({y_k}^* - y_k)$ is the fine-grained PDF of Y_z and Y_k. Deriving a transport equation for Ψ and averaging yields an equation for the joint PDF (see Eq. 56 in Klimenko & Bilger (1999)). After manipulation of this equation, an unclosed equation is found, which reduces to Eqs.1.3 & 1.6 under the primary closure hypothesis.

In the context of LES, ensemble averaging is employed:

$$< Y_k(\mathbf{x},t)|z > = \overline{Y_k(\mathbf{x},t)|z} = \frac{\int_{\mathbf{x}'} Y_k \delta(z - \zeta(\mathbf{x}',t)) G_\Delta(\mathbf{x} - \mathbf{x}') d\mathbf{x}'}{P(z)} \tag{1.7}$$

with ζ the fine-grained mixture fraction and G_Δ a positive defined space filter of width Δ. To take into account density variations, a Favre averaging is often preferred (Bushe & Steiner, 1999; Navarro-Martinez *et al.*, 2005; Kim, 2005), defined as:

$$\widetilde{Y_k(\mathbf{x},t)}|_z = \frac{\overline{\rho Y_k(\mathbf{x},t)|_z}}{\overline{\rho}|_z} \tag{1.8}$$

and

$$\widetilde{P(z)} = \frac{P(z)\overline{\rho}|_z}{\overline{\rho}}. \tag{1.9}$$

With these notations, the filtered mass fraction of species k is: $\widetilde{Y_k(\mathbf{x},t)} = \int \widetilde{Y_k(\mathbf{x},t)}|_z \widetilde{P(z)} dz$ and Eqs.1.3 & 1.6 are still valid (Navarro-Martinez *et al.*, 2005).

Although it provides very good results (see refs in Table 1.1), the downside of this approach is its complexity. On top of a closure for the equations themselves (Eqs. 1.3 and 1.6), closures for the conditioned quantities ($\widetilde{\mathbf{v}|_z}$, $\widetilde{N|_z}$,$\widetilde{W|_z}$, ...) must also be provided. Furthermore, as it is the unconditioned quantities that are of interest, a shape for $\widetilde{P(z)}$, the PDF of mixture fraction, should be provided. A β-shape is often assumed, based upon Y_z and its fluctuations (Bushe & Steiner, 1999), but the model is not universal. Also, Eq. 1.3 & 1.6 are resolved for each species *plus* a sufficient sample space of Y_z, which may lead to excessive computational requirements so that, usually, CMC grids are coarser than the LES grid. This further calls for specific techniques to conistently couple LES with CMC quantities. Sometimes, the spatial dimensionality can be reduced in the equations, to make the problem computationally affordable, leading to so called "0D/1D or 2D-CMC" resolutions, but loosing

information in the process. Because of all of these subtlelties, the method is not systematic. In particular, the primary closure hypothesis fails if conditional fluctuations are not small, as it is the case if differential effects are important (Kronenburg & Bilger, 2001), for then the e_Y term in Eq. 1.3 needs further attention. Extinction/autoignition problems also require special treatments, and DePaola (2007) suggests resorting to higher order closures for the conditional chemical source term, an approach that introduces a whole new set of equations to solve.

1.3.4.b PDF-LES

If the equations describing the fluid motion are directly filtered at the LES scales, a closure for the source term in Eq. 1.2 should be provided. The idea behind PDF subgrid models is that fluctuations lost by the filtering procedure can be retrieved by introducing a PDF. These PDF can be presumed (with a β-shape for example) or resolved. In a way, the CMC procedure can be considered as a sort of presumed-PDF method, where the shape of $\mathrm{P}(Y_z)$ was assumed, but the distribution of the conditioned quantities were directly accounted for. Presumed PDF methods are only interesting when the chemistry can be described by a few control variables, like in the CMC approach. Of more interest are resolved PDF methods.

In resolved PDF approaches applied to LES, a density weighted filtered PDF for the N_s+1 species of interest -plus enthalpy, $\mathbf{\Phi}$ is defined:

$$\widetilde{P_{sgs}}(\mathbf{\Phi},\mathbf{x},t) = \frac{\int \rho(\mathbf{x}')\Psi_{N_s+1}(\mathbf{\Phi},\mathbf{x}',t)G_\Delta(\mathbf{x}-\mathbf{x}')d\mathbf{x}'}{\overline{\rho}} \tag{1.10}$$

where Ψ_{N_s+1} is the fine-grained PDF of $\mathbf{\Phi}$. The equation governing its evolution reads, (Colucci *et al.*, 1998; Gao & O'Brien, 1993; Jones & Navarro-Martinez, 2009):

$$\begin{aligned} &\overline{\rho}\frac{\partial\widetilde{P_{sgs}}(\mathbf{\Phi})}{\partial t} + \overline{\rho}\widetilde{u_j}\frac{\partial\widetilde{P_{sgs}}(\mathbf{\Phi})}{\partial x_j} + \sum_{\alpha=1}^{N_s+1}\frac{\partial}{\partial\Psi_\alpha}[\overline{\rho}\dot{\omega}_\alpha(\mathbf{\Phi})\widetilde{P_{sgs}}(\mathbf{\Phi})] = \\ &-\frac{\partial}{\partial x_i}\left[\Gamma\frac{\partial\widetilde{P_{sgs}}(\mathbf{\Phi})}{\partial x_i}\right] - \sum_{\alpha=1}^{N_s+1}\sum_{\beta=1}^{N_s+1}\frac{\partial^2}{\partial\Psi_\alpha\partial\Psi_\beta}\left[\left(\frac{\mu}{\sigma}\overline{\frac{\partial Y_\alpha}{\partial x_i}\frac{\partial Y_\beta}{\partial x_i}|\mathbf{Y}=\mathbf{\Phi}}\right)\widetilde{P_{sgs}(\mathbf{\Phi})}\right] \end{aligned} \tag{1.11}$$

In this derivation, unity Lewis numbers have been assumed, as it is almost always the case with this type of approach. The transport coefficient is given by Γ, which includes a gradient assumption to model the PDF transport by sub-grid turbulent fluctuations. The last term on the right hand side, referred to as the "micro-mixing term", represents the effect of molecular diffusion on the sub-grid PDF and must be modeled.

This PDF transport equation cannot be solved directly, and two techniques are generally employed: Lagrangian Monte Carlo approach, or the Eulerian stochastic field method. With the first one, the phase space is described by particles corresponding to a particular state, following a stochastic motion (Colucci *et al.*, 1998). The filtered chemical source term can then be evaluated from the reconstructed PDF. The Eulerian stochastic field method is the technique used in most studies employing a PDF-LES presented in Table 1.1. With this approach, an ensemble of N stochastic fields ξ_n^α is transported (typically, in between 5 and 15) for each species α (see, e.g., Valiño (1998) or Sabel'nikov & Soulard (2005)), and filtered quantities are retrieved by direct averaging (Jones & Navarro-Martinez, 2009).

This method yields excellent results. However, here also, the number of equations to solve can quickly become prohibitive, since about 10 stochastic fields are usually required. Furthermore, as with the CMC-LES method, many unclosed quantities appear in the equations, and choosing a proper model is, here again, strongly case-dependent.

1.4 Objectives and structure of the PhD thesis

Over the past 30 years, CERFACS has developed an expertise in Computational Fluid Dynamics (CFD) and more specifically in LES with the solver AVBP, co-developed with the IFPEN [7]. AVBP is continuously improved by the work of students and senior researchers, and has been successfully employed to study a wide

[7] Institut Français du pétrole et énergies nouvelles

range of turbulent flows applications, including combustion, in relatively complex geometries. Historically, the inclusion of chemistry in AVBP was done through the use of global schemes, with a thickened flame chemistry/turbulence interaction model (TFLES). Irreversible one-step chemistries in simple 2D configurations were first considered (Colin *et al.*, 2000), before two-step (2S) schemes were introduced in more complex geometries (Selle *et al.*, 2004; Franzelli *et al.*, 2012). A systematic methodology to produce 2S schemes for any type of fuel, valid over a wide range of equivalence ratio, was developed by B. Franzelli during her PhD thesis Franzelli *et al.* (2010), along with a whole set of dedicated pre and post-processing AVBP tools. More recently, tabulation has also been implemented in AVBP (Vicquelin, 2010), with a dedicated filtered combustion model (Auzillon, 2011). These developments paved the way to many reacting LES studies over the past few years.

As said in the introduction, the available computational power is fast increasing, and the use of more refined chemistry descriptions are becoming affordable. The primary objective of this PhD thesis is to investigate in more depth the possibilities offered by ARC in LES, in terms of description of the flame structure and dynamics; and to confront this approach to the more usual techniques: tabulation and global mechanisms. Such a comparison is highly valuable in the current context of growing interest for more detailed chemistry descriptions in order to gain insights on pollutants formation. Another objective is to implement ARC as well as all the necessary environment in AVBP. In view of the previous discussion, the chosen framework to couple chemistry with turbulence is the TFLES model. This model appears as the "simplest" of all approaches presented so far, and it does not require the formulation of modeling assumptions or simplifications. It is therefore very easily coupled with ARC and, together, the framework has great potential to address the complexity of real aeronautical combustor geometries.

The work of this PhD thesis is strongly correlated with that of Jaravel (2016), who also worked with ARC chemistries in the context of pollutant prediction -NO_x and CO. In collaboration, implementation of ARC in the LES solver AVBP was achieved, including special treatments to deal with the stiffness or with the cost associated to the classical evaluation of the source terms, see Section 6.3.3. Extension of the DTFLES model of Colin *et al.* (2000) to multi-step chemistries was performed by Jaravel (2016); this model is discussed in Section 6.2.2 of the present work. This development allowed a successful preliminary series of validations of the ARC-DTFLES methodology in AVBP, on simple configurations such as 3D laminar premixed flames and 2D strained counterflow diffusion flames, a subset of which is presented in Chapter 7 of Jaravel (2016). Full scale validation of the methodology in a quasi DNS of a turbulent non-premixed configuration (Sandia flame D) was also performed by Jaravel (2016).

In parallel and complementing these achievements, the present work focuses on:

- The methodology to obtain case-specific ARCs, with a review of the dedicated techniques and tools available, as well as detailed examples of derivations with the tool YARC (Pepiot, 2008) (Chapters 3 and 4).
- The comparison, in terms of prediction capabilities and CPU cost, of employing an ARC in place of a more usual look-up table or global scheme, in a realistic sooting non-premixed swirled combustor (Chapter 7). The impact of the chemistry description on soot formation is investigated.
- The overall feasibility of considering real, multi-component kerosene fuels in complex LES simulations through ARC. This includes a detailed investigation of the feasibility of implementing a traditional multi-component surrogate description in LES (Section 4.4), in contrast with a novel hybrid chemistry model (Xu *et al.*, 2017*b*) (HyChem). LES of a two-phase flow configuration featuring a lean direct Jet A injection is performed with an HyChem model (Chapter 8).

Part I

Combustion chemistry

Chapter 2

Chemistry of combustion

Contents

2.1 Introduction

As discussed in the introduction, combustion is a very complex phenomenon, characterized by the interaction and competition of various physical and chemical processes, with associated length scales and time scales ranging from nanoseconds to years. In real life, the oxidation of hydrogen, for example, which is one of the simplest reaction process, requires countless collisions of numerous species (or elementary reactions) before reaching some kind of macroscopic equilibrium state. That final state is much dependent upon the temperature and pressure of the environment, as well as upon the initial mixture state. The accurate description and prediction of this process through computer modeling would require as much as 10 species interacting through a 30 reactions scheme (e. g., Boivin (2011)). Usually, what we call a *detailed reaction scheme* is in fact a collection of physical, elementary reactions occurring between a specified set of species that allows to describe with the most accurate precision the evolution of a reactive system in all possible configurations. The reaction of hydroxy radicals (OH) with molecular hydrogen (H_2) forming water and hydrogen atoms is such an elementary reaction $OH + H_2 -> H_2O + H$, and describes a mechanism that effectively occurs when an OH molecule collides with an H_2 molecule.

Three types of elementary reactions exist: *unimolecular, bimolecular* and *trimolecular reactions.*

- Unimolecular reactions describe the dissociation of a given reactive molecule A to form products, $A -> Products$. They usually have a first-order reaction rate, which means that the rate at which the reaction proceeds can be expressed linearly in terms of the concentration of the reactive molecule A as $k[A]$.

- Bimolecular reactions proceed through the collision of two molecules A and B, according to the reaction equation, $A + B -> Products$. These are the most frequent type of reactions. They follow a second-order rate law of the type $k[A][B]$.

- Trimolecular reactions involve three reactant molecules, $A + B + C- > Products$. Usually, trimolecular reactions are recombination reactions that form the products, and they obey a third-order rate law. The reason a third body is often needed in recombination reactions is that those are exothermic reactions, and the third body must carry away some of the energy. Trimolecular recombination reactions are very important, as will be exemplified in the next Section.

2.2 Reaction pathways of hydrocarbon oxidation

Hydrocarbons are molecules composed of carbon and hydrogen atoms (C_nH_m), and as such, they share several common features. Furthermore, the collection of elementary reactions, or reaction pathways, needed to describe the oxidation of heavy hydrocarbons are usually comprised of at least part of the reaction pathways of lighter hydrocarbons. Good examples illustrating this are the mechanism for C2-C3 fuel combustion developed by Wang *et al.* (1999*a*), and the mechanism(s) for the description of fuel components as surrogates, developed over the past years by Narayanaswamy and co-workers [1]. This permits a general discussion on hydrocarbon oxidation.

2.2.1 Presentation of the chain reaction sequence

Of tremendous importance in hydrocarbon oxidation is the presence of *radicals*. A radical is a compound with an unfilled outer electron configuration, and is highly reactive. Their electron cravings make them efficient intermediates in reaction schemes. Contrary to what could be concluded at first glance, the fact that radicals are usually present in very small amounts throughout the combustion process shows that they play a central role in chemical kinetics: as soon as they are produced, they react and disappear. Examples of radicals include the hydroxyl radical OH and the oxygen and hydrogen atoms O and H. The different types of reactions encountered in the combustion of hydrocarbons involve radicals in a chain of reactions that can be sequenced (Strahle, 1993) :

- **Chain initiation steps** are characterized by the formation of reactive species such as radicals, from the initial stable species.
- **Chain propagation steps** are characterized by a reactive intermediate species reacting with stable species to form another reactive species.
- **Chain branching steps** are similar to chain propagation steps with the exception that more reactive species have to be produced than reactive reactants where consumed.
- **Chain termination steps** reform stable species from reactive ones.

Chain branching reactions are particularly important, especially in ignition processes (Warnatz *et al.*, 1995; Strahle, 1993). An illustration of such a scheme is given hereafter with the most important reactions with respect to ignition in the hydrogen-oxygen system (Warnatz *et al.*, 1995).

(0)	$H_2 + O_2 = 2OH*$	chain initiation
(1)	$OH* + H_2 = H_2O + H*$	chain propagation
(2)	$H* + O_2 = OH* + O*$	chain branching
(3)	$O* + H_2 = OH* + H*$	chain branching
(4)	$H* = 1/2H_2$	chain termination
(5)	$H* + O_2 + M = HO_2 + M$	chain termination

The last reaction is an example of a trimolecular recombination reaction. The M here refers to any inert molecule (in the atmosphere, generally N_2 and O_2), that poses as a third compound. That type of reaction is called a three-body reaction. It involves two species and yields one single product species, but it requires a third body M to stabilize the excited product by collision.

One of the biggest issue arises from the fact that the privileged reaction pathways (e. g., leading to auto-ignition) of a specific fuel, and comprising all of those different steps, depend greatly upon the considered application and its temperature, pressure and equivalence ratio conditions. Three regimes can be distinguished, depending upon the initial temperature:

[1] http://krithikasivaram.github.io

1. **A low temperature oxidation mechanism**, characterized by a temperature < 650 K
2. **A moderate temperature oxidation mechanism**, with a temperature ranging from 650 K to 1000 K, which will be governed by HO_2 and H_2O_2 chemistry
3. And **a high temperature oxidation mechanism**, characterized by a temperature > 1000 K

In theory, a detailed mechanism for a specific fuel should account for each one of those different regimes. Going back to Fig. 1.7(b), showing the ignition delay of a mixture of iso-octane with air, the three different zones are clearly distinguished: up until 700 K and above 1000 K, the ignition timing is decreasing with the increase of the temperature, but in between, the reverse is observed. This zone is usually labeled the Negative Temperature Coefficient (NTC) zone, and stems from the competition between the high and low temperature reaction pathways. Unfortunately, this type of behavior is very much fuel specific at low temperature and can lead to very complex reaction systems.

A review of the different types of elementary reactions comprising typical hydrocarbon reaction mechanisms is provided hereafter.

Synthetic review of the different types of reactions

- **Initiation steps** :
  - These can be unimolecular, by *homolysis*, a dissociation process where the molecule breaks at a $C-C$, $C-H$, $C-O$, $O-O$ or $O-H$ location, with each of the fragments retaining one of the originally bonded electron,
  $$CH_3CH_3 -> 2CH_3*$$
  - or bimolecular by *hydrogen atom abstraction*,
  $$CH_3CH_2CH_3 + O_2 -> CH_3CH_2CH_2* + HO_2*$$

  The activation energies of the homolysis initiations are usually way higher than those of the bimolecular initiations (by a factor 2) and as such, are important steps at high temperature only (see the next paragraph).
- **Propagation and branching steps** :
  - *Additions* : They consist in the combination of molecules to form a larger one. Of importance is the addition of a radical on a double bond location,
  $$CH_2 = CH_2 + H* -> CH_3CH_2*$$
  and the oxygen addition (double bond too) to a radical molecule,
  $$CH_3CH_2* + O_2 -> CH_3CH_2OO*$$
  Those reactions are particularly important when the temperature is low, due to their low activation energies.
  - *Isomerizations* : is the rearrangement of the atoms inside a molecule. The result is a molecule with the same chemical formulae, or an isomer.
  $$CH_3CH_2OO* -> CH_2*CH_2OOH$$
  - *Dissociations* : A bond breaks in the species, producing two smaller compounds. Of interest in combustion are dissociations leading to the formation of a ring, or *cyclization*; specifically those leading to the formation of cyclic ethers, compounds composed of an oxygen atom linked to a linear carbonated chain, encountered at low temperatures:
  $$CH_2*CH_2OOH -> CH_2OCH_2 + OH*$$
  Of importance also are β *scissions*, where the splitting leads to the formation of a smaller radical and an unsaturated compound (with at least one complex bond), encountered at high temperatures:
  $$CH_3CH_2CH_2CH_2* -> CH_3CH_2* + CH_2 = CH_2$$

Another important type of dissociations, contributing to the switching from low temperature to high temperature pathways, is what we will call *internal oxidation*, where peroxyl radicals ($ROO*$) split from their two oxygen atoms:

$$CH_3CH_2OO* -> CH_2CH_2 + HO_2*$$

Finally, chain branching types of dissociations are also frequent, one of the most important being:

$$H_2O_2(+M) -> OH* + OH* (+M)$$

responsible, for instance, for the third explosion limit of hydrogen shown in Fig. 1.7.

– Hydrogen atom exchanges: Amongst those type of reactions, we will mention those involving an oxygen molecule stealing an hydrogen atom from an an alkyl radical,

$$CH_3CH_2* + O2 -> CH_2CH_2 + HO_2*$$

and classical H *abstraction* by a radical, which is an important source of chain branching,

$$CH_4 + O* -> CH_3* + OH*$$

Those last reactions play a key role in combustion, and constitutes the majority of the propagation reactions.

- **Termination reactions** :
  - Of interest are *combinations*, where two radicals combine to produce a molecule
  - and *disproportionation*, where two radicals combine to produce two molecules.

$$CH_2CH*CH_2 + HO_2* -> CH_3CHCH_2 + O_2$$

This non-exhaustive list of important reactions is mostly concerned with alkane oxidation (C_nH_{2n+2}). First off, because alkanes are the most representative constituents of today's commercial fuels and thus, deserve all of our attention; but also because not much can be found on the oxidation of other types of hydrocarbon, such as alkenes (e.g. ethylene), alkynes (e.g. acetylene) and aryls (e.g. benzene). Furthermore, the few articles available on the literature today on that subject stress that the oxidation processes of such hydrocarbons are fairly similar to that of the alkanes, at least when the carbon chain is not too large (Mehl *et al.*, 2008; Touchard *et al.*, 2005).

The rest of this presentation will therefore focus on alkane oxidation, but keeping in mind that fuel specificities may modify these general considerations.

2.2.2 High and intermediate temperature oxidation chemistry

As presented previously, the initiation steps are responsible for the initial decomposition of the reactants, and lead to the formation of the radicals. At high temperature, chain initiation steps consist of thermal homolysis of the hydrocarbon into smaller alkyls,

$$R -> R_1* + R_2*$$

but also of the attack of the hydrocarbon by H*, *O* and *OH radicals, that have been generated by the chain-branching steps of the oxyhydrogen reaction system (Battin-Leclerc *et al.*, 2000; Warnatz, 2000),

$$R + H* -> R* + H_2$$

Those alkyls then decompose very quickly into alkenes and smaller alkyl radicals, through β-scission for instance. Actually, the reactions leading to C1-C2 fragmentation are commonly considered too fast to be rate limiting, and eventually, only insights on the chemistry of radicals such as the hydrogen H*, methyl CH_3* and ethyl C_2H_5* radicals is required (see Fig. 2.1). The remaining radicals actively participate in chain propagation and chain branching steps, as they can react with oxygen and amongst themselves in a series of chain branching reactions. At the core of chain branching, remains the reaction:

$$H* + O_2 -> *OH + O*$$

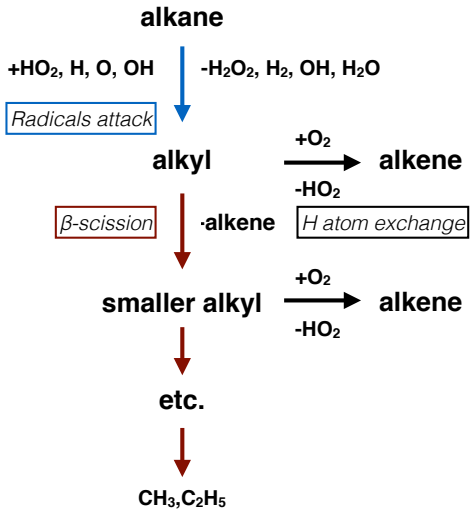

Figure 2.1: High temperature alkyl radical decomposition, from (Warnatz, 2000).

In the intermediate temperature range previously discussed (higher NTC region, typically $850K < T < 1000K$) the following termination and metathesis reactions are privileged,

$$2HO_2 * -> H_2O_2 + O_2$$
$$HO_2 * + RH -> H_2O_2 + R*$$

eventually leading to the homolysis of the H_2O_2 molecule, so called *degenerate chain branching*,

$$H_2O_2 -> 2HO*$$

which will increase the production of the highly reactive *OH radical, and eventually lead to an exponential acceleration of the reaction rates. This behavior is known to lead to auto-ignition.

2.2.3 Low temperature oxidation chemistry and NTC region

At low temperature, numerous secondary pathways involving interaction with radicals develop, as there is not enough energy to split the bonds and break molecules into smaller alkyls. As a first consequence, the chain initiation steps consist almost exclusively in the attack of the hydrocarbon by small radicals and oxygen. The oxygen addition on the produced alkyl radicals constitute the privileged pathway, leading to the formation of peroxyalkyl radicals that, in turn, isomerize or directly disproportionate,

$$R * + O_2 -> ROO*$$

$$ROO * -> *QOOH$$
$$ROO * + HO_2 * -> ROOH + O_2$$

This last step is prone to lead to further degenerate branching of the carboxylic acid and to the active production of reactive chain carriers. The isomer products are subject to new oxygen additions, leading to the formation of di-hydroperoxyalkyls, or can decompose to cyclic ethers and oxygenated compounds that will also lead to the production of reactive chain carriers.

$$*QOOH + O_2 -> *OOQOOH$$
$$*QOOH -> products + X*$$

Overall, the low temperature oxidation paths are inextricable and very fuel dependent, which makes them difficult to predict. As a consequence, the reduction of kinetic schemes at low temperature is less efficient than at higher

temperature, because a lot of species have to be kept in order to account for those diverse pathways. This is readily seen on Fig. 2.2 that summarizes the discussed pathways for alkane oxidation. The reversibility of the oxygen addition ((1) in the aforementioned Figure) when the temperature increases to the benefit of the oxidation path ((2) in the aforementioned Figure) leads to an overall reduction of the reaction rate, that induces the appearance of the NTC regime mentioned previously. Indeed, in this range (lower NTC region, typically $650K < T < 800K$), the generation of H_2O_2 is in fact chain terminating because the activation energy of the degenerate chain branching remains too high. Accounting for this range is of importance, for example, when studying spark-ignition engines, when cool flames responsible for engine knock are susceptible to occur.

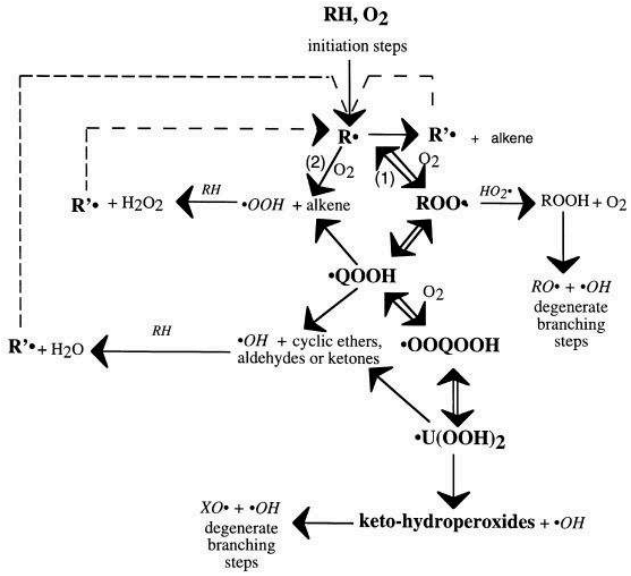

Figure 2.2: Simplified scheme for the oxidation of alkanes, from (Battin-Leclerc *et al.*, 2000). (1) low temperature pathways and (2) high temperature pathways.

2.2.4 Pollutant formation

A concise review of the mechanisms of formation of the pollutants of interest in this work are given hereafter, namely, CO, NO_x and soot, with emphasis on the reaction steps and pathways through which they proceed. These pathways complement the ones discussed in the two previous Sections.

2.2.4.a NO_x

NO and NO_2 are nitrogen oxides, collectively called NO_x. NO is the predominant nitrogen oxide emitted by combustion devices. For reasons discussed in the introduction, it is harmful to human health, and therefore it is of interest to accurately understand its generation process. NO_x chemistry is rather complex, as it involves the carbonated phase, and spans large range of timescales. It is usually thought of as a post-flame phenomenon, but NO_x formation actually occurs in the reactive zones as well. Still, different formation mechanisms have be identified, also labelled *formation routes*. The three major ones, relevant under gas-turbine conditions are the Thermal route, the Prompt route and the N_2O route (Correa, 1993; Miller & Bowman, 1989).

- Thermal NO is also known as the Zeldovich NO, because it is described by the extended Zeldovich mechanism (Zeldovich, 1946):

$$\begin{aligned} O + N_2 &= NO + N \\ N + O_2 &= NO + O \\ N + OH &= NO + H \end{aligned}$$

  As the first reaction has a very high activation energy, due to the triple bond in the N_2 molecule, this route is only significant at high temperature, typically above 1800 K, so that thermal formation of NO

occurs mostly in the burnt gases. Furthermore, the first reaction is also very slow, and reaching equilibrium requires very long residence times, so that in typical combustion devices, exhaust concentrations of NO remain well below equilibrium values. Finally, predictions from this mechanism are very sensitive to the concentrations of radicals O and OH and coupling with the combustion process is necessary (Miller & Bowman, 1989).

- Another mechanism, important especially under fuel-rich conditions, is the Prompt NO mechanism, suggested by Fenimore (1971, 1976). The prompt refers to a fast process occurring in the flame's core from the interaction of N_2 with radicals generated by fuel oxidation. CH* is sought to play a central role in this mechanism, through the radical attack:

$$N_2 + CH = HCN + N$$

and subsequently, rapid oxidization of HCN into NO, through species like NCO. However, the direct formation of HCN has been regarded as unphysical in recent publication (Miller *et al.*, 2005) and the reaction :

$$N_2 + CH = NCN + C$$

is now preferred (Moskaleva & Lin, 2000). Contribution from this route in the post-flame is generally negligible, because hydrocarbon radicals are usually unavailable.

- N_2O is mainly formed by the addition of N_2 and O (and collision with a third body), under relatively low temperature. N_2O then reacts with radicals to form NO. It can be a substantial route under fuel-lean, high pressure conditions, when CH radicals are no longer produced, and is therefore a route to preserve when studying aero-engine combustors.

Fuel-nitrogen can also be an important source of NO, when considering realistic fuels. It stems from the nitrogen chemically bound in the fuel. However, the fuel representation should account for the N atom in its composition.

2.2.4.b CO

CO is an important intermediate in the way of converting the fuel to products, as it is the sole precursor of CO_2. It usually peaks in the flame zone, and the most important pathways leading to its formation involve the formaldehyde species (CH_2O) and the formyl radical (HCO). CO subsequently oxidize into CO_2 in a chain of very slow reactions, involving radicals such as OH and O, which are incidentally involved in other faster competitive reactions. Under lean conditions, or around stoichiometry, as it should theoretically be the case in new technologies, equilibrium values are usually low and high CO levels in gas-turbine exhausts stems from short residence times and other unsteady phenomena (extinction, wall interactions, mixtures inhomogeneities due to spray combustion, etc.) perturbing the radical pool.

2.2.4.c Soot

Phenomenology Soot are fractal-like aggregates of very small spherical primary particles. Those primary particles, when looked under the microscope, are found to be made of crystallite, which are stacked carbonaceous layers (see Fig. 2.3(a)). Soot also contains a non-negligeable amount of hydrogen: the soot atomic C/H ratio ranges from 8 to 12. Of course, the exact composition and extent of soot aggregates depend on the local conditions, flame type and fuel characteristics.

The bulk of soot mass is commonly regarded as being in the form of polynuclear aromatic hydrocarbon (PAH), which are condensed aromatic ring structures (Bockhorn, 1994). PAHs are usually formed under rich conditions (with intermediate temperature) from unburned hydrocarbon intermediates. The formation of the initial aromatic rings is not well understood, but is thought to include precursors like C_3H_3, C_4H_5 or C_5H_5 in a series of steps that are still the subject of discussions (Frenklach, 2002; Glassman & Yetter, 1987). They can also be a product of fuel pyrolysis. PAHs then grow and coalesce, until they form a nuclei of a few nanometers in diameter: this is known as the *soot inception* phase. This phase, which is also still not clearly understood due to its apparent versatility (Calcote, 1981), is however commonly regarded as being dominated by the kinetics of the acetylene species (C_2H_2), e. g., through the so-called HACA mechanism (H-abstraction-C_2H_2-addition) of

Frenklach & Wang (1991*a*), illustrated in Fig. 2.3c. Subsequently, mass growth of the particles occur, through surface reactions with the gas-phase (also thought to be dominated by C_2H_2), until they reach a size of about 30 nm, beyond which particles aggregate (or coalesce) into fractal like structures, as reported on Fig. 2.3(b).

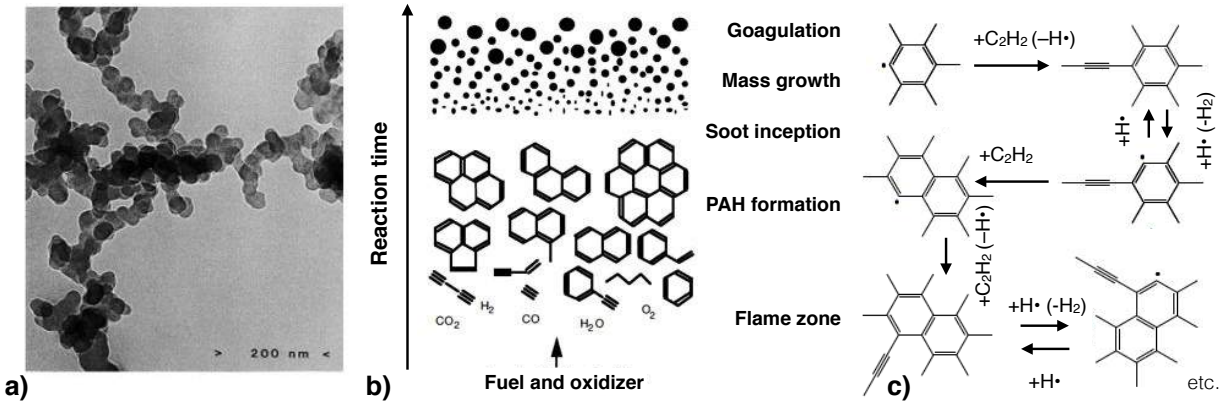

Figure 2.3: a) Visual of soot aggregates, from (Warnatz *et al.*, 1995), b) elementary processes of soot formation, adapted from (Bockhorn, 1994) and c) the HACA principle.

The routes leading to the formation of soot precursors should theoretically already be included in the pathways of fuel oxidation discussed in Section 2.2.2 and 2.2.3. However, the subsequent formation and growth of PAHs until soot inception requires to add many specific pathways not necessarily considered. Finally, the process following soot inception can no longer be considered as a gas-phase chemistry, and requires special treatment.

Solid phase modeling Following Kennedy (1997), soot models can be categorized into three main classes: empirical, semi-empirical and detailed. Empirical models basically reduce to correlations obtained from experiments. Semi-empirical models include part of the physics of the problem, by considering a simplified reaction scheme of a few key steps (Leung *et al.*, 1991; Moss *et al.*, 1995). In that sense, it is the equivalent of the global mechanisms for gas phase chemistry discussed earlier. One such model widely employed in gas turbine applications is the two-step semi-empirical model proposed by Leung *et al.* (1991). This model, which will be further detailed in Section 7.4, consists of two rate equations: one for the soot mass fraction Y_s, and the other for the soot number density n_s measuring the ratio of soot particles number to the total volume. In its original formulation, the model assumes that acetylene is the sole soot precursor, and only retains O_2 in the oxidation processes. By modifying the model constants related to the reaction rates, this simple model has been applied under a wide range of operating conditions, in various configurations (Bolla *et al.*, 2013; Lecocq *et al.*, 2013).

The use of detailed soot models in LES is more recent, and limited to academic configurations due to the additional complexity introduced by the various pathways to consider, associated with an increase in computational requirements. The treatment of surface reactions (or heterogeneous chemistry) and particles interactions in particular, through which soot aggregates grow, is a very complex phenomenon requiring sufficient knowledge of the size, shape and surface "active" sites of the particles (Blanquart & Pitsch, 2009). Usually, LES computations employing a detailed soot model rely on the relatively complex method of moments, or the computationally expensive sectional (or bins) method. Information about these detailed soot models, as well as a plethora of references can be found on the recent comparative study of Roy & Haworth (2016).

2.3 Reaction rates

2.3.1 Rate laws and elementary reaction rates

For a given reaction between reactants A_i, $i \in \mathcal{R}$ written in the general form:

$$\sum_{i \in \mathcal{R}} \nu_i' A_i -> \mathcal{P} \tag{2.1}$$

where $\mathcal{P}$ stands for the set of products and ν_i' for the stoichiometric coefficient of species A_i; the *rate law* describes how fast the transformation proceeds and specifies the dependency of the reaction rate upon the temperature,

pressure and concentration of the chemical species involved. As said in Introduction, it usually takes the general form, for a specific A_i species:

$$\frac{d[A_i]}{dt} = -k \prod_{j \in \mathcal{R}} [A_j]^{\nu'_j} \tag{2.2}$$

The sum of the exponents is the order of the reaction, generally 1, 2 or 3. For a "physical" reaction, the behavior of the reaction rate coefficient k is very much temperature dependent, and can be expressed in the general Arrhenius form:

$$k = AT^n exp\left(\frac{-E_a}{RT}\right) \tag{2.3}$$

where T is the temperature, R is the universal gas constant, A is the pre-exponential factor or frequency factor (units dependent upon the type of reaction), n is the temperature exponent and Ea is the activation energy (kJ/mol). Indeed, not all molecular collisions result in a reaction, and a minimum kinetic energy level is required (see Fig. 2.4). This is taken into account through the factor $exp(-E_a/RT)$, giving the fraction of all collisions that have sufficient energy (greater than E_a). A and E_a can be determined from experiment or statistical mechanics calculations.

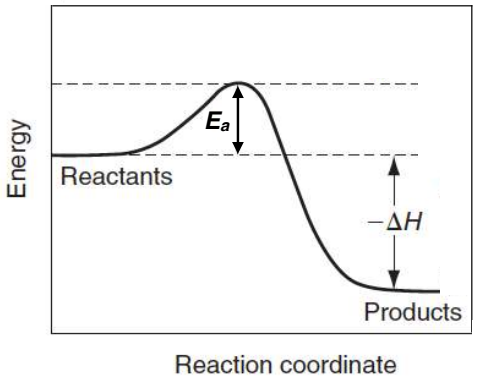

Figure 2.4: Energy profile of an exothermic reaction. $-\triangle H$ stands for the energy gap between the reactants and the products states. From (Glassman & Yetter, 1987)

Most reactions are not one-way, and the reverse reaction occurs as well, albeit with a different reaction rate. Forward and backward reaction rates are denoted by k_f and k_b, respectively. To comply with the thermochemical equilibrium state, they are related through the pressure equilibrium constant $K_p(T)$, by:

$$k_b = \frac{k_f}{K_p(T)} = \frac{k_f}{\left(\frac{p_0}{RT}\right)^{\sum_{k \in N_s} \nu_{tot,k}} exp\left(\frac{\Delta S_r^0}{R} - \frac{\Delta H_r^0}{RT}\right)} \tag{2.4}$$

where N_s denotes the total number of species, and $\nu_{tot,k}$ is the total stoichiometric coefficient of species k in the reaction. ΔH_r^0 and ΔS_r^0 stand for the reaction enthalpy and entropy variations (see Section 2.3.3), and p_0 is the standard atmospheric pressure (1 bar).

2.3.2 Pressure dependency

The reaction rate coefficient k is susceptible to carry a pressure dependency, for two kinds of reactions: unimolecular/recombination *fall-off* reactions and chemically activated bimolecular reactions (see Section. 2.1). Generally speaking, the rate for unimolecular/recombination fall-off reactions increases with increasing pressure, while the rate for chemically activated bimolecular reactions decreases with increasing pressure. Methyl recombination provides such an example of a unimolecular/recombination fall-off reaction:

$$C_2H_6 -> 2CH_3$$

In the high-pressure limit, this is the appropriate description of the reaction, but in the low-pressure limit, a third-body collision is required (see Section. 2.1) to appear explicitly in the expression of the reaction, due to the fact that the concentration of collision partners M becomes very low:

$$C_2H_6 + M -> 2CH_3 + M$$

This means that, at very high pressures, the reaction follows a first order rate law $k_{\text{inf}}[A]$, whereas at low pressures, the reaction follows a second order first law $k_0[A][M]$. When such a reaction is at either limit, the Arrhenius expression of the reaction rate is applicable. However, when the pressure and temperature are such that the reaction is in between the limits, the rate expressions are more complicated. The simplest way of formulating this pressure dependency is due to Lindemann (1922) :

$$k = k_{\text{inf}} \left(\frac{Pr}{Pr+1} \right) \tag{2.5}$$

where the pressure dependent factor Pr is expressed as $k_0[M]/k_{\text{inf}}$. The concentration $[M]$ is almost always expressed as that of a mixture, stating that the collisional partner could be any species. More accurate models for unimolecular processes lead to more complex forms of the dependence upon the reduced pressure Pr. These can be accounted for by multiplying the Lindemann expression (eq. 2.5) by a broadening factor F. This is the case in the Troe formulation (Gilbert *et al.*, 1983), as well as in the SRI formulation (Stewart *et al.*, 1989). An example of such varying coefficient rate is plotted against the pressure in Fig.2.5. The shape of the curve is better understood, in view of what was just discussed, by stating that the dependence upon the pressure follows the same trend than that upon the concentration of the third body M.

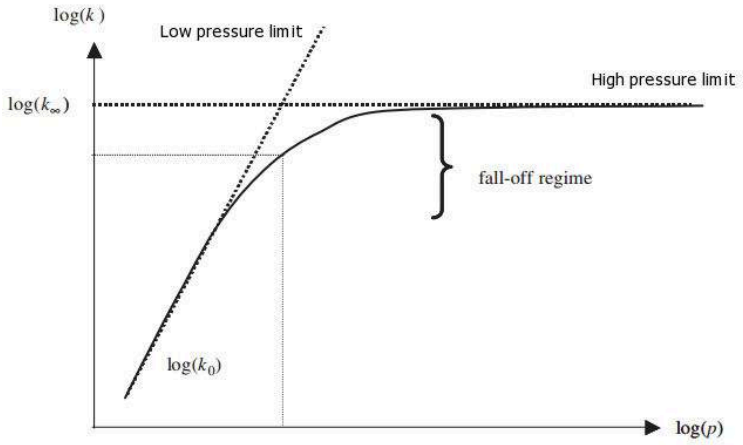

Figure 2.5: A schematic fall-off plot for a unimolecular rate constant as function of pressure.

Chemically activated reactions also see their reaction rate coefficient expressed as a function of the reduced pressure. For such a derivation, see e.g. Carr (2007)

2.3.3 Thermochemistry

The energy difference between the reactant's state and the product's state of any reaction, as depicted in Fig. 2.4, is referred to as the *reaction enthalpy* $\Delta H_r^0(T)$ (kJ/mol). It strongly depends upon the temperature T of the system. This energy stems from the re-arranging of the chemical bonds, and it is closely related to the *formation enthalpy* of the species involved.

The textbook definition of the formation enthalpy for a specific species k, $\Delta h_{f,k}^0(T)$ (kJ/mol) at a specific temperature T is: *The heat released from producing 1 mole of a substance from its constituting elements, at that same temperature T*. Note that with this definition, the enthalpy of formation of any element at the reference temperature is zero. The chosen reference temperature is usually taken to be $T = 298$ K, although this is not always the case. However, recognizing that enthalpy is a state function independent of the formation path as long as the final state remains the same, the enthalpies of formation of a species k at different temperatures T and T'

are linked through:

$$\Delta h^0_{f,k}(T') = \Delta h^0_{f,k}(T) + [h_k(T') - h_k(T)] - \sum_{l \in N_e} a_l [h_l(T') - h_l(T)] \tag{2.6}$$

where $[h_k(T') - h_k(T)] = \int_T^{T'} c_{p,k} dT$ is the k-th species (or l-th element) *sensible enthalpy*, and a_l are the coefficients of an elementary reaction expressed as in Eq. 2.1, forming the species k from its constituting elements $l \in N_e$. The first two terms on the RHS together define the k-th species *total enthalpy* $h_{tot,k}$, so that another expression for Eq. 2.6 is:

$$\Delta h^0_{f,k}(T') = h_{tot,k}(T') - \sum_{l \in N_e} a_l h_{tot,l}(T') \tag{2.7}$$

(since for any element l, $\Delta h^0_{f,l}(T) = 0$). Formation enthalpies are usually obtained experimentally and tabulated,

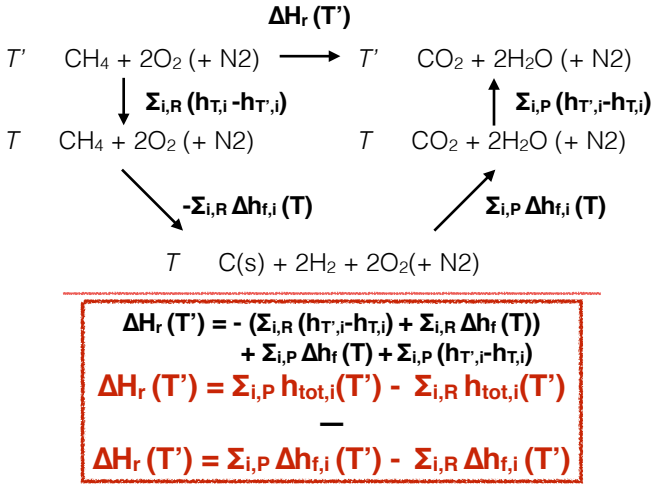

Figure 2.6: Heat released by the combustion of methane with air, divided in a series of steps with known enthalpy release.

while sensible enthalpies are provided as polynomials (NASA formulation).

With these definitions, the theoretical heat released by a reaction r at any specified temperature T' can be obtained by a succession of steps with known enthalpy release (see Fig. 2.6, providing that the formation enthalpies are known at T):

$$\Delta H^0_r(T') = \sum_{k \in \mathcal{P}} \nu''_k h_{tot,k}(T') - \sum_{k \in \mathcal{R}} \nu'_k h_{tot,k}(T') \tag{2.8}$$

where ν'_k, resp. ν''_k, denotes the stoichiometric coefficients of the reactants, resp. products, in the reaction r. This expression is equivalent to the more conventional form, for any temperature T:

$$\Delta H^0_r(T) = \sum_{k \in \mathcal{P}} \nu''_k \Delta h^0_{f,k}(T) - \sum_{k \in \mathcal{R}} \nu'_k \Delta h^0_{f,k}(T) \tag{2.9}$$

Reactions will release heat if $\Delta H^0_r(T) < 0$ (exothermic reactions, Fig. 2.4), or consume heat if $\Delta H^0_r(T) > 0$ (endothermic reactions). When applied to a global reaction for a specific fuel, as illustrated in Fig. 2.6 for the case of methane with air, and when taken at the conventional temperature $T = 298$ K, this concept allows to determine the theoretical calorific value of the fuel. However, as previously discussed, the combustion of any fuel proceeds through many steps, and this idealized vision relying upon a global reaction scheme is not realistic. This will be the subject of the next Section.

2.3.4 The reaction scheme in combustion systems

As stressed before, chemistry in combustion systems actually proceeds through multiple reaction steps. This is traditionally modeled by a *reaction scheme* involving N_s chemical species in a series of M_r reversible elementary

reactions (Poinsot & Veynante, 2005; Williams, 1985*a*):

$$\sum_{1<k<N_s} \nu'_{kj}[X_k] \rightleftharpoons \sum_{1<k<N_s} \nu''_{kj}[X_k], \quad for \quad j \in [1, M_r] \tag{2.10}$$

where $[X_k]$ stands for species k molar concentration. With this model, the rate of a reaction j can be measured in terms of the rate laws of its forward ($k_{f,j}$) and backward ($k_{b,j}$) components, as (see Section 2.3.1):

$$Q_j = k_{f,j} \prod_{k \in N_s} [X_k]^{\nu'_{kj}} - k_{b,j} \prod_{k \in N_s} [X_k]^{\nu''_{kj}} \tag{2.11}$$

Of course, all the reaction rates have to be considered in describing the temporal evolution of the concentration of the species involved. In homogeneous mixtures, the modeling reduces to the following initial value problem (for example, in Vadja *et al.* (1985)):

$$\frac{d\mathbf{c}(\mathbf{c}, \mathbf{k})}{dt} = \dot{\omega}(\mathbf{c}, \mathbf{k}), \quad \mathbf{c}(t_0) = \mathbf{c_0} \tag{2.12}$$

where for convenience, $\mathbf{c}$ now denotes the molar concentration vector of dimension N_s, and $\mathbf{c_0}$ is the initial value. $\mathbf{k}$ is the vector of reaction rate coefficients of dimension M_r and $\dot{\omega}$ is the molar production rate vector (kmol/m^3/s). Components of the right hand side vector of Eq. 2.12 are expressed as follows (Poinsot & Veynante, 2005; Williams, 1985*a*):

$$\dot{\omega}_k = \sum_{0<j<M_r} \nu_{tot,kj} Q_j \tag{2.13}$$

where the total stoichiometric coefficient of species k in reaction j, $\nu_{tot,kj} = \nu''_{kj} - \nu'_{kj}$, is employed.

The heat released $\dot{\omega}_T$ (kJ/m^3/s) by such a system of reactions is finally expressed with the help of the standard enthalpies of formation, at a reference temperature T_{ref}, as:

$$\dot{\omega}_T = \sum_{0<k<N_s} \dot{\omega}_k \Delta h^0_{f,k}(T_{ref}) \tag{2.14}$$

Chapter 3

Methods for the derivation of reduced reaction mechanisms

Contents

3.1 Introduction

In the previous Chapter, we have discussed the different pathways through which hydrocarbons oxidize. We have seen that they are much dependent upon the initial conditions (temperature, pressure, etc.), and that they can involve many species and reactions, especially when trying to predict pollutant formation. With that in mind, the limitations of empirical (global or semi-global) mechanisms and tabulation techniques employed so far in the literature to reduce the overall computational cost of CFD simulations are better understood.

This Chapter starts by a brief presentation of empirical mechanisms and techniques based upon reduced manifolds to which belongs tabulation. Then, a definition is given for the physically-oriented Analytically Reduced Chemistry (ARC) recently proposed as an alternative chemistry model in the literature. Finally, the main techniques, as well as their theoretical grounds, employed to derive ARC are listed.

3.2 Empirical reduction techniques: global or semi-global reaction mechanisms

So-called *global mechanisms* for hydrocarbon oxidation, consider that only a few representative species interact through one to four purely descriptive reactions. The idea behind this methodology is to fraction the global reaction of fuel ($C_\alpha H_\beta O_\gamma$) oxidation:

$$C_\alpha H_\beta O_\gamma + \left(\alpha + \frac{\beta}{4} - \frac{\gamma}{2}\right)(O_2 + 3.76N_2) \rightleftharpoons \alpha CO_2 + \frac{\beta}{2}H_2O + 3.76\left(\alpha + \frac{\beta}{4} - \frac{\gamma}{2}\right)N_2 \tag{3.1}$$

where α, β, γ are real numbers that depend upon the stoichiometry, into intermediate steps. Two-steps mechanisms usually employ CO as an intermediate (see, e. g. Franzelli *et al.* (2010)) to include the CO/CO_2 equilibrium

in order to yield correct prediction of the adiabatic fame temperature, while four-steps mechanisms add the H_2 species (see, e. g. Jones & Lindstedt (1988)). The reaction constants are usually expressed in an Arrhenius form (see Section 2.3.1), where the various parameters are adapted by comparisons with experimental data, inside a specified operating range. With this methodology, good predictions of global flame features (flame temperature or laminar flame speed) are obtained, but the physics of the problem (i.e., the true chemical pathways) is completely lost. Furthermore, as already stressed, pollutant information is either unavailable (soot, NO_x) or inaccurate (CO).

Also, because these reaction schemes give a correct global flame behavior, they are computationally cheap and very easy to implement. As such, they have been widely employed in LES (refs were provided in Introduction, Section 1.3). Methodologies for their systematic development exist, see Franzelli (2011) for example.

3.3 Mathematical reduction techniques based on manifolds generation

Since the problem of chemical kinetics stems from its high dimensionality, logic dictates to try and find a way to reduce the number of controlling parameters. This is usually done by analyzing the system's evolution in the phase space, which is the space spanned by the species, the temperature, etc. Methods belonging to this category usually rely on some sort of timescale separation, i. e., they postulate the existence of a manifold (a subspace) spanned by slow processes, on which all kinetic trajectories eventually relax. Amongst these methods, two are worth mentioning, namely, the Rate-Controlled Constrained Equilibrium (RCCE) method which reduces to a manifold of constrained equilibrium compositions and has received much attention in the past decade; and the Intrinsic Low Dimensional Manifold (ILDM) technique interested with the subspace spanned by a few controlling species, and whose natural extension led to modern tabulation methods.

3.3.1 Rate-Controlled Constrained Equilibrium (RCCE)

RCCE was proposed by Keck & Gillespie (1971). The method is based directly on the Second Law of thermodynamics: it is assumed that a reacting system relaxes to complete equilibrium through a sequence of constrained-equilibrium states, at a rate imposed by a certain class of slow reactions. Basically, the evolution of the kinetic system relies on successive equilibrium calculations, via minimization of the free energy (Gibbs or Helmholtz), with time evolving constraints (typically, the concentrations of combinations of leading species). As a result, the total number of ODE required to describe the system's evolution is reduced to the total number of constraints, and contrary to the Quasi Steady State approximation (QSS, see Section 3.4.2.a), the solution depends only upon the rate constants of those rate-controlling reactions. An interesting feature of this method is that it eliminates the need for estimating the rates of unknown reactions of peripheral importance; instead, one starts with a small number of constraints to which it is possible to add more if necessary. The methods, in its original form, gives overall good results, but does not provide significant enough calculation time savings to be considered really efficient (Keck *et al.*, 1988), even with the use of an improved algorithm (Hamiroune *et al.*, 1998). Furthermore, the constraints vary with the system under investigation, and there is no systematic method to select them *a-priori*.

In recent years however, the RCCE method has been reformulated into a differential algebraic problem, and applied to chemistry related problems where transport is involved, namely one-dimensional counterflow CH_4/Air flames, by Jones & Rigopoulos (2005). Very good results where obtained on that configuration, although it was stressed again that this method is not of great interest unless a systematic procedure to derive constraints is developed. Such a procedure has recently been proposed by Rigopoulos & Lovas (2009), where a method based on the Level Of Importance (LOI) is used to determine the relevant constraints (species with larger time scales in this case) in a parameter range of interest. This method proved to be very efficient, and the calculations with the obtained reduced chemistry provided CPU savings of one or two orders of magnitude on a propane/air one-dimensional laminar flame simulation, when compared to simulations with the original detailed chemistry (containing over 100 chemical species). The method has also been coupled *on-the-fly* to a LES/CMC approach for turbulent reactive flow modeling of a turbulent non-premixed ethylene flame with relatively good success, although further investigations of CPU savings are required (Lovas *et al.*, 2011).

It is interesting to note that with this reformulation of the problem, the RCCE method could be assimilated to a mechanism obtained by applying the QSS approximation (see, e.g. the LES/CMC computation of the *Cabra*

Flame of Navarro-Martinez & Rigopoulos (2011)). However, it is presented separately for one main reason: evaluation of the constraints (the leading species) rely, through the chemical mechanism, upon the concentration of the constrained species, which are not *directly* evaluated through kinetic relations but rather through thermochemical considerations.

3.3.2 Intrinsic Low Dimensional Manifold (ILDM) and tabulation

The ILDM method of Maas & Pope (1992) aims at decoupling the fast from slow timescales, based on an eigenvector analysis of the governing equations in a homogeneous chemical reaction system (without transport). Considering that enthalpy, pressure and N species describe the state space, the goal is to identify an attractive reduced manifold spanned by only a few controlling species, and to find a mapping for all other species. This is based on the observation that in a closed system with no pressure or enthalpy variation, all kinetic trajectories in the phase space tend to meet (see Fig. 3.1). Then, it is argued that it is always possible to construct such a subspace.

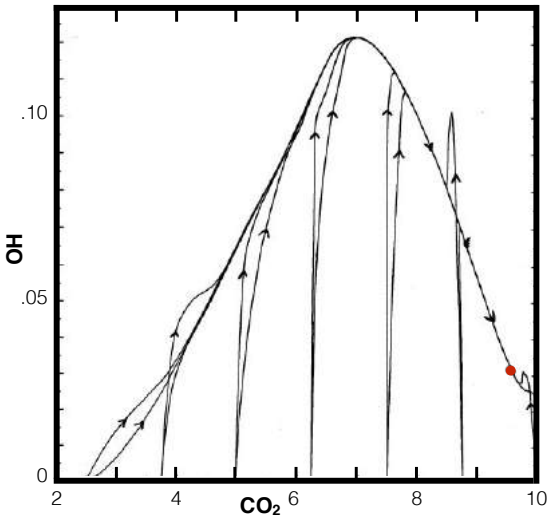

Figure 3.1: Projection into the OH/CO_2 plane of sample trajectories in the state space for a CO/H_2/Air system. The red dot represent equilibrium. From (Maas & Pope, 1992)

The method is automatized, and can yield manifolds of any specified dimension. ILDM cannot be assimilated to an ARC because no analytical expression for the reduced subspace can be obtained and quantities are retrieved via tabulations instead.

ILDM is at the root of current *flamelet* tabulation techniques where, instead of considering trajectories spanned by homogeneous systems, one-dimensional canonical configurations are investigated. Indeed, it was found that the effects of transport and low temperature, not taken into account in ILDM, are non negligeable and lead species trajectories in the phase space to stray from the purely kinetic manifold. Other manifold-based reduction techniques have attempted to include low temperature chemistry and transport effects, as it is the case of ICE-PIC Ren *et al.* (2006) or REDIM of Bykov & Maas (2007), but they will not be discussed further. In the following, we focus on tabulation techniques employing a specific one-dimensional flamelet archetype, namely, premixed flames.

Belonging to this category, are the concepts of flame-generated manifold (FGM) (Oijen *et al.*, 2001) or Flame Prolongation of ILDM (FPI) (Gicquel *et al.*, 2000) , which are sensibly equivalent. Emphasis is put on the FPI technique, since it will be employed in this PhD thesis. The idea is to describe combustion by a collection of small unstrained laminar one-dimensional premixed flames. The flamelet solutions identify a series of specific paths in the state space from fresh gas to burnt gas. Then, as in the ILDM technique, a couple of controlling parameters are identified as coordinates to build a flamelet manifold and retrieve all other quantities of interest (species, temperature, etc.). In classical FPI, two controlling parameters are used, and need to be transported in the simulation:

- The mixture fraction Y_z which is a passive scalar characterizing the degree of mixing between a stream of

fuel and a stream of oxidizer. Its definition is based on the conservation of an element, or a combination of N_e elements (Poinsot & Veynante, 2005; Bilger, 1989):

$$Y_z = \frac{\beta - \beta_O}{\beta_F - \beta_O} \tag{3.2}$$

with

$$\beta = \sum_{l \in N_e} \gamma_l \sum_{k \in N_s} a_{l,k} \frac{W_l Y_k}{W_k} \tag{3.3}$$

where β_O and β_F are evaluated, respectively, in the oxidizer and fuel inlets; γ_l and W_l are the weighting factors and molecular weights associated to the l-th element, and $a_{l,k}$ stands for the number of elements l in one molecule of species k. Specifically, the weighting factors used in the *Bilger* definition employed in this work are:

$$\gamma_C = 2/W_C \quad \gamma_H = 1/(2W_H) \quad \gamma_O = -1/W_O \quad \gamma_N = 0 \tag{3.4}$$

When all species and heat diffuse at the same rate, the mixture fraction follows a classical passive scalar transport equation:

$$\frac{\partial \rho Y_z}{\partial t} + \frac{\partial \rho u_j Y_z}{\partial x_j} = \frac{\partial}{\partial x_j}\left(\rho D \frac{\partial Y_z}{\partial x_j}\right) \tag{3.5}$$

- The progress variable Y_c which is a reactive scalar characterizing the progress of the reaction. It should evolve monotonically throughout the flame, and allow a one to one correspondence with the quantities of interest. It is usually defined as a combination of species, such as CO, CO_2 and H_2O for example:

$$Y_c = Y_{CO} + Y_{CO_2} \tag{3.6}$$

and normalized to yield values in between zero in fresh gases and one in burnt gases:

$$c = \frac{Y_c - Y_{c,f}}{Y_{c,b} - Y_{c,f}} \tag{3.7}$$

where subscripts f and b stands for values of Y_c obtained in fresh and in burnt gases at equilibrium, respectively. The progress variable follows a classical scalar transport equation with a source term:

$$\frac{\partial \rho Y_c}{\partial t} + \frac{\partial \rho u_j Y_c}{\partial x_j} = \frac{\partial}{\partial x_j}\left(\rho D \frac{\partial Y_c}{\partial x_j}\right) + \rho \dot{\omega}_c \tag{3.8}$$

For a given pressure and temperature, the two dimensions Y_z and Y_c are discretized, and a 2D table is constructed by computing unstrained laminar one-dimensional premixed flames with a detailed mechanism. To do so, chemistry solvers such as CHEMKIN (Kee *et al.*, 2000) or CANTERA (Goodwin *et al.*, 2014) may be used. Any state corresponding to specific Y_z and Y_c can be retrieved by interpolation. Outside of the flammability limits, equilibrium computations are often employed. It was shown that with this formulation, FPI eventually reduces to ILDM under high temperature conditions (Gicquel *et al.*, 2000), where chemistry dominates over transport.

It is of course possible to extend the method to include complex effects, by adding entry variables. For example, the enthalpy is used to consider heat losses (Fiorina *et al.*, 2003), or another progress variable can be added to describe slow pollutant formation (Godel *et al.*, 2009).

3.4 The concept of Analytically Reduced Chemistry (ARC)

Driven by the same necessity to reduce the high dimensionality of chemistry for implementation in CFD, physically-oriented approaches have been developed. The fundamental aspect of reduced chemistries obtained by these methods, to which we refer by Analytically Reduced Chemistry or ARC, is that expressions for all quantities of interest (species) are readily obtained and rely directly upon the detailed chemistry model. In particular, the rate constants are not modified, contrarily to fitted schemes discussed in Section 3.2. As such, ARC can be considered as reduced *mechanisms*, and the concepts of species and reactions continue to prevail. Typically,

retaining 10 to 30 species is nowadays affordable in CFD simulations with the current available computational power. It is expected that, by keeping the core physics of the problem, the operating range naturally broadens outside of specified targets, species evolutions should naturally yield realistic levels, and that the general behavior of the kinetic system is more trustworthy and realistic.

Two different types of reduction can be applied to a detailed reaction scheme, to yield:

- A **skeletal mechanism** where a set of unnecessary species and reactions has been discarded,
- An **analytical mechanism**, either from a skeletal scheme, or from the original detailed one. Borrowing from manifold reduction tools, a time-scale analysis is performed, and reactions are combined in order to express the evolution of a few fast species through algebraic relations.

Both reductions have their respective set of tools and techniques. The most common procedure for skeletal reduction is to first identify and eliminate *redundant* species (and associated reactions), before identifying and eliminating *redundant* reactions (terminology from Turányi (1990*a*)). Techniques pertaining to analytical reduction mostly deal with stiffness reduction.

ARC is not a new concept. They have been obtained in a brute way, through sensitivity and uncertainty analysis using experience, chemical intuition and a try-and-error approach, long before the advent of modern computers (Griffiths, 1995). In fact, the Quasi-Steady State approximation, enabling to perform the analytical reduction, dates back to the early 20's where it was referred to as the Bodenstein method (Turányi & Tóth, 1992). In particular, detailed mechanisms for the oxidation of hydrogen and methane have been widely investigated (Gutheil & Williams, 1991; Smooke & Giovangigli, 1991) during the second half of the last century; noteworthy are the series of papers by Turanyi and co-workers on the subject, which can be found online [1]. The limitation in these studies to small hydrocarbons is due to several facts. First, the investigated mechanisms were all that computational capacities were able to handle at that time. Furthermore, comprehensive understanding of the underlying kinetic process of heavier hydrocarbons is rather recent. Finally, it has long been known that the heaviest hydrocarbon mechanisms rest strongly on lighter hydrocarbon mechanisms, from which they derive their main features.

Most of these primitive techniques, in their original formulation at least, were costly and not well suited to the study of heavier hydrocarbon oxidation mechanisms. This fact, coupled with the growing need for comprehensive chemical schemes outside of the pure chemistry community, has driven the emergence of efficient techniques with solid mathematical grounds to help perform kinetic reductions in a systematic fashion. Those usually entail some sort of investigations of the equations describing the evolution of the concentrations of the species in a (often homogeneous) combustion system, which have been made possible by the continuously increasing available computational power. Indeed, many techniques are well designed for numerical implementation in preexisting chemistry or combustion simulation codes, usually as post processors, e.g. CARM (Chen, 1997), or more recently, the G-scheme (Valorani & Paolucci., 2009). Such codes are able to both carry the model reduction and perform the subsequent numerical integration of the derived set of differential equations, thus simplifying the crucial validation step. Other codes are exclusively post processors, and need to be fed with formatted zero or one-dimensional simulations results on which they apply the same kind of techniques. This is the case for KINALC [2] (Turányi *et al.*, 1997), S-STEP (Massias *et al.*, 1999), or YARC (Pepiot, 2008), employed in this work. The trend today is towards a systematic reduction of any detailed chemical scheme, with limited prior chemistry knowledge; and flexibility to adapt to the simulation requirements.

An overview of the most common techniques associated to both types of reduction is provided hereafter, along with examples of their use. The review is presented in a chronological order, starting with the oldest techniques.

3.4.1 From detailed schemes to skeletal schemes

3.4.1.a Sensitivity analysis

The sensitivity analysis method basically investigates the output of a system at time t_2, when a parameter variation has been introduced at an earlier time t_1 (either controlled or not). The comparison between the

[1] http://garfield.chem.elte.hu/Turanyi/ttpub.html
[2] http://respecth.hu/

system's outputs, with and without parameter variations, help determine which parameters contribute most to the solution variability and thus have to be known with the best possible accuracy to reproduce the correct system behavior. In the context of chemical kinetics, the system is usually composed of the concentrations of a set of species, but could be extended to include temperature, flame speed and other variables of interest. The parameters may include the reaction rates coefficients, Arrhenius parameters or the physical conditions such as pressure and temperature. Sensitivity analysis has been extensively used over the past decades to reduce detailed mechanisms, and remains today very common practice. In practice, most kinetic reductions start by a sensitivity study of the detailed mechanism.

Different methods for the estimation of the sensitivities exists, depending on whether the variability is investigated at a specified point of time and/or space, (local sensitivities); or over the entire domain of interest (global sensitivities). However, global sensitivities have not been used with much success in the derivation of reduced kinetic mechanisms, with the exception of the FAST method (McRae *et al.*, 1982), and thus will not be discussed in detail here. Another classification of sensitivity methods is based on whether the variability is investigated on a single output parameter, for example, the concentration of a reactant; or on a collection of output parameters, for example, the concentration of a subset of species simultaneously. A distinction is also often made with the type of output. A comprehensive review on these techniques and their applications is provided by Turányi (1990*b*), Hamby (1994) or Griffiths (1995).

Local concentration sensitivities When performing concentration sensitivities, the objective is to investigate the effect of modifying the reaction rates on selected species concentrations. In this way, the redundancy of reactions can be investigated one by one. The analysis relies on the concentration sensitivity matrix, defined as:

$$\mathbf{S}_{i,j} = \left(\frac{\partial c_i}{\partial k_j} \right) \tag{3.9}$$

As it is more convenient to deal with dimensionless quantities, the sensitivity matrix is often normalized. The resulting $\mathbf{S}$ matrix is then defined as:

$$\mathbf{S}^*_{i,j} = \left(\frac{\partial \ln(c_i)}{\partial \ln(k_j)} \right) \tag{3.10}$$

The first order partial derivatives are referred to as first-order local concentration sensitivity coefficients(Turányi, 1990*b*). Then, using a Taylor expansion and neglecting high order terms, the following estimation of the variation of the concentration of the i-th species Δc_i induced by a variation of the j-th reaction rate coefficient Δk_j around the original value is obtained:

$$\Delta c_i \approx \sum_j \frac{\partial c_i}{\partial k_j} \Delta k_j \tag{3.11}$$

Several methods have been used to evaluate the coefficients of this sensitivity matrix. The most common one is a brute force method described by Olsson & Andersson (1987), where the matrix coefficients are obtained by successive simulations of the system, with and without perturbations. It is readily seen as being a highly non efficient way to proceed. Furthermore, the value of the perturbation to apply has to be specified in each case. More powerful methods exist, and make use of the differentiation of Eq. (2.12) with respect to the j-th reaction rate (Valko & Vajda, 1984):

$$\frac{d}{dt}\frac{\partial c_i}{\partial k_j} = \frac{\partial \dot{\omega}_i(\mathbf{c}, \mathbf{k})}{\partial k_j} = \sum_{0<l<N_s} \frac{\partial \dot{\omega}_i(c_l)}{\partial c_l}\frac{\partial c_l}{\partial k_j} + \frac{\partial \dot{\omega}_i(k_j)}{\partial k_j} \tag{3.12}$$

In Eq. 3.12, $\mathbf{J}_{i,j} = \left(\frac{\partial \dot{\omega}_i}{\partial c_j} \right)$ is the Jacobian matrix. The most accurate algorithm for the resolution of these sensitivity differential equations is called the Decoupled Direct Method (DDM) (Valko & Vajda, 1984) and was first applied in chemical kinetics by Dunker (1981). Other techniques exist, noteworthy is the Green's function (Dougherty & Rabitz, 1979) which has been employed in many studies, for example in the work of Edelson & Allara (1980) to investigate the sensitivity of pyrolysis of propane and n-butane in the intermediate temperature range.

As was stressed in Turányi *et al.* (1989), the investigation of the concentration sensitivity matrix is rather difficult and not completely adequate, due to a "memory effect" in studying directly the effects upon species concentrations. Rather, sensitivities of the (net) rate-of-productions, $\dot{\omega}$ in eq. 2.12, are examined.

Local rate-of-production sensitivities This type of sensitivity analysis investigates the effect of varying the rate coefficient of a reaction j upon the (net) rate-of-production of a species i, which can be modelled as a rate-of-production sensitivity matrix $\mathbf{F}$:

$$\mathbf{F}_{i,j} = \left(\frac{\partial \dot{\omega}_i}{\partial k_j} \right) \tag{3.13}$$

or equivalently:

$$\mathbf{F}^*_{i,j} = \left(\frac{\partial ln(\dot{\omega}_i)}{\partial ln(\mathbf{k})} \right) \tag{3.14}$$

It is worth mentioning that, when considering only irreversible reactions, the normalized rate-of-production sensitivity matrix reads:

$$F^*_{i,j} = \frac{\nu_{i,j} Q_j}{\sum_{0<j<N_r} \nu_{i,j} Q_j} \tag{3.15}$$

$F_{i,j}$ is then the ratio of the rate of production -or consumption- of species i in reaction j to the net rate of its concentration change. As such, scanning for a very large element in the rows of an important species readily reveals rate limiting reaction steps (Turányi *et al.*, 1997). This type of analysis bears a resemblance with specific analysis of reaction pathways and species fluxes, which will be described later.

Jacobian sensitivities So far, the focus has been on identifying a subset of important reactions. It is also interesting, to investigate the system's response to a variation in the concentrations of a subset of species. This effect can be investigated through an objective function involving the Jacobian. For a specific i-th species it writes:

$$BJ_i = \sum_{0<l<N_I} \left(\frac{\partial \ln(\dot{\omega}_l)}{\partial \ln(c_i)} \right)^2 \tag{3.16}$$

Where the summation runs over all N_I species of interest. This type of analysis is referred to as overall sensitivity analysis of the Jacobian. The BJ_i coefficients, evaluated for different species i, allow to rank them, so as to have an idea of the most important ones (the ones with the highest coefficient value). However, these coefficients only reflect the direct effect of species i on all (or a set of) species of interest, and do not provide any information about indirect links between species. For that reason, it is recommended to iterate the evaluation of BJ_i, in a process described e. g. in Tomlin *et al.* (1992) and Lepage (2000).

3.4.1.b Principal Component Analysis (PCA)

The Principal Component Analysis method is a pure mathematical tool, aiming at reducing the dimensionality of a system by finding a reduced set of variables that retain most of the original information. In chemical kinetics, PCA analysis is widely employed to investigate the various matrices of sensitivities presented in the previous Section. It can be, for example, applied to the concentration sensitivity matrix to rule out redundant reactions and acquire information about potential QSS, as was done in a formaldehyde oxidation mechanism by Vadja *et al.* (1985). More often applied to the rate of production matrix, it offers an efficient way to select a minimum set of important elementary reactions. Examples in the literature include the analysis of a low-temperature mechanism for the pyrolysis of propane and n-butane by Turányi (1990*a*), the study of a detailed mechanism for hydrogen combustion by Turányi *et al.* (1997) or the reduction of a mechanism for the oscillatory oxidation of hydrogen Tomlin *et al.* (1992).

PCA relies on the definition of an objective response function Q, whose formulation depends upon the quantity monitored. To estimate, for instance, the response of the concentration of a subset of N_I important species to a perturbation of the vector of reaction rates $\mathbf{k}$ (of dimension N_r), the following expression -evaluated at different times $t_s, s \in [0, q]$, is used:

$$Q(\alpha) = \sum_{0<t_s<q} \sum_{0<i<N_I} \left(\frac{c_{i,t_s}(\alpha) - c_{i,t_s}(\alpha_{\mathbf{0}})}{c_{i,t_s}(\alpha_{\mathbf{0}})} \right)^2 \tag{3.17}$$

where α stands for the normalized reaction rates $ln(\mathbf{k})$. Using a Taylor expansion around α_0 and neglecting the higher-order terms leads to an approximate response function (Vadja *et al.*, 1985):

$$Q(\alpha) = (\Delta\alpha)^T \tilde{S}^T \tilde{S}(\Delta\alpha) \tag{3.18}$$

where $\tilde{S}$ stands for the q stacked S concentration sensitivity matrices. The PCA method consists in diagonalizing the $\tilde{S}^T\tilde{S}$ $(N_r \times N_r)$ matrix, in order to express it in a $P\Lambda P^T$ form, where the columns of P are normed eigenvectors associated with the eigenvalues of the diagonal matrix Λ. This introduces a new set of variables, or principal components (by a change in coordinates) Ψ:

$$\mathbf{\Psi} = P^T\alpha \tag{3.19}$$

Eq. (3.18) then writes:

$$Q(\alpha) = (\Delta\mathbf{\Psi})^T\Lambda\Delta\mathbf{\Psi} = \tilde{Q}(\mathbf{\Psi}) \tag{3.20}$$

which further reduces to:

$$\tilde{Q}(\mathbf{\Psi}) = \sum_{0<j<N_r} \lambda_j(\Delta\Psi_j)^2 \tag{3.21}$$

where the λ_j are the eigenvalues of the system.

The general idea is that, once the principal axes (which are determined by the eigenvectors) have been identified, along with their associated eigenvalues, it is straightforward to identify the perturbations that will lead to the largest solution modification, as they are associated to the largest eigenvalues. Thus, important reactions are identified by the "largest" eigenvector elements associated with "significant" eigenvalues. By the same reasoning, if a reaction parameter k_j does not appear in any "significant enough" eigenvalue group[3], then this reaction parameter can be said to have no, or little, effect on the solution and can be safely removed from the mechanism. The selection of these significant eigenvalues and large eigenvector elements is an important step, and requires dedicated thresholds.

As said previously, the same analysis can be performed on the rate-of-production sensitivities ($\mathbf{F}$ matrix), if the objective function is defined as the overall variation in the net rate-of-production of chosen species. This analysis yields more information, as the time dependence is implied.

3.4.1.c Uncertainty Analysis

A system can be sensitive to an input parameter in two different ways. First, the variability or uncertainty associated with a sensitive input parameter can propagate through the model to ultimately have a large contribution to the overall output variability. Second, the output of a system can be highly correlated with an input parameter, so that a small variation of its value results in a large output change. This latter phenomenon is the one investigated by the sensitivity analysis presented before, but such analysis does not tell us anything about the parameter importance, or role in the output variability. Indeed, a sensitive input parameter can be controlled accurately, so that its contribution to the output variability will ultimately be insignificant. Parameters that have key roles on output variability are referred to as important parameters.

Numerous different mathematical theories exist, which aim at quantifying the output variability in terms of important input parameters. However, they all require for the modeler to have an idea *a-priori* of the input parameter variability. For a detailed review of available techniques and applications, see Hamby (1994); Turányi (1990*b*, 2002); Zador *et al.* (2006). One frequently used method in the literature is the direct method, which uses the semi-normalized sensitivity concentration matrix $\mathbf{S}^\dagger$ (the original $\mathbf{S}$ matrix is only normalized by k_j) to calculate the error propagation:

$$V(c_i) = \sum_{0<j<N_r} \left(\frac{\partial c_i}{\partial \ln k_j}\right)^2 V(\ln k_j) = \sum_{0<j<N_r} V_j(c_i) \tag{3.22}$$

where V stands for the concentration variance of species i, which can be seen as a local evaluation of uncertainties in model predictions. The method is only valid for small uncertainties. The individual terms in the sum, $V_j(c_i)$, are contributions from each reaction to the total uncertainty of the concentration of species i.

[3] An eigenvalue group of reactions is composed of those reactions associated with the highest eigenvector elements -according to a user defined threshold- of this eigenvalue.

3.4.1.d Rate-of-production analysis and Path Flux analysis

Comparing rates of competing reactions is a mean to select the most important ones for the application under consideration. It has been performed in a brute-way by Edelson & Allara (1980) to reduce a detailed mechanism for alkane pyrolysis to 38 species and 98 reactions, or by Frenklach & Wang (1991*b*) who used a reference reaction's rate to assess the importance of all other in auto-ignition and premixed flame computations.

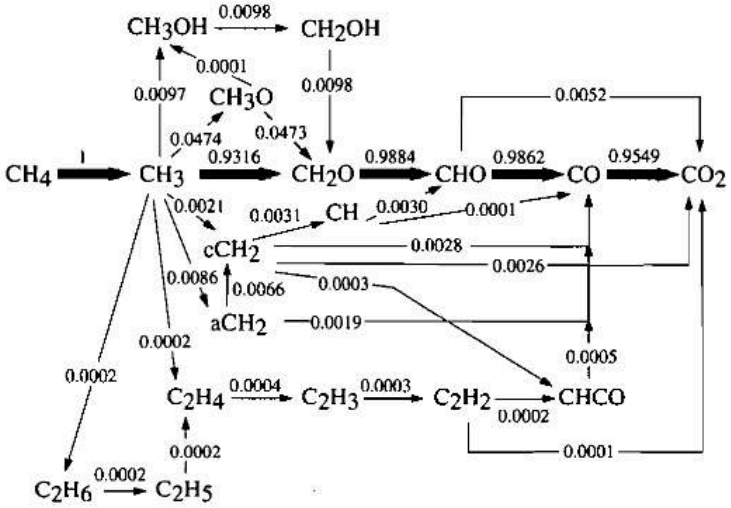

Figure 3.2: Example of a schematic diagram of an instantaneous C flux in a lean premixed methane/air flame ($\phi = 0.5$, P = 1 bar, $T_{ini} = 400\,\mathrm{deg}\,C$). From (Frouzakis & Boulouchos, 2000).

A more systematic way to identify key pathways in a mechanism is provided by the appreciation of the atomic exchanges between species, at specified times during the combustion process (or specified positions, in laminar flames for example). This knowledge provides frozen pictures, or *flowcharts*, leading to a better understanding and quantification of the reaction network: such a flowchart is illustrated in Fig.3.2, where the thick array identifes the most important pathway. Ultimately, it provides insights not only upon the privileged pathways and associated reactions but, as can be seen on Fig. 3.2, also upon the set of necessary species. Atomic pathways are usually considered since, if species concentrations evolve in the system during the reaction, the elements concentrations remain constant and can thus be viewed as unbiased markers.

Formally, the *flux* of an element A from species i to species i' through reaction j is expressed as (Revel *et al.*, 1994; Frouzakis & Boulouchos, 2000):

$$\phi(A,j)_{i->i'} = \frac{Q_j n_{A,i} n_{A,i'}}{N_{A,j}} \tag{3.23}$$

where $N_{A,j}$ is the total number of atoms A in reaction j and $n_{A,i}$ (resp. $n_{A,i'}$) stands for the number of atoms A in the species i (resp. i'). By adding the contribution of all reactions j, the *instantaneous net flux* (outgoing or incoming) from species i to species i': $\phi(A)^{net}_{i->i'}$ is obtained. The sum of all the positive net fluxes from a species i provides the *instantaneous outgoing flux* of element A from species i, towards all other species:

$$\phi(A)^{-}_{i} = \sum_{0<i'<n} Max(\phi(A)^{net}_{i->i'}, 0) \tag{3.24}$$

while the sum of all negative fluxes provides the *instantaneous incoming flux* of element A to species i, also obtained by considering the sum of all positive net fluxes from other species:

$$\phi(A)^{+}_{i} = \sum_{0<i'<n} Max(\phi(A)^{net}_{i'->i}, 0) \tag{3.25}$$

Integrating the incoming and outgoing atomic fluxes over the whole duration/domain, yields *total incoming/outgoing fluxes*, $\Phi(A)^{+}_{i}$ and $\Phi(A)^{+}_{i}$. This is illustrated in Fig. 3.3.

With these definitions, an accurate estimation of species interaction throughout the reaction process is given by identifying the most significant fluxes for each important element (typically, C, H and O). To help with this

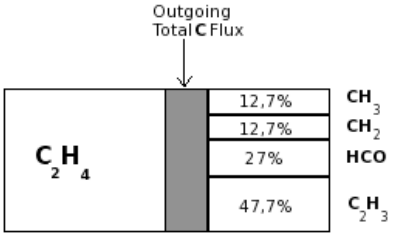

Figure 3.3: Example of a schematic diagram of an integrated outgoing Carbon flux from species C_2H_4, to species CH_3, CH_2, HCO and C_2H_3 (Lepage, 2000).

identification, the total fluxes are often normalized by the total outgoing fluxes of the provider species (the fuel species). Normalized fluxes lower than a specified threshold can be used to discard associated species and reactions to simplify the scheme (Lepage, 2000). It is also possible to substract the total outgoing fluxes from the incoming one $\Phi(A)_i^+ - \Phi(A)_i^-$, for every element and for one particular species i with small total fluxes, and if it is close to zero, to assume it as a Quasi Steady State species.

These flowcharts have been used by Revel *et al.* (1994) to derive a global mechanism for methane combustion, by Lepage (2000) and Luche (2003) for the derivation of a reduced kinetic mechanisms for the oxidation of kerosene surrogates, and by Sun *et al.* (2010) for the derivation of n-heptane and n-decane reduced mechanisms, in contrast with the DRG method. The downside is that a threshold has to be specified, that depends upon the type of atomic flux considered as well as upon the application range.

3.4.1.e Directed Relation Graph (DRG) method

Given an initial set of important species, the Directed Relation Graph (DRG) method provides an efficient way of identifying the species strongly coupled to them. DRG can be represented by a graph similar to the one displayed in Fig. 3.4, where each node represents a species, and the thickness of the directed vertex from node A to node B is proportional to the (instantaneous or global) contribution of species B in the production rate of A ("A depends on B"). Consequently, starting from a node representing a species A, one can identify the weakest paths leading to the less strongly coupled species and remove them safely. In that sense, the DRG also belongs to the category of rate-of-production analysis. However, the analysis focuses on species fluxes rather than atomic fluxes.

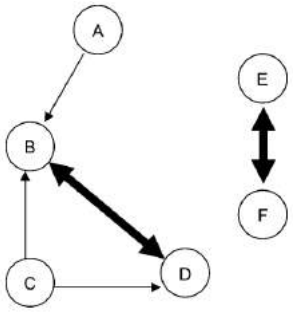

Figure 3.4: Example of a DRG in a scheme with 6 species, from (Lu & Law, 2005).

Several expressions for the construction of the DRG can be found on the literature. Defined first by Lu & Law (2005), the original instantaneous definition reads:

$$r_{AB} = \frac{\sum_{0<j<m} |\nu_{A,j} Q_j \delta_B^j|}{\sum_{0<j<m} |\nu_{A,j} Q_j|} \tag{3.26}$$

where the summation runs over all reactions in the mechanism, and δ_B^j is the Kroenecker symbol whose value is unity if the reaction j involves species B and zero otherwise. To identify the species to keep in the mechanism, a

threshold ϵ has to be specified so that any species B satisfying $r_{AB} < \epsilon$ can be safely discarded. The technique was applied to reduce at a skeletal level a detailed ethylene mechanism (Lu & Law, 2005), and later successfully to n-heptane and iso-octane mechanisms with a fully automated procedure (Lu & Law, 2006*a*), before deriving a complete ARC scheme for methane oxidation (Lu & Law, 2008*a*). It was suggested in a subsequent publication (Lu *et al.*, 2011) to adapt the values of ϵ to the species under investigation, in a process labelled DRG with expert knowledge (DRGX); this was employed to investigate surrogate mixtures of biodiesel, starting from a very comprehensive detailed mechanism for C_8-C_{16} n-alkanes, with much success. It should be noted that in all studies reported so far, the reduction was carried out with auto-ignition or extinction as targets, while the accuracy of the reduced schemes on configurations involving transport were evaluated *a-posteriori*.

Eq. 3.26, however, does not allow to differentiate between species that contribute equally to both consumption and production of the target species, and those that contribute exclusively to one or the other. To introduce this aspect, a new definition of the DRG was provided by Pepiot-Desjardins & Pitsch (2008):

$$r^*_{AB} = \frac{|\sum_{0<j<m} \nu_{A,j} Q_j \delta^j_B|}{max(P_A, C_A)} \tag{3.27}$$

where P_A and C_A stands for the production and consumption, respectively, of species A. This quantity is always well defined, and bounded between 0 and 1. This formulation is more accurate than the previous one whenever a species' consumption and production rates are comparable. This is illustrated as follows: considering that a species A is exclusively consumed by reactions involving another species B, then logic dictates that species B can be safely removed only if $C_A << P_A$. As soon as production and consumptions are of the same order, removing B from the mechanism leads to the building up of species A, and so, any evaluation of r_{AB} should be of the order of unity. This is the case when employing Eq. 3.27, but not if the formulation of Eq. 3.26 is chosen (see Fig. 3.5).

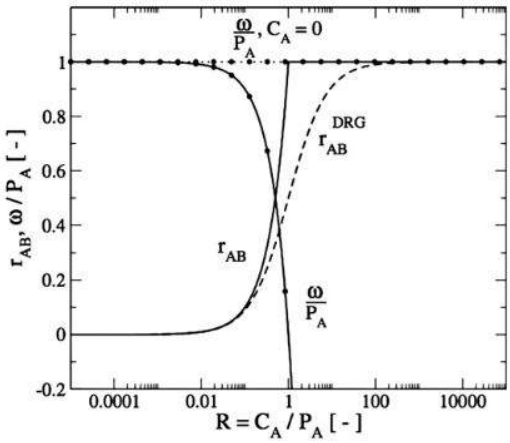

Figure 3.5: Illustration of the behavior of two DRG coefficients: solid line is Eq. 3.27 while the dashed line is Eq. 3.26. Lines with dots represent the source term of a species A, being consumed exclusively through reactions containing a species B, normalized by its production rate P_A. From Pepiot-Desjardins & Pitsch (2008).

Further improvements to the definition of Eq. 3.27 take into account the possibility of removing a set of species $\{S\}$ simultaneously:

$$r^*_{AB,\{S\}} = \frac{|\sum_{0<j<m} \nu_{A,j} Q_j \delta^j_{B,\{S\}}|}{max(P_A, C_A)} \tag{3.28}$$

where $\delta^j_{B,\{S\}}$ is unity if the j-th reaction involves B or any species in subset $\{S\}$, and 0 otherwise.

Now, there may exist important indirect paths between species, that is, a series of reactions starting from a species A might indirectly lead to the production of species B. To evaluate these links, a path dependent coefficient may be evaluated:

$$r_{AB,p} = \min_{1<i<n-1} r^*_{S_i S_{i+1}} \tag{3.29}$$

where $S_1 = A$ and $S_n = B$ and S_i are on the way. With that definition, a path p from A to B is characterized by its weakest link. This naturally leads to the definition of a global coefficient:

$$R_{AB} = \max_{all\ p} r_{AB,p} \tag{3.30}$$

Intuitively, the longer is the path p, the smaller $r_{AB,p}$ should be, which is not reflected in Eq. 3.29. This was considered by Pepiot-Desjardins & Pitsch (2008), who recast Eq. 3.29 to include a degree of error propagation:

$$r^*_{AB,p} = \prod_{1<i<n-1} r^*_{S_i S_{i+1}} \tag{3.31}$$

with now:

$$R^*_{AB} = \underset{all\ p}{max}\ r^*_{AB,p} \tag{3.32}$$

To obtain a global picture of species interactions, the global coefficients R^*_{AB} should be obtained for several sampling points. Importance should be accorded to the state in which the important target species are at any sampling point t chosen for the reduction procedure: if an important target species S_T is no longer active, its importance, when looking for strongly related species, should decrease in consequence. Such a scaling factor $\alpha_{S_T,t}$ was proposed by Pepiot-Desjardins & Pitsch (2008), based on atomic flux considerations. Eventually, the importance of a species A can be estimated through a global coefficient:

$$\overline{R^*_A} = \underset{\substack{t\ in\ sample \\ S_T\ in\ targets}}{max} \left(\alpha_{S_T,t} R^*_{S_T A,t}\right) \tag{3.33}$$

Such a method allows to rank species according to their importance with respect to a set of target species, in order to safely remove unimportant ones. The same procedure can be applied to remove unimportant reactions, by ranking them according to a parameter defined similarly to Eq. 3.27 (Pepiot, 2008).

This method, along with its improvements, has been automatized and implemented in an efficient tool for the reduction of detailed mechanism, YARC, by Pepiot (2008). This tool was employed by its author to successfully derive reduced mechanisms for the combustion of n-heptane (Pepiot & Pitsch, 2008) and iso-octane (Pepiot-Desjardins & Pitsch, 2008). It was also used in the Phd Thesis of Jaravel (2016), to derive ARC for methane and n-dodecane oxidation with NO_x prediction capabilities (Schulz *et al.*, 2017; Jaravel *et al.*, 2016). It is the tool employed in this work.

3.4.1.f Chemical Lumping

Another interesting way of expressing the system with a reduced number of variables is provided by combining, or "lumping" a subset of N_l species into a pseudo-species, $\hat{y}$. Eventually, the kinetics of a reaction system that was originally described in terms of a number N_s of variables by :

$$\frac{dy}{dt} = f(y) \tag{3.34}$$

can be described in terms of a number $\hat{N}_s < N_s$ of variables:

$$\frac{d\hat{y}}{dt} = \hat{f}(\hat{y}) \tag{3.35}$$

Where the lumped species are expressed in terms of the original species by a lumping transformation h:

$$\hat{y} = h(y) \tag{3.36}$$

The problem at hand is threefold :

- Determine which species to lump;
- Determine how the individual species contribute to the concentration of the lumped species they are a part of, so, defining the lumping transformation h;
- Estimate kinetic parameters for the lumped species.

The problem can be tackled in different ways, depending on whether :

- The original system of differential equation f describing the kinetic system is linear or nonlinear (first order system);
- Nonlinear lumping is authorized, in which case the lumping transformation h cannot be described by a matrix;
- Some level of error is accepted in the transformation.

Mathematically based approaches, originated by Wei & Kuo (1969) and further developed by Genyuan & Rabitz (1989); Genyuan *et al.* (1994), in which exact linear or nonlinear lumping techniques have been examined in detail all present the disadvantage to be too formal and present stringent mathematical restrictions that render their application difficult in practice. Furthermore, no automatized rigorous procedure exists to find an optimum lumping transformation in the case of nonlinear lumping techniques. Fortunately, in practice, some degree of error is acceptable in the lumped model, leading to more realistic and affordable approximate lumping techniques.

Other classes of approaches are chemically-based, and rely upon the specificities of the system to lump. Usually, those techniques restrict themselves to approximate linear lumping which are much easier to implement and automatize in a computer program. The choice of the species to lump is based on similar molecular composition or reactive properties. Huang *et al.* (2005) developed an easy-to-implement criterion based upon species' formation rates to select the species to lump, the distribution of which inside the lump can be evaluated directly from the individual production rates of the species. This technique was applied successfully as part of a multi-reduction strategy to derive a reduced model for the oxidation of fuel-rich methane mixtures in a closed vessel under isothermal conditions. However, the criterion relies upon instantaneous formation rates and thus, species with very different chemical properties can end up in the same lump. Furthermore, the relative contribution of each species inside a group is computed explicitly at run time, which is not very efficient. More common chemically-based lumping techniques rely upon isomer species (i. e. species with similar composition and structure). The distribution of the isomers within each lump species is generally fixed, and can be determined based on different considerations. Zeppieri *et al.* (2000), for example, assume a partial equilibrium distribution between isomers of equal carbon number. Lu & Law (2008*b*), used a constant averaged relative distribution of the isomers over a wide range of conditions to derive a reduced mechanism for n-heptane oxidation while Pepiot-Desjardins & Pitsch (2008) determined that distribution based upon statistical information obtained from the detailed scheme. This latter procedure was integrated in a general multi-stage reduction strategy that led to the successful derivation of reduced schemes for n-heptane and iso-octane oxidation; and was also implemented in a the aforementioned reduction tool YARC (Pepiot, 2008).

3.4.2 From skeletal schemes to analytically reduced schemes

3.4.2.a The Quasi Steady State Approximation (QSSA)

The disparities in the represented timescales of detailed kinetic mechanisms are usually still present in skeletal reduced mechanisms. They lead to many difficulties in numerical simulations. A common solution is to consider that some species inside the mechanism, namely those with very short characteristic timescales, are in a quasi-stationary state. Lu & Law (2006*b*) gave an accurate definition of a QSS species: ≪ *A QSS species typically features a fast destruction time scale, such that its small or moderate creation rate is quickly balanced by the self-depleting destruction rate, causing it to remain in low concentration after a transient period. The net production rate of the QSS species is therefore negligible compared with both the creation and the destruction rates, resulting in an algebraic equation for its concentration* ≫. Using the formalism developed in previous Sections, this leads to:

$$\frac{dc_i}{dt} = \dot{\omega}_i(\mathbf{c}, \mathbf{k}) \approx 0 \text{ , for QSS species } i \tag{3.37}$$

With this approximation, the (net) rate-of-production expressions for QSS species lead to a set of algebraic equations, involving a variable number of species concentrations and reaction rates. Solving an ODE is no longer required to obtain the concentration of QSS species, thus lowering the order of the nonlinear system of differential equations (Eq. 2.12). In addition, by construction, the fastest species (i. e. fastest reaction rates) are no more explicitly transported, thus reducing the chemical mechanism's stiffness. As an example, let us consider the chain of reactions between species A, B and C:

$$A \overset{k_1}{\rightarrow} B \overset{k_2}{\rightarrow} C \tag{3.38}$$

Rate laws for each species are given by:

$$\frac{d[A]}{dt} = -k_1[A]$$
$$\frac{d[B]}{dt} = k_1[A] - k_2[B]$$
$$\frac{d[C]}{dt} = k_2[B]$$

Assuming initial conditions where A is the only species present $[A]_{t=0} = [A_0]$ gives an analytical solution for the system of the form (Warnatz, 2000):

$$[A] = [A_0]exp(-k_1 t)$$
$$[B] = [A_0]\frac{k_1}{k_1 - k_2}\left(exp(-k_2 t) - exp(-k_1 t)\right)$$
$$[C] = [A_0]\left(1 - \frac{k_1}{k_1 - k_2}exp(-k_2 t) + \frac{k_2}{k_1 - k_2}exp(-k_1 t)\right)$$

In the limit $k_2 >> k_1$, which is the condition for considering species B as QSS, the solution reduces to:

$$[A] = [A_0]exp(-k_1 t)$$
$$[B] = [A]\left(\frac{k_1}{k_2}\right)$$
$$[C] = [A_0]\left(1 + exp(-k_1 t)\right)$$

(an equivalent result is obtained by setting $d[B]/dt = 0$). The number of time dependent equations to solve has been reduced from 3 to 2, and the concentration of species B is now obtained directly from the concentration of other species A and C. In real systems, however, due to the numerous reaction rates composing a mechanism, such algebraic equations are often non linear, and may prove to be very complex for only a few QSS species. In such a case, truncation can be invoked to provide additional simplification. This basically consists in neglecting the concentration of species always present in very small quantities. However, this often requires a non negligible amount of user input. Alternatively, the nonlinear terms in the algebraic relations may simply be discarded. With this approximation, the nonlinear equations are approximated by a set of linear equations, referred to as LQSSA in Lu & Law (2006*b*), who designed a systematic method based on graph theory to obtain analytic solutions for complex expressions of QSS species concentrations.

It can be interesting to estimate the error introduced on the concentration of certain relatively important QSS species, when obtained via Eq. 3.37 instead of Eq. 2.12. This difference is referred to as the instantaneous QSSA error by Turányi *et al.* (1993) (QSSAS when evaluated for a single QSS species, QSSAG when evaluated on a group of QSS species). The simplest procedure is to calculate both solutions with and without QSSA, but this is obviously inefficient. An alternative method based on the Jacobian has been developed by Turányi *et al.* (1993) to estimate this error with great accuracy in a limited number of calculation steps. Naturally, as the error further propagates along the solution trajectory of the chemical system, it causes an overall error on the non-QSS species as well; but in practice, and if the QSS species are properly selected, this impact is insignificant. This points out the importance of the QSS selection, as well as the need to employ various sampling points to perform this selection. Indeed, from their definition, one can see that in many cases QSS species are radical species which could be identified based on a "try and error approach". However, this is not always the case, and some sort of automated procedure for their identification is necessary. A few popular techniques are reported hereafter.

3.4.2.b Time-scale analysis for the selection of QSS species

Computational Singular Perturbation (CSP) CSP is a technique proposed by Lam (1985) to extract information from a stiff set of equations in the form of Eq. 2.12, by analyzing the characteristic timescales of the system.

The idea is to re-express the rate-of-production vectors from Eq. 2.12 in a new set of basis vectors of dimension n, $\mathbf{v_d}$, which indicate the directions followed by a linear combination of the original reaction rates, f^d:

$$\dot{\omega} = \sum_{0<d<n} \mathbf{v_d} f^d \tag{3.39}$$

The f^d vectors are called the amplitudes or modes of the chemical system, and reads:

$$f^d = \mathbf{w^d} \cdot \dot{\omega} \tag{3.40}$$

with $\mathbf{w^d}$ being the set of inverse row basis vectors:

$$\mathbf{w^d} \cdot \mathbf{v_b} = \delta^d_b, \quad d, b \in [1, n] \tag{3.41}$$

Each of the additive terms in Eq. 3.39 in this context is called a reaction mode. The basis vectors are defined to differentiate species according to whether their evolution is explosive, fast, slow or dormant. This analysis is carried out on the basis of an eigenvalue-eigenvector decomposition of the matrix $\mathcal{M}$ linking the amplitudes f^d, to their derivative:

$$\frac{\partial f^d}{\partial t} = \sum_{0<b<n} \mathcal{M}_b{}^d f^b \tag{3.42}$$

$\mathcal{M}$ depends on the local Jacobian, as well as on the new basis vectors (see e.g. Lam & Goussis (1991, 1994), for a more thorough description of the mathematics behind the CSP method). The idea is to find a set of directions that will uncouple the different amplitudes associated to them; i.e try to have $\mathcal{M}$ as diagonal as possible in Eq. 3.42. Eigenvalues reciprocals have time dimension and are subsequently referred to as timescales $(\tau(d))_{d\in[1,n]}$. These timescales can be ranked from the smallest to the largest, thus providing a ranking of the amplitudes and of the reaction modes as well.

Once the proper decomposition of $\dot{\omega}$ is found -and after refinement if necessary (Lam & Goussis, 1991, 1994)- the next step is to choose a cutting timescale $\tau(n_c)$ as being the smallest timescale considered, and then to find out the decomposition of each species' rate-of-production along the n_c fastest modes only -so, on a fast subspace:

$$\dot{\omega}_{fast} = \sum_{0<d<n_c} \mathbf{v_d} f^d \tag{3.43}$$

Or, starting from the expression of $\dot{\omega}$ provided by Eq. 2.12:

$$\dot{\omega}_{fast} = \left(\sum_{0<d<n_c} \mathbf{Q}_d \right) \cdot \dot{\omega} \tag{3.44}$$

where the $\mathbf{Q}_d$, $d \in [1, n_c]$ are the set of fast projection matrices (of dimension $n \times n$):

$$\mathbf{Q}_d = \mathbf{v}_d \, \mathbf{w}^d \tag{3.45}$$

Furthermore, the i-th diagonal elements of the fast projection matrices $(\mathbf{Q}_d)_{d\in[1,n_c]}$ form a set of fast subspace radical pointers of the i-th species onto the d-th mode. According to Lam & Goussis (1994), whenever the sum of the i-th fast subspace pointers $\sum_{0<d<n_c} \mathbf{Q}_d(i)$ is greater than a specified threshold ϵ, then the i species is well decomposed onto the fast subspace, and is thus a good QSS candidate.

Amongst the firsts to investigate a detailed mechanism with CSP are Goussis & Lam (1992), interested with methanol oxidation. In this paper, the authors provide a good overview of the possibilities offered by the CSP to shed light on the kinetic process. Algorithms based on CSP were later designed to systematically identify QSS species and derive global mechanisms, e. g., the one developed by Massias *et al.* (1999) (S-STEP) which was employed to derive a 7-step mechanism for methane/air oxidation, with laminar flames as a target. The procedure employs truncation of the QSS algebraic relations. Another algorithm employing a global criterion based on those local considerations was also designed and used by Lu *et al.* (2001) (ARC-CSP) to derive reduced mechanisms for the high temperature of H_2/Air and CH_4/Air oxidation. The same authors have also employed the CSP method recently as part of a multi-reduction strategy (Lu & Law, 2008*a*).

Level of Importance (LOI) method Although the CSP method is very thorough, its implementation reduces to an eigenvalue problem, and generating them can require considerable CPU time. An alternative is to perform a chemical lifetime analysis. The species involved in the chemical mechanism each have a specific lifetime which is defined as the time elapsed from its creation to its consumption. It is usually dependent upon other species concentration and temperature, and can differ from several orders of magnitude between species. Those with the shortest overall lifetimes could be potential QSS species.

A generalized interpretation of species lifetimes can be based on the diagonal elements of the Jacobian (at least in homogeneous systems):

$$\tau_i = |\mathbf{J}_{ii}^{-1}| \tag{3.46}$$

This quantity is very easy to extract during a simulation, or to post-processed as long as the chemical source terms and species concentrations are available. Furthermore, this quantity can easily be rescaled according to the combustion process under investigation, for example in non homogeneous systems such as flames (Lovas *et al.*, 2000). However, this quantity alone is not sufficient. Indeed, recall from the definition of a QSS species specifies that it is present in very small quantities throughout the combustion process. As such, a second criterion based on the concentration of potential QSS could be added, but all stable species would still be regarded as non-QSS. Sensitivity investigations are therefore also needed, because if a species has a low impact on a desired target, a larger error is acceptable in its concentration. A selection parameter based on all these considerations was proposed by Lovas *et al.* (2000), named LOI, and was employed in the reduction of a methane/air mechanism based on laminar premixed flames:

$$LOI_i = S_{P,i} c_i \tau_i \tag{3.47}$$

The $S_{P,i}$ denotes the sensitivity of a relevant parameter P (ignition timing, laminar flame speed) on species i. This criterion is very easy to implement, and produces similar reductions when compared to those obtained with the CSP analysis for QSS detection (Lovas *et al.*, 2002).

A variant of this method has also been used by Pepiot-Desjardins & Pitsch (2008) with great success in deriving a reduced iso-octane mechanism for adiabatic auto-ignition at constant volume; and was also implemented in the multi-stage reduction code YARC (Pepiot, 2008).

3.4.2.c The Partial Equilibrium Assumption (PEA)

Another common method to analytically reduce skeletal schemes consists in identifying the fastest reactions in a kinetic scheme. The idea is to identify an attracting reaction manifold spanned by only a subset of reactions. In this way, the number of independent rate equations is reduced to a minimum basis, enabling to replace redundant expressions by algebraic expressions function of that of the basis. Eventually, the changes in the concentration vector can be decomposed into an "equilibrium" and a "non-equilibrium" contribution, where the equilibrium component has been simplified. This equilibrium component is often associated with fast timescales, thus also, removing some of the stiffness from the problem (Rein, 1992).

Goussis (2012) analyzed and compared the assumptions and equations leading to both QSSA and PEA systems, and concluded that the first is a limiting case of the second. In that sense, QSSA is often preferred, since it allows to reach a higher degree of reduction.

Chapter 4

Automatic ARC generation: the YARC tool

Contents

4.1 Multi-stage reduction tools

4.1.1 Principle

The different reduction techniques outlined in Chapter 3 were classified according to the level of reduction they allow to achieve. It is obvious that techniques belonging to different category complement each other, and that one cannot hope to obtain the best possible ARC by employing only one of them. For example, trying to determine QSS candidates directly on a full detailed scheme comprised of hundreds of species will most certainly result in many non-linearities in the QSS expressions. The "know-how" developed in the combustion community over the past decades revealed that to perform an efficient reduction, it is best to proceed in steps, applying a different tool at each reduction stage. For instance, it is best to investigate potential QSS approximation in an already reduced skeletal mechanism. This led to the design of multi-step reduction tools, usually fully automated. The required inputs consist of a detailed mechanism, a set of *targets*, and some sort of error tolerance. Targets, in this context, stand for both the canonical problem employed for the reduction, and the quantities to reproduce with the best accuracy. For example, if say, the ultimate goal is to investigate a sooting ethylene non premixed jet, it may be desirable to generate an ARC for ethylene oxidation with a good prediction of C_2H_2, based on one-dimensional counterflow configurations.

	Strategy I (Lu & Law, 2008*a*)	**Strategy II** : YARC (Pepiot, 2008)	**Strategy III** : KINALC (Turányi, 1990*a*)
STEP I	DRG(X/ASA)	DRGEP Chemical Lumping	Jacobian investigations (remove species) PCA (remove reactions)
STEP II	QSS via CSP pointers	QSS via LOI	QSS via error estimation (Turányi *et al.*, 1993)
Examples	(Lu & Law, 2008*a*,*b*) and more online: (Lu, 2008)	(Pepiot-Desjardins & Pitsch, 2008) (Pepiot & Pitsch, 2008; Jaravel, 2016)	(Tomlin *et al.*, 1992) and more online: (Turányi, 1981)

Table 4.1: Literature review of multi-step reduction strategies

As already said, multi-step reduction strategies have been employed in the literature to derive ARC for various purposes. Table 4.1 reports three such strategies, along with references which have all already been mentioned in the previous Chapters. All follow the same structure: first, a skeletal reduction is performed, where unimportant species are removed before considering redundant reactions, and finally, QSS approximations are performed, resulting in ARC with a specified number of species and a set of expressions for the calculation of the source terms involving the QSS species. In some cases, the species could be reorganized in a series of "steps", to identify the main chemical processes (see e.g. Boivin (2011)).

4.1.2 The YARC tool

YARC is a multi-step automated reduction tool developed by Pepiot (2008) during her PhD thesis. The tool consists of a series of libraries written in Pearl, implementing the DRGEP and chemical Lumping for skeletal reduction, and the LOI for QSS selection, as depicted in Table 4.1. It is fully coupled with the chemistry solver FlameMaster (Pitsch, 1988), which solves the targeted canonical test cases to be sampled. The reduction can be performed on various test cases (see Section 4.2) which can be combined. A set of important parameters are also provided by the user, such as specific species mass fractions, in order to steer the reduction towards the desired application and to monitor their evolution throughout the reduction process. YARC generates several reduced mechanisms with increasing error level, as well as output files containing information about each reduced mechanism. The overall process is illustrated on Fig. 4.1. Examples of ARC generation for different fuels, target

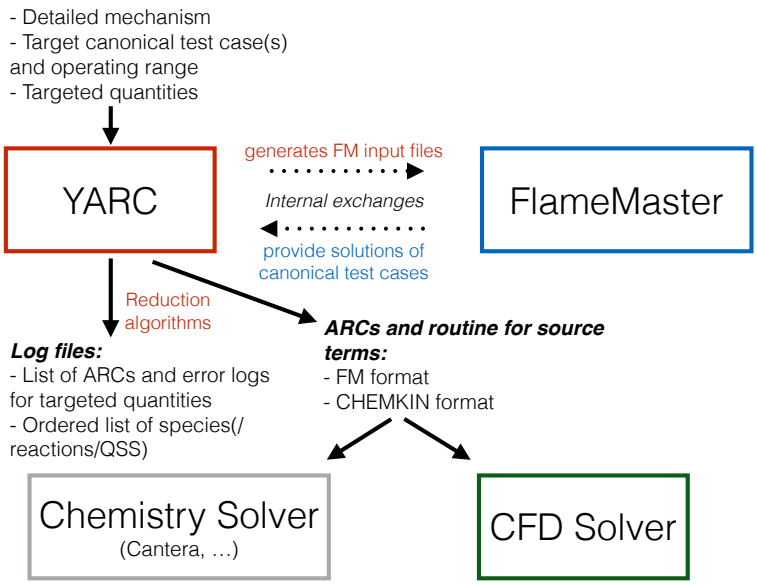

Figure 4.1: Diagram of YARC

configurations and detailed mechanisms will be presented in Sections 4.3 & 4.4. A subset of these ARCs will be further employed in real 3D configurations in Part III of this PhD thesis.

4.2 Canonical test cases

The canonical test cases employed to perform and assess the validity of the reduction of a detailed mechanism include zero and one dimensional configurations. Belonging to the first category, are constant volume or constant pressure autoignition simulations and extinctions in perfectly stirred reactors. Species evolutions in plug flow reactors and shock tubes can also be considered. With these types of simulation, it is the time evolution of homogeneous mixtures inside a vessel that is of interest. Belonging to the second category are steady unstretched and stretched premixed laminar flames, as well as steady strained laminar diffusion flames. In this work, all ARC derivations employed auto-ignition in constant volume reactors and laminar unstretched premixed flames as test cases. However, *a-posteriori* validation was always performed on laminar strained premixed and diffusion test cases as well.

4.2.1 Autoignition

A sketch of the evolution of quantities during the autoignition of a stoichiometric mixture of methane and air at an initial temperature of 1000 K is provided in Fig. 4.2. Of interest here is the autoignition delay τ_{ig}, which can be defined as the time when a certain amount of radical is produced, for example the maximum of radical OH. It can also be defined as the time when the maximum of temperature gradient occurs.

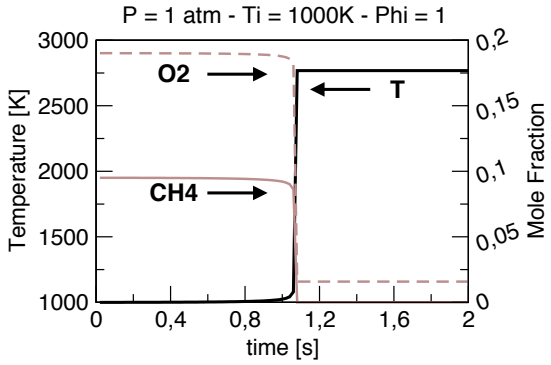

Figure 4.2: Time evolution of the autoignition process of a mixture of methane and air at an initial temperature of 1000 K.

4.2.2 Laminar premixed flames

This canonical test case corresponds to a situation where the fuel and the oxidant are perfectly mixed prior to combustion. The flame region can be decomposed in three layers, as illustrated on a 1D laminar premixed flame in Fig. 4.3 (b):

- A *preheat* zone, which is chemically inert, and where the premixed mixture is progressively heated by backward diffusive fluxes from the reaction zone.
- An *inner reaction* zone (in red in Fig. 4.3b) of thickness δ_l^0 (to be defined) where the fuel is decomposed into smaller compounds and where the bulk of heat release occurs. This region is also characterized by the presence of many radicals involved in the chain of reaction discussed in Section 2.2.1.
- A *post-flame* zone where intermediate species are converted to products, characterized in particular by the chemistry of CO and CO_2. It is also the zone where NO_x reactions occur.

To describe premixed flames, the same quantities as introduced in Section 3.3.2 are employed, namely, the mixture fraction Y_z and normalized progress variable c. Another quantity of interest is the equivalence ratio ϕ, which is related to the mass balance of the stoichiometric global reaction (Eq. 2.1):

$$\nu'_F F + \nu'_O O - > Products \tag{4.1}$$

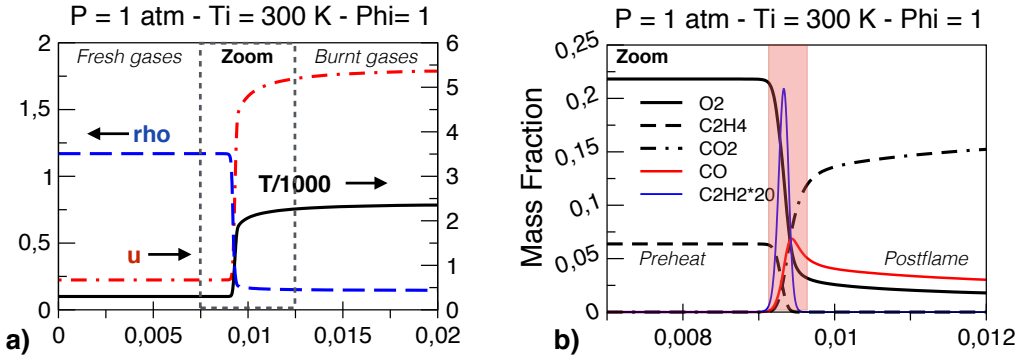

Figure 4.3: Spatial profiles of an unstretched one-dimensional premixed ethylene/air laminar flame: a) entire flame region and b) zoom on the reaction zone.

by

$$\phi = s\frac{Y_F}{Y_O} \tag{4.2}$$

where

$$s = \frac{\nu'_O W_O}{\nu'_F W_F} \tag{4.3}$$

with W_F and W_O the fuel and oxidant molecular mass, respectively, and Y_F and Y_O the mass fraction of fuel and oxidizer present in the fresh gases. The equivalence ratio is a global quantity, characterizing the deviation to stoichiometry of a premixed mixture; With $\phi = 1$ corresponding to stoichiometry.

Flame thickness Premixed flames have an intrinsic thickness. Amongst the different definitions provided in the literature, two are of particular interest:

- the diffusion thickness $\delta = D_{th}/s_l^0$, where s_l^0 is the laminar flame speed (see next Section). This definition is derived from scaling laws and easy to evaluate (Poinsot & Veynante, 2005), but too approximative in practice
- the thermal thickness δ_l^0, which is preferred, evaluated directly from the temperature gradient:

  $$\delta_l^0 = \frac{T_b - T_f}{max(|\nabla T|)} \tag{4.4}$$

  with subscripts b and f denoting burnt and fresh gases, respectively.

Flame speeds Premixed flames are also characterized by their propagation speed s_l, which may be calculated either from the velocity or kinetic properties. However, as the velocity changes through the flame (due to density variations), using it to define s_l entails choosing a particular evaluation location. It is convenient to use the progress variable and define s_l at a given value c^*. In 3D, defining s_l thus requires to monitor the evolution of the c^* iso-surface.

Along the c^* iso-surface, the normalized local gradient of c defines the flame front normal direction:

$$\mathbf{n} = -\left.\frac{\nabla \mathbf{c}}{|\nabla \mathbf{c}|}\right|_{c^*} \tag{4.5}$$

It is pointing towards the fresh gases, as illustrated on Fig. 4.4. On this figure, several velocities are identified:

- The flame front (identified as the c^* iso-surface) velocity $\mathbf{w}$, expressed in a fixed reference frame. It expresses the motion of the c^* iso-surface. By definition, it satisfies:

  $$\left.\frac{\partial c}{\partial t}\right|_{c^*} + \nabla c|_{c^*} \cdot \left.\frac{\partial \mathbf{x}}{\partial t}\right|_{c^*} = \left.\frac{\partial c}{\partial t}\right|_{c^*} + \nabla c|_{c^*} \cdot \mathbf{w} = 0 \tag{4.6}$$

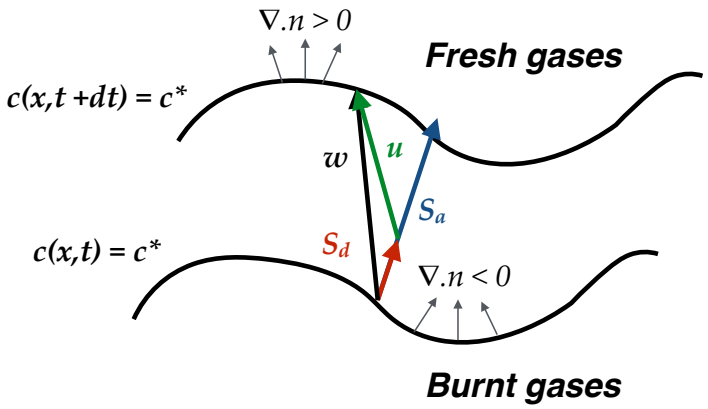

Figure 4.4: Propagating laminar premixed flame front, adapted from Poinsot & Veynante (2005).

- $S_a = \mathbf{w} \cdot \mathbf{n}$, the projection of the flame front velocity on the flame front normal, denoting the *absolute* speed at which an iso-level of progress variable propagates relative to a fixed reference frame. Employing Eqs. 4.5 & 4.6, S_a is expressed as:

$$S_a = \frac{1}{|\nabla c|}\bigg|_{c^*} \frac{\partial c}{\partial t}\bigg|_{c^*} \tag{4.7}$$

- The *displacement* speed S_d is the component of the flame front velocity actually due to flame propagation, so, it is the flame front velocity minus the flow field contribution $\mathbf{u}$:

$$\mathbf{S_d} = \mathbf{w} - \mathbf{u} \tag{4.8}$$

Since the flame can only propagate normal to itself, S_d can be re-expressed in the more convenient way:

$$S_d = \mathbf{w} \cdot \mathbf{n} - \mathbf{u} \cdot \mathbf{n} = S_a - \mathbf{u} \cdot \mathbf{n} \tag{4.9}$$

and finally, using the expression for $\mathbf{n}$:

$$S_d = \left[\frac{1}{|\nabla c|}\frac{\partial c}{\partial t} + \mathbf{u}\frac{\nabla c}{|\nabla c|}\right]_{c^*} = \frac{1}{|\nabla c|}\bigg|_{c^*} \frac{Dc}{Dt}\bigg|_{c^*} \tag{4.10}$$

where D/Dt is the total derivative. By making use of the species equation, Eq. 5.2, and the fact that c is a combination of species, we get an explicit expression for S_d (Echekki & Chen, 1999), made of a *diffusion* and a *reaction* contribution:

$$S_d = \left[\frac{\nabla \cdot (\rho D_c \nabla c) + \dot{\omega}_c}{\rho |\nabla c|}\right]_{c^*} \tag{4.11}$$

where D_c is the diffusion coefficient of the progress variable. This formulation puts forward the fact that the intrinsic flame speed stems from a balance between diffusion and reaction (Gran *et al.*, 1996). The diffusion contribution can be further split into a *normal* component and a *tangential* component. The tangential component directly involves the curvature, $\nabla \cdot \mathbf{n}$, sketched in Fig. 4.4. :

$$S_d = \left[\frac{\mathbf{n} \cdot \nabla(\rho D_c \mathbf{n} \cdot \nabla c) - \rho D_c |\nabla c| \nabla \cdot \mathbf{n} + \dot{\omega}_c}{\rho |\nabla c|}\right]_{c^*} \tag{4.12}$$

To account for the gas expansion through the flame, a density-weighted flame displacement speed is usually preferred:

$$S_d^* = \frac{\rho}{\rho_f} S_d \tag{4.13}$$

- Finally, the *consumption* speed S_c expressing the speed at which fuel is consumed across the flame front is defined as:

$$S_c = -\frac{1}{\rho_f (Y_F^f - Y_F^b)} \int \dot{\omega}_F \mathbf{dn} \tag{4.14}$$

This is the only global flame speed definition, very easy to compute in simulations.

Note that in stationary 1D laminar premixed flames, $S_a = 0$, such that the following is verified for the laminar flame speed s_l^0:

$$s_l^0 = S_c = -u_0 = -S_d^* \tag{4.15}$$

Strain, Curvature and Strech Premixed flame fronts in 3D simulations are stretched by the non-uniformities of the flow. This leads to a variation of the flame surface area, quantified as the fractional rate of change of a flame surface element A (Buckmaster, 1979; Poinsot & Veynante, 2005):

$$\kappa = \frac{1}{A}\frac{dA}{dt} \tag{4.16}$$

For a thin flame sheet, flame stretching stems from in-plane effects, and can thus be expressed as (Candel & Poinsot, 1990):

$$\kappa = \nabla \cdot \mathbf{w} - \mathbf{nn} : \nabla \mathbf{w} \tag{4.17}$$

where $\mathbf{nn} : \nabla = n_i n_j \partial / \partial x_j$ represents the gradient operator normal to the flame surface. Since $\mathbf{w}$ is the sum of a flow and a flame component : $\mathbf{w} = \mathbf{u} + S_d \mathbf{n}$, Eq. 4.17 is more conveniently reexpressed as:

$$\kappa = \nabla \cdot \mathbf{u} - \mathbf{nn} : \nabla \mathbf{u} + S_d \nabla \cdot \mathbf{n} \tag{4.18}$$

where the contribution from the flow, the *tangential* strain rate, and the contribution from the flame topology and motion, the *curvature* effect, are better distinguished.

Targeted quantities When targeting one-dimensional premixed laminar flames in the reduction process, the quantities of interest are often: δ_l^0, the burnt gas state (T, mass fractions) and s_l^0. It is also interesting to monitor the overall production/consumption of other species X across the flame front:

$$\dot{\omega}_X^{tot} = \int \dot{\omega}_X dx \tag{4.19}$$

This is the case, for instance, for pollutant species such as CO or NO for which such quantities provide a first measure of the total amount of pollutants expected at the exhaust of a combustor.

The response to stretch is evaluated in terms of S_c and $\dot{\omega}_X^{tot}$, for selected species. However, it should be noted that, in one-dimensional computations, the stretch reduces to a tangential strain only. In fact, there is no easy way to assess *a-priori* the response of the chemical mechanism to curvature in 3D flows.

4.2.3 Laminar diffusion flames

Diffusion flames represent the case where the fuel and oxidizer are not mixed before combustion. The fuel and oxidizer are fed through separate inlets, in a counterflow or coflow configuration. Mixing is driven by the diffusion of the reactants towards the reaction zone, and a flame front is localized around the stoichiometric line. Figure 4.5 (a) provides a sketch of a strained counterflow configuration. In that sense, laminar diffusion flames are fundamentally different from laminar premixed flames in that they do not propagate nor have an intrinsic well defined thickness: they live where the flow conditions allow. A global characterization of the degree of strain a seen by the flame is provided by:

$$a = \frac{u_F + u_O}{L} \tag{4.20}$$

where u_F and u_O are, respectively, the fuel and oxidizer inlet velocity, and L is the distance separating the two inlets. The quantities Y_z and c can be employed to describe the flame structure (see Section 3.3.2). In a first approximation, where all species are assumed to have unity Lewis numbers, the pure mixing lines can be described in the Y_z space (see Figure 4.5 (b)):

$$Y_F^m = Y_F^0 Y_z \quad Y_O^m = Y_O^0 (1 - Y_z) \tag{4.21}$$

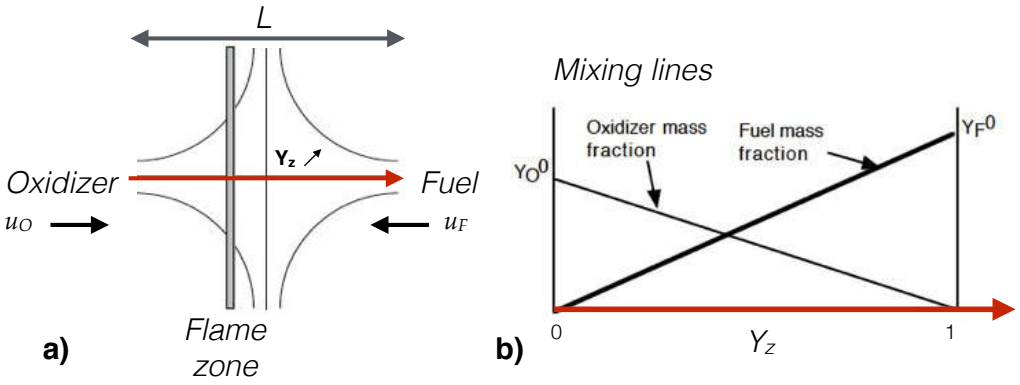

Figure 4.5: a) Sketch of a stretched counterflow flame configuration and b) mixing lines.

where Y_F^0 and Y_O^0 are, respectively, the fuel and oxidizer initial mass fraction in their respective streams. With these definitions, a local equivalence ratio can be related to the mixture fraction by:

$$\Phi = s\frac{Y_F^m}{Y_O^m} = s\frac{Y_F^0}{Y_O^0}\frac{Y_z}{1-Y_z} \tag{4.22}$$

In practice, this is a very good approximation even with a more elaborated transport description, since the Bilger mixture fraction (used in this work) is not too sensitive to preferential diffusion. A sketch of the structure of a counterflow diffusion flame is provided in Fig. 4.6, for a small global strain rate $a = 150s^{-1}$. Three zones are easily identified: a reaction zone (in red) framed by two diffusion layers. The reaction zone can be characterized as the zone where the progress variable peaks. In that sense, a reaction zone thickness centered around stoichiometry,

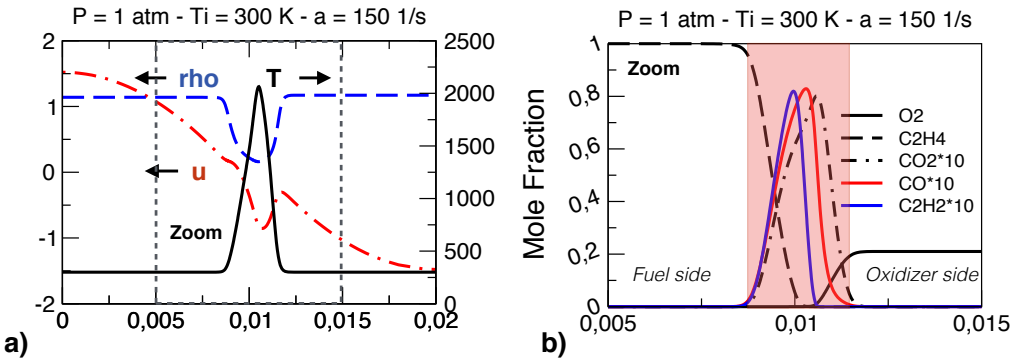

Figure 4.6: Spatial profiles, along the central axis, of a strained diffusion ethylene/air laminar flame: a) entire flame region and b) zoom on the reaction zone.

δ_r, can be defined. However, as already said, this quantity depends upon the flow conditions rather than upon chemistry. A diffusion layer thickness δ_d can also be defined, identifying the region where the mixture fraction goes from 0 to 1. If simplified transport is assumed (unity Lewis numbers) δ_d can be closely related to the scalar dissipation rate $\chi = 2D(\nabla Y_z)^2$ which, together with Y_z, provides a very convenient framework to characterize and study the structure of diffusion flames:

$$\delta_d = \sqrt{D/\chi_{st}} \tag{4.23}$$

χ_{st} stands for the scalar dissipation rate evaluated at $Y_z = z_{st}$. In this simplified framework, the scalar dissipation rate is shown to be directly proportional to the strain rate:

$$\chi = \frac{a}{\pi} exp\left[-2\left(erf^{-1}(1-2Y_z)^2\right)\right] \tag{4.24}$$

Since the flame is usually located in the vicinity of $\Phi = 1$, χ_{st} provides a good approximation of the strain seen by the flame. Diffusion flames do not have flame speeds, and the rate at which fuel is consumed is directly proportional to the square root of χ_{st}. In that sense, diffusion flames are much more sensitive to local flow conditions than premixed flames. In particular, excessive straining eventually leads to a quenching of the flame.

Targeted quantities The strain rate a_{ext} (or dissipation rate χ_{ext}) at which quenching occurs, the evolution of the global fuel consumption (Eq. 4.19) and the evolution of the maximum temperature or major species with increasing strain rate are usually the quantities of interest when targeting this type of canonical configuration in a reduction process. An example of maximum temperature evolution in strained counterflow ethylene/air flames at 3 bars and initial temperature of 300 K is shown on Fig. 4.7

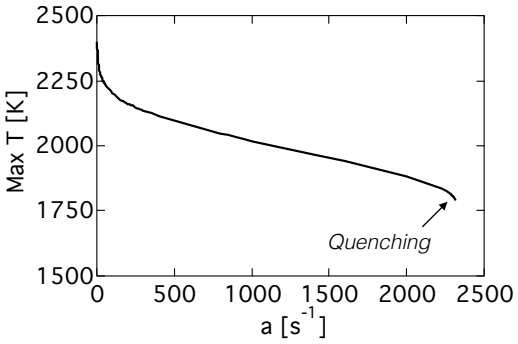

Figure 4.7: Evolution of maximum temperature with strain rate a in a series of counterflow diffusion ethylene/air flames. P = 3 bars, T_i = 300 K.

4.3 Application 1: ARC for Ethylene/air oxidation

4.3.1 Choice of the detailed mechanism

Ethylene is the smallest alkene, and is thought to be one of the main precursor of soot. As such, it has been widely studied from both an experimental and computational point of view, and many authors have developed their own specific detailed mechanisms. Amongst them, 5 have been selected based on their availability, operating range, size and general acceptance in the community. They are listed in Table 4.2. Note that in this table, reactions are not necessarily irreversible.

Acronym	Reference	Size
W&F	(Wang & Frenklach, 1997)	99 species 533 reactions
W&L	(Wang *et al.*, 1999*b*)	75 species 529 reactions
USCII	(Wang *et al.*, 2007)	111 species 784 reactions
CRECK (C1-C3 high and low T mechanism)	(Ranzi *et al.*, 2012)	107 species 2642 reactions
N&B	(Narayanaswamy *et al.*, 2010)	158 species 1049 reactions

Table 4.2: Considered detailed mechanisms for ethylene/air oxidation

A series of experimental laminar flame speed (s_l) and autoignition (τ_{ig}) data for various pressure, temperature and composition are reported in the review by Ranzi *et al.* (2012) as well as on the website of Prof. Wang [1]. A subset of these data was employed to evaluate and compare the global performance of each of these mechanisms. The solver CANTERA (Goodwin *et al.*, 2014) is used, along with a mixture-averaged evaluation of the transport data (see Section 5.2).

Figure 4.8 top reports s_l at an initial temperature of 300 K, for different pressures. All mechanisms perform reasonably well, with the exception of the W&F scheme, overpredicting s_l over the entire range of equivalence ratio. The USCII and CRECK mechanisms underpredict s_l around stoichiometry for P = 5 atm, which is one of the target pressure for the configuration FIRST considered in Chapter 7. Furthermore, the computations with both the W&F and CRECK mechanisms are difficult to converge, even in these simple laminar test cases. A rapid analysis of timescales (based on the diagonal of the Jacobian) did not reveal any significantly small timescale for these mechanisms; however, the CRECK mechanism exhibits a lot of lumped reactions which might slow down the computation. These lumped reactions are also difficult to handle with YARC. In view of the auto-ignition

[1] http://ignis.usc.edu/Mechanisms/USC-Mech%20II/USC_Mech%20II.htm

delay shown at the bottom of Fig. 4.8, the W&F mechanism is suspected to exhibit strong nonlinearities in the reaction rate expressions, although this is has not been thoroughly investigated and is just the general impression after using this mechanism on simple test cases. Based on these observations, the mechanisms retained at this point are the W&L and the N&B. The N&B is finally chosen, because it is more recent, and part of a modular comprehensive reaction mechanism still under development [2].

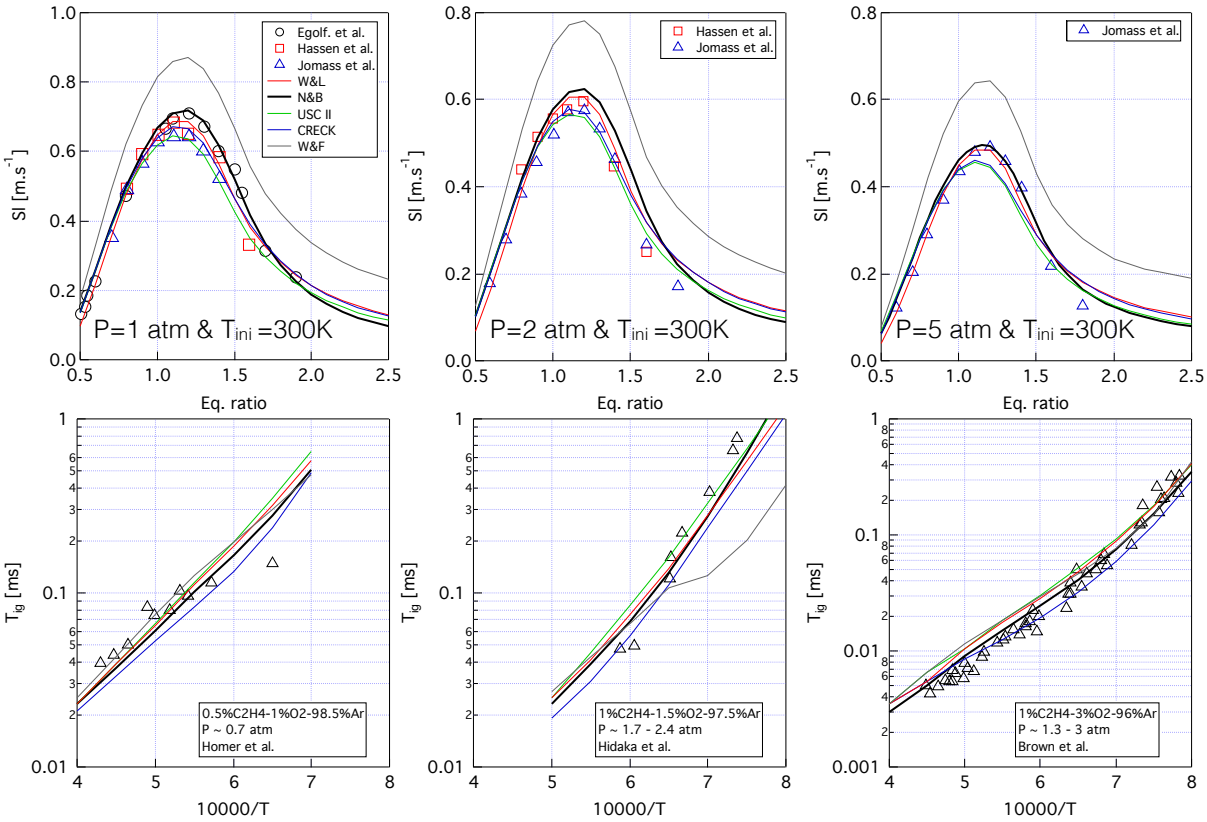

Figure 4.8: Comparison of experimental laminar flame speeds and auto-ignition results with computations performed with the solver CANTERA and various detailed kinetic schemes (see Table 4.2).

In the next Subsections, YARC is used to perform a series of multi-step reductions of the N&B mechanism, targeting the operating range and canonical cases believed *a-priori* to be relevant to FIRST. All reductions start by a skeletal step by employing the DRGEP method, see Table 4.1. Since the mechanism is of reasonable size and the targeted hydrocarbon is small, no lumping is considered here. To illustrate the efficiency of the YARC tool, different operation range (low versus high temperature auto-ignition), canonical test cases (auto-ignition versus laminar premixed flames) and constraints (acetylene) are employed, and the overall effect on the produced skeletal mechanisms is investigated. The list and acronyms of each reduction performed is listed in Table 4.3. Finally, the search for QSS candidates and the derivation of a fully reduced ARC is performed in the last Subsection.

Case name	**Canonical test cases**	**Targeted range**	**Targeted constraints**
AI HT case	Auto-ignition (AI)	3 atm / 1300-1700 K / $\phi = 0.5$-1.5	C_2H_4 CO CO_2 OH HR
AI LT case	Auto-ignition (AI)	3 atm / 800-1100 K / $\phi = 0.5$-1.5	C_2H_4 CO CO_2 OH HR
PF case	Laminar premixed flames (PF)	3 atm / 300 K / $\phi = 0.5$-1.5	C_2H_4 CO CO_2 OH HR
Ref case	AI	3 atm / 1300-1700 K / $\phi = 0.5$-1.5	C_2H_4 CO CO_2 OH HR
	PF	3 atm / 300K / $\phi = 0.5$-1.5	C_2H_4 CO CO_2 OH HR
C_2H_2 case	AI	3 atm / 800-1700 K / $\phi = 0.5$-1.5	same + C_2H_2
	PF	3 atm / 300K / $\phi = 0.5$-1.5	same + C_2H_2

Table 4.3: List and specifications of reductions performed with YARC.

[2] http://krithikasivaram.github.io/

4.3.2 Effect of the targeted canonical test cases

4.3.2.a 0D test cases

Two skeletal reductions have been performed, one targeting high temperature autoignition (AI HT) the other one low temperature autoignition (AI LT). DRGEP is applied to identify important species. It is important to note that, as the DRGEP algorithm is only applied once at the beginning to order the species, the reduction should be performed several times in a row. Indeed, removing species and reactions eventually reorganizes pathways and propagates error in a way that is difficult to predict *a-priori*. Running several DRGEP in a row, on successively reduced mechanisms, is a way to ensure that the ranking of species is still relevant and to speed up the reduction process. Of course, error checks have to be performed very often, and the overall process still relies upon the user, especially when trying to derive mechanisms with the smallest possible size. Let us take as an example the AI HT case.

Derivation of an AI HT skeletal mechanism At the beginning, there are 158 species. A first go at the DRGEP algorithm ranks the species, and a series of mechanisms are constructed (one every 5 removed species) before being tested. The error on the prediction of constraining targets is then calculated, as illustrated on Fig. 4.9 (a) exhibiting the error on autoignition delay. A jump is observed around 40 species, indicating the minimum number of species for an appropriate reduced mechanism.

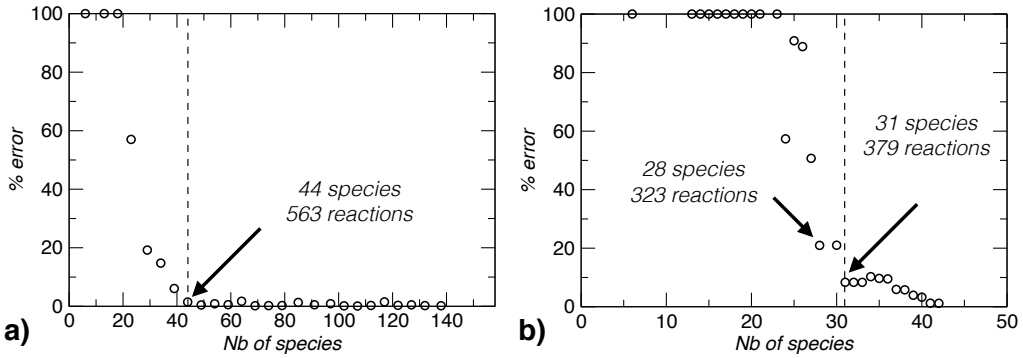

Figure 4.9: Illustration of the DRGEP procedure: (a) on the detailed mechanism (first DRGEP procedure) and (b) on the 44 species and 563 reactions mechanism (second DRGEP procedure).

Authorizing a maximum error of 1.5% leads to the selection of a mechanism containing 44 species and 563 reactions. If the process is reiterated on this first mechanism, a second mechanism comprised of 31 species and 379 reactions is identified by the jump in autoignition delay error, shown on Fig. 4.9 (b). Of course, one has to be careful in that errors are now *relative* to the last reduced mechanism. Eventually, it will be necessary to estimate the error relative to the original detailed mechanism. The process is reiterated once more (third DRGEP procedure), and a final mechanism of 28 species and 316 irreversible reactions is obtained before the error levels become too important. A quick error estimation against the detailed mechanism on the targeted range reveals that the maximum error on τ_{ig} is $< 10\%$ for $T > 1400$ K, and peaks around 30% for $T = 1300$ K; with a maximum error for the species evolution always $< 5\%$. For the sake of simplicity, only autoignition delay predictions are considered in the rest of the discussion to assess the accuracy of a skeletal mechanism -and it has been verified that it is the most constraining target in the present case. Additionally, note that, in order to illustrate the performances of the various reduced mechanisms derived throughout this Chapter (plots and graphs), operating points are randomly chosen amongst the targeted operating range.

Now, as predicted, the subsequent DRGEP process have reordered the species. For instance, keeping the order determined by the second DRGEP process to derive a 28 species mechanism directly would have resulted in a mechanism containing 28 species and 323 reactions, as shown in Fig. 4.9 (b). However, the list of species considered in each 28 species mechanism differ: the 28 species and 323 reactions, for example, does not retain C_3H_3 nor C_3H_2O, two species contained in the 28 species and 316 reaction mechanism because the third DRGEP procedure placed them at the top of the importance list. It is then interesting to compare those two 28 species mechanisms and to investigate their differences. In this case, the global performances of the 28 species and 323 reactions mechanism are slightly better, since the error on τ_{ig} is consistently $< 20\%$ for $T > 1300$ K (so, in the entire derivation range). A closer investigation reveals that this mechanism performs better in the medium/high

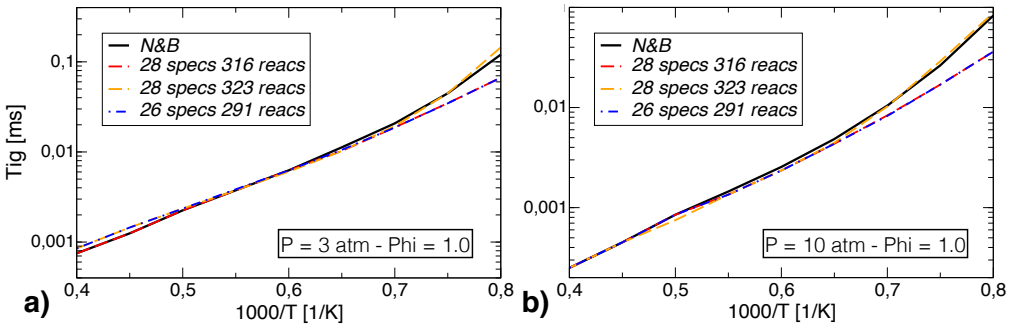

Figure 4.10: Example of performances of several skeletal mechanisms in the high temperature range.

temperature range, whereas the 28 species and 316 species performs better in the very high temperature range, see Fig. 4.10 & 4.11: two successive DRGEP procedures tend to strengthen the targeted operating range (T $>$ 1300 K corresponds to 1/T $<$ 0.77).

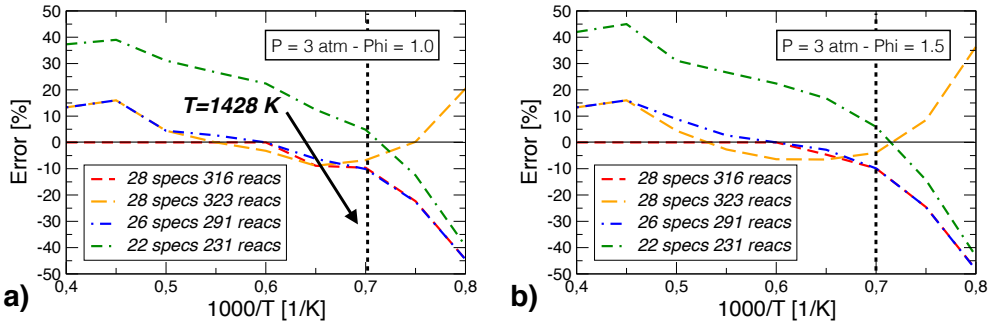

Figure 4.11: Relative errors on predicted τ_{ig} for the various skeletal mechanisms throughout the high temperature range, for two operating points.

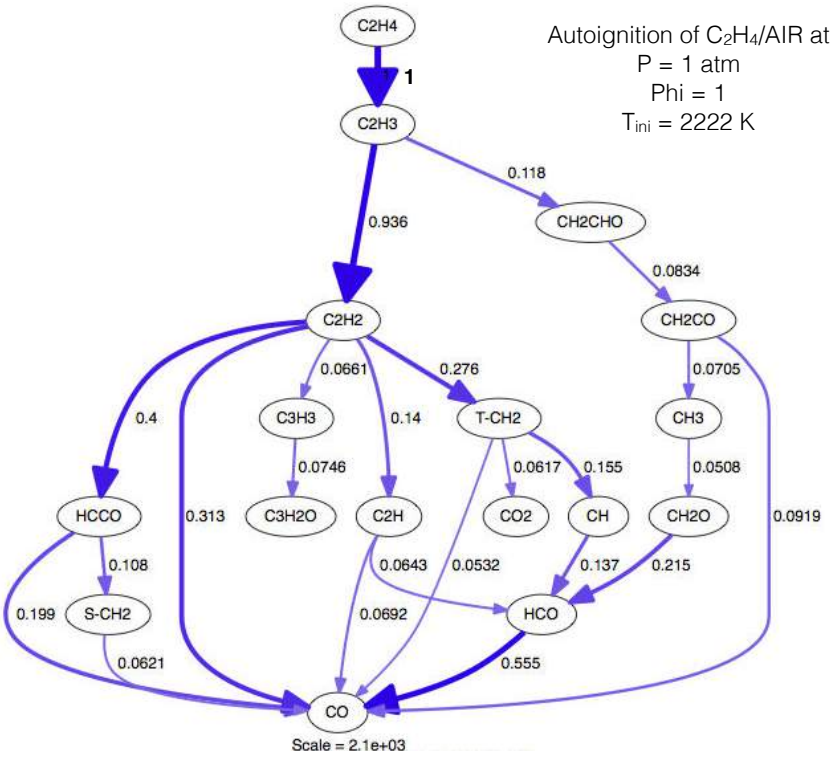

Figure 4.12: Reaction path diagram following C with the detailed mechanism.

Since the performances of both 28 species skeletal mechanisms seem however acceptable for T > 1400 K, it might be interesting to only keep those species present in both, to obtain the smallest possible skeletal mechanism targeting the HT range with good accuracy (i. e. $\tau_{ig} < 10 - 20$ %). The resulting reduced mechanism contains 26 species and 291 reactions. Its performances are as expected similar to that of the worst 28 species mechanism in each temperature region (see Fig. 4.10 & 4.11), so that no additional error is introduced in this case (although it might not always be true). It is important to underline that this skeletal mechanism could not have been obtained directly without the 3 successive DRGEP procedures. In fact, after a certain level of reduction has been attained, some trial-and-error and/or sensitivity analysis is almost always inevitable.

Finally, note that the performances of all skeletal mechanisms in predicting HT (High Temperature) autoignition remain acceptable even well outside of the targeted operating range, as for example at P =10 atm, $\phi = 1.0$ shown on Fig. 4.10 (b). This is the result of the reduction process being "physically-oriented" and conserving the main relevant pathways, and of the kinetic process under investigation evolving continuously within the operating range, so that an ARC performance will slowly worsen outside of its derivation range (see Fig. 4.11). To illustrate this argument, two plots are presented in Fig 4.12 & 4.13, depicting the main pathways followed during autoignition of an ethylene/air mixture at atmospheric pressure, $\phi = 1$ and initial temperature of T = 2222 K, when employing the detailed mechanism and the 26 species skeletal mechanism. It is readily seen that these plots look similar. One has to be careful, however that this conclusion does not necessarily apply to other canonical test cases (in particular, when transport play an important role). In the present case for example, global performances on simple premixed laminar 1D test cases, such as s_l, are poorly predicted. This will be further discussed in a next paragraph.

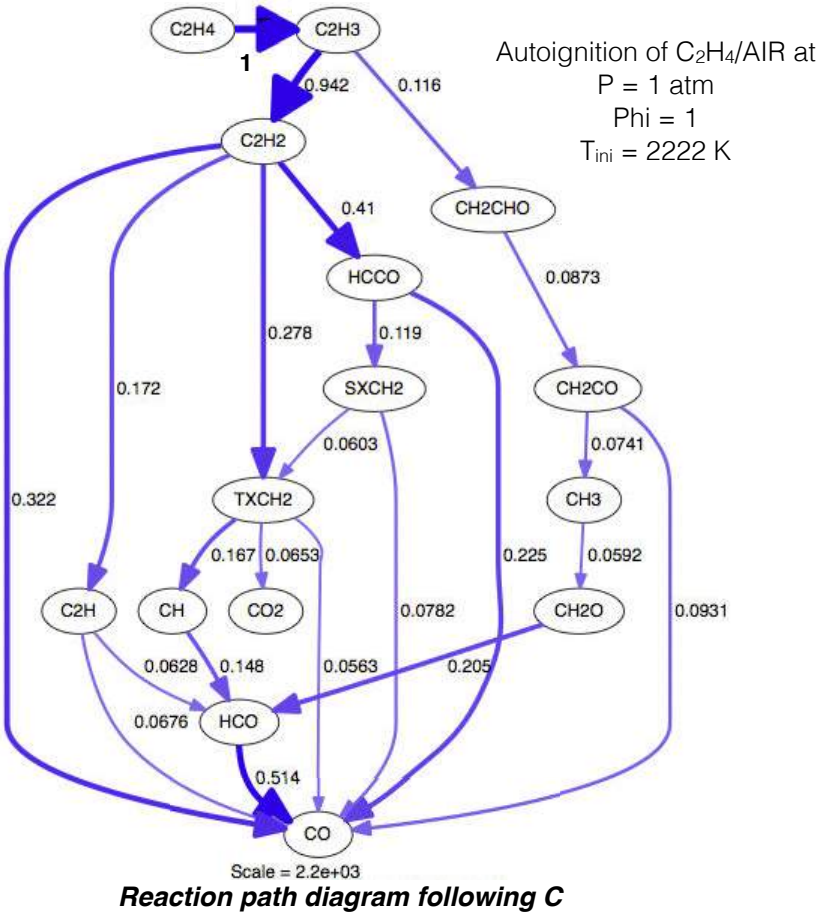

Figure 4.13: Reaction path diagram following C with the skeletal mechanism containing 26 species and 291 reactions.

To illustrate the flexibility of the method, the derived 26 skeletal mechanism is submitted to a last DRGEP step. Indeed, keeping in mind the experimental uncertainties, final configuration under interest (turbulence, etc.) and other sources of error, one might want a smaller reduced mechanism with less accuracy. By allowing a maximum of 40-50% error on autoignition delay throughout the entire operating range (so, by worsening the performances of the mechanism towards very high temperatures), a skeletal mechanism containing only 22 species and 231 reactions can be derived, see Fig. 4.14 & 4.11.

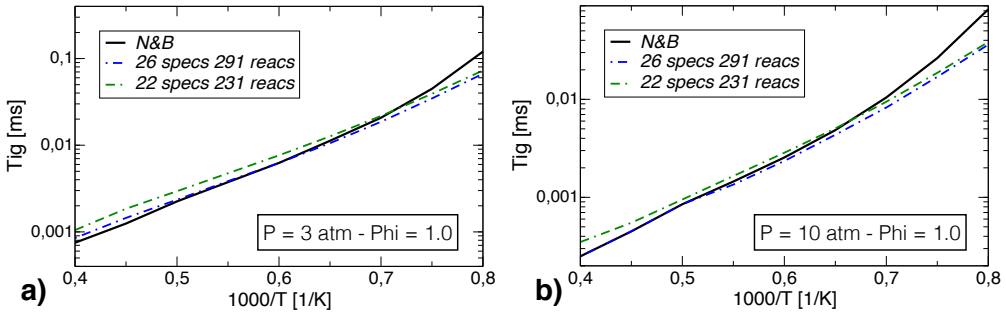

Figure 4.14: Example of performances of the 22 species and 231 reactions skeletal mechanism in the high temperature range.

To sum up, in this paragraph, three skeletal mechanisms have been derived for the prediction of high temperature autoignition. The most comprehensive one contains 28 species and 316 reactions, and performs extremely well in the range $1400 < T < 2000$ K. The error on autoignition delay and targeted species evolution never exceeds 10% and 5%, respectively. This mechanism was derived directly, with 3 successive DRGEP procedures applied on successively reduced mechanisms, which were identified by the error logs. A 26 species mechanism containing 291 reactions, performing also well under the same operating conditions, but with higher error levels at very high temperature has been obtained next, with some input from the user. Finally, with some try-and-error, a smaller 22 species and 231 reactions skeletal mechanism exhibiting a maximum of 50% error on autoignition delay throughout the entire HT range ($T > 1300$ K) was obtained.

This first simple example illustrates that YARC is a very powerful tool, able to carry a radical reduction even with minimum input form the inexperienced user (going from 158 to 28 species represents a species reduction of 82%). The 26 species and 291 reactions mechanism is now retained and referred to as the HT mechanism.

AI HT versus AI LT skeletal mechanisms Applying the same methodology in the range targeted by the AI LT case results in a skeletal mechanism comprising 27 species and 271 reactions. A first observation is that amongst the species retained in the HT and LT skeletal mechanisms, only 21 are common to both. Another observation, is that the performances of these mechanisms in predicting autoignition delay, when confronted to each other and to the detailed mechanism for the entire temperature range, are very different (see Fig. 4.15). This is not surprising since they have each been drastically reduced to perform very well only in their respective targeted range.

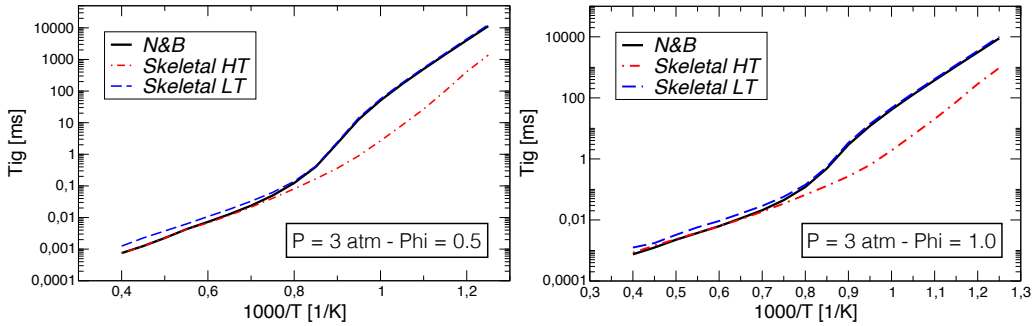

Figure 4.15: Examples of performances of the HT and LT skeletal mechanisms on the entire temperature range, for two operating points.

However, it is also readily observed that the LT skeletal mechanism is more accurate over the entire temperature range: the maximum error on the prediction of autoignition delay never exceeds 80% when it almost reaches 100% on the LT range with the HT skeletal mechanism, see Fig. 4.16. Indeed, it is known that the medium/low temperature range autoignition is more challenging to capture, and that mechanisms targeting this range will usually be more exhaustive (although here only by one species). It is also underlined that it is not possible, as was done for the HT mechanism, to remove more species while keeping the accuracy level reasonable: removing any species at this point will result in errors in the LT range reaching those of the HT mechanism.

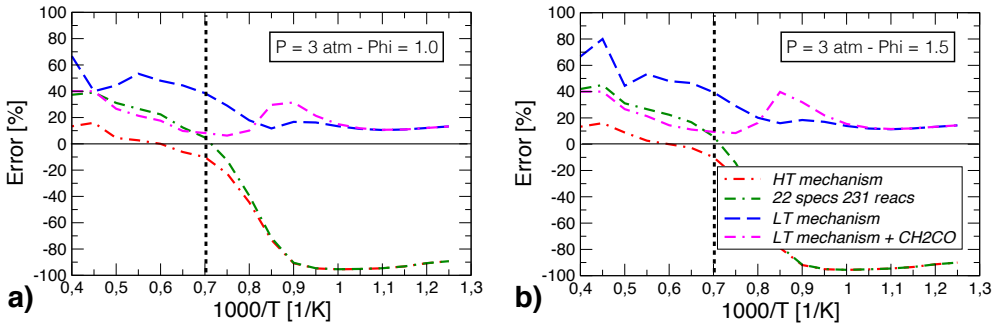

Figure 4.16: Relative errors on predicted τ_{ig} for several skeletal mechanisms throughout the entire temperature range, for two operating points.

A skeletal mechanisms for the entire temperature range Now, considering the HT range, a 22 species and 231 reactions skeletal mechanism with better performances on the HT range than the present LT mechanism was derived, see Fig. 4.16 (note that the tests with the 22 species and 231 reactions mechanism on the LT range were performed *a-posteriori*). When comparing species present in both HT and LT mechanisms, it appears that all species kept in the 22 species and 231 reactions mechanism are also present in the LT mechanism, except for CH_2CO which was discarded. Since this is the only noticeable difference, and since the pathways analysis performed in the previous paragraph (see Fig. 4.12) showed that this species is part of an important pathway at high temperature, a new LT mechanism is derived by considering CH_2CO in an attempt to improve the behavior on the HT range. This new LT mechanism (labelled LT mechanism + CH_2CO) contains 28 species and 291 reactions, and its performances are now acceptable over the entire temperature range, as shown on Fig. 4.17. Of course, such a mechanism might have been derived directly, if the entire temperature range had been specified as a target for the skeletal derivation !

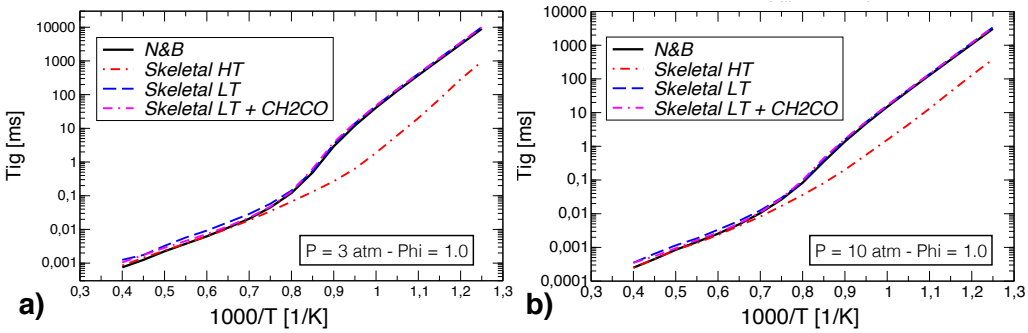

Figure 4.17: Examples of performances of the LT + CH_2CO skeletal mechanisms on the entire temperature range

A note about other canonical test cases As already said, the performances of each reduced mechanism worsen progressively outside of their respective targeted operating range. What about other canonical test cases ? A series of 1D calculations with CANTERA reveals that none of the AI skeletal mechanisms derived so far enable to recover the correct s_l^0 of laminar ethylene/air premixed flames at P = 3 bars and T_{ini} = 300 K, see Fig. 4.18 (a). However, they are able to retrieve with little error the temperature evolution, as well as the evolution of some important species across premixed flame fronts. This fact is illustrated on Fig 4.18 (b), displaying the evolution of CO and OH computed with the LT mechanism + CH_2CO across a typical 1D premixed flame front (P = 3 atm, $\phi = 1$, T_i = 300 K).

This is an important observation. Indeed, it is often argued that autoignition and extinction delays are most constraining in that they require to consider more pathways than laminar premixed or diffusion flames. However, recently, Jaouen *et al.* (2016) derived a reduced mechanism for methane/vitiated-air combustion along various trajectories in the phase space, and found that the inclusion of laminar premixed flames as a target in their algorithm was necessary to retrieve the laminar flame speed accurately. This supports the previous findings. Therefore 1D canonical test cases must be included in the derivation process, as is done below.

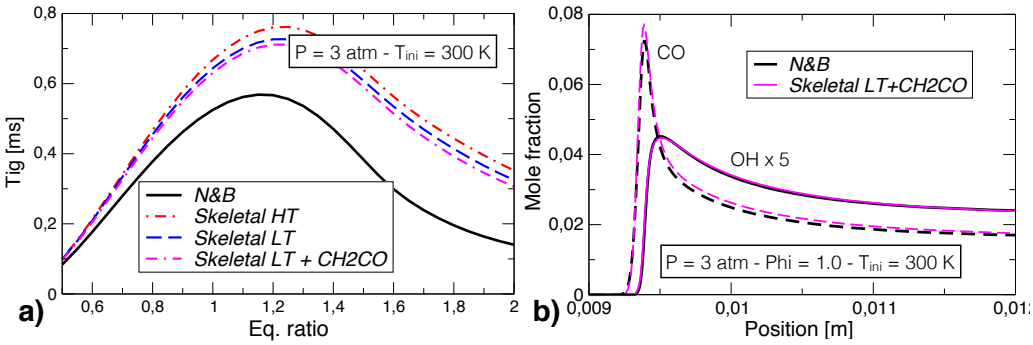

Figure 4.18: 1D laminar premixed flames calculations with the various AI skeletal mechanisms: (a) s_l^0, (b) Evolution of CO and OH across the flame front for $\phi = 1$, with the detailed and LT+CH_2CO skeletal mechanism.

4.3.2.b 1D test cases

In view of the previous discussion, it appears that including 1D test cases in the reduction loop is necessary to derive an ARC able to account for s_l^0. Before selecting the canonical test cases, however, a few questions come to mind:

- Is a reduction only based on 1D test cases able to retrieve auto-ignition delays ?
- Is a reduction based on unstrained laminar premixed flames able to account for strained structures ?
- Is a reduction based on unstrained laminar premixed flames able to account for diffusion structures ?
- Which test case is the most constraining in practice (in terms of number of species to keep) ?

From literature review, it is expected that the answer to the second and third points is positive. To shed some light on the other questions, a reduction is performed on the basis of unstrained laminar premixed flames solely. The targeted range is summarized on Table 4.3, *PF* case. A sketch of the reduction process is presented in Fig. 4.19. The reduction, when targeting 1D test cases, is a bit more involved than for autoignition problems. As

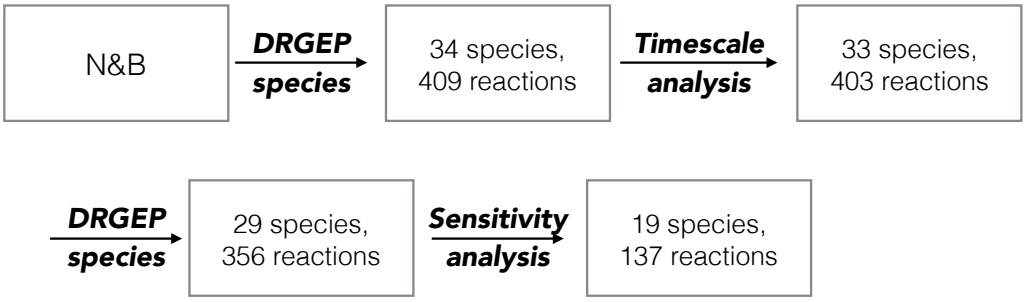

Figure 4.19: Reduction process of the PF case.

previously underlined, retrieving the species spatial evolutions does not guarantee a correct laminar flame speed. Of course, this observation goes both ways. Furthermore, retrieving the species/temperature distribution and overall behavior in the flame zone does not guarantee that proper equilibrium levels are reached. This amounts to saying that there are many quantities to monitor, and checks need to be performed often during the reduction process.

As done previously, the first reduction step is performed by employing the DRGEP for species elimination. The obtained 34 species and 409 reactions mechanism performs extremely well in the targeted range of reduction, as can be seen on Figs. 4.20 - 4.22, in red. The resulting error on s_l (Fig. 4.20 (b)) never exceeds 5% in the derivation range ($0.5 < \phi < 1.5$), and is contained within 20% if the range is extended to $\phi < 2.0$. The evolution of species of interest, characterized by peak values -usually found in the flame front, and equilibrium values, are also very well captured. CO peaks (Fig. 4.21 (a)-(b)) and equilibrium levels (Fig. 4.21 (c)-(d)) are particularly

well reproduced, throughout the entire extended equivalence ratio range. Peak levels of C_2H_2 (Fig. 4.22 (a)-(b)) are equally well captured. Error on OH (Fig. 4.22 (d)) maximums is found to rapidly worsen outside of the targeted equivalence ratio range, but remain acceptable considering the very low levels in the rich side.

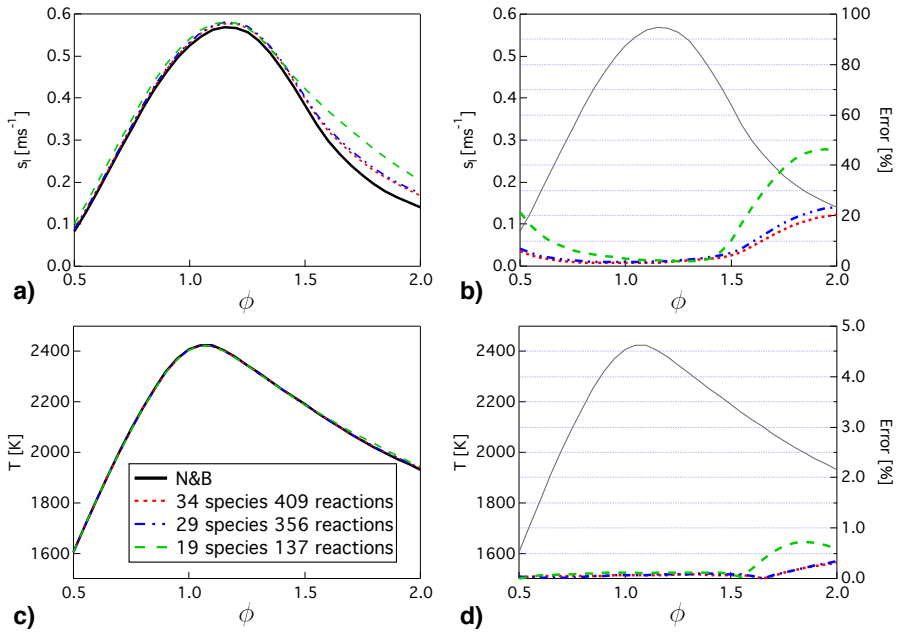

Figure 4.20: 1D laminar premixed flame calculations at $P = 3$ bars and $T_{ini} = 300K$, with the various PF skeletal mechanisms: global quantities.

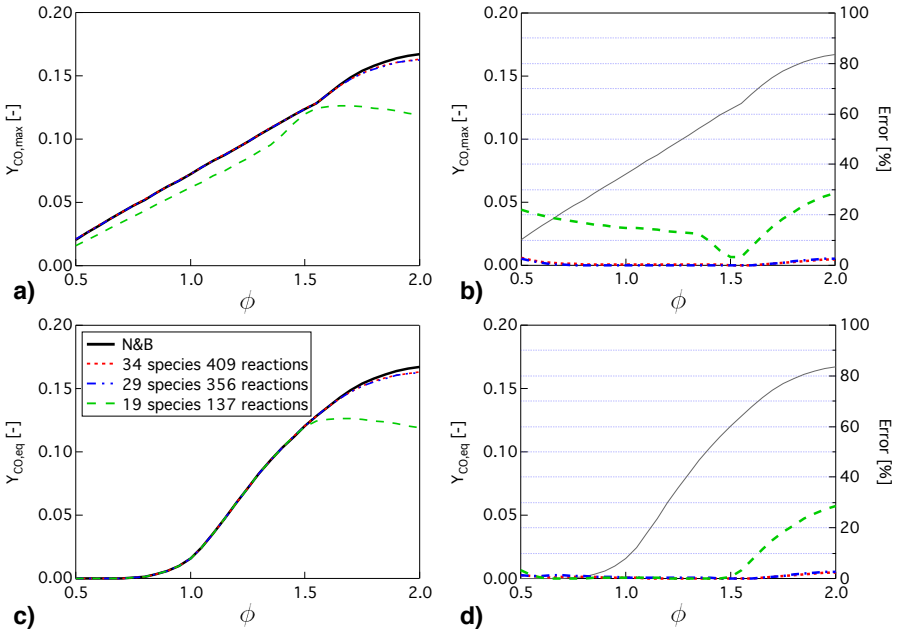

Figure 4.21: 1D laminar premixed flame calculations at P = 3 bars and T_{ini} = 300 K, with the various PF skeletal mechanisms: focus on CO species.

These 1D test cases reveal that the C_2H_5O species has a characteristic timescale much smaller than all other species (insights on how the timescale analysis is performed will be provided on Section 6.3.3). A rapid check further reveals that this species remains in very low concentration, and only appears in a few reactions. However, YARC places it very high in the list of species to keep. Since it would be impossible to transport such a short living species in a 3D computation, it is attempted to force its elimination and all associated reactions. It is observed that this does not affect the mechanism performances too much, so that it was decided to continue from

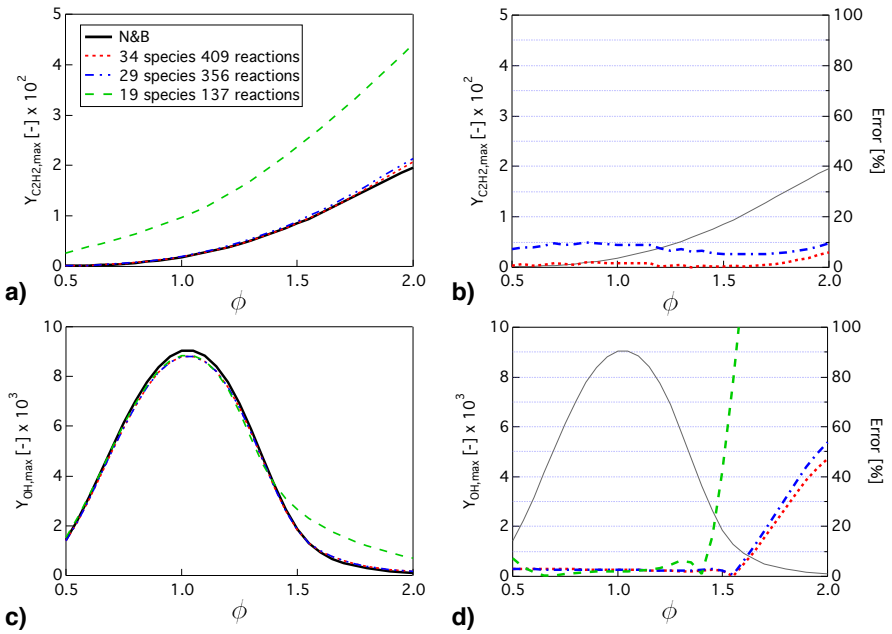

Figure 4.22: 1D laminar premixed flame calculations at P = 3 bars and T_{ini} = 300 K,, with the various PF skeletal mechanisms: focus on C_2H_2 and OH species.

there. A second DRGEP species reduction on this 33 species and 403 reactions mechanism produces a skeletal mechanism composed of 29 species 356 reactions, predicting equally well s_l^0, major species and temperature evolutions throughout the extended equivalence ratio range (in blue in Figs. 4.20-4.22). The performances degrade somewhat on C_2H_2 predictions (Fig. 4.22 (b)), but it is reminded that this species was not part of the reduction targets.

From there, as in the 0D test cases, further reduction requires a certain amount of input from the user. A last DRGEP procedure is attempted, leading to many "jumps" in the s_l^0 error log, displayed with black circles in Fig. 4.23 (a). The three most important jumps are identified by hashed lines. This is the sign of nonlinearities of the reaction mechanism; and it emphasizes once more that s_l^0 and species evolutions do not necessarily have the same requirements. Indeed, the error log based on equilibrium values of CO -red squares in Fig. 4.23 (a)- displays a monotonic behavior. In fact, when drastically reduced mechanisms exhibit the correct s_l^0, it often stems from a series of error compensations.

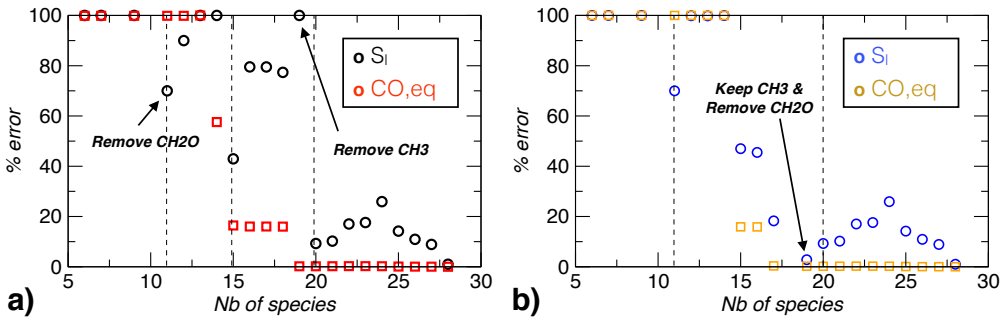

Figure 4.23: Error log of the DRGEP procedure on the 29 species 356 reactions mechanism: (a) "natural" procedure and (b) "forced" procedure (see text).

This investigation reveals that the species ordering determined by YARC might not be the "best" possible one. In fact, it might be interesting to try and alter the ordering in-between the 10^{th} and 20^{th} position, where the performances of the successive reduced mechanisms exhibit the most non-monotonic behavior. An efficient way to do this in practice, is to identify species involved in the first jump and in the last significant jump. In this particular case, the last jump involves the CH_2O species, and the first jump the CH_3 species. To test these species, the list generated by YARC during the last DRGEP procedure is "forced" by "moving down" the CH_2O species (so, decreasing its importance), and new series of reduced mechanisms are generated and tested by YARC.

It is found that inserting CH_2O right before CH_3 results in the best compromise, leading to a quasi-monotonic evolution of the mechanisms performance both in terms of s_l^0 and main species equilibrium values, as depicted in Fig. 4.23 (b). With this new ordering, a very small skeletal mechanism composed of 19 species and 137 reactions is derived. Its performances inside the targeted range and on the targeted quantities (reactants, CO and OH) remain good, as can be seen on Fig. 4.20- 4.22, in green. However, predictions worsen -sometimes dramatically- outside the derivation range or for species that were not targeted, such as C_2H_2 displayed in Fig. 4.22 (a)-(b).

It has been possible, at least in this case, to reduce the number of species and reactions more drastically by targeting unstrained 1D laminar premixed flames rather than autoignition. From there, it is possible to address the first question listed at the beginning of this section.

Predictions of autoignition delay The performances of the PF skeletal mechanisms are now attested on AI test cases. Figure 4.24 confirms that the 34 species and 409 reactions mechanism performs really well on the range targeted by the AI cases. This is not surprising, since this mechanism includes the LT + CH_2CO mechanism, so that the error levels are similar to that of this mechanism (see Fig 4.17). However, both smaller mechanisms performances worsen on the LT range, and the 19 species and 137 reactions mechanism (referred to as the PF mechanism hereafter) is even unable to auto-ignite for $T > 1250K$. This analysis leads us to the conclusion that, for the considered cases at least, targeting autoignition or premixed laminar flames lead to very different reduced mechanisms, and that one cannot hope to obtain the smallest possible mechanism accounting for both s_l^0 and τ_{ig} without considering all canonical test cases. Another conclusion is that accounting for autoignition delay is more constraining than premixed flames quantities, in that it requires more species and more pathways.

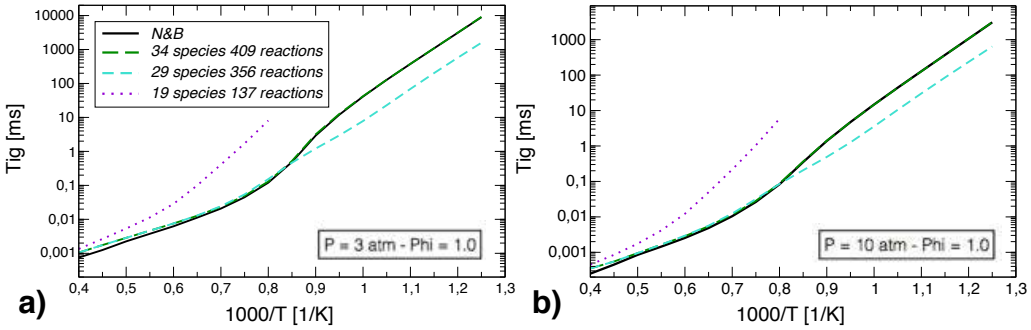

Figure 4.24: Example of performances of the PF mechanisms on autoignition delay predictions.

Performance on strained 1D premixed laminar flames The performances of the PF skeletal mechanisms are now attested on strained PF test cases. A comparison of temperature and major species (CO, OH) evolutions across strained laminar premixed flames with various strain rates is provided on Fig. 4.25. The performances of the PF mechanism are good, although the peak values of CO are underestimated for all strain rates. It appears that in this case, the answer to the second question raised at the beginning of this section is positive. In fact, this conclusion is not that surprising, since strained premixed structures are still dominated by kinetic processes, and the kinetic pathways are preserved by the reduction process.

Performance on strained 1D diffusion laminar flames It was underlined in Section 4.2.3 that diffusion flames are more controlled by the flow than the chemistry. As a consequence, diffusion structures are less accurately captured by the PF mechanism. It can be seen on Fig. 4.26 (a) that global tendencies are retrieved, but that errors nonetheless increase with the strain rate. The extinction strain rate, in particular, is not correctly predicted with this mechanism. Profiles of major species across flame fronts exhibit however the right trends.

Since diffusion structures are fundamentally different from premixed structures, for completeness, tests on these canonical test cases are also performed with the LT + CH_2CO mechanism (developed for the entire AI range), and reported on Fig. 4.26. The performances of this mechanism are better than that of the PF mechanism; with more accurate OH predictions over the entire range of strain rate, and excellent predictions of global CO production (important to retrieve the correct EICO, a common pollutant indicator). Note that the performances of the (PF) 34 species and 409 reactions mechanism, which contains the LT + CH_2CO mechanism, are thus equally good (not shown). It is however noted that the LT + CH_2CO mechanism requires to transport 10 more

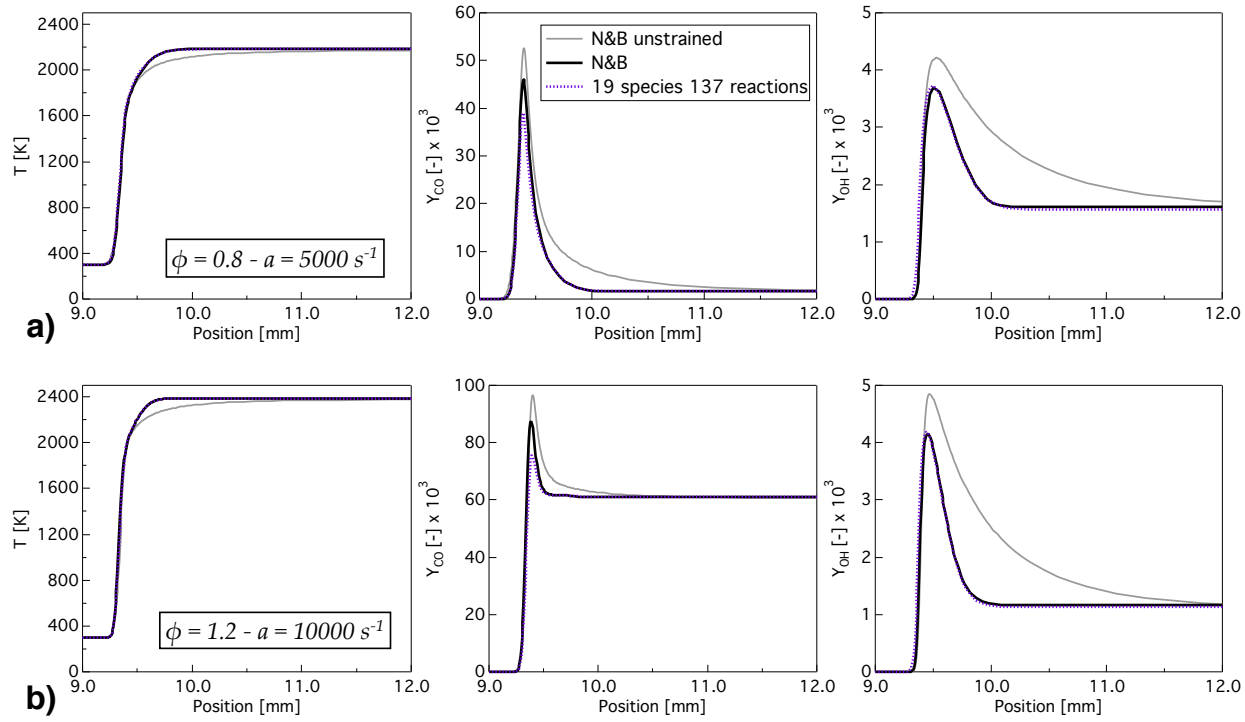

Figure 4.25: Example of performances of the PF mechanisms on strained laminar premixed flames at $P = 3$ bars and $T_{ini} = 300K$: a) $\phi = 0.8$, $a = 5000s^{-1}$ and b) $\phi = 1.2$, $a = 10000s^{-1}$. Unstrained quantities are also plotted (grey solid line) for comparison.

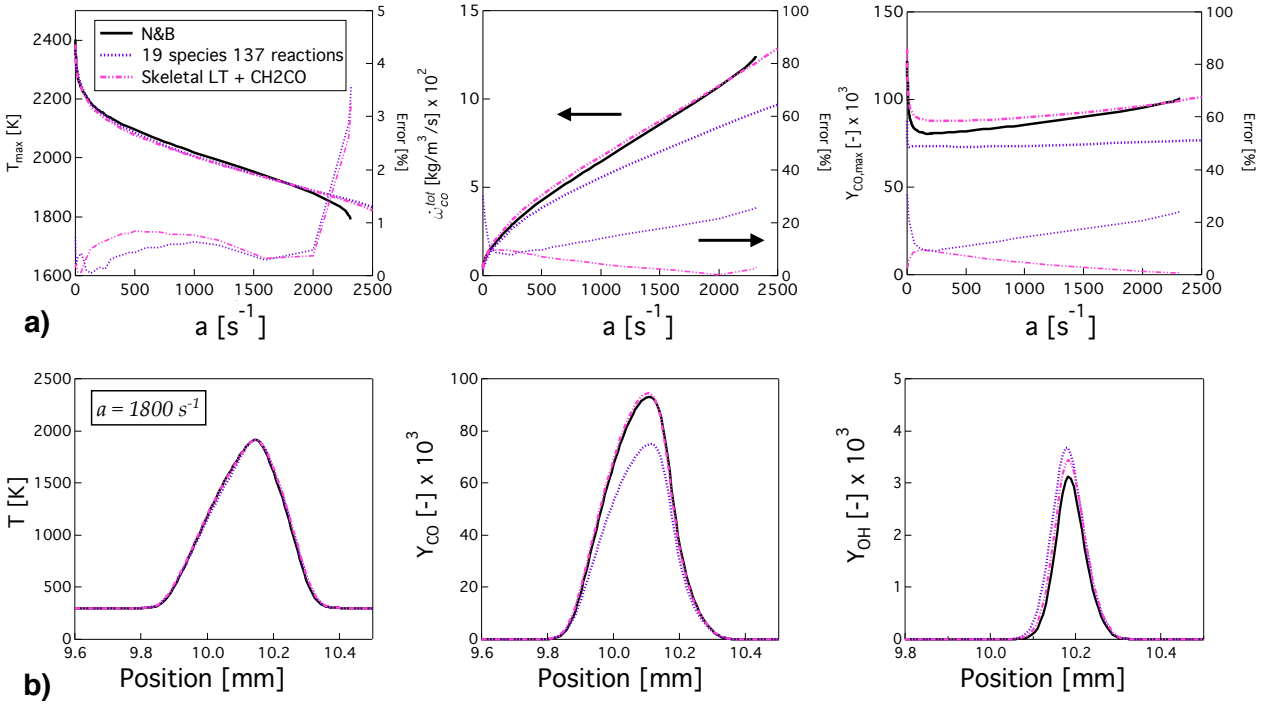

Figure 4.26: Example of performances of the PF mechanisms on strained laminar diffusion flames at $P = 3$ bars and $T_{ini} = 300K$: a) global evolution with strain rate and b) profiles across a diffusion flame with $a = 1800s^{-1}$.

species than the PF mechanism, and that the extinction strain rate is still overestimated. In fact, it appears that none of the mechanisms derived so far are able to retrieve the extinction strain rate, which is thus pinpointed as being a separated phenomenon, requiring additional targets. In the literature, it is argued that targeting extinctions in constant pressure reactors rather than AI in constant volume reactors might enable to better

preserve kinetic pathways. It was not attempted in this work, due to a lack of time, but this is a possible way for improvements of the reduction process.

It appears that the prediction capabilities of a mechanism derived on the basis of PF test cases exhibit similar levels of error on diffusion flames than on premixed flames (about 20% for global quantities and major species maximums for the PF mechanism, see Fig 4.26 (a) and Fig 4.20 - 4.22), at least concerning major species evolutions across flame fronts submitted to increasing strain rates. The same can be said about ARC derived on the basis of AI test cases. As such, diffusion structures are identified as being the less constraining of all test cases investigated so far, as long as retrieving the extinction strain rate accurately is not necessary.

4.3.2.c Summary

A few conclusions can be drawn from this series of elementary tests. They can be summarized as follows:

- Accounting for τ_{ig} on the LT range usually require to consider more species and to preserve more pathways than accounting for τ_{ig} on the HT range
- Species evolutions across PF can be recovered with a mechanism reduced by targeting AI cases, but accounting for s_l accurately requires to consider PF test cases as a target
- Targeting AI or PF test cases separately eventually lead to distinct reduced mechanisms, each preserving distinct kinetic pathways; and one cannot hope to derive the smallest possible ARC accounting for both s_l and τ_{ig} without considering all canonical test cases
- From all considered test cases in this work, targeting specifically PF test cases results in the smallest set of species
- With the exception of the extinction strain rate, the predicting capabilities of an ARC targeting PF test cases exhibit similar levels of error on the prediction of strained premixed and diffusion flames
- None of the test cases considered in this work allow to retrieve the correct extinction strain rate

This summary provides a set of guidelines, tips and general "know-how" for future users of YARC and/or users of other similar reduction tools. However, one must bear in mind that the situation can get more complicated when dealing with heavier hydrocarbons, or a blend of hydrocarbons, as will be seen in Section 4.4.3.c. In particular, neither the lumping nor LOI techniques were employed until now. The LOI will be employed in the next section, to identify potential QSS candidates and reach a deeper level of reduction.

4.3.3 Effect of the constraining targets: C_2H_2

Since one of the objectives of this PhD thesis is the LES simulation of a gaseous burner, for which experimental soot levels are available, it is necessary to employ a chemistry description able to accurately predict acetylene levels, used as the main soot precursors (see Section 2.2.4.c). Starting from the 34 species and 409 reaction mechanisms developed considering PF test cases, the reduction is now steered by adding C_2H_2 and AI test cases to the list of targets.

4.3.3.a Skeletal mechanism: ARC_29_C2H4NARA

The exact characteristics of the skeletal reduction with acetylene as a target are reported in Table 4.3, C_2H_2 case. The reduction procedure is similar to the previous one, and is sketched in Fig. 4.27. Here also, some user input was required to reach the best possible skeletal mechanism (to go from 31 to 29 species). Note that it has been decided to keep the C_2H_5O species in this case, since removing it led to bad performances in the AI LT range. From the analysis of the reactions kept in the 31 species and 380 mechanism, it appears that the species involved in the least reactions is CH_3O_2, and always together with species CH_3O. Both species are eventually discarded, and a mechanism consisting of 29 species and 355 reactions is obtained, referred to as the ARC_29_C2H4NARA mechanism in what follows. Note that in this case, adding C_2H_2 as a target did not change significantly the species order. HCCO and CH_2CO are moved up since they are involved in many C_2H_2 pathways. The 29 species

conserved are: N_2, H, H_2, HO_2, H_2O, H_2O_2, O, O_2, OH, CO, CO_2, CH_2O, CH_2CO, CH_3, CH_4, C_2H_2, C_2H_4, C_2H_6, S-CH_2, CH, C, HCO, C_2H_5O, HCCO, T-CH_2, C_2H_3, CH_2CHO, C_2H_5, CH_3CHO.

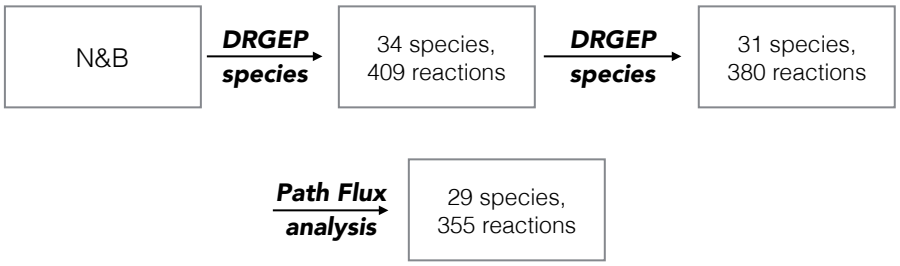

Figure 4.27: Reduction process of the C_2H_2 case.

Validation on AI test cases The mechanism overall performances on 0D test cases are well within acceptable error margins, considering that the application (see Chapter 7) is not expected to exhibit auto-ignition. The global performances over the targeted range, computed as a normalized $L2$ error over the temperature range, are provided in Table 4.4; while examples of results are provided in Fig. 4.28, for both targeted (a) and non-targeted (b) operating points. It is stressed again that the most difficult target is τ_{ig} when considering AI cases; indeed, species evolutions are usually very well reproduced, as can be seen on the Table. The *extended range* of operating conditions consist of AI with T_{ini} = 800-2500 K and P = 1-10 atm.

Global Error	*Extended range (T,P for AI, ϕ,T,P for PF)*	*Targeted range (see Table 4.3)*
Auto-ignition (AI)	$\phi = 0.5$: <50% (τ_{ig}) - < 1% (T-CO, OH) $\phi = 1.0$: <60% (τ_{ig}) - < 1% (T-CO, OH) $\phi = 1.5$: <70% (τ_{ig}) - < 1% (T-CO, OH)	< 50% (τ_{ig}) - < 1% (T-CO, OH)
Premixed flames (PF)	<12% (s_l) - < 10% (CO, C_2H_2) <1% (T_{ad}) - < 50% (OH)	< 2% (s_l) - < 5% (CO, OH) <1% (T_{ad}) - < 10% (C_2H_2)

Table 4.4: Summary of error levels of the ARC_29_C2H4NARA mechanism on various test cases.

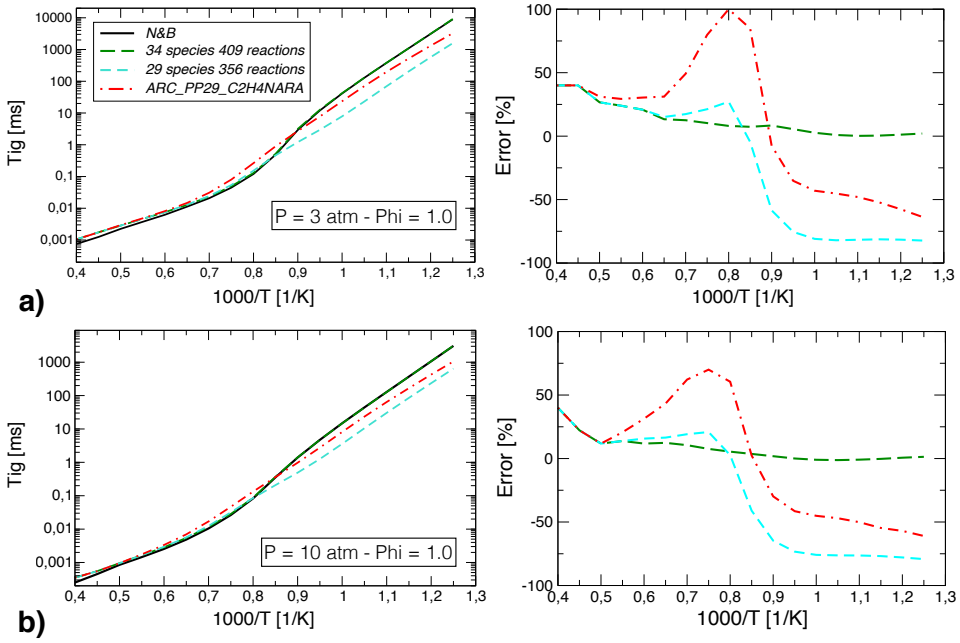

Figure 4.28: Left: value and right: error on τ_{ig} computed with the ARC_29_C2H4NARA mechanism, on (a) targeted and (b) not targeted operating points.

Validation on PF Table 4.4 also reports maximum relative error levels on selected targets (for species, errors are calculated on peak and equilibrium values), obtained with the ARC_29_C2H4NARA mechanism directly in the *extended* PF range, which consists of T_{ini}= 300-700 K, P = 1 - 5 bars and 0.5< ϕ < 2.0.

As expected from the series of derivations on 0D and 1D test cases performed earlier, the performances of the ARC_29_C2H4NARA mechanism are very good on strained 1D premixed flames also, belonging to the targeted operating range. Fig. 4.29 displays maximum levels of major species for a series of strained flames, at two representative ϕ. It can be seen that the error levels are negligible and, overall, constant over the range of strain.

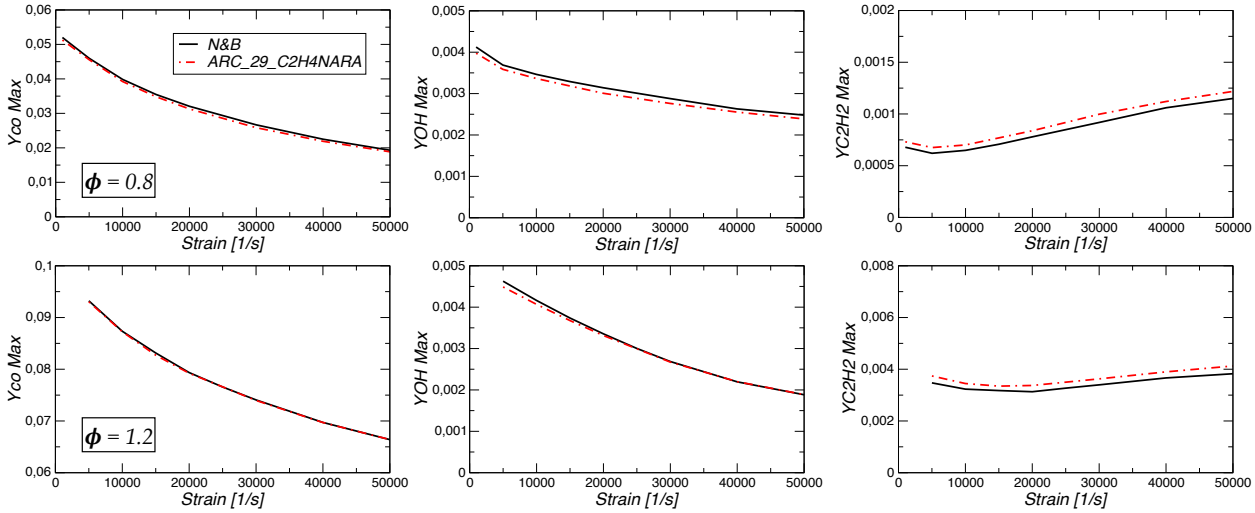

Figure 4.29: Example of performances of the ARC_29_C2H4NARA mechanism on peak levels of species in strained laminar premixed flames at $P = 3$ bars and $T_{ini} = 300K$.

4.3.3.b Analytical mechanism: ARC_18_C2H4NARA

The last step of the reduction technique presented in Table 4.1 consists in identifying QSS candidates. This step is also performed with YARC. The targets remain unchanged. In one run, 11 species are put in QSS: S-CH_2, CH, C, HCO, C_2H_5O, HCCO, T-CH_2, C_2H_3, CH_2CHO, C_2H_5, CH_3CHO. The resulting mechanism is labelled ARC_18_C2H4NARA in what follows, and will be employed and extensively validated against the detailed mechanism in Chapter 7. The QSS step usually degrades very little the mechanism's performances. Indeed, the error log of computations with successive ARC, resulting from incrementing the number of QSS, usually present a very distinct jump: the error goes from virtually nothing to 100%. The maximum set of QSS species is thus easily identified.

To illustrate that the performances of the skeletal mechanism and the analytical mechanism are very similar, Fig. 4.30 displays 1D unstrained laminar premixed flame profiles. It is noted that both mechanisms employ different transport models (as reported on Fig. 4.30). Indeed, ARC are usually coupled to a simplified transport description to be employed in 3D simulation codes. This is the case in the LES code AVBP, where the simplified transport model (TranAVBP) is based on a single constant Schmidt number for each species, as reported on Table 4.5, and a constant Prandtl number (here 0.68). Details about the various transport models will be provided in Section 5.2.3. Note that validations of the ARC mechanism thus require a modified version of CANTERA, to be performed with the same simple transport.

The skeletal mechanism will not be employed further. As already mentioned, the global performances of the ARC_18_C2H4NARA (with TranAVBP) will be assessed in Section 7.3, against the performances of the detailed mechanism (with TranMix).

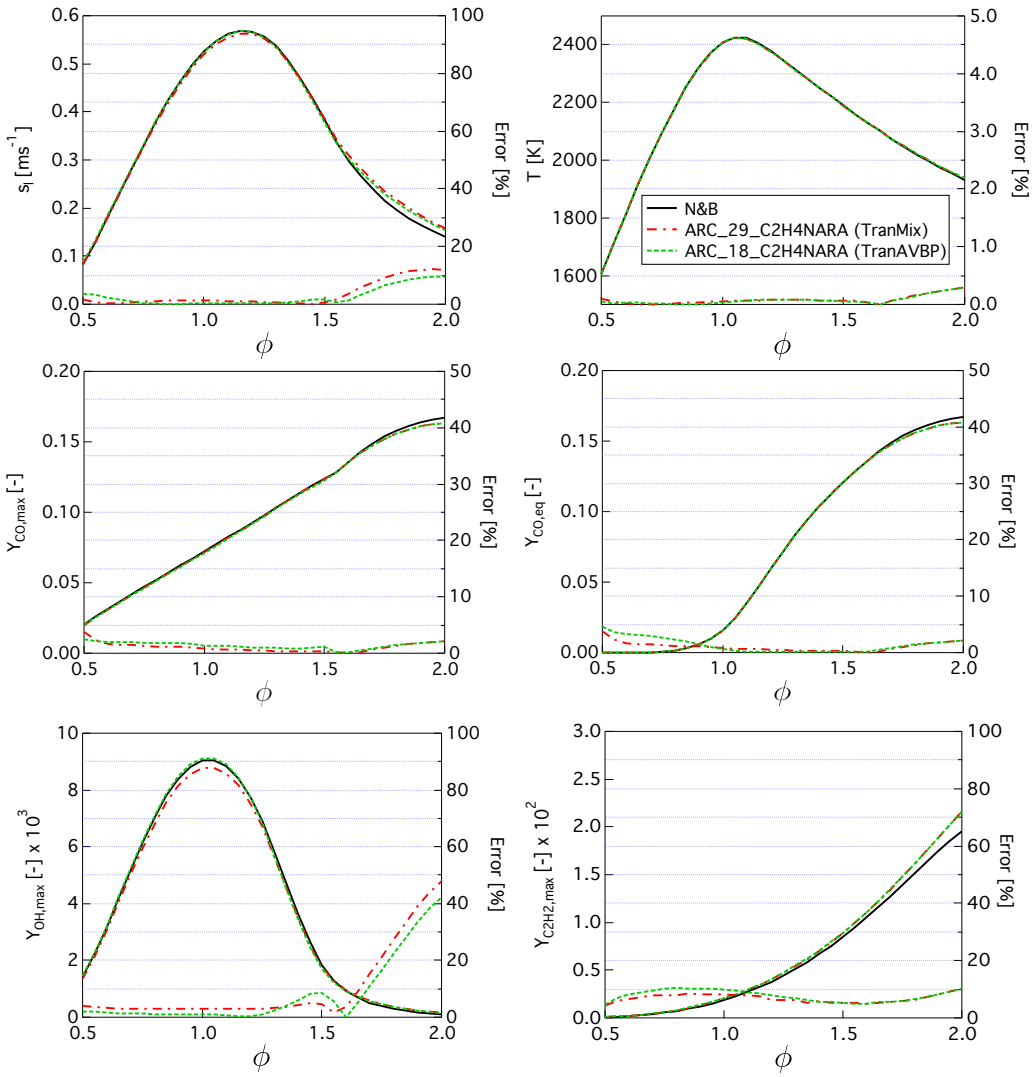

Figure 4.30: Comparison of performances of the ARC_18_C2H4NARA mechanism against those of the ARC_29_C2H4NARA mechanism on peak levels and equilibrium values of important species in 1D unstrained laminar premixed flames at $P = 3$ bars and $T_{ini} = 300K$.

Species	N_2	H	H_2	HO_2	H_2O
Schmidt number	0.69096	0.12028	0.16695	0.70700	0.64670
Species	H_2O_2	O	O_2	OH	CO
Schmidt number	0.72627	0.49841	0.74841	0.50371	0.71661
Species	CO_2	CH_2O	CH_2CO	CH_3	CH_4
Schmidt number	0.92165	0.95208	0.99060	0.63809	0.65707
Species	C_2H_2	C_2H_4	C_2H_6		
Schmidt number	0.84138	0.83775	1.0017		

Table 4.5: Schmidt numbers of the species involved in the ARC_18_C2H4NARA mechanism, employed for the TranAVBP model.

4.4 Application 2: ARC for Jet-A

4.4.1 Preliminary considerations

As already mentioned in the Introduction, a great challenge faced today in reactive flow simulations concerns the uncertainties and complexity of real fuels' composition. In order to emulate the desired properties of a specified

fuel, one must, in particular, come up with a surrogate description able to do so, for which it is desirable to obtain a detailed mechanism. Two preliminary steps to the reduction must then be performed:

- Choosing an *appropriate* surrogate formulation
- Deriving a *compact* detailed mechanism for the chosen surrogate; meaning, a mechanism retaining only the necessary kinetics

The first step is crucial and generally depends upon the type of application under consideration. The usual multi-component formulation is first reviewed, along with some general considerations about the different types of fuels that are also relevant to a novel, *hybrid* chemistry method, introduced in a second part.

4.4.1.a Surrogate formulation

Classical approach Surrogates consist of a blend of a few key representative hydrocarbons. Indeed, it has long been thought that if the main chemical classes of representative constituents are accounted for, all important properties of the fuel should be retrieved. Aviation fuels are mainly composed of alkanes, alkenes and aromatics, as depicted in Fig. 4.31. However, the distribution and representative constituents of each class vary with the origin of the shipment, the refinement process, and even simply with time, leading to high uncertainties of composition. Figure 4.32 lists averaged compositions and properties for the main types of modern aviation fuels (see, also the very exhaustive Chevron Technical Review on Aviation Fuels [3] discussing the different types of kerosenes).

Compound class	Typical structure	Name
n-paraffin (*n*-alkane)	$CH_3-(CH_2)_{10}-CH_3$	*n*-dodecane
iso-paraffin	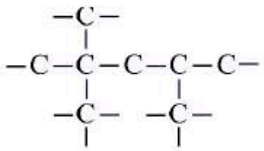	iso-octane
Naphthene (cycloparaffin)	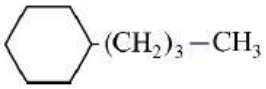	butyl cyclohexane
Aromatic	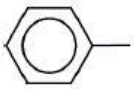	toluene
Alkene	$CH_2=CH-CH_2-CH_2-CH_3$	1-pentene

Figure 4.31: Classes of representative components of aviation fuels, with examples. From Edwards & Maurice (2001)

Ideally, both physical (density, molecular weight MW, H/C ratio, viscosity, etc.) and chemical (τ_{ig}, s_l^0, sooting tendency TSI, etc.) properties should be matched by a comprehensive surrogate description (Edwards & Maurice, 2001). However, this is often too constraining. The limited number of available representative of each class of constituent further complicates this task. Studies interested with gaseous configurations mainly aim at emulating chemical properties, but the picture is more complex when two-phase flow configurations are considered. The rate of evaporation, for instance, becomes an important parameter, the characteristics of which are very dependent upon physical properties (e. g., volatility). The auto-ignition delay, characterized experimentally through the Derived Cetane Number (DCN) is also widely recognized as being an important parameter, especially in the NTC region. These two targets are however difficult to evaluate *a-priori* for a surrogate mixture, although some automated packages exist (see, e.g. Lemmon *et al.* (2002)) for estimating them based on the properties of the different components. One of the most important physical property, easy to evaluate, remains the H/C ratio, since it eventually governs the overall equivalence ratio and thus indirectly the heat release. It has also been shown to have an importance regarding ignition at high temperature (Narayanaswamy *et al.*, 2016).

[3] https://www.cgabusinessdesk.com/document/aviation_tech_review.pdf

Property	Avgas	JP-4	JP-5	JP-7	JP-8 (Jet A/A-1)	RP-1
Approximate formula[a]	C_7H_{15}	$C_{8.5}H_{17}$	$C_{12}H_{22}$	$C_{12}H_{25}$	$C_{11}H_{21}$	$C_{12}H_{23}$
H/C ratio	2.09	2.00	1.92	2.07	1.91	1.95
Boiling range, °F (°C)	115–295 (46–145)	140–460 (60–240)	360–495 (180–260)	370–480 (190–250)	330–510 (165–265)	350–525 (175–275)
Freeze point, °F (°C)[b]		−80 (−62)	−57 (−49)	−47 (−44)	JP-8/Jet A-1: −60 (−51); Jet A: −50 (−45)	−55 (−48)
Flash point, °F (°C)		−10 (−23)	147 (64)	140 (60)	127 (53)	134 (57)
Net heating value,		18,700	18,500	18,875	18,550	18,650
Btu/lb (kJ/kg)		(43,490)	(43,025)	(43,895)	(43,140)	(43,370)
Specific gravity, 16°C (60°F)	0.72	0.76	0.81	0.79	0.81	0.81
Critical temperature, °F (°C)		620 (325)	750 (400)	750 (400)	770 (410)	770 (410)
Critical pressure, psia (atm)		450 (30.5)	290 (19.5)	305 (20.5)	340 (23)	315 (21.5)
Average composition						
Aromatics, vol%	25	10	19	3	18	3
Naphthenes		29	34	32	35	58
Paraffins		59	45	65	45	39
Olefins	10	2	2		2	
Sulfur, ppm		370	470	2	490	20

[a]For illustration of average carbon number, not designed to give accurate H/C ratios.
[b]Typical.

Figure 4.32: Typical compositions and properties of aviation fuels. From (Edwards, 2003)

These considerations have led to the development of guidelines then followed by systematic strategies to develop and evaluate the relevance of multi-component surrogates. They are all based upon a (modular) relevant subset of the aforementioned properties. In the pioneering work of Wood *et al.* (1989), a surrogate made up of a blend of 14 hydrocarbons was derived to reproduce the distillation and compositional characteristics of a JP-4. Violi *et al.* (2002) developed several surrogates with at least 5 constituents to represent a JP-8, targeting volatility (boiling curve) and sooting tendencies. Many other attempts employed different targets for fuel emulation, resulting in various formulations reported in the reviews by Dagaut & Cathonnet (2006) or more recently Pitz & Mueller (2011), as well as in the introduction of the paper by Dooley *et al.* (2012). Considering an exhaustive list of constituents is, however, not a viable option for implementation in CFD simulations, and recent work limit them to at most 4 compounds. Dooley *et al.* (2012), for example, developed a methodology to design surrogates based upon the matching of the radical pool of a real fuel *and* the matching of 4 combustion property targets (MW, TSI, H/C, DCN). They applied the strategy to a type of Jet-A (POSF 4658) fuel and derived 3 and 4 components surrogates that they validated experimentally. Employing a similar technique, but from a numerical point of view and focusing only on individual components that have been previously carefully studied, Narayanaswamy *et al.* (2016) developed an automated constrained optimization tool to derive an optimal surrogate for average Jet-A/JP-8. A similar tool, albeit with a different set of targets, has also been developed by Kim *et al.* (2014) and later by Ahmed *et al.* (2015) in the context of ground transportation internal combustion engines.

A more thorough overview of the considerations one has to go through to formulate an adequate multi-component surrogate can be found in the recent publication of Kim *et al.* (2014).

Alternative approach: HYbrid CHEMistry (HyChem) So far, the surrogate formulation has relied upon distinct hydrocarbon components. Another modeling approach has recently been proposed by Xu *et al.* (2017*b*,*a*), and is briefly presented hereafter. Details can be found in the aforementioned publications. The methodology relies on the assumption that any fuel, no matter its complexity, would decompose into a handful of components when heated, and that it is the distribution of these pyrolysis products in the reaction zone that will mainly impact the subsequent radical buildup and heat release rate. The pyrolysis intermediates are dominated by ethylene (C_2H_4), methane (CH_4), hydrogen (H_2), propene (C_3H_6), *iso*-butene (i-C_4H_8), 1-butene (1-C_4H_8), benzene (C_6H_6) and toluene (C_7H_8). In that sense, the combustion process can be decomposed into a fuel pyrolysis step and a subsequent oxidation step of the pyrolysis products: this is the basis of the two-step HYbrid CHEMistry (HyChem) approach. Kinetic model for a particular real fuel can thus be obtained by merging a fuel-specific pyrolysis model comprised of a few lumped reactions, yielding the composition of the primary pyrolysis products, and a detailed foundational fuel chemistry model (C1-C4 kinetic mechanism). The "fuel", in that case, is a mono-component lumped species. Its pyrolysis model is derived from shock-tube and flow-reactor experiments. The resulting HyChem model captures shock-tube ignition delay times and laminar flame speeds over a wide range of pressure, temperature and equivalence ratio. It also predicts the counterflow non-premixed

flame extinction strain rates over a range of fuel dilution. The HyChem model is schematized in Fig. 4.33

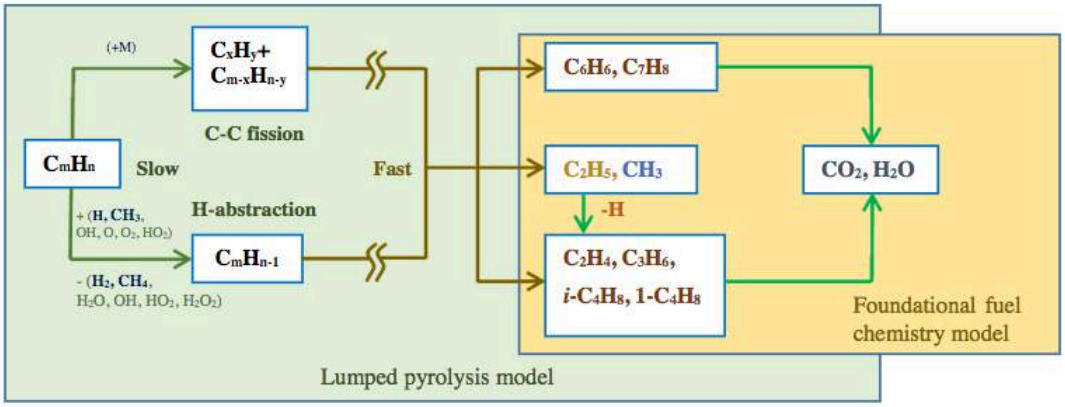

Figure 4.33: The structure of the HyChem model, consisting of a lumped pyrolysis model for fuel decomposition and a detailed kinetic model for the oxidation of the decomposition intermediates to produce final combustion products. From Xu *et al.* (2017*a*)

4.4.1.b Detailed mechanism for surrogates

Once a proper surrogate formulation has been determined, one way to obtain a compact detailed mechanism is to rely on a tool such as the Component Library Framework (CLF) developed by (Narayanaswamy *et al.*, 2016). This tool will produce a minimum kinetic scheme, by selecting sub-mechanisms for the individual components from a comprehensive modular parent mechanism. It is also possible to rely on a comprehensive mechanism directly, but the size of such a mechanism might be discouraging, and strong non-linearities between individual components might appear. Of course, with the HyChem methodology, the choice of the detailed mechanism is easier since a mechanism has to be provided for the C_2-C_3 chemistry solely, while a set of lumped reactions are provided for the fuel breakdown along with the characteristics of the mono-component surrogate.

4.4.2 Jet-A POSF10325 specifications

In view of what was just discussed, it is important to adapt the surrogate description to match the properties of the specific fuel under consideration. In what follows, we will be further interested with an average, commercial Jet A fuel (the POSF10325) which was procured from the Shell Mobile refinery in June 2013 as a part of tests conducted by the National Jet Fuel Combustion Program. Its properties are summarized in Table 4.6, while the distillation, liquid density and viscosity curves are reported in Fig. 4.34.

Mol. Weight	Composition (mass fraction [%])				
[kg/kmol]	Aromatics	*iso*-Paraffins	*n*-Paraffins	Cycloparaffins	Alkenes
159	18.66	29.45	20.03	31.86	<0.001
H/C	Δh_c [MJ/kg]	DCN	T_{10} [K]	$T_{90} - T_{10}$ [K]	μ_l(322 K) [mPa s]
1.90	43.1	48.3	450.0	67.8	1.17

Table 4.6: Properties of Jet A (POSF10325)

For this fuel, a recent study by Edwards (2017) reports the derivation of two multi-component surrogates, both comprised of three hydrocarbons representative of three amongst the main classes reported in Fig. 4.31: a n-alkane, an iso-alkane and an aromatic. The precise composition of each surrogates is reported in Table 4.7. They were constructed to match the H/C ratio, smoke point, and DCN.

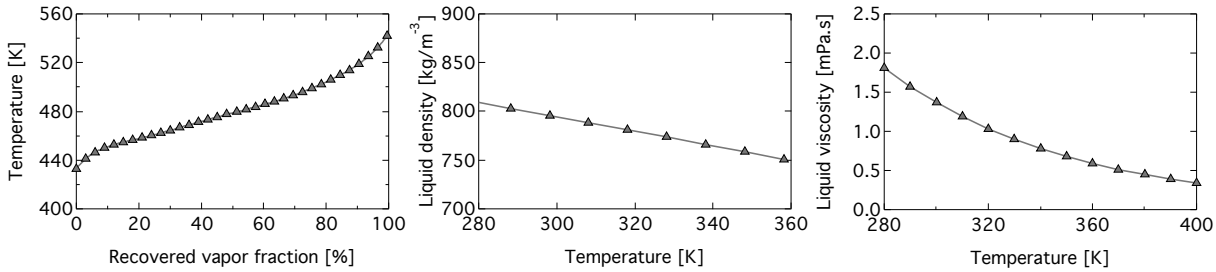

Figure 4.34: Physical properties of Jet A (POSF10325)

Components	Surrogate 1 Vol %	Surrogate 2 Vol %
n-dodecane	59.3	0
n-hexadecane	0	52.6
iso-octane	18.4	25.1
1,3,5 trimethyl benzene	22.2	22.2

Table 4.7: Surrogates for the Jet A (POSF10325) proposed in Edwards (2017)

4.4.3 Classical multi-component surrogate

4.4.3.a Surrogate formulation

To emulate the properties of the Jet-A POSF10325 discussed in Section 4.4.2, an optimization tool of the type described in Narayanaswamy *et al.* (2016) was employed. The constraints and targeted properties are as follow:

- Targeted properties: H/C ratio, MW, DCN
- Maximum of 3 components
- The components have to be well characterized, and part of a modular comprehensive mechanism

The liquid density, and average formulae (C and H content) were also monitored. The surrogate properties were estimated from that of the components following simple mixing rules:

$$\begin{aligned} MW_{mix} &= \sum_i P_i MW_i \\ nC_{mix} &= \sum_i P_i nC_i \\ nH_{mix} &= \sum_i P_i nH_i \\ H/C_{mix} &= \frac{nH_{mix}}{nC_{mix}} \\ DCN_{mix} &= \sum_i V_i DCN_i \\ \rho_{l_{mix}} &= \sum_i V_i \rho_{l_i} \end{aligned} \tag{4.25}$$

where P_i (resp., V_i) stands for the gas molar percentage (resp., liquid volume percentage) of species i in the surrogate mixture (mix) composition.

This type of optimization tool, however, does not prescribe the components to employ. From a literature review, it was found that the only surrogates proposed for the specific Jet A POSF10325 are the ones of Edwards (2017) reported in Table 4.7. However, other types of Jet A have very similar characteristics. For example, the Jet A POSF4658 employed, e.g., by Dooley *et al.* (2012); Kim *et al.* (2014), which is modeled with different 3 components surrogates, as reported in Table 4.8.

It is interesting to note the disparities in the chosen components. For instance, Surrogates 3 and 4 have none in common. Furthermore, since only 3 components are retained, a choice had to be made between each class reported in Fig. 4.31. Usually, a *n*-alkane and an aromatic are retained, while a choice is made between cyclo-alkanes and *iso*-alkanes. Alkenes are never included in 3-component surrogates. Several reasons are advanced by the authors. All agree that it is important to generate a radical pool during combustion that is similar to the one of the real fuel; and in that regard, since many species share the same radical production/consumption capabilities, some constituents can be safely discarded. Dooley *et al.* (2012) reckon that the contribution from *n*-alkanes and cyclo-alkanes is similar in terms of provided *chemical functionalities*, and that inclusion of the latter could be omitted. The same authors acknowledge, however, that the transition from NTC to high temperature ignition behavior is improved by considering the functionalities of cyclo-alkanes (Dooley *et al.*, 2014). This last argument, along with the recognition that the pathways allowed by these ring structures are specific and unique, is employed by Narayanaswamy *et al.* (2016) who preferred to retain a cyclo-alkane representative.

Components	Surrogate 3 Mole %	Surrogate 4 Mole %	S_{10325} Mole %
n-dodecane	30.3	0	37.0
n-decane	0	42.7	0
iso-octane	0	33.0	27.5
methylcyclohexane	48.5	0	0
m-xylene	21.2	0	35.5
toluene	0	24.3	0
Refs.	$\mathcal{S}_I$ Narayanaswamy *et al.* (2016)	1^{st} Generation surrogate Dooley *et al.* (2012)	

Table 4.8: Surrogates for Jet A (POSF4658).

The range of important properties (H/C ratio, MW, DCN ...) covered by the choice of components made in the aforementioned studies is best illustrated on a series of maps, such as those displayed in Fig. 4.35. In this representation, borrowed from the work of Cornell (2002) and Morganti *et al.* (2013), each vertex represents a pure constituent while edges represent binary mixtures. A point in the diagram corresponds to a specific 3-compounds surrogate composition, expressed in percentages of total mole fraction of fuel. The diagram is discretized with 231 points, corresponding to 21 points along each edge. The specific surrogate composition chosen by the different authors are also reported, with red stars. The first observation is that none of the aforementioned surrogates seems suitable to the configuration under investigation (NASA-LDI) in this PhD thesis, in comparison with the values of Table 4.6. In particular, the molecular weight is well underestimated by all proposed surrogates, with the exception of the Surrogate 2 (Edwards, 2017) having to resort, however, to the very heavy and complex hexadecane species. The H/C ratio is always overestimated, with values around 2 instead of the experimentally determined value of 1.9.

From the information gathered in the literature, it appears that there are many different reported values for DCN of single components, and that the simple mixing rule for extrapolation to multi-component surrogates may not bear physical meaning (values reported for the DCN of Surrogate 2 by Edwards (2017) and computed with the mixing rule employing component DCN prescribed in the Component Library Framework (Narayanaswamy *et al.*, 2016) give very different values, for example). Therefore, it was decided to prioritize the matching of the MW and H/C ratio and to consider the DCN as marginally important. Also, it was decided to include a *n*-alkane, an aromatic and to prefer an *iso*-alkane rather than a cyclo-alkane since it is the most common approach. For the *n*-alkane, *n*-dodecane appeared as a good compromise between a high MW and induced complexity. Furthermore, this species has been widely employed and studied in the literature, both experimentally and numerically, since many mono-component kerosene surrogates rely on *n*-dodecane. For the same reasons, *iso*-octane is chosen as an *iso*-alkane representative. The choice of the aromatic was dictated by its availability in the detailed mechanism. The comprehensive mechanism from Narayanaswamy *et al.* (2016) was employed, of which a subset was already used in the context of ethylene/air oxidation (see Section 4.3). It contains *m*-xylene, which appeared as the best compromise between MW and complexity, since more than one-ringed structures are not usually considered unless sooting tendencies are seeked for. Toluene might have been employed instead. The map of H/C ratio, MW and DCN ranges covered by these three components is shown on the bottom right diagram of Fig. 4.35. It is readily seen that it is not possible to exactly meet all targeted properties with these components, and that some sort of compromise will have to be made. Actually, amongst all considered surrogates, only the components employed in the formulation of Surrogate 2 Edwards (2017) would allow to recover all experimental values of MW, H/C ratio and DCN.

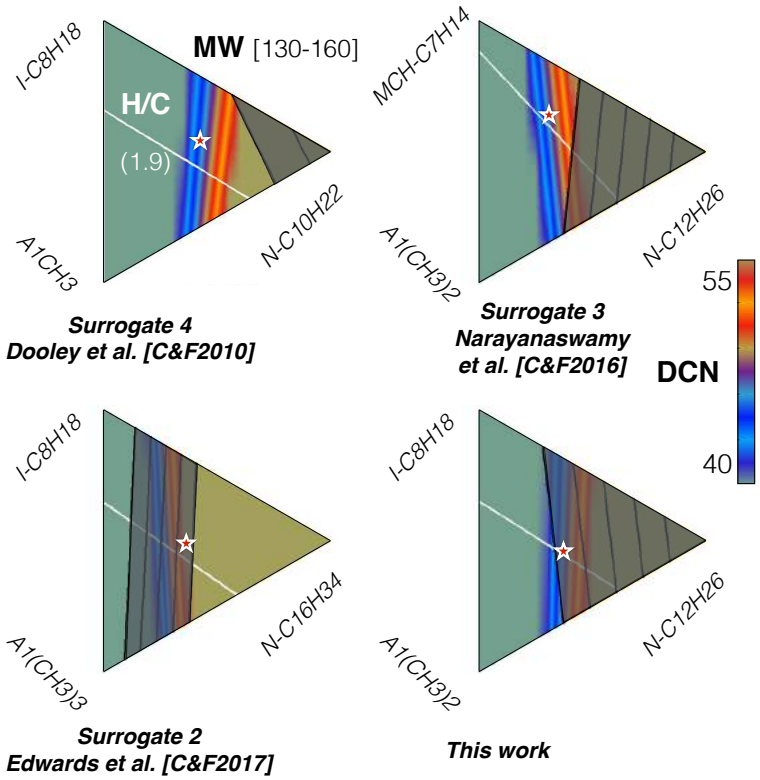

Figure 4.35: Illustration of the ranges of H/C ratio, MW and DCN covered by 3-components surrogates made up of different hydrocarbons. The specific surrogate composition chosen by the authors are reported with red stars. White lines mark the H/C ratio = 1.92, black lines mark values of MW in the range [130-160].

The targets of Table 4.6 were fed to the optimization tool and the surrogate S_{10325} (red star in the bottom right diagram of Fig. 4.35), described in the last column of Tables 4.8 & 4.9, was eventually obtained. The targeted properties of the Jet A POSF10325 are again reported in Table 4.9, to allow a direct comparison.

Target properties	Jet A (POSF10325)	S_{10325}
H/C ratio	1.90	1.91
Average formulae	$C_{11.37}H_{21.87}$	$C_{9.48}H_{18.12}$
MW	159	132
DCN	48.3	47.1
Liquid density [kg/l]	0.8	0.76
Composition [% mole fraction]	20.03% Total n-paraffins 29.45% Total iso-paraffins 18.66% Aromatics 31.86% Total cycloparaffins	37.0% *n*-dodecane 27.5% *iso*-octane 35.5% *m*-xylene

Table 4.9: Combustion property targets employed for the derivation of the surrogate S_{10325}.

4.4.3.b Detailed mechanism with the CLF

A detailed mechanism containing only the relevant kinetic pathways to the chosen surrogate components was extracted from the comprehensive detailed mechanism reported in Narayanaswamy *et al.* (2016), employing the CLF described in the same paper. The resulting detailed mechanism, called JetA2_3COMP, is comprised of 261 species and 1535 reactions.

4.4.3.c ARC derivation

One important finding of this work is that reducing the detailed mechanism JetA2_3COMP for the multi-component surrogate S_{10325} is very challenging, due to the competing and interfering pathways of the three components. The strong non-linearity of the system prevents reducing the original kinetic mechanism to an acceptable size for use in LES: in practice, it is impossible to fall under 60 species without introducing significant errors on one of the targets. The CO/CO_2 equilibrium is particularly difficult to accurately reproduce. This might, of course, be attributed to the choice of components, or to an inadequacy of the retained initial detailed mechanism. Nonetheless, these results stress that the multi-component strategy in LES is far from straightforward.

Two types of reduction have been attempted:

- Deriving a reduced mechanism by targeting each component separately
- Deriving a reduced mechanism for the surrogate formulation directly

The first approach rests on the assumption that a mechanism able to describe the chemistry of each component will describe the chemistry of any mixture of these components. If this assumption is intuitive, it nonetheless needs to be verified. In the present case, it was found to be true, to some extent. Indeed, no significantly large errors were obtained with multi-component computations, when performed with a reduced mechanism preserving the accuracy of each component... However, keeping the error levels reasonable on *every* component requires to keep a very large number of species ! The smallest skeletal mechanism able to do so, on the targeted range reported in Table 4.10, is composed of 139 species and 1148 reactions. This mechanism represents a species reduction of about 47%, but remains obviously too large to be considered for a direct implementation in LES.

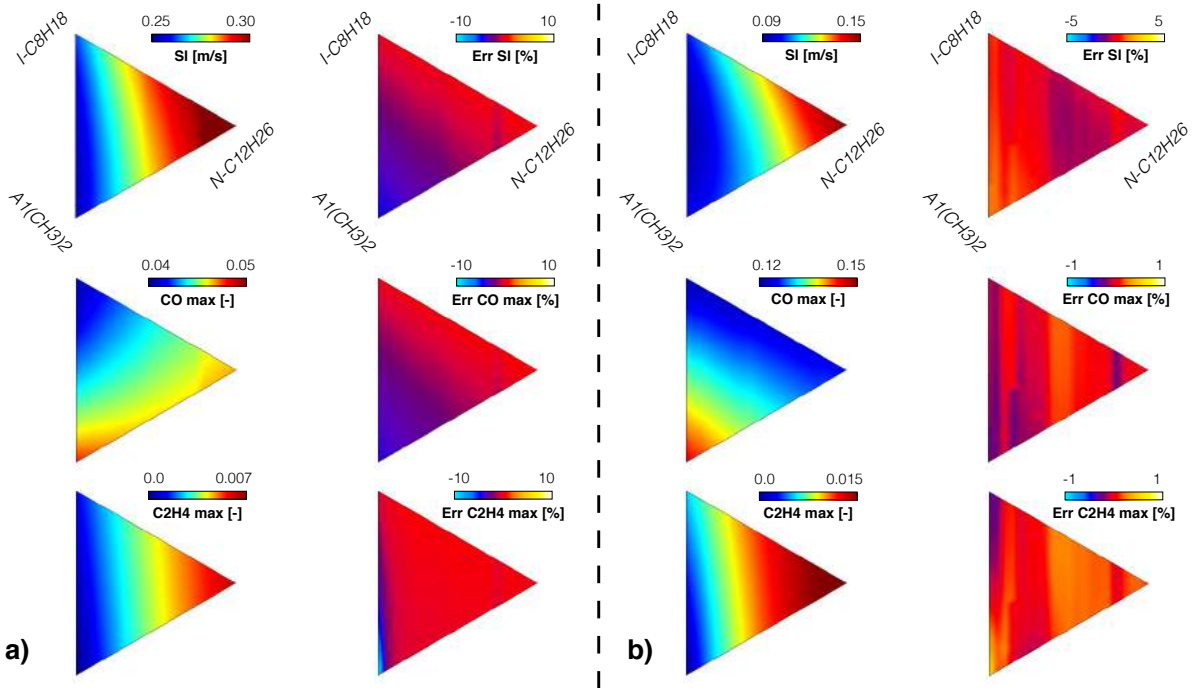

Figure 4.36: Left columns: s_l and maximum CO and C_2H_4 species in PF flames, for various 3-components surrogates made up of *n*-dodecane, *iso*-octane and *m*-xylene. Computations with JetA2_3COMP. Right columns: relative errors on the same quantities when computed with the 139 species and 1148 reactions reduced mechanism. T_i = 300 K, P = 1 atm and a) ϕ = 0.8, b) ϕ = 1.5.

A quantitative investigation of the reduction strategy is provided on Fig. 4.36 (a) and (b). The left most columns present values of s_l as well as maximum of CO and C_2H_4 species obtained for a large range of surrogate compositions, on PF test cases, with the JetA2_3COMP mechanism. The right most columns present the relative error obtained from these quantities, when employing the 139 species and 1148 reactions mechanism to perform the computations. From Fig 4.36 (a), presenting results for one of the operating points exhibiting the largest errors, it can be seen that the error slowly propagates from mono-component mixtures towards binary

and tertiary mixtures. In particular, the $m-$xylene component is found to be the most difficult component to accurately emulate in the present reduction. Note from both Figures, however, that some non-linearities are observed throughout the surrogate composition domain, due to the non-linearities of the multiple pathways of each components. If they rarely exceed the maximum observed relative error on computations performed with mono-component mixtures, these "error non-linearities" tend to become more pronounced as the reduction proceed. As such, there is no guarantee that the error levels remain reasonable for any surrogate composition provided that a "reduced enough" mechanism preserving the accuracy of each component could be obtained.

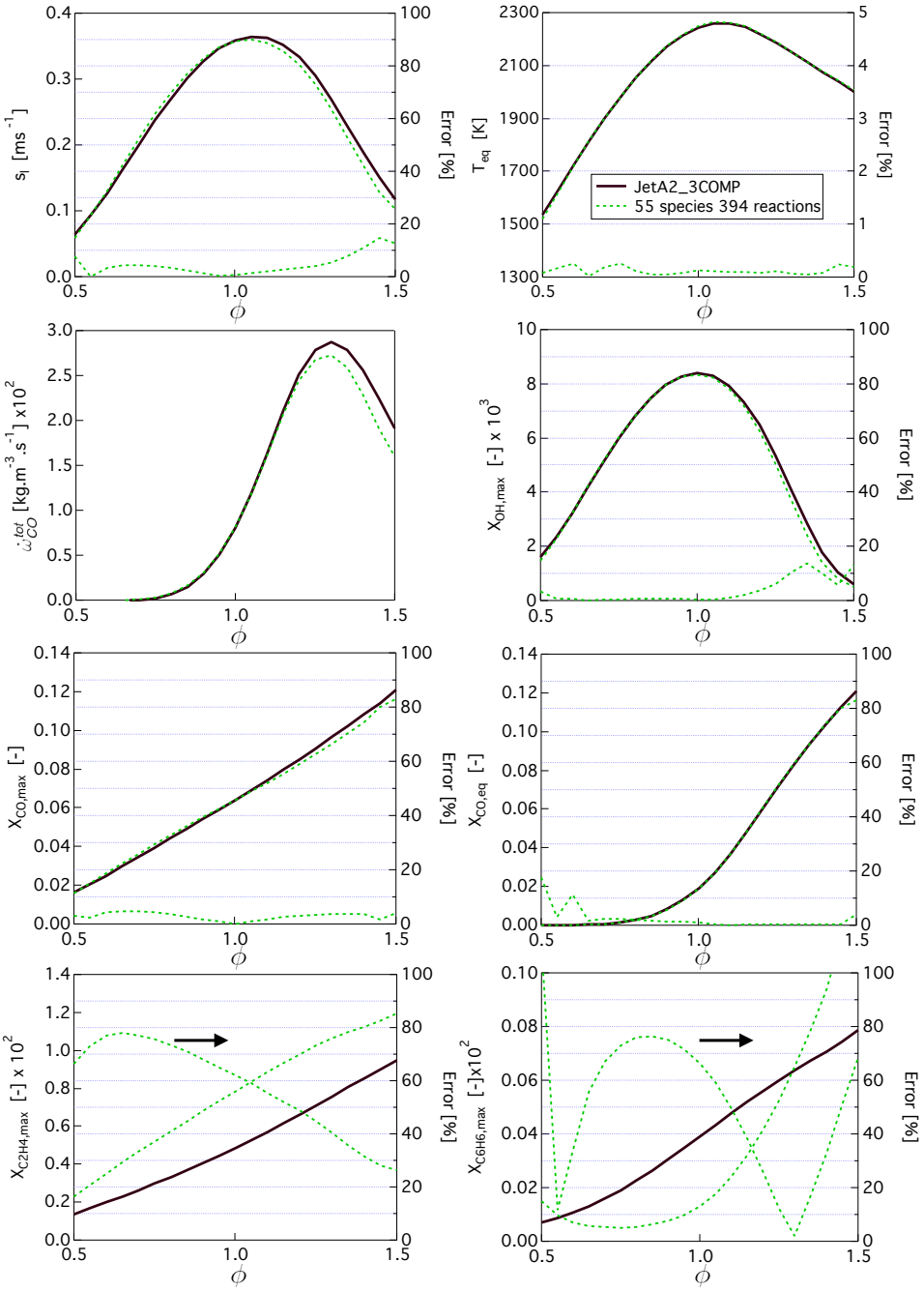

Figure 4.37: Performances of the skeletal mechanism composed of 55 species and 394 reactions, on PF test cases. $T_i = 300$ K and P = 1 atm.

Following these findings, the second type of reduction is now tested. With this approach, the reduction is performed by directly targeting the S_{10325} surrogate composition, specified in Table 4.9. By targeting the range reported in Table 4.10, a skeletal mechanism composed of 55 species and 394 reactions is obtained. The global performances of this mechanism are assessed on PF and AI test cases, and examples of validations on PF test cases are provided on Fig. 4.37. As can be seen, despite the relatively exhaustive list of species retained, a

compromise has to be made between the various targets: a relative error greater than 40% is almost systematically observed on the C_2H_4 species profiles, even in the targeted range. Also, it is observed that this mechanism already displays a large error on important but not targeted quantities, such as C_6H_6 or C_2H_2 for example. Additionally, as is apparent from the profile of maximum C_6H_6 species (Fig. 4.37), the level of error and evolution of global quantities with equivalence ratio is somewhat unpredictable; revealing that the pathways of each component start to compete and interfere with each other beyond a certain degree of reduction. In the case under consideration, any further reduction attempt resulted in unacceptably bad performances on crucial targets, such as s_l or the CO/CO_2 equilibrium. The next step would be to search for potential QSS. However, due to the relatively large size of the mechanism, this search is not facilitated. Furthermore, to reach an acceptable size for LES, about half of the species should be identified as potential QSS. This is obviously not the case, and the reduction procedure is not able to produce a suitable, LES compliant, mechanism for the S_{10325} surrogate.

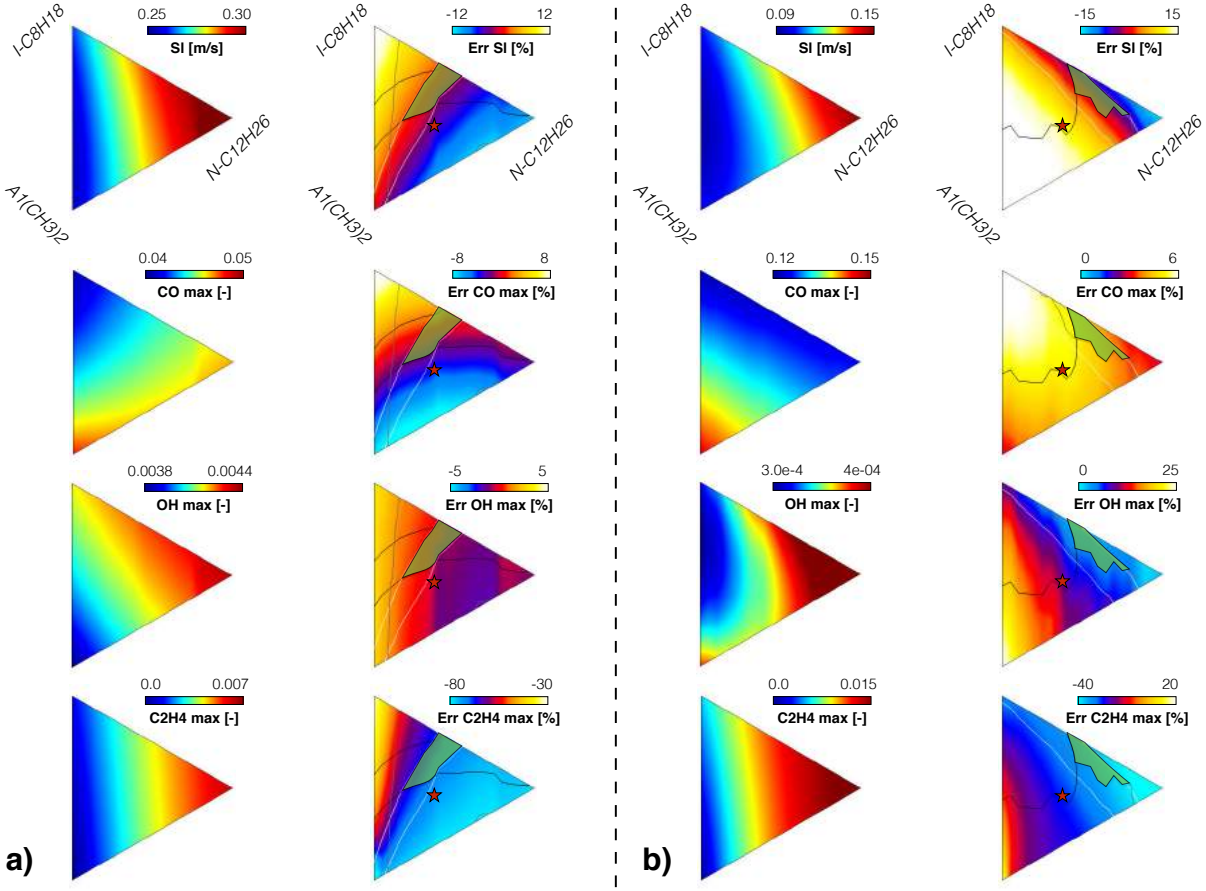

Figure 4.38: Left columns: s_l and maximum of selected species in PF flames, for various 3-components surrogates made up of *n*-dodecane, *iso*-octane and *m*-xylene. Computations with JetA2_3COMP. Right columns: relative errors on the same quantities when computed with the 55 species and 394 reactions mechanism. T_i = 300 K, P = 1 atm and a) ϕ = 0.8, b) ϕ = 1.5. White iso-contours represent the region where +/- 2% error is reached on s_l. Black iso-contours represent the region where +/- 2% error is reached on maximum of CO. Grey iso-contours represent the region where +/- 2% error is reached on maximum of OH. The green region marks the zone where the errors on all three quantities are comprised in between -2% and 2%.

As specified previously, kerosenes are complex blends of various hydrocarbons, and their exact composition might vary from one batch to the other. The question then arises, if an ARC derived for a given surrogate is still valid for another, but close, surrogate. To answer this question, the region of validity around the initial surrogate composition, for a set of relevant targets, is reported in the previously introduced diagrams. Results are presented in Fig. 4.38 (a) and (b), where PF test cases at two different ϕ were again considered. For simplicity, the analysis is limited to s_l, and the CO and OH species. One notable observation is that, if the error computed over the mixture composition for one specific target exhibits a more or less continuous behavior, the different targets errors are conflicting. In fact, identifying a region with minimum errors on all important species is not even always possible, as would be the case, for example, if C_2H_4 was added to the list of targets. The problem is further complicated when several operating points are considered, since, as can be seen from Fig. 4.38, the several regions of minimum error might not overlap.

This analysis has led to the conclusion that emulating the behavior of a real fuel with a multi-component mixture in the context of LES might not be the best approach.

4.4.4 Alternative approach: HYbrid CHEMistry (HyChem)

4.4.4.a Detailed mechanism

Fortunately, as introduced before, another methodology has been developed to emulate real fuel's behavior: the HyChem approach. In this Section, a HyChem model for the Jet A POSF10325 discussed in Section 4.4.2 is presented. The detailed mechanism is comprised of three parts: a lumped reaction scheme for fuel pyrolysis, a comprehensive detailed mechanism for the combustion of the pyrolysis products (foundational mechanism), and a sub-mechanism for NO_x predictions.

Fuel breakdown Following the HyChem methodology, the fuel breakdown is described by a few lumped reactions. For the Jet A POSF10325 fuel (Version I), 6 reactions are required. They read:

$$\begin{aligned}
POSF10325 \rightarrow\ & 2.95\ C_2H_4 + 0.39\ C_3H_6 \\
& + 0.195\ \text{i-}C_4H_8 + 0.1833\ C_6H_6 \\
& + 0.15\ C_6H_5CH_3 + H + CH_3 \\
POSF10325 + H \rightarrow\ & H_2 + 0.05\ CH_4 + 2.83083\ C_2H_4 + 0.48616\ C_3H_6 \\
& + 0.243083\ \text{i-}C_4H_8 + 0.1925\ C_6H_6 \\
& + 0.1575\ C_6H_5CH_3 + 0.4\ H + 0.6\ CH_3 \\
POSF10325 + CH_3 \rightarrow\ & 1.05\ CH_4 + 2.83083\ C_2H_4 + 0.48616\ C_3H_6 \\
& + 0.243083\ \text{i-}C_4H_8 + 0.1925\ C_6H_6 \\
& + 0.1575\ C_6H_5CH_3 + 0.4\ H + 0.6\ CH_3 \\
POSF10325 + OH \rightarrow\ & H_2O + 0.05\ CH_4 + 2.83083\ C_2H_4 + 0.48616\ C_3H_6 \\
& + 0.243083\ \text{i-}C_4H_8 + 0.1925\ C_6H_6 \\
& + 0.1575\ C_6H_5CH_3 + 0.4\ H + 0.6\ CH_3 \\
POSF10325 + O_2 \rightarrow\ & HO_2 + 0.05\ CH_4 + 2.83083\ C_2H_4 + 0.48616\ C_3H_6 \\
& + 0.243083\ \text{i-}C_4H_8 + 0.1925\ C_6H_6 \\
& + 0.1575\ C_6H_5CH_3 + 0.4\ H + 0.6\ CH_3 \\
POSF10325 + HO_2 \rightarrow\ & H_2O_2 + 0.05\ CH_4 + 2.83083\ C_2H_4 + 0.48616\ C_3H_6 \\
& + 0.243083\ \text{i-}C_4H_8 + 0.1925\ C_6H_6 \\
& + 0.1575\ C_6H_5CH_3 + 0.4\ H + 0.6\ CH_3
\end{aligned}$$

Foundational detailed mechanism Similarly to what is prescribed by Xu *et al.* (2017*a*), the detailed mechanism for the pyrolysis products is chosen to be the USCII mechanism. It was presented and employed in this work in the context of ethylene/air oxidation, in Section 4.3.1.

NO_x chemistry NO_x reaction pathways are often decoupled from the carbonated phase in that they are often added as a complementary set to existing hydrocarbon mechanisms. However, as seen in Section 2.2.4.a, the levels of NO_x can rely heavily upon the available amount of carbonated radicals, such as CH. Unfortunately, the chemistry of such radicals is not well understood, nor are they specifically targeted when deriving kinetic schemes for combustion applications. As a result, different kinetic schemes developed for the same fuel can yield very different levels of H, CH, ... which will eventually translate into very different NO levels. In his PhD thesis, Jaravel (2016), for example, underlined that the level of NO predicted in laminar 1D premixed methane/air flames by the GRI 2.11 mechanism (Bowman *et al.*, 1995) differed from that of the GRI 3.0 mechanism (Bowman *et al.*, 1999) by about a factor 2. The same was observed by Moesl *et al.* (2012) for *n*-decane oxidation.

Due to both a lack of experimental data and kinetic schemes available for NO_x prediction in real fuels, the NO_x sub-mechanism of the Luche scheme (Luche, 2003) is used, which appeared as the best compromise. A total of 17 additional species and 245 additional (irreversible) reactions need to be considered.

4.4.4.b ARC derivation

The detailed mechanism without NO_x is labelled JetA2_USCII, while the complete mechanism will be referred to as JetA2_USCII_NOx. The latter is comprised of a total of 129 species and 1572 irreversible reactions. Since the number of species remain reasonable, no lumping is employed. The derivation procedure is similar to what was described for ethylene/air oxidation: first species and reactions are removed by employing the DRGEP technique, to obtain the smallest possible skeletal mechanism; then QSS candidates are identified by the LOI method. The procedure is somewhat complicated by the NO_x sub-mechanism, and two reductions were performed. The first reduction is performed without considering the NO_x sub-mechanism. An ARC comprised of 27 transported species and 12 QSS species is derived, labelled ARC_27_JetA2 hereafter. The characteristics of the derivation are provided in Table 4.10 (*Ref.* case), while Fig. 4.39 (a) provides a sketch of the derivation.

Case name	**Canonical test cases**	*Targeted range*	**Targeted constraints**
Ref. case	PF	1 atm / 300K / ϕ = 0.8-1.3	CO CO_2 C_2H_4 OH HR
	AI	1 atm / 1300-1700 K / ϕ = 0.8-1.3	CO CO_2 C_2H_4 OH HR
NO_x case	PF	same	same + NO
	AI	same	same + NO

Table 4.10: List and specifications of reductions performed with YARC.

Since the ARC_27_JetA2 mechanism does not contain the CH species, the NO_x sub-mechanism cannot be added directly to it. Instead, the same set of species that were discarded in this mechanism except CH are removed from the initial detailed mechanism JetA2_USCII. From there, the NO_x sub-mechanism is added, and a DRGEP procedure to remove unnecessary species is performed. Targets for the derivation are provided in Table 4.10 (*NO_x* case); they only differ from that of the Ref. case in that the species NO is now of interest. A skeletal mechanism of 46 species and 547 reactions is derived, amongst which 17 species are found to be good QSS candidates. The whole reduction process is sketched in Fig. 4.39 (b). The final ARC is labelled ARC_29_JetA2NOx in what follows.

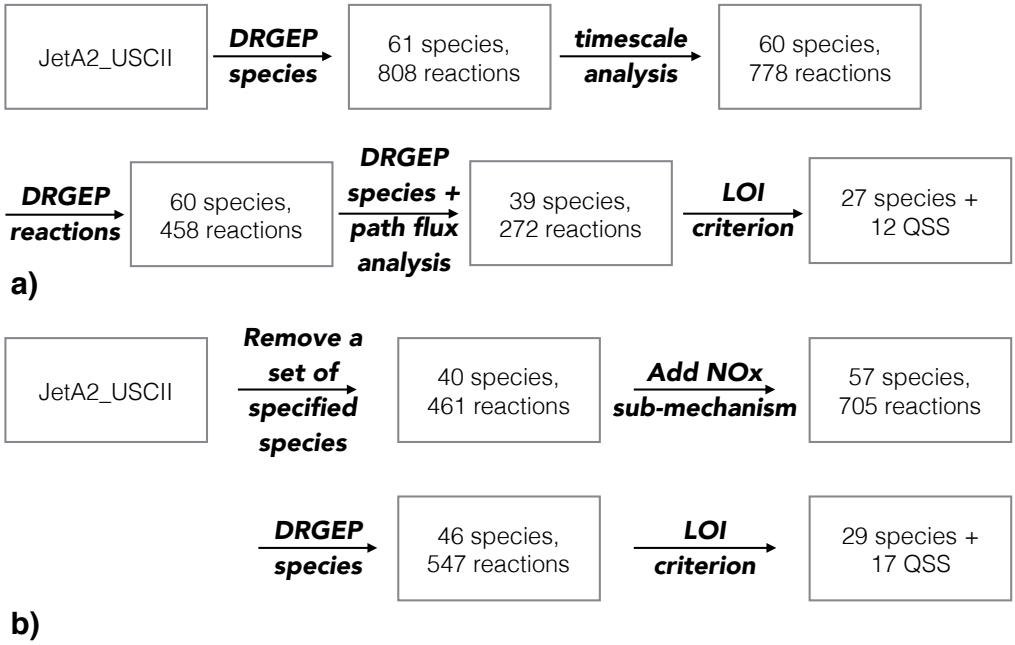

Figure 4.39: a) Derivation of the ARC_27_JetA2 and b) derivation of the ARC_29_JetA2NOx.

The performances of both ARC are assessed in canonical test cases relevant to the NASA-LDI configuration that will be studied in Chapter 8. Examples of 1D validations are presented in Figs. 4.40-4.42. Note that comple-

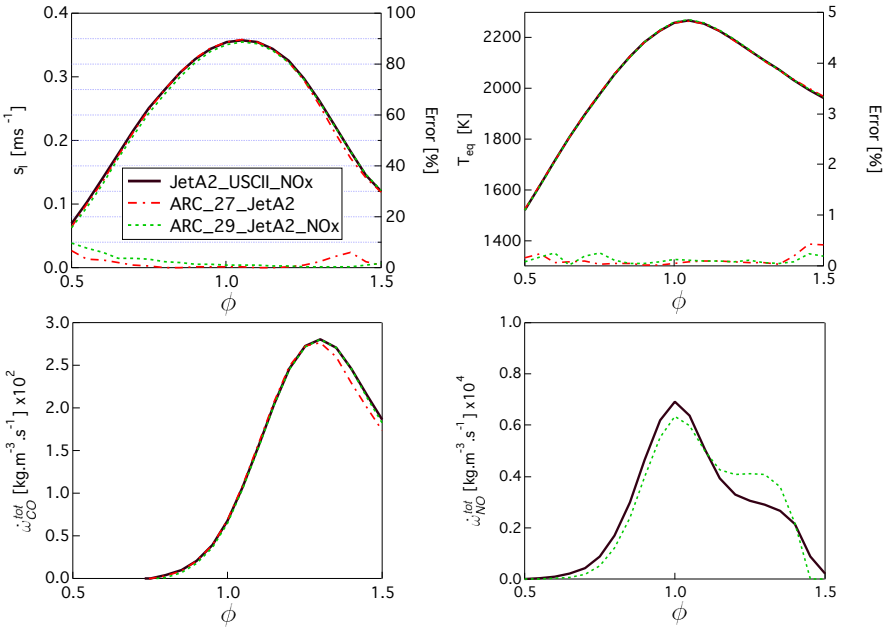

Figure 4.40: Validation of ARC_27_JetA2 and ARC_29_JetA2NOx on global quantities and burnt gas temperature of 1D unstretched laminar premixed flames at P = 1 bar and T_{ini} = 300 K.

mentary validations will be presented in Chapter 8. As can be seen from the graphs, the NO species is the most difficult target to reproduce. However, due to the aforementioned uncertainties on NO_x chemistry, it is considered acceptable. All other targets are very well reproduced over the entire extended range of equivalence ratio. The major pyrolysis product is ethylene, but other pyrolysis products such as benzene and major intermediates such as acetylene might also be of interest. Their error levels are thus monitored *a-posteriori*, as displayed on the plots of Figs. 4.41. The higher error levels for such non targeted species were to be expected. Overall, results are considered very satisfactory.

It is readily seen that this methodology is far more attractive than the classical multi-component approach. Indeed, the reduction procedure was facilitated by the use of a single mono-component lumped fuel species. The level of reduction eventually reached is comparable to that reported in the literature for *n*-dodecane (Vié *et al.*, 2015; Jaravel, 2016) or lighter mono-component surrogates.

The ARC_29_JetA2NOx mechanism will be employed in Chapter 8. As underlined before, AVBP uses a simplified transport, TransAVBP. This model requires single Schmidt numbers for each species, and a constant Prandtl number. These data are reported on Table 4.11.

Species	N_2	H	H_2	HO_2	H_2O
Schmidt number	0.69086	0.12175	0.20341	0.73717	0.54500
Species	H_2O_2	O	O_2	OH	CO
Schmidt number	0.74229	0.47607	0.73249	0.48525	0.74221
Species	CO_2	CH_2O	CH_2CO	CH_3	CH_4
Schmidt number	0.94654	0.84886	1.00381	0.66620	0.66941
Species	C_2H_2	C_2H_4	C_2H_6	C_3H_6	I-C_4H_8
Schmidt number	0.87434	0.88245	0.97020	1.24102	1.40336
Species	C_5H_6	$C_6H_4O_2$	C_6H_5O	C_6H_6	$C_6H_5CH_3$
Schmidt number	1.44217	1.66697	1.58507	1.55014	1.73499
Species	POSF10325	NO	HCN	NO_2	
Schmidt number	2.39974	0.74897	0.84600	0.84131	

Table 4.11: Schmidt numbers of the species involved in the ARC_29_JetA2NOx mechanism, employed in AVBP computations.

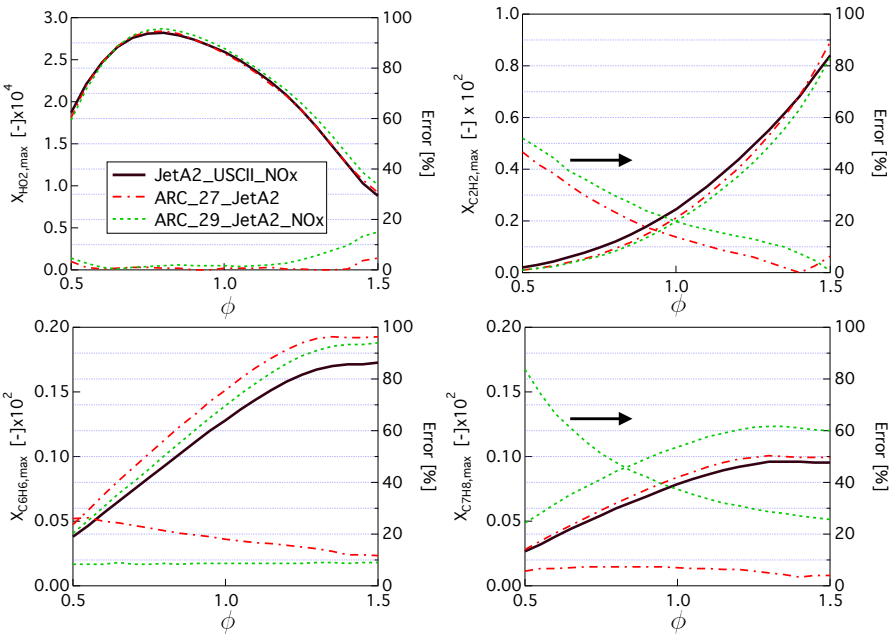

Figure 4.41: Validation of ARC_27_JetA2 and ARC_29_JetA2NOx on peak values of major non-targeted pyrolysis products (HO_2, C_6H_6, C_7H_8) + C_2H_2, in 1D unstretched laminar premixed flames at P = 1 bar and T_{ini} = 300 K.

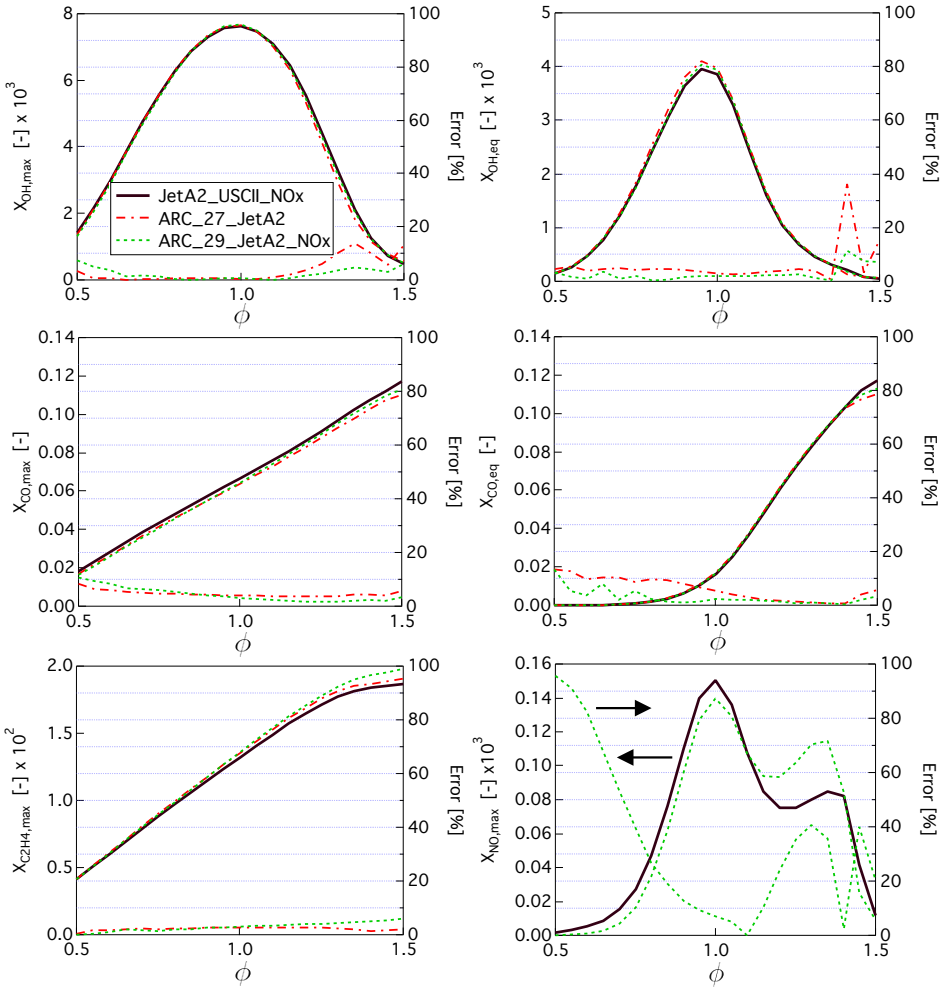

Figure 4.42: Validation of ARC_27_JetA2 and ARC_29_JetA2NOx on peak and equilibrium values of major targets, in 1D unstretched laminar premixed flames at P = 1 bar and T_{ini} = 300 K.

Part II

Fundamentals of turbulent reactive flows

Chapter 5

Conservation equations for turbulent reacting flows

Contents

5.1 The unfiltered reactive Navier-Stokes equations

One way to obtain the Navier-Stokes equations for multicomponent reactive mixtures, describing the conservation of mass, momentum and energy, is to rely upon the kinetic theory of gases at the microscopic level. This is an interesting approach because certain expressions naturally appear, which may be shown to represent the fluxes of mass, momentum and energy. In particular, second order effects such as the *Soret* and *Dufour* effects are directly accounted for.

For a gaseous mixture made up of N components, the system can be represented by a high-order distribution function of $6N$ variables $f^{(N)}$, which is very difficult to determine (N is of the order of the Avogadro's number). Fortunately, the properties of a *dilute* gas can be sufficiently well approximated by the first order distribution functions $f^{(1)}$ (Hirschfelder *et al.*, 1969; Kee *et al.*, 2005). Those are shown to be completely characterized by the species i retained, and will thus be denoted f_i. $f_i(\mathbf{x}, \mathbf{v_i}, t)\delta\mathbf{x}\delta\mathbf{v_i}$ represents the number of molecules of species i which, at time t, lies in a unit volume element about $\mathbf{x}$ and have velocities within a unit range about $\mathbf{v_i}$. These distribution functions satisfy Boltzmann equations. The conservation equations can be directly derived from the Boltzmann equations without knowledge of the distribution functions (see e.g. Chapter 7 in Hirschfelder *et al.* (1969)). However, approximate solutions are required to derive expressions for the fluxes appearing in the conservation equations. Amongst the existing techniques, Enskog's perturbation theory is the most popular. In the context where collision times are smaller than reaction characteristic times, the distribution functions are expanded in a series $f_i = f_i^0 + f_i^1\zeta...$, where $1/\zeta$ measures the frequency of collisions. Keeping only the first order terms in the linearized Boltzmann equations leads to the Navier-Stokes equations, expressed here with Einstein index notation:

$$\frac{\partial \rho u_j}{\partial t} + \frac{\partial \rho u_i u_j}{\partial x_i} = -\frac{\partial P}{\partial x_j} + \frac{\partial \tau_{ij}}{\partial x_i} \quad \text{for } j = 1, 3 \tag{5.1}$$

$$\frac{\partial \rho Y_k}{\partial t} + \frac{\partial \rho u_i Y_k}{\partial x_i} = -\frac{\partial J_{k,i}}{\partial x_i} + \dot{\omega}_k \quad \text{for } k = 1, N \tag{5.2}$$

$$\frac{\partial \rho E}{\partial t} + \frac{\partial \rho u_i E}{\partial x_i} = -\frac{\partial q_i}{\partial x_i} - \frac{\partial u_i P}{\partial x_i} + \frac{\partial u_j \tau_{ij}}{\partial x_i} + \dot{\omega}_T \tag{5.3}$$

with u_j the j^{th}-component of the velocity, P the static pressure, Y_k the mass fraction of the k^{th}-species, E the total energy and $\dot{\omega}_k$ and $\dot{\omega}_T$ the k^{th} species and energy chemical source term, respectively (see Eqs. 2.13 & 2.14). Eqs. (5.1)-(5.3) are referred to as the momentum, species and energy conservation equations respectively. The transport fluxes τ_{ij}, $J_{k,i}$ and q_i appearing in each equations are then explicitly given by:

$$\tau_{ij} = \mu\left(\frac{\partial u_i}{\partial x_j} + \frac{\partial u_j}{\partial x_i}\right) + \left(\kappa - \frac{2}{3}\mu\right)\left(\frac{\partial u_k}{\partial x_k}\delta_{ij}\right) \tag{5.4}$$

$$J_{k,i} = \rho Y_k V_{k,i} \tag{5.5}$$

$$q_i = -\lambda\frac{\partial T}{\partial x_i} + \sum_{k=1}^{N} J_{k,i}h_k + DE \tag{5.6}$$

where DE stands for the Dufour effect (see e. g., Hirschfelder *et al.* (1969) or Ern & Giovangigli (1995)), λ is the heat conduction coefficient of the mixture, μ and κ are the shear and volume viscosity, respectively; and where $V_{k,i}$ are the species diffusion velocities, expressed as:

$$V_{k,i} = -\frac{1}{X_k}\sum_{j=1}^{N}\frac{W_k}{W}D_{kj}d_{j,i} - \frac{D_k^T}{\rho Y_k}\frac{1}{T}\frac{\partial T}{\partial x_i} \quad \text{for} \quad k = 1, N \tag{5.7}$$

where W_k and W are the species and mixture molecular weight, respectively, and with D_{kj} the multicomponent diffusion coefficients, D_k^T the thermal coefficient, and $\mathbf{d_j}$ the j^{th}-species diffusion driving force, expressed as:

$$d_{j,i} = \frac{\partial X_j}{\partial x_i} + (X_j - Y_j)\frac{1}{P}\frac{\partial P}{\partial x_i} \tag{5.8}$$

These exhaustive formulations are usually simplified, depending upon the combustion problem under investigation. In our context, the following assumptions are made:

- The Soret effect, which represents the diffusion of mass arising from temperature gradients in Eq. 5.7 has usually a small effect and can be safely neglected (Poinsot & Veynante, 2005)
- The Dufour effect, which is the opposite of the Soret effect, is also neglected
- The volume viscosity κ is not considered, since it becomes important only when compressibility effects are dominant
- For the same reasons, pressure gradients are neglected in Eq. 5.8

In addition, since the evaluation of the $V_{k,i}$ can be tedious (Ern & Giovangigli, 1994), the classical *Hirschfelder and Curtiss* approximation is employed, which has been shown to provide the best first-order approximation to the exact expressions, yielding:

$$\rho Y_k V_{k,i} = -\rho D_k \frac{W_k}{W}\frac{\partial X_k}{\partial x_i} \tag{5.9}$$

with D_k now representing a global diffusion coefficient of the species k into the rest of the mixture, expressed in terms of the *binary* coefficients of species k and j, $\mathcal{D}_{jk}$:

$$D_k = \frac{1 - Y_k}{\sum_{j\neq k} X_j/\mathcal{D}_{jk}} \tag{5.10}$$

Note that with this approximation, the global mass is not conserved. To enforce it, a correction velocity V_i^c is introduced:

$$V_i^c = \sum_{k=1}^{N} D_k \frac{W_k}{W}\frac{\partial X_k}{\partial x_i} \tag{5.11}$$

The final expression for the fluxes reads:

$$\tau_{ij} = \mu\left(\frac{\partial u_i}{\partial x_j} + \frac{\partial u_j}{\partial x_i}\right) - \frac{2}{3}\mu\left(\frac{\partial u_k}{\partial x_k}\delta_{ij}\right) \tag{5.12}$$

$$J_{k,i} = \rho Y_k (V_{k,i} + V_i^c) \tag{5.13}$$

$$q_i = -\lambda\frac{\partial T}{\partial x_i} + \sum_{k=1}^{N} J_{k,i} h_k \tag{5.14}$$

The transport coefficients λ, μ as well as the binary diffusion coefficients are still, however, undetermined. The next Section provides approximate expressions of various degrees of accuracy.

5.2 Expression for the transport coefficients

5.2.1 Simplified kinetic theory

When two molecules come close to one another, they undergo very complex interactions. A *simplified* kinetic theory of gases is based on the assumption that the particles are rigid spheres of mass m and diameter d, all traveling at the same speed in only 6 different directions in space, and interacting with one another only during collision (elastic collision). This type of interaction is represented on Fig. 5.1a. With these assumptions, the different coefficients can be expressed in terms of the *rate of molecular collision* -or the number of collisions suffered by one molecule per unit time Ω, and the *mean free path* -or the average distance traveled by a molecule between collisions l (see, e.g., Kee *et al.* (2005)). This ultra simplified point of view is in approximate agreement with experiment, and allows to draw some observations. First off, with the definitions for Ω and l, the coefficients of viscosity and thermal conductivity are found to be pressure independent, and increase with the square root of the temperature. The coefficient of diffusion is found to be inversely proportional to the pressure and to vary as the three-halves power of the temperature.

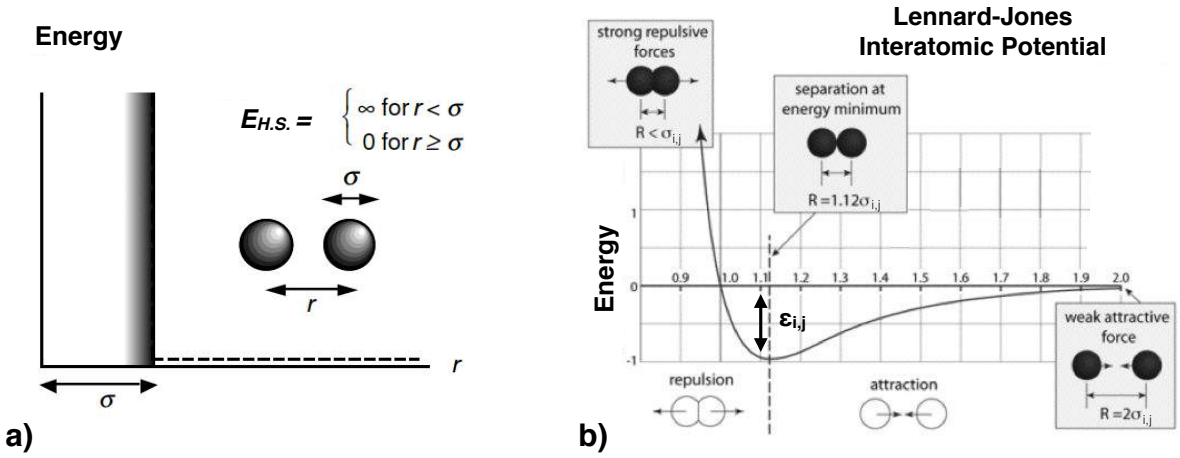

Figure 5.1: a) Hard sphere potential representation vs b) Lennard-Jones 6-12 potential representation.

5.2.2 The Lennard-Jones potential and the mixture averaged rules (TranMix)

Pure species properties From a more rigorous point of view, the evaluation of the pure species transport coefficients rely upon the determination of a set of collision integrals $\Omega^{(l,s)}$, containing information about the dynamics of the molecular collisions (Hirschfelder *et al.*, 1969). These, in turn, directly depend upon molecular

interactions through the angle of deflection, which characterizes how much species are deviated from their path when they collide. In reality, molecular interactions are complex functions of the shape and properties of the pair of species, as well as of their environment, intermolecular distance, etc. They are often approximated by a Lennard-Jones 6-12 potential $V_{i,j}$ (see Fig. 5.1b), relating the evolution of the potential energy of the pair of species (i, j) to their intermolecular distance r. This function depends upon the collision diameter $\sigma_{i,j}$, and the depth of the intermolecular potential $\epsilon_{i,j}$:

$$V_{i,j} = 4\epsilon_{i,j}\left(\left(\frac{\sigma_{i,j}}{r}\right)^{12} - \left(\frac{\sigma_{i,j}}{r}\right)^{6}\right) \tag{5.15}$$

This model assumes that species interactions occur in two phases. First, species attract each other (term in the power of 6) until they become bounded and reach an equilibrium distance (occurring when the minimum potential energy is reached). If the species are further brought together, repulsion begins to occur, and the bounding energy drastically increases (term in the power of 12). The parameters associated to this model are the species diameters σ_i, molecular mass m_i, dipole moments μ_i, polarizabilities α_i and Lennard-Jones potential well depth ϵ_i.

The collision diameter and depth of the intermolecular potential are expressed by:

$$\sigma_{i,j} = \chi^{-\frac{1}{6}}\frac{1}{2}(\sigma_i + \sigma_j) \tag{5.16}$$

$$\epsilon_{i,j} = \chi^2\sqrt{(\epsilon_i\epsilon_j)} \tag{5.17}$$

where χ is unity if the molecules are either both polar or nonpolar; or a function of the reduced polarizabilities of the nonpolar (n) molecule $\alpha_n^* = \alpha_n/\sigma_n^3$ and reduced dipole moment of the polar (p) molecule $\mu_p^* = \mu_p/\sqrt{\epsilon_p\sigma_p^3}$ otherwise:

$$\chi_{n,p} = 1 + \frac{1}{4}\alpha_n^*\mu_p^*\sqrt{\frac{\epsilon_p}{\epsilon_n}} \tag{5.18}$$

With this choice of model for the potentials, the transport coefficients of the pure species can be expressed in terms of a set of reduced collision integrals $\Omega^{(l,s)*}$ that indicate the deviation from the idealized rigid-sphere model:

$$\mu_i = \frac{5}{16}\frac{\sqrt{\pi m_i k_B T}}{\pi{\sigma_i}^2\Omega^{(2,2)*}} \tag{5.19}$$

$$\mathcal{D}_{i,j} = \frac{3}{16}\frac{\sqrt{2\pi k_B^3 T^3/m_{i,j}}}{P\pi\sigma_{i,j}^2\Omega^{(1,1)*}} \tag{5.20}$$

where $m_{i,j} = m_i m_j/(m_i + m_j)$ is the reduced molecular mass for the (i, j) species pair. See e. g. Kee *et al.* (2000) for an expression of the $\Omega^{(l,s)*}$.

Expressions for the individual species conductivities are more complex. They are often assumed to be composed of translational, rotational, and vibrational contributions:

$$\lambda_i = \frac{\mu_i}{W_k}(f_{tr}C_{v,tr} + f_{rot}C_{v,rot} + f_{vib}C_{v,vib}) \tag{5.21}$$

where the expressions for the molar heat capacities $C_{v,x}$ are different depending on whether the molecule is linear, non linear, or composed of a single atom. The f_x functions depend on many parameters specific to each species, a complete definition of which can be found, e. g., in the CHEMKIN manual (Kee *et al.*, 2000).

Mixture averaged properties The mixture transport coefficients can now be evaluated from the pure species coefficients previously discussed. Several empirical mixing rules exist. A good compromise between accuracy and efficiency is provided by the so-called *mixture-averaged* rule, which is the formalism employed in every one-dimensional computations performed in this PhD thesis (with the solver CANTERA (Goodwin *et al.*, 2014)). The mixture-averaged viscosity is expressed by the Wilke formula (Wilke, 1950):

$$\mu = \sum_k \frac{\mu_k X_k}{\sum_j X_j \Phi_{k,j}} \tag{5.22}$$

where

$$\Phi_{k,j} = \frac{1}{8}\left(1+\frac{W_k}{W_j}\right)^{-\frac{1}{2}}\left[1+\left(\frac{\mu_k}{\mu_j}\right)^{\frac{1}{2}}\left(\frac{W_j}{W_k}\right)^{\frac{1}{4}}\right]^2 \tag{5.23}$$

And the mixture-averaged thermal conductivity is evaluated from a combination averaging formula (Mathur *et al.*, 1967):

$$\lambda = \frac{1}{2}\left(\sum_k X_k\lambda_k + \frac{1}{\sum_k X_k\lambda_k^{-1}}\right) \tag{5.24}$$

5.2.3 Non-dimensional numbers and constant transport coefficients (TranAVBP)

It is readily seen that the computation of the mixture-averaged transport coefficients can become very expensive. As such, simplified diffusion laws are used in a majority of CFD solvers, such as the code AVBP employed in this PhD thesis. Usually, the viscosity, thermal conductivity and global species diffusion coefficients are no longer computed based on the pure species coefficients. In particular, the tedious evaluations of the binary coefficients are no longer required. Instead, constant non-dimensional numbers assessing the relative contribution of each phenomenon are employed. These are:

- The Prandtl number $Pr = \mu C_p/\lambda$, comparing momentum and heat transport, also expressed as $Pr = \mu/\rho D_{th}$ where $D_{th} = \lambda/\rho C_p$
- The species Lewis numbers $Le_k = \lambda/\rho C_p D_k$ assessing the relative importance of the heat and k-th species diffusion
- The Schmidt numbers $Sc_k = \mu/\rho D_k$, comparing momentum and the species k molecular diffusion

where $C_p = \sum_k Y_k C_{p,k}$ is the mixture heat capacity. From the formulae we see that the specification of a Prandtl number, a Schmidt number for each species, and an expression for the viscosity leads to a very easy and efficient determination of the transport coefficients.

In practice, this model offers a very good compromise between accuracy and efficiency, and is retained in this work. Additionally, when the configuration under consideration employs air as oxidant, the viscosity can be fitted to that of the air, through a Power or a Sutherland law function of the temperature. A Power law is retained in this PhD thesis:

$$\mu = c_1\left(\frac{T}{T_{ref}}\right)^b \tag{5.25}$$

where c_1 is the reference viscosity at the temperature $T_{ref} = 475$ K, here set to 2.5034e-5; and $b = 0.6695$ is a model constant.

Determination of simplified transport coefficients for ARC The Prandtl and Schmidt numbers of certain species can exhibit strong variations across a flame front. These quantities also vary with the operating point and the type of combustion regime under consideration. As such, choosing a single value for an entire targeted range is not straightforward. If it is common practice to employ the burnt gases value at stoichiometry, this choice is not founded on theoretical grounds. Fig. 5.2 displays typical evolutions of species Schmidt numbers across 1D laminar premixed flames, for various equivalence ratio; while Fig. 5.3 displays the s_l evolution with equivalence ratio for different choice of Sc and Pr numbers. Operating conditions correspond to that of the FIRST configuration.

We see that despite the aforementioned variations of Sc and Pr numbers, predicted s_l remain fairly similar, whatever the chosen set of constants. The best solution that comes to mind is to formulate the problem as a constrained optimization problem, where the Sc and Pr would be allowed to vary in a small interval around their $\phi = 1$ value, for instance. No direct algorithm implementation of this method has been performed in this work; however the optimization was performed "by hand", with the laminar flame speed, burnt gas temperature, and integrated CO values as targeted quantities. The resulting set of parameters were given, for each ARC employed in this work, in the dedicated paragraphs of Chapter 4.

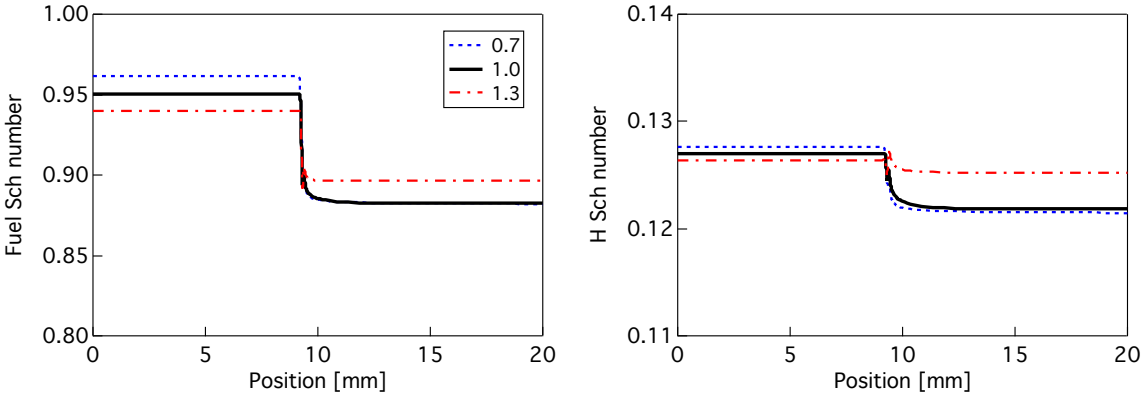

Figure 5.2: Evolution of a) C_2H_4 and b) H species Schmidt numbers across 1D laminar premixed flames at P = 3 atm and T_{ini} = 300 K. Computations with the ARC_18_C2H4NARA mechanism.

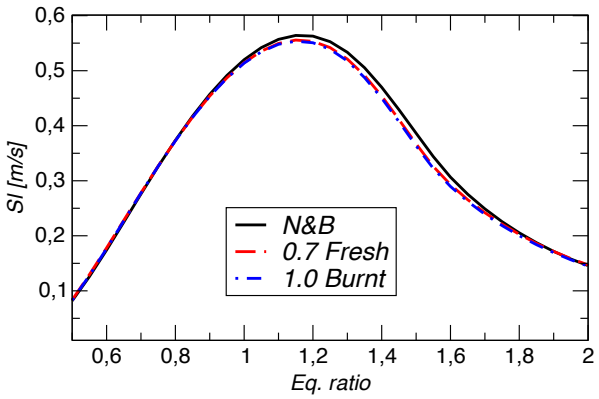

Figure 5.3: Evolution of laminar flame speed with equivalence ratio for different choice of species Schmidt numbers. P = 3 atm and T_{ini} = 300 K. Computations with the ARC_18_C2H4NARA mechanism.

Impact of the transport modelling An evaluation of the impact of employing the TranAVBP model instead of TranMix, in both CANTERA and AVBP (1D as well as 3D test cases), is presented in Chapter 7 of the PhD thesis of Jaravel (2016). It was found that global performances of laminar premixed flames were most affected by the choice of transport model on the rich side, a trend not necessarily retrieved in this study, were neither the lean nor the rich side are significantly impacted (see for example Fig. 4.30). Comparisons between species profiles obtained in CANTERA (any model) versus that in AVBP (TranAVBP) are, however, consistent with the findings of Jaravel (2016), were slight overshoots were observed for intermediate carbon species, especially in lean cases. This does not affect the major species profiles.

Chapter 6

Modeling of turbulent reactive flow

Contents

6.1 The Large Eddy Simulation (LES) formalism

6.1.1 The challenges induced by turbulence

In practice, all flows encountered in complex geometries are turbulent. They are characterized by the appearance of statistical fluctuations of all the N.-S. variables around their mean values. Macroscopically, the flow appears to be composed of vortices of various sizes and lifespan. One of the main challenge associated with the numerical resolution of these flow configurations is that the relevant range of length and time scales to consider is very exhaustive. This is all the more true when the flow is highly turbulent. A first evaluation of the degree of turbulence is provided by the Reynolds number $Re = \rho UL/\mu$, comparing inertia forces associated to the flow velocity U and length scale L, with viscous forces. When the Re is large, inertia forces are dominant and the flow is characterized by a wide variety of scales, from the largest at the integral length scale l_t to the smallest at the *Kolmogorov* scale η_k. The ratio of these length scales is better expressed in terms of a turbulent Reynolds number Re_T:

$$\frac{l_t}{\eta_k} = Re_T^{3/4} = \left(\frac{\rho u_t l_t}{\mu}\right)^{3/4} \tag{6.1}$$

where u_t is a measure of the turbulent velocity fluctuations.

The energy cascade Following the concept of the *energy cascade* introduced by Richardson (1922), energy is thought to be transferred by an inviscid process from the largest energetic scales to the smallest scales, where it eventually dissipates through viscous action. In this *dissipation zone*, centered around the Kolmogorov scale, the inertia forces and the viscous forces balance so that the Re number is of the order of unity. Central to this theory is the first similarity hypothesis of Kolmogorov, stating that the statistics of these small-scale motions have a universal form, uniquely determined by the kinematic viscosity ν and the dissipation rate ε. Given these two parameters, the Kolmogorov length, time and velocity scales are thus uniquely determined (Pope, 2000):

$$\eta_k = (\nu^3/\varepsilon)^{\frac{1}{4}} \tag{6.2}$$

$$\tau_k = (\nu/\varepsilon)^{\frac{1}{2}} \tag{6.3}$$

$$u_k = (\varepsilon\nu)^{\frac{1}{4}} \tag{6.4}$$

In between η_k and l_t, the second similarity hypothesis states that there exists an *inertial range*, where the statistics of the motion have a universal form uniquely determined by ε. In this range, the rate at which energy is transferred between eddies is independent of their length scale, and scales as ε. A schematic view of this energy cascade in a homogeneous isotropic turbulence is provided in phase space in Fig. 6.1. The energy density E is plotted versus the eddies wave numbers $k = 1/l$. The inertial range is characterized by a constant slope (in log-log scale) $E(k) \approx k^{-\frac{5}{3}}$.

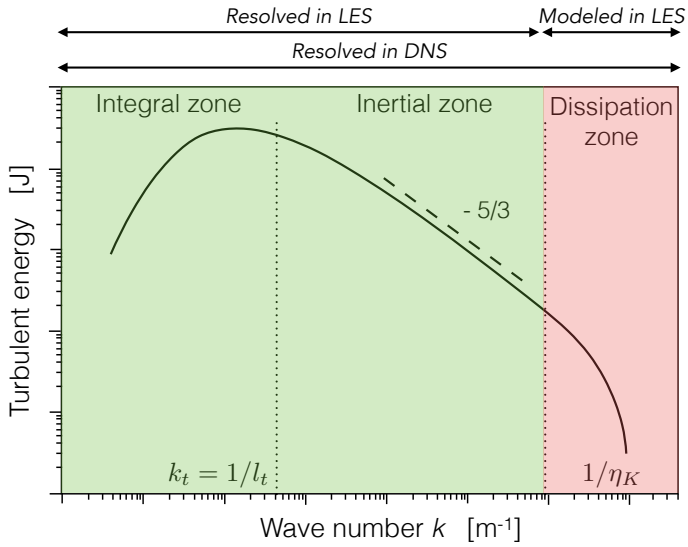

Figure 6.1: Sketch of density energy spectrum E(k) in a homogeneous isotropic turbulence, along with the distinction of the integral, inertial and dissipation zones.

Numerical approaches The numerical resolution of the N.-S. equations for the whole range of relevant length and time scales could be performed by Direct Numerical Simulation (DNS). However, from Eq. 6.1 we see that the number of mesh points required will approach $10^3 Re_T^{9/4}$, for a discretization of the Kolmogorov scales with $\approx$ 10 points in all directions. The total computational effort will eventually come up to scale with Re^3 for a homogeneous turbulence. Obviously, the DNS of realistic configurations characterized by high Re numbers, are currently out of reach. Some sort of simplification hypothesis have to be employed. An approach that has received a great amount of attention in the combustion community for the past twenty years is the Large Eddy Simulation (LES) approach.

In LES, a separation of the scales is assumed, between the largest turbulent scales that are completely resolved, and the smallest scales that must be modeled (see Fig. 6.1). LES is thus referred to as a *filtered* approach, for which subgrid-scale (sgs) closures must be provided. Due to the universal nature of the smallest scales, deriving

such models is expected to be facilitated. Furthermore, the prediction capability of LES is expected to be very high since a large part of the physics of the phenomena of interest in turbulent flows are associated with large scale and mid-scale motions, which are explicitly resolved.

6.1.2 The filtered reactive Navier-Stokes equations in LES

The balance equations for LES are obtained from the continuity and N.-S. equations (Eqs. 5.1-5.3) by convolution with a filtering operator of size Δ. When applied to a quantity $\mathcal{Q}$, the result is denoted by $\overline{\mathcal{Q}}$, and reads:

$$\overline{\mathcal{Q}(\mathbf{x},t)} = \int \mathcal{Q}(\mathbf{y},t)\mathcal{G}_\Delta(\mathbf{x}-\mathbf{y})\mathbf{dy} \tag{6.5}$$

Two types of LES can be distinguished, whether the filtering operation is applied explicitly to the conservation equations or results from a coarse mesh resolution. The latter is referred to as *implicit* LES and will be employed in this PhD thesis. In this case, Δ is approximately equal to the mesh size. When variable density effects are taken into consideration, a Favre averaged formulation is usually preferred to avoid the emergence of a source term in the filtered mass conservation equation (Poinsot & Veynante, 2005):

$$\widetilde{\mathcal{Q}} = \frac{\overline{\rho\mathcal{Q}}}{\overline{\rho}} \tag{6.6}$$

This formalism yields:

$$\frac{\partial\overline{\rho}}{\partial t} + \frac{\partial\overline{\rho}\widetilde{u}_i}{\partial x_i} = 0 \tag{6.7}$$

$$\frac{\partial\overline{\rho}\widetilde{u}_j}{\partial t} + \frac{\partial\overline{\rho}\widetilde{u}_i\widetilde{u}_j}{\partial x_i} = -\frac{\partial\overline{P}}{\partial x_j} + \frac{\partial}{\partial x_i}\left[\overline{\tau}_{ij} - \overline{\rho}(\widetilde{u_i u_j} - \widetilde{u}_i\widetilde{u}_j)\right] \quad \text{for } j = 1,3 \tag{6.8}$$

$$\frac{\partial\overline{\rho}\widetilde{Y}_k}{\partial t} + \frac{\partial\overline{\rho}\widetilde{u}_i\widetilde{Y}_k}{\partial x_i} = -\frac{\partial}{\partial x_i}\left[\overline{J}_{i,k} + \overline{\rho}(\widetilde{u_i Y_k} - \widetilde{u}_i\widetilde{Y}_k)\right] + \overline{\dot{\omega}}_k \quad \text{for } k = 1,N \tag{6.9}$$

$$\frac{\partial\overline{\rho}\widetilde{E}}{\partial t} + \frac{\partial\overline{\rho}\widetilde{u}_i\widetilde{E}}{\partial x_i} = -\overline{\frac{\partial u_i P}{\partial x_i}} - \frac{\partial}{\partial x_i}\left[\overline{q_i} + \overline{\rho}(\widetilde{u_i E} - \widetilde{u}_i\widetilde{E})\right] + \overline{\tau_{ij}\frac{\partial u_j}{\partial x_i}} + \overline{\dot{\omega}}_T \tag{6.10}$$

Closure must be provided for the filtered viscous ($\overline{\tau}_{ij}$, $\overline{J}_{i,k}$, $\overline{q_i}$) and turbulent (sgs) fluxes, as well as for the filtered source terms appearing in the RHS of these equations. Models for the fluxes are discussed in the rest of this Section, while turbulence-chemistry interaction models are the subject of Section 6.2.

6.1.3 Filtered viscous fluxes

The filtered viscous fluxes appearing in the LES governing equations are given by:

- **Laminar filtered stress tensor $\overline{\tau_{ij}}$**:

$$\overline{\tau_{ij}} = \overline{\mu\left(\frac{\partial u_i}{\partial x_j} + \frac{\partial u_j}{\partial x_i}\right) - \frac{2}{3}\mu\left(\frac{\partial u_k}{\partial x_k}\delta_{ij}\right)} \tag{6.11}$$

$$\text{approximation: } \overline{\tau_{ij}} \simeq \overline{\mu}\left(\frac{\partial\widetilde{u_i}}{\partial x_j} + \frac{\partial\widetilde{u_j}}{\partial x_i}\right) - \frac{2}{3}\overline{\mu}\left(\frac{\partial\widetilde{u_k}}{\partial x_k}\delta_{ij}\right) \tag{6.12}$$

$$\text{and: } \overline{\mu} \simeq \mu(\widetilde{T}) \tag{6.13}$$

- **Diffusive species flux vector** $\overline{J}_{i,k}$:

$$\overline{J}_{i,k} = \overline{-\rho\left(D_k\frac{W_k}{W}\frac{\partial X_k}{\partial x_i} - Y_k V_i^c\right)} \tag{6.14}$$

$$\text{approximation: } \overline{J}_{i,k} \simeq -\overline{\rho}\left(\overline{D}_k\frac{W_k}{W}\frac{\partial \widetilde{X}_k}{\partial x_i} - \widetilde{Y}_k\widetilde{V}_i^c\right) \tag{6.15}$$

$$\text{with: } \widetilde{V}_i^c = \sum_{k=1}^{N}\overline{D}_k\frac{W_k}{W}\frac{\partial \widetilde{X}_k}{\partial x_i} \tag{6.16}$$

$$\text{and: } \overline{D}_k \simeq \frac{\overline{\mu}}{\overline{\rho}Sc_k} \tag{6.17}$$

- **Filtered heat flux** $\overline{q}_i$:

$$\overline{q_i} = \overline{-\lambda\frac{\partial T}{\partial x_i} + \sum_{k=1}^{N}J_{i,k}h_{s,k}} \tag{6.18}$$

$$\text{approximation: } \overline{q_i} \simeq -\overline{\lambda}\frac{\partial \widetilde{T}}{\partial x_i} + \sum_{k=1}^{N}\overline{J}_{i,k}\widetilde{h}_{s,k} \tag{6.19}$$

$$\text{with: } \overline{\lambda} \simeq \frac{\overline{\mu}\overline{C_p}(\widetilde{T})}{Pr} \tag{6.20}$$

where simple gradient assumptions have been employed.

6.1.4 Turbulent sgs fluxes closure

The unresolved scales effect on the filtered quantities appearing in Eqs. 6.7-6.10 must be modeled. Sgs closures are given by:

- **Unresolved Reynolds tensor** $\overline{\tau}_{ij}^{sgs} = -\overline{\rho}(\widetilde{u_i u_j} - \widetilde{u}_i\widetilde{u}_j)$:

$$\overline{\tau}_{ij}^{sgs} = \overline{\rho}\nu_t\left(\frac{\partial \widetilde{u}_j}{\partial x_i} + \frac{\partial \widetilde{u}_i}{\partial x_j}\right) - \frac{2}{3}\overline{\rho}\nu_t\left(\frac{\partial \widetilde{u}_k}{\partial x_k}\delta_{ij}\right) \tag{6.21}$$

  where ν_t is the sgs kinematic viscosity for which various expressions have been established (see Section 6.1.5).

- **Unresolved species fluxes** $\overline{J}_{i,k}^{sgs} = \overline{\rho}(\widetilde{u_i Y_k} - \widetilde{u}_i\widetilde{Y}_k)$:

$$\overline{J}_{i,k}^{sgs} = -\overline{\rho}\left(D_k^t\frac{W_k}{W}\frac{\partial \widetilde{X}_k}{\partial x_i} - \widetilde{Y}_k\widetilde{V}_i^{c,t}\right) \tag{6.22}$$

$$\text{with: } \widetilde{V}_i^{c,t} = \sum_{k=1}^{N}D_k^t\frac{W_k}{W}\frac{\partial \widetilde{X}_k}{\partial x_i} \tag{6.23}$$

$$\text{and: } D_k^t = \frac{\mu_t}{\rho Sc_k^t} \tag{6.24}$$

  where Sc_k^t is the turbulent Schmidt number of species k, fixed to a value of 0.6 for each species in the present work.

- **Unresolved energy flux** $\overline{q}_i^{sgs} = \overline{\rho}(\widetilde{u_i E} - \widetilde{u}_i\widetilde{E})$:

$$\overline{q}_i^{sgs} = -\lambda_t\frac{\partial \widetilde{T}}{\partial x_i} + \sum_{k=1}^{N}\overline{J}_{i,k}^{sgs}\widetilde{h}_{s,k} \tag{6.25}$$

$$\text{with: } \lambda_t = \frac{\mu_t\overline{C}_p}{Pr^t} \tag{6.26}$$

  where Pr^t is the turbulent Prandtl number chosen equal to 0.6 in the present work.

6.1.5 Modeling of the sgs stress tensor

LES models for the sgs stress tensor (Eq. 6.21) generally rely on the assumption that the effect of the sgs on the resolved field is purely dissipative (Boussinesq (1877) hypothesis). This assumption is essentially valid within the cascade theory introduced by Kolmogorov (1941). The most usual models are further derived on the theoretical ground that the LES filter is spatially and temporally invariant. Two models falling into this category are employed in the present work. They both rely on the introduction of a turbulent kinematic viscosity, ν_t, and only differ through its expression: the WALE (Wall Adapting Local Eddy-viscosity) and the SIGMA model. Other models are implemented in AVBP, a description of which can be found, e. g., in the AVBP Handbook [1]. Noteworthy is the classical Smagorinsky model (Smagorinsky, 1963) which has been widely employed in various configurations (and fields !), but is known to be too dissipative and will therefore not be employed in the present work.

- **The WALE model**

$$\nu_t = (C_w \Delta_x)^2 \frac{(s^d_{ij} s^d_{ij})^{3/2}}{(\widetilde{S}_{ij}\widetilde{S}_{ij})^{5/2} + (s^d_{ij} s^d_{ij})^{5/4}} \tag{6.27}$$

with

$$s^d_{ij} = \frac{1}{2}(\widetilde{g}^2_{ij} + \widetilde{g}^2_{ij}) - \frac{1}{3}\widetilde{g}^2_{kk}\delta_{ij} \tag{6.28}$$

and

$$\widetilde{S}_{ij} = \frac{1}{2}\left(\frac{\partial \widetilde{u}_j}{\partial x_i} + \frac{\partial \widetilde{u}_i}{\partial x_j}\right) \tag{6.29}$$

where $C_w = 0.4929$ is the model constant and $\widetilde{g}_{ij}$ is the resolved velocity gradient. The WALE model was developed by Nicoud & Ducros (1999) for wall bounded flow in an attempt to recover the correct scaling laws in near wall regions. The main drawback associated with this model is that sgs viscosity will activate in regions of solid rotation, such as near the exit of a swirled injection system.

- **The SIGMA model** is based on singular values (σ_1, σ_2 and σ_3) of a tensor built using resolved velocity gradients:

$$\nu_t = (C_\sigma \Delta_x)^2 \frac{\sigma_3(\sigma_1 - \sigma_2)(\sigma_2 - \sigma_3)}{\sigma_1^2} \tag{6.30}$$

where $C_\sigma = 1.35$ is the model constant. This operator was proposed by Nicoud *et al.* (2011) to overcome some drawbacks observed in most of the static models, such as the one discussed in the WALE section. Indeed, it presents the interesting property to vanish in various laminar flow configurations (pure shear, pure rotation, pure dilatation/contraction, ...), in good accordance with the expected behavior. Like the WALE model, it will also vanish with the proper asymptotic behavior near solid boundaries.

6.2 Turbulence-chemistry interactions

6.2.1 Classification of the turbulent combustion regimes

The modeling of the filtered source terms appearing in Eqs. (6.9)-(6.10) requires to have an idea of the regime of combustion, i. e., the degree to which fuel and oxidant are mixed and the relative intensity of the turbulence to that of the chemistry. This usually requires some sort of classification of the different regimes, in terms of characteristic length and timescales. The first distinction that is usually considered in choosing a model is whether the fuel and oxidant are provided together in a premixed or partially premixed fashion or if they are fed separately to the reaction zone. The limiting cases are the canonical *premixed* and *diffusion* flames that were introduced in Section 4.2.

[1] http://cerfacs.fr/∼ avbp/AVBP_V6.X/HANDBOOK

6.2.1.a Premixed turbulent combustion

A premixed flame front can be characterized in this context by its *diffusive* thickness δ and by its velocity s_l^0, yielding a characteristic timescale:

$$\tau_c = \frac{\delta}{s_l^0} \tag{6.31}$$

This corresponds roughly to the time required for the flame front to propagate over its own thickness. At the same time, the flame interacts with eddies crossing its path. The degree to which the flame front is perturbed by these encounters depends as a first approximation on the ratio of characteristic timescales:

$$Da = \frac{\tau_t}{\tau_c} = \frac{l_t}{\delta}\frac{s_l^0}{u_t} \tag{6.32}$$

$$Ka = \frac{\tau_c}{\tau_K} \tag{6.33}$$

Where $\tau_t = l_t/u_t$ is the characteristic timescales of the most energetic turbulent structures (integral scale) and $\tau_K = \eta_K/u_K$ is that of the smallest structures (Kolmogorov scale). Da is the *Damköhler* number and Ka is the *Karlovitz* number. Using the relation $s_l^0 \approx \mu/\rho\delta$ -stemming from a Prandtl number of the order of unity yielding $\mu/\rho \approx D^{th}$, and the relations (6.2)-(6.4), the Ka number can be assimilated to a length scale ratio:

$$Ka = \frac{\delta}{s_l^0}\frac{\eta_K}{u_K} = \left(\frac{\delta}{l_K}\right)^2 \tag{6.34}$$

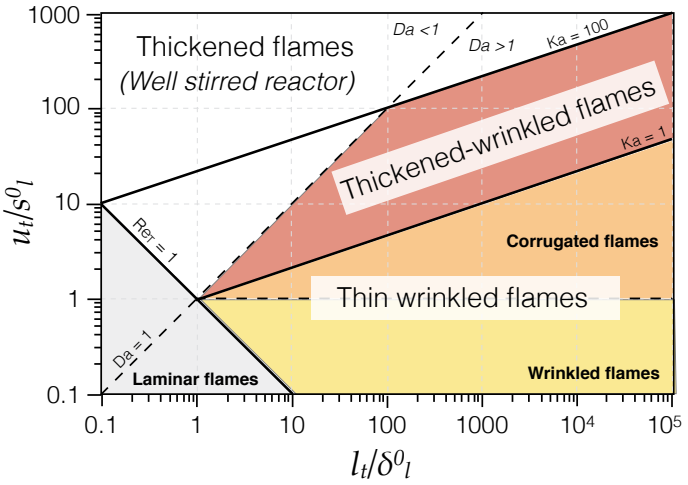

Figure 6.2: Turbulent combustion regimes in terms of length and velocity scales, adapted from Borghi (1988); Peters (1999).

Several cases must be distinguished depending upon the values assumed by these numbers:

- For high Damköhler numbers ($Da >> 1$) the chemistry is fast enough so that the internal structure of the flame front does not have enough time to be modified by the turbulent eddies. However, the flame front might be stretched and corrugated by the flow. The reaction zone is then assimilable to a collection of thin "flamelet" elements.
- For small Damköhler numbers ($Da << 1$) the turbulent timescale being much faster than the chemical timescale, the reactants and products have enough time to mix together before reaction. The limiting case is assimilable to a well stirred reactor.
- For high Karlovitz numbers, the flame is significantly thicker than the smallest Kolmogorov eddies, which are then susceptible to penetrate in the reaction zone. If $1 < Ka < 100$ then these eddies are able to interfere with the preheat zone; and if $Ka > 100$ then they can interfere with the whole flame front.

As the Ka, Da and Re_T numbers are linked, the transitions between regimes can be characterized by only two of them. Further, as Ka can be re-expressed as:

$$Ka = \left(\frac{u_t}{s_l^0}\right)^{3/2} \left(\frac{l_t}{\delta}\right)^{-1/2} \tag{6.35}$$

and Re_T as:

$$Re_T = \left(\frac{u_t}{s_l^0}\right) \left(\frac{l_t}{\delta}\right) \tag{6.36}$$

A premixed combustion diagram ("Borghi" diagram) with all information can be constructed in function of l_t/δ and u_t/s_l^0, see Fig. 6.2. The internal structure of flames belonging to each category presented in the combustion diagram are illustrated on Fig. 6.3. The turbulent flame thickness δ_T^0 is here identified as the region between the mean temperatures of 300 and 2000 K. δ_T^0 is decomposed into a mean preheat and a mean reaction zone. Small structures are able to penetrate in the preheat zone whenever $Ka > 1$. The review of Borghi (1988) provides a complete and accessible description of the premixed regimes.

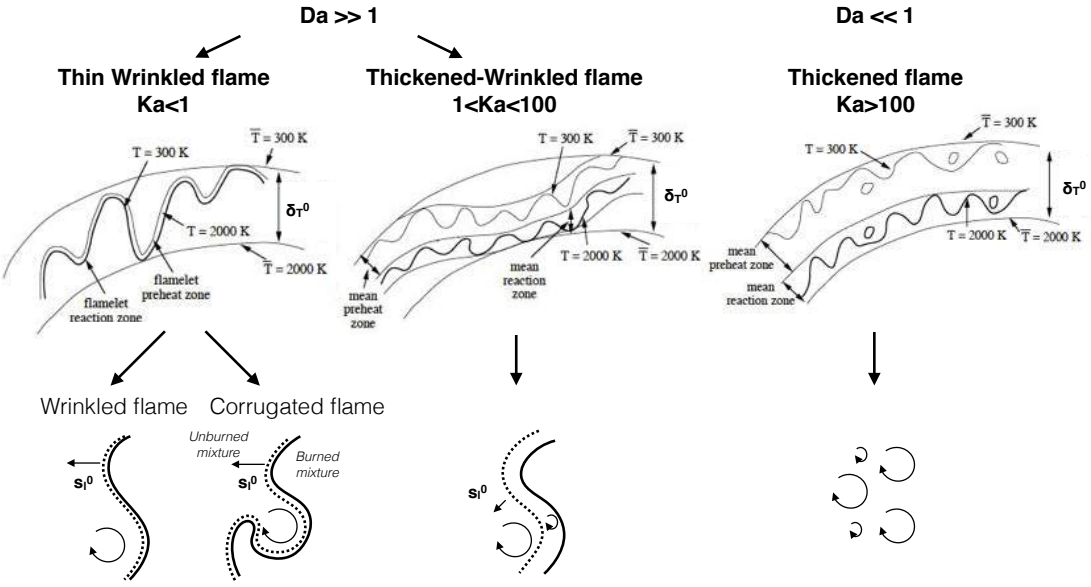

Figure 6.3: Turbulent premixed combustion regimes illustrated in a case where the fresh and burnt gas temperatures are 300 and 2000 K respectively, adapted from Poinsot & Veynante (2005)

Of course, it is emphasized that these are only qualitative observations, based on many simplifications. In particular, unsteady effects and multi-species chemistry might complicate the picture.

6.2.1.b Diffusion turbulent combustion

It was stressed in Section 4.2 that diffusion flames are very sensitive to the flow field. A flow field Damköhler number Da^{fl} comparing flow and chemistry time scales can be defined as:

$$Da^{fl} = \frac{\tau_f}{\tau_c} \tag{6.37}$$

where $\tau_f = 1/\chi_{st}$, and the chemical time scale τ_c is related to the reaction thickness, but has no general expression. Asymptotic theory proves that this Damköhler number relates the flame reaction and diffusion length scales (Linan, 1974):

$$\frac{\delta_r}{\delta_d} = (Da^{fl})^{-1/a} \tag{6.38}$$

were $a = \nu'_F + \nu'_O + 1$ is obtained from the stoichiometric coefficients of the global fuel/oxidizer reaction. The different length scales are illustrated in Fig. 6.4 (a), and were defined in Section 4.2.

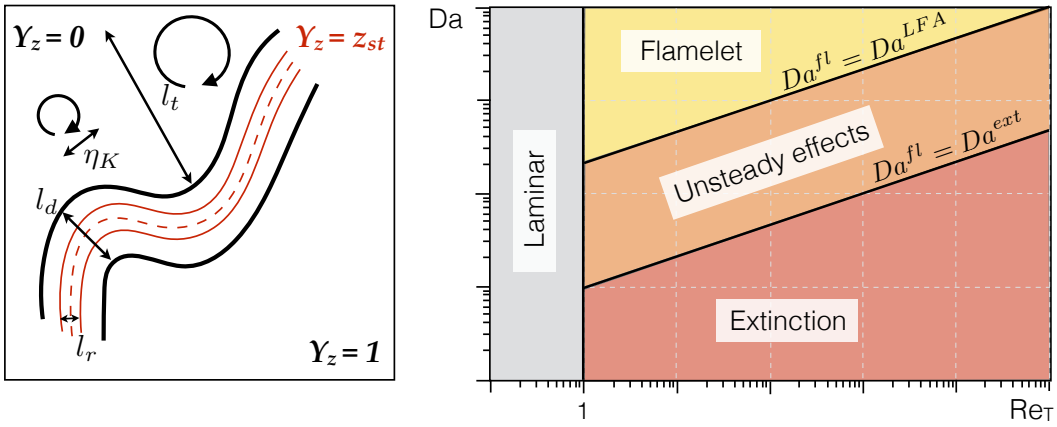

Figure 6.4: a) Illustration of the turbulent diffusion flame length scales and b) non-premixed combustion regimes function of the turbulent Reynolds number and the Damköhler number (Cuenot & Poinsot, 1994; Veynante & Vervisch, 2002)

The Da^{fl} has been identified by Cuenot & Poinsot (1994) as an important controlling parameter in non-premixed configurations, that can be employed to characterize the ability of turbulent vortices to modify the structure of laminar diffusion flames. This study introduces several transitional Damköhlers:

- For $Da^{fl} > Da^{FLA}$, the chemistry is very fast and the laminar flame keeps its laminar structure. LFA stands for Laminar Flamelet Assumption.
- For $Da^{ext} < Da^{fl} < Da^{FLA}$ the flame structure is modified but the diffusion flame is not quenched because of unsteady effects.
- For $Da^{fl} < Da^{ext}$ the flame cannot sustain the too high strain and quenches.

These informations can be reported in a diagram such as the one presented in Fig. 6.4. The controlling parameters chosen to identify the different regimes are the turbulent Reynolds number Re_T and the original Da number which are related through $Da \approx \alpha\sqrt{Re_T Da^{fl}}$, where α is a proportionality factor (Veynante & Vervisch, 2002).

6.2.1.c Summary

The first conclusion that can be drawn from looking at both combustion diagrams is that for a sufficiently high Da, the flow can be assimilated to a collection of thin flamelets (either premixed or non-premixed). In fact, most combustion applications are believed to fall into that category. Note that the popular premixed/non-premixed tabulated chemistry description discussed in Section 3.3.2, and employed in many simulations throughout the literature, are supposedly only valid in this regime. Usual models for turbulence-chemistry interactions can thus be classified into two main categories: the ones assuming an infinitely thin reaction zone, exclusively developed for applications falling within the flamelet regimes; and the ones that attempt to account for the reaction zone, supposedly valid over a larger portion of the combustion diagrams.

Belonging to the first category, are almost exclusively models for premixed turbulent combustion applications. One notable exception, amongst the pioneering models, is the Eddy Dissipation Model (EDM) of Magnussen & Hjertager (1977) based on the earlier Eddy Break-up Model concept of Spalding (1977). This model postulates that the local state of turbulence has a strong influence on the local rate of reaction, through molecular mixing, and is thus often the rate limiting phenomenon. The EDM is valid for both premixed and non-premixed configurations; however, its use in the LES community is limited (Hu *et al.*, 2006; Stein *et al.*, 2013). Another model worth mentioning is the level-set method, based on the G-equation proposed by Williams (1985*b*), and later reformulated for LES by Pitsch & de Lageneste (2002) and Pitsch (2005), based on a formulation of Peters (1999). The G-equation describes the motion of an iso-scalar surface separating the domain into a region of fresh mixture and a region of burnt gases. The formulation from Pitsch (2005), improved by Moureau *et al.* (2009) is valid over both the thin wrinkled flame and the thickened-wrinkled flames premixed regimes. However, probably due to a somewhat involved formulation when trying to solve simultaneously for the flame structure, its use in LES is also sparse. Noteworthy are the papers from Knudsen *et al.* (2010, 2015), performing LES by coupling the G-equation with a partially-premixed tabulated chemistry description to ensure a sufficient flame front resolution. Bearing

some resemblance with the G-equation is the Flame Surface Density description (Vervisch *et al.*, 1995; Hawkes & Cant, 2000; Ma *et al.*, 2014), where the flame is also identified as a surface, subject to straining and curvature effects. The flame surface density $\sum$ is introduced, for which an equation has to be solved, providing direct closure for the reaction rates. As we will see shortly, similarly to the G-equation, the FSD can be employed in conjunction with other models to include information lost in the LES filtering. In this case, when recast as a flame wrinkling, it can be employed as an *efficiency* function to retrieve the lost sgs flame surface.

Models of the second type are of more interest in this PhD thesis, since the objective is to model complex chemistry effects, a feature that a model based on a thin reaction front could not allow easily. Introduced as early as in the 80's in the context of turbulent reacting flows by O'Brien (1980), PDF models, a subset of which were discussed at length in the Introduction, allow to cover practically any regime of interest, and are therefore the subject of a very active and diverse field of research. These combustion models are especially well suited to tabulated chemistry descriptions, but they have been coupled to other chemistry descriptions (e.g., within the CMC framework or through resolved PDF approaches, Section 1.3.3). A review on the use of PDF method in LES can be found, e.g., in Veynante & Vervisch (2002) or more recently in Haworth (2010). The first of these review also provides an overview of many other turbulence-chemistry interaction models. Another possibility, as underlined in Section 1.3.3, is to artificially thicken the reaction zone. The basic idea of this approach, proposed by Butler & O'Rourke (1977), is to consider a flame thicker than the actual one, but having the same laminar flame speed. It is supposedly valid over the entire premixed combustion diagram, but care must be taken in that the interaction between turbulence and chemistry may be modified, since the Da number is decreased (see Eq. 6.32). As such, a model to recover the lost turbulence-chemistry information should be employed. The most common approach relies upon an estimation of the flame wrinkling.

The Artificially Thickened Flame combustion model for LES (DTFLES) that is employed in this PhD thesis (see Section 6.2.2), was formulated for LES by Colin *et al.* (2000). Both configurations studied in this work exhibit premixed and diffusion structures, but the premixed regime is always largely dominant in zones were large thickening factors are required. Additionally, when diffusion structures are encountered, they are almost always identified as such by the model, which is able to deactivate. Indeed, work under progress in the context of another PhD thesis by Shum-kivan (2017) suggests that non-premixed flames adapt to the local grid spacing, and do not require special treatment (at least for the mesh sizes under consideration in this work). Finally, many studies have employed the DTFLES on partially premixed configurations successfully Legier *et al.* (2000); Franzelli *et al.* (2012); Esclapez *et al.* (2015); Jaravel *et al.* (2016). For all those reasons, this model is believed to be well suited in the present context. A more in-depth discussion about the DTFLES method and its implementation in the LES solver AVBP is provided hereafter.

6.2.2 The Dynamically Thickened Flame model for LES (DTFLES)

6.2.2.a Original method

The basic idea of this approach is to consider a flame thicker than the actual one, but having the same laminar flame speed. This done through rescaling of time and space:

$$x \mapsto \mathcal{F}x \quad t \mapsto \mathcal{F}t \tag{6.39}$$

corresponding to a thickening of the reaction zone by a factor $\mathcal{F}$, obtained by:

$$\dot{\omega}_k \mapsto \frac{\dot{\omega}_k}{\mathcal{F}} \tag{6.40}$$

for each species k. The diffusivities are accordingly multiplied by the same factor:

$$D_k \mapsto \mathcal{F}D_k \quad D_{th} \mapsto \mathcal{F}D_{th} \tag{6.41}$$

in order to recover the right s_l^0 (see Section 4.2):

$$s_l^0 \propto \frac{D_{th}}{\delta_l} = \frac{\mathcal{F}D_{th}}{\mathcal{F}\delta_l} \tag{6.42}$$

Gradients across the flame are decreased, species profiles are broadened, allowing a sufficient level of resolution on a coarse grid. Maximum values of heat release and reaction rates are lowered, but integrals across the flame front are conserved.

Now, applying a uniform thickening in the whole domain accelerates diffusion in non reactive zones, where the thickening is not necessary. A Dynamically Thickening procedure, depending on the flame position and the local resolution is therefore preferred (DTFLES method of Legier *et al.* (2000)). The thickening factor $\mathcal{F}$ is now evaluated locally, based upon the values of a sensor $\mathcal{S}$ detecting the presence of a reaction front:

$$\mathcal{F} = 1 + (\mathcal{F}_{max} - 1)\mathcal{S} \tag{6.43}$$

where $\mathcal{F}_{max}$ depend upon the local resolution Δ_x, and is specified such that at least n points discretize the flame front:

$$\mathcal{F}_{max} = \frac{n\Delta_x}{\delta_l} \tag{6.44}$$

n is the minimum number of points required to properly describe the flame front, and should usually be of the order of 5. The flame thickness δ_l is extracted from canonical test cases. For an irreversible one-step reaction chemistry, $\mathcal{S}$ is solely dependent upon both the local temperature and the reactants mass fractions, through a modified reaction rate Ω_{irr}:

$$\Omega_{irr} = Y_F^{n_F} Y_O^{n_O} exp\left(-\Gamma \frac{E_a}{RT}\right) \tag{6.45}$$

where Γ is a constant introduced to extend the sensor to the preheat region. To detect reaction zones, identified as the regions where Ω_{irr} is *significant*, $\mathcal{S}$ compares Ω_{irr} to that obtained from canonical one-dimensional test cases:

$$\mathcal{S} = tanh\left(\beta' \frac{\Omega_{irr}}{\Omega_{1D,irr}}\right) \tag{6.46}$$

where $\beta' \approx 50$.

This classical methodology suffers from mainly two drawbacks:

- Since the laminar flame front is thickened, its interaction with turbulence is modified, as small vortices cannot wrinkle the flame front anymore. As a result, the flame surface is reduced, and the flame consumption, in particular, is underestimated.
- A generalization of $\mathcal{S}$ is necessary when working with reduced multi-step chemistries, by taking into account via the sensor the fact that several reactions might now be of importance in detecting the flame front.

Both points are addressed in what follows.

6.2.2.b An efficiency function to retrieve the lost sgs flame surface

To compensate for the lost sgs flame wrinkling, an efficiency function $\mathcal{E}$ is employed, allowing to recover the correct turbulent flame burning:

$$\dot{\omega}_k \mapsto \frac{\mathcal{E}\dot{\omega}_k}{\mathcal{F}} \tag{6.47}$$

and

$$D_k \mapsto \mathcal{E}\mathcal{F}D_k \quad D_{th} \mapsto \mathcal{E}\mathcal{F}D_{th} \tag{6.48}$$

such that:

$$s_l^0 \mapsto \mathcal{E}s_l^0 \tag{6.49}$$

This function has been developed from Direct Numerical Simulations (DNS) results. It is defined as the ratio between the wrinking of the unthickened flame of thickness δ_l and that of the thickened flame of thickness $\mathcal{F}\delta_l$:

$$\mathcal{E} = \frac{\Xi(\delta_l)}{\Xi(\mathcal{F}\delta_l)} \tag{6.50}$$

Several formulations exist for the wrinkling function Ξ. In this work, the Colin efficiency function is employed (Colin *et al.*, 2000):

$$\Xi = 1 + \alpha(Re_T)\Gamma\left(\frac{\Delta_e}{\delta_l}\frac{u'_{\Delta_e}}{s_l^0}\right)\frac{u'_{\Delta_e}}{s_l^0} \tag{6.51}$$

where Δ_e is the size of the effective filter and Γ is a function taking into account the sgs strain rate of all length scales smaller than Δ_e. The effective filter size is usually larger than the mesh grid size. Accordingly, u'_{Δ_e} is not the common subgrid scale LES turbulent velocity, and requires further modeling assumptions. A similarity assumption is retained, and some work goes into a formulation that removes the dilatational part of the velocity field (see Colin *et al.* (2000) for details).

6.2.2.c A modified sensor for reduced multi-step chemistries

The approach proposed by B. Franzelli A sensor for multi-step chemistry was developed in the PhD. thesis of (Franzelli, 2011), based on the consumption/production rate of a subset of important species k:

$$\mathcal{S} = min\left(\frac{\dot{\omega}_k}{\dot{\omega}_{1D,k}}, 1\right) \tag{6.52}$$

In order to capture the preheat region, the sensor is first *clipped*:

$$\mathcal{S} = 1 \quad if \quad \mathcal{S} > 0.01 \tag{6.53}$$

before a series of *filtering operations* are applied. The resulting sensor is sufficiently large to encompass the relevant reaction zone, see Fig 6.5. The main drawback of this technique is its CPU cost. Indeed, the filtering

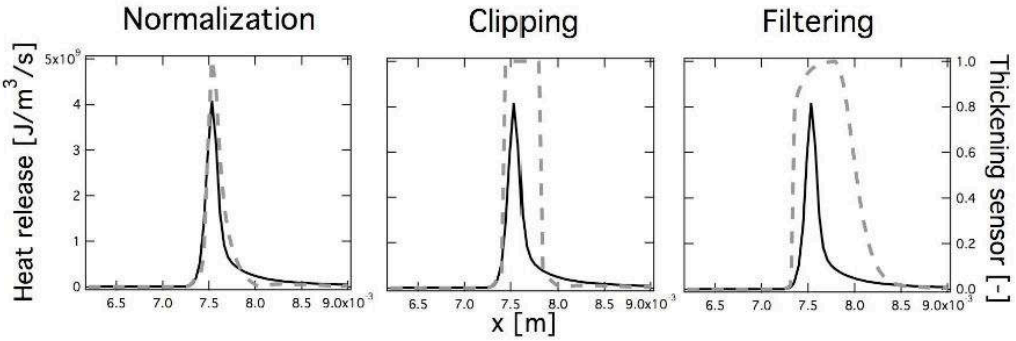

Figure 6.5: Construction of the sensor for multi-step chemistries, from Franzelli (2011). In black : Heat release rate, in grey: sensor.

operations have to be performed at least 5 times. The task is further complicated by the high partitioning on parallel architectures because of the increased MPI communications. As pointed out by Jaravel (2016), another issue comes from the fact that this method is not easily parametrizable, so that providing a set of guidelines to follow whenever a new chemistry is employed is not straightforward. To remedy these drawbacks, an improved method has been developed in the PhD thesis of Jaravel (2016), and is now briefly outlined.

The approach proposed by T. Jaravel The steps to follow are similar to that just presented:

- Construct a sensor localized around the highly reacting inner flame region
- Enlarge its width by a spatial filtering operation

It is argued that employing the fuel source term to construct the sensor results in an optimal shape, not extending too much into the post-flame region, where the grid resolution is usually sufficient in practice. Furthermore, the shape of a sensor based on the fuel source term is also more conveniently controlled than a sensor based on the

heat release rate (see Jaravel (2016)). To detect the reaction zone, the sensor is here also based on comparisons with 1D values:

$$\mathcal{S} = max\left[min\left(2\mathcal{F}_{max}\frac{|\dot{\omega}_F|}{|\dot{\omega}_{1D,F}|} - 1, 1\right), 0\right] \tag{6.54}$$

Actually, this sensor bears many resemblance with Eq. 6.46, where the function *tanh* has been replaced by clipping the function $x \mapsto (2x-1)$; and an adequate value for β' has been identified as being equal to $2\mathcal{F}_{max}$. This sensor correctly identifies the flame zone, but is spatially too narrow and does not, in particular, encompass the preheat region.

An efficient way to enlarge the sensor is provided by introducing a passive scalar $\psi(\mathbf{x})$ with specific diffusive properties D_ψ; and forcing it to follow the sensor's shape by employing a sensor-constrained relaxation source term $\dot{\omega}_\psi$:

$$\frac{\partial \rho\psi}{\partial t} + \nabla\cdot(\rho\mathbf{u}\psi) = \nabla\cdot(\rho D_\psi \nabla\psi) + \rho\dot{\omega}_\psi \tag{6.55}$$

with:

$$\dot{\omega}_\psi = \frac{\psi_0 - \psi(\mathbf{x})}{\tau_0} \quad if \quad \mathcal{S}(\mathbf{x}) > 0.8 \tag{6.56}$$

$$\dot{\omega}_\psi = \frac{0 - \psi(\mathbf{x})}{\tau_1} \quad if \quad \mathcal{S}(\mathbf{x}) < 0.05 \tag{6.57}$$

ψ_0 is the maximum value of $\psi(\mathbf{x})$. The larger τ gets, the slower the relaxation is towards the desired value. Since the goal is to force ψ to follow the sensor in the reaction front (when $\mathcal{S}(\mathbf{x}) > 0.8$), but to encompass a larger region, τ_1 should be significantly larger than τ_0. Specifically, since the passive scalar should encompass the preheat region, it is possible to add a temperature dependance to the source term, yielding:

$$\dot{\omega}_\psi = \frac{0 - \psi(\mathbf{x})}{\tau_{1,b}} \quad if \quad \mathcal{S}(\mathbf{x}) < 0.05 \quad and \quad T > 1600K \tag{6.58}$$

$$\dot{\omega}_\psi = \frac{0 - \psi(\mathbf{x})}{\tau_{1,f}} \quad if \quad \mathcal{S}(\mathbf{x}) < 0.05 \quad and \quad T \leqslant 1600K \tag{6.59}$$

with $\tau_{1,f} >> \tau_{1,b}$. The final sensor reads:

$$\hat{\mathcal{S}} = max[min(\psi(\mathbf{x}), 1), \mathcal{S}(\mathbf{x})] \tag{6.60}$$

It is summarized in Fig. 6.6. From a numerical point of view, ψ is initialized with $\mathcal{S}$ before being advanced with the transport Eq. 6.55 at each iteration, leading to a shape like the one shown in Fig. 6.6. The filtered sensor is obtained by clipping, as displayed in green, at each iteration.

To sum-up, the controlling parameters of the sensor width $\Delta_{\hat{\mathcal{S}}}$ are:

- Its maximum value ψ_0
- Its diffusivity D_ψ
- The relaxation factor τ_0 towards the maximum value in the flame front
- The relaxation factor τ_1 towards 0 outside of the flame front, which can eventually take two different values depending on whether the relaxation is towards the fresh or burnt gases

$\Delta_{\hat{\mathcal{S}}}$, the sensor width, is linked to these controlling parameters through the following relation:

$$\Delta_{\hat{\mathcal{S}}} \propto \sqrt{D_\psi \tau_1} log(\psi_0) \tag{6.61}$$

We see that the value of τ_0 does not enter this formulation. It is chosen to be $\approx 10\Delta_t$ for stability reasons. Also, the dependence upon the maximum value ψ_0 is very weak, and it is fixed to a value of 20 in the present work.

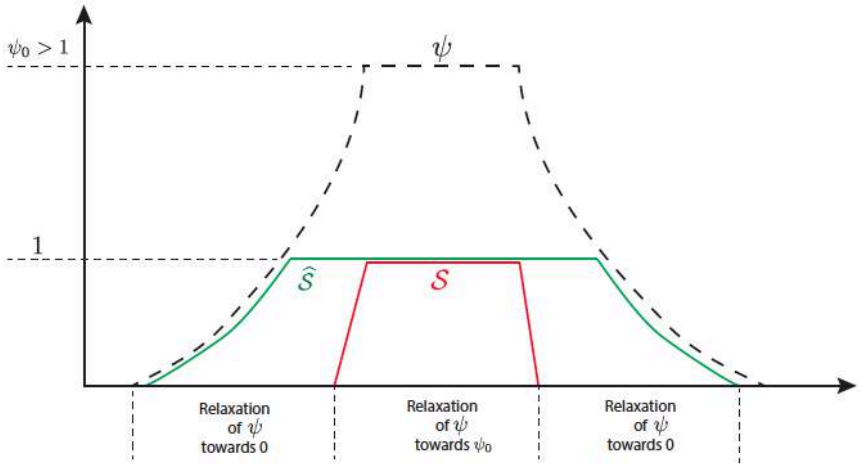

Figure 6.6: Illustration of the principle of the sensor filtering procedure, from Jaravel (2016).

Eventually, we see that the sensor can be controlled by only two parameters: the relaxation factor τ_1 and the diffusivity of ψ. These parameters can be related to premixed flame characteristics, by introducing two scaling numbers α and β:

$$\tau_1 = \alpha\tau_c = \alpha\frac{\delta}{s_l^0} \tag{6.62}$$

$$D_\psi = \beta D_{th} \tag{6.63}$$

Substituted into Eq. 6.61, these numbers lead to:

$$\Delta_{\hat{\mathcal{S}}} \propto \sqrt{\beta\alpha}\sqrt{\frac{\delta}{s_l^0}D_{th}} \tag{6.64}$$

and, with the relation $\delta = D_{th}/s_l^0$ (see Section 4.2), to:

$$\frac{\Delta_{\hat{\mathcal{S}}}}{\delta} \propto \sqrt{\beta\alpha} \tag{6.65}$$

This rewriting allows to obtain a sensor which scales directly with the flame thickness, enabling the generalization of the procedure: choosing a specific α and β completely determine the sensor's behavior, regardless of the local conditions, or local thickness factor $\mathcal{F}$, since applying the DTFLES correction to Eq. 6.55 leads to:

$$\Delta_{\hat{\mathcal{S}}} \propto \sqrt{\beta\alpha}\mathcal{F}\delta \tag{6.66}$$

A thorough analysis of the sensitivity of the sensor to α and β is provided in the PhD thesis of Jaravel (2016). It was verified in practice that the asymptotic relation Eq. 6.66 holds perfectly in the burnt gases; meaning, whenever one of the parameters is divided by r, the sensor width is accordingly divided by $\sqrt{r}$. However, the situation is less perfect in the cold side, where $\Delta_{\hat{\mathcal{S}}}$ is reduced by more than a factor $\sqrt{r}$. It is illustrated on Fig 6.7, where a normalized temperature profile across a thickened premixed methane/air laminar flame computed with AVBP is plotted. The dotted line represents the baseline $\hat{\mathcal{S}}$, and the dashed dotted line is the modified sensor for D_ψ divided by 4, i. e., β divided by 4. It was also verified that the shape of the sensor adapts itself to the flame region whenever the thickening factor $\mathcal{F}$ is modified but the controlling parameters are kept constant, accordingly with Eq. 6.66.

This methodology will be employed throughout this PhD thesis. Values for α and β will be specified at a later time. The diffusivity D_ψ is chosen equal to that of the fastest diffusive species in the kinetic mechanism under consideration, usually, the H atom.

It is emphasized that, while this sensor provides a very convenient framework, it requires to transport an additional species. In that regard, that the CPU gain when compared to the method of B. Franzelli is not always clear in practice. Another method, based upon geometrical considerations, is currently under development at CERFACS, in the PhD thesis of B. Rochette.

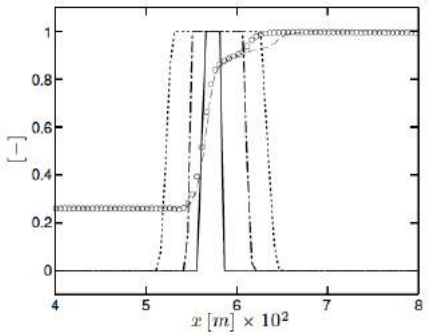

Figure 6.7: Normalized temperature profile across a thickened 1D unstrained premixed methane/air laminar flame, from Jaravel (2016). Solid line : unfiltered sensor, dotted line: baseline filtered sensor, dashed-dotted line: modified filtered sensor.

6.3 The LES code AVBP

6.3.1 Presentation

The development of the AVBP solver started in the mid-nineties on the initiative of Schönfeld & Rudgyard (1999). The goal was to develop an efficient code handling unstructured grids of any element type in order to study complex geometries. It has grown to become a massively-parallel code solving the compressible reacting N.-S. equations. AVBP is originally based on an explicit *Cell-Vertex* Finite Volume formulation (Rudgyard, 1993) where the solution variables are stored at the nodes but the flux integration is computed on the cells. The cell residuals are then distributed back to the nodes in order to obtain the updated solution. This constitutes the *Gather-Scatter* operation. From this perspective, *Cell-Vertex* schemes have a close affinity with weighted residual Finite Element methods (Morton & Paisley, 1989), and Colin & Rudgyard (2000) took advantage of this to implement FE schemes in AVBP. Over the last decade, AVBP has been optimized to have a good scalability on thousands of processors on various machine architectures, allowing to have a reasonable return time even with large grid sizes ($\mathcal{O}^7$).

6.3.2 Numerical schemes

A complete review of the numerical schemes implemented in AVBP, for both the convective and diffusive terms, is presented in the PhD thesis of Lamarque (2007). The two convection numerical schemes used in this work are:

- The **Lax-Wendroff (LW) scheme** is the adaptation of the Finite Difference Lax-Wendroff scheme (Lax & Wendroff, 1960) to the CV method. It is a FV centered scheme using an explicit time integration with a single Runge-Kutta step. Its accuracy is 2^{nd} order in both space and time. Its main advantage stems from the fact that its formulation includes a streamwise dissipative stabilization term making it quite robust, and a mass lumping operation resulting in a low computational cost.
- The **Two step Taylor-Galerkin 'C' (TTGC) scheme** developed by Colin & Rudgyard (2000) is a finite element scheme of the continuous Taylor-Galerkin family (Donea & Huerta, 2003). Its accuracy is of third order in both space and time (4^{th} order on regular grid (Moureau *et al.*, 2005)). Specifically built for LES, TTGC has good properties regarding dissipation and dispersion. However, these advantages make it less robust than the LW scheme and the explicit mass matrix inversion increases the computational cost (about 2.5 time more expensive than LW).

The numerical discretization methods in AVBP, being spatially centered and low-diffusive, are prone to dispersion errors and point-to-point oscillations (also known as *wiggles*) in the vicinity of steep solution variations. In particular, those spurious waves can threaten the stability of the computation and lead to unphysical behavior such as negative mass fraction values. To limit the occurrence of such errors, it is common practice to add a so-called Artificial Viscosity (AV) term directly to the nodal residuals. These AV models are characterized by their linear preserving property, which leaves unmodified a linear solution on any type of element. The models are based on a combination of a *shock capturing* term (called 2^{nd} order AV) and a *background dissipation* term

(called 4^{th} order AV or hyper-viscosity). The 2^{nd} order AV smooths local gradients, and introduces artificial dissipation. It is activated only in certain regions of the flow, based on a specific sensor value (see the AVBP Handbook for precisions about the different available sensors). The 4^{th} order AV is mainly used to control spurious high-frequency wiggles, and it is activated everywhere.

6.3.3 Challenges of reduced multi-step chemistries

6.3.3.a Integration of the stiffness

ARC are characterized by a variety of species, spanning a large range of timescales. In particular, the inclusion of intermediates can significantly stiffen the overall chemistry integration. It is interesting to be able to quantify the degree of stiffness of a mechanism *a-priori*, before integration in the LES solver. Indeed, for stability reasons, the timescales $\tau_{c,k}$ of each k-th species should remain larger than the integration time step Δ_t. A local quantification of the $\tau_{c,k}$ is provided by investigating the diagonal of the Jacobian matrix, similarly to what is done to select QSS species with the *LOI* method (see Section 3.4.2.b):

$$\tau_{c,k} = \frac{1}{|\mathbf{J}_{k,k}|} \tag{6.67}$$

This term can be directly extracted in the solver CANTERA during a computation. This estimation does not take species interactions into account, but it nonetheless contains the leading order term in most cases. Searching for the minimum $\tau_{c,k}$ for each k-th species, amongst a sufficient sample S of points across a series of 1D flames provides an efficient way to spot the "problematic" species, i.e., those with $min_{s\in S}(\tau^s_{c,k}) < \Delta_t$. It is illustrated on Fig. 6.8, for the skeletal mechanism ARC_29_C2H4NARA developed in Section 4.3: the minimum timescales are identified by sampling a series of 1D premixed flames at P = 3 bars, T_{ini} = 300 K, and ϕ ranging from 0.5 to 1.5. They are represented by dark bars. The integration time step of the FIRST simulation is also reported.

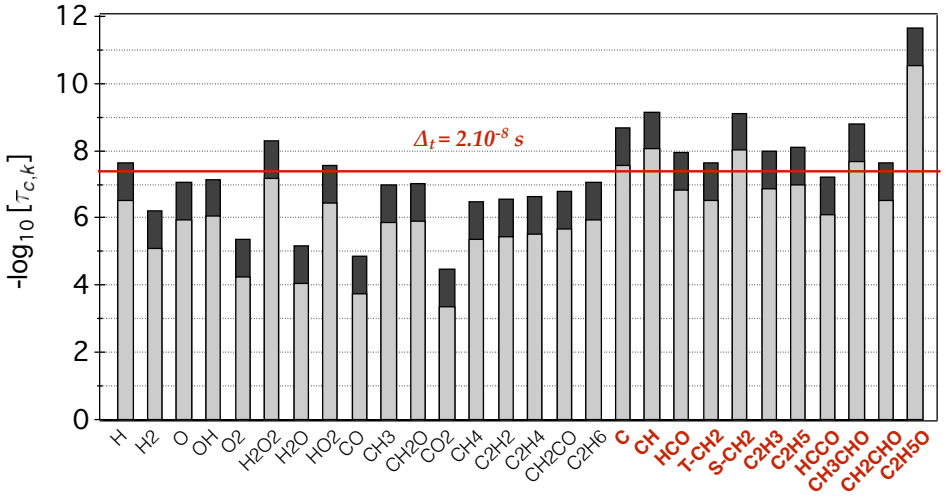

Figure 6.8: Species chemical timescales extracted from one-dimensional test cases with the ARC_29_C2H4NARA mechanism. The integration time step Δ_t corresponding to the FIRST configuration is identified by the red line. QSS species are also identified in red. Dark bars stands for the unthickened timescales, grey bars represent thickened timescales.

As this simulation employs the DTFLES model with a thickening ranging from 1 to 13, the actual timescales will be larger. Indeed, remember that the thickening of the flame front acts a sort of dilatation of the fields. The timescales corresponding to the limiting case of $\mathcal{F} = 13$ are also reported in grey in Fig. 6.8. Real timescales lie somewhere in between. We readily see that YARC identified most of the "problematic" species as being QSS candidates. However, some species could not be removed without introducing significant errors. This is the case of H_2O_2, H and HO_2. These species require a specific integration strategy, to prevent them from threatening the stability of the computation and to avoid employing an unpractically small timestep. A way to achieve this is provided by sub-iterating the computation of the chemical source terms (see the PhD thesis of Jaravel (2016) for example). However, to be consistent, this method would require sub-iterating the temperature as well, and is thus CPU consuming. A semi-implicit strategy is preferred in this work, and it is presented hereafter.

Semi-implicitation of the stiffness Since only a small subset of species are problematic, a semi-implicit method can be applied to them without affecting the resolution of the rest of the system. We start with the expression of the k-th species source term (Section 2.3.4):

$$\frac{\partial Y_k}{\partial t} = \dot{\omega}_k = \dot{\omega}_k^+ - \dot{\omega}_k^- \tag{6.68}$$

where the source term has been divided according to whether reactions are consuming ($\dot{\omega}_k^-$) or producing ($\dot{\omega}_k^+$) the k-th species. An Euler explicit integration of this equation is provided by:

$$\frac{Y_k^{n+1} - Y_k^n}{\Delta_t} = \dot{\omega}_k^+(\mathbf{Y}^n, T^n, P^n) - \dot{\omega}_k^-(\mathbf{Y}^n, T^n, P^n) \tag{6.69}$$

If we limit the analysis to linear coupling between the "problematic" species, the consuming source term can be rewritten as:

$$\dot{\omega}_k^-(\mathbf{Y}^n, T^n, P^n) = f(Y_{p\neq k}^n, T^n, P^n) Y_k^n \tag{6.70}$$

A semi-implicitation reformulation is obtained by substituting Y_k^{n+1} to Y_k^n in Eq. 6.70:

$$\frac{Y_k^{n+1} - Y_k^n}{\Delta_t} = \dot{\omega}_k^+(\mathbf{Y}^n, T^n, P^n) - f(Y_{p\neq k}^n, T^n, P^n) Y_k^{n+1} \tag{6.71}$$

$$Y_k^{n+1}(1 + f(Y_{p\neq k}^n, T^n, P^n)\Delta_t) = \dot{\omega}_k^+(\mathbf{Y}^n, T^n, P^n)\Delta_t + Y_k^n \tag{6.72}$$

$$Y_k^{n+1} - Y_k^n = \frac{\dot{\omega}_k^+(\mathbf{Y}^n, T^n, P^n)\Delta_t}{(1 + f(Y_{p\neq k}^n, T^n, P^n)\Delta_t)} + \left(\frac{1}{(1 + f(Y_{p\neq k}^n, T^n, P^n)\Delta_t)} - 1 \right) Y_k^n \tag{6.73}$$

$$\frac{Y_k^{n+1} - Y_k^n}{\Delta_t} = \frac{\dot{\omega}_k^+(\mathbf{Y}^n, T^n, P^n)}{(1 + f(Y_{p\neq k}^n, T^n, P^n)\Delta_t)} - \frac{f(Y_{p\neq k}^n, T^n, P^n) Y_k^n}{(1 + f(Y_{p\neq k}^n, T^n, P^n)\Delta_t)} \tag{6.74}$$

And finally, by identification with Eq. 6.70, one gets:

$$\dot{\omega}_k(Y_{p\neq k}^n, Y_k^{n+1}, T^n, P^n) = \frac{\dot{\omega}_k(\mathbf{Y}^n, T^n, P^n)}{(1 + f(Y_{p\neq k}^n, T^n, P^n)\Delta_t)} \tag{6.75}$$

This method is more efficient than the sub-iterating procedure, because chemical source terms only have to be evaluated once. Furthermore, by construction, an implicit method prevents or at least limit the occurrence of unphysical negative undershoots. However, this method cannot always be employed in practice since, for instance, the problematic species cannot be quadratically coupled (i.e., they should only appear once in every equation in which they are involved). Furthermore, the semi-implicit method is not always consistent: the source terms of all other species should theoretically also be evaluated with the updated $Y_{k\in\mathcal{P}}^{n+1}$, where $\mathcal{P}$ is the set of problematic species, computed with the above procedure:

$$\dot{\omega}_k = \dot{\omega}_k(Y_{p\notin\mathcal{P}}^n, Y_{\mathcal{P}}^{n+1}, T^n, P^n) \tag{6.76}$$

Ensuring this consistency requires a splitting of the source term evaluation, and precludes any sort of coupling between problematic species, something that is almost impossible to enforce for large mechanisms. An iterative procedure would allow to overcome those restrictions, loosing however the advantage of looping through the source term calculation routine only once. Additionally, ensuring the convergence of such an iterative procedure is not straightforward.

The semi-implicit methodology, with its imperfections, is found to be very efficient nonetheless, and is thus systematically employed throughout this PhD thesis for the short living but important H_2O_2 and HO_2 species. A numerical validation of this technique was provided in the PhD thesis of Jaravel (2016) for methane/air oxidation. For completeness, an example of HO_2 profile in a fully resolved 1D premixed ethylene/air flame computed, on the one hand, with CANTERA and no implicitation and, on the other hand, with AVBP and semi-implicitation is shown in Fig. 6.9 (black and red curves, respectively). Both computations use simplified transport. For clarity, the CANTERA solution is interpolated on the AVBP grid. Additionally, a thickened flame profile ($\mathcal{F} = 5$) is also reported (blue curve), computed with AVBP and the semi-implicitation procedure. The profile is rescaled by $1/\mathcal{F}$. The results show that all integrations give very similar results.

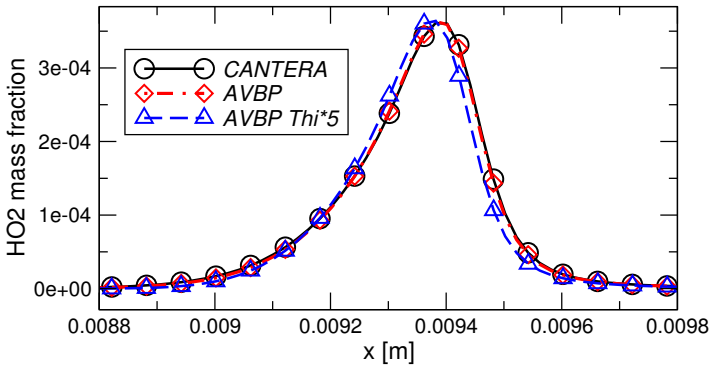

Figure 6.9: HO_2 mass fraction profile across a 1D ethylene/air premixed laminar flame at 3 bars, $\phi = 2.3$ and $T_{ini} = 300$ K. The kinetic scheme employed is the ARC_19_C2H4NARA. Legend in the text.

6.3.3.b Numerical evaluation of the chemical source terms

As presented in Section 6.3.2, the evaluation of the chemical source terms normally depends upon the chosen numerical scheme. With the **LW** scheme, the evaluation is performed at the mesh nodes, along with all the other transported variables. The **TTGC** scheme, however, employs a *gather-scatter* strategy, where the evaluation of the chemical source terms is performed at the cell center (gather operation) before residuals are distributed to the mesh nodes (scatter operation), where they are stored. This operation is very costly in practice, especially when a large number of species are transported. In addition, for tetrahedral meshes, there are in average more cell centers than mesh nodes, further increasing the number of computations to perform for an integration at the cells center. In his PhD thesis, Jaravel (2016) evaluated that the time spent on the chemical source term evaluation can amount for as much as 50% of the total computational time, when evaluating the source term at the cells center. If integrated at the mesh nodes directly, the source terms only account for about 15% of the total computational time, with a very limited impact in terms of accuracy. In this work, the same strategy is employed.

6.3.3.c A word about diffusivity

In practice, either the species chemical lifetimes or the acoustic time step will determine the integration time step in a compressible code like AVBP. However, it is noted that under some circumstances, the viscous time step τ_v might also be relatively small, and it is all the more true that the thickening (and efficiency in a turbulent computation) is increased. Indeed, ARC employ different Sc numbers for each species, and some light radicals such as H or H_2 are usually very diffusive (small Sc numbers). As a first approximation the viscous timescale -based on H being present in the mechanism and being the most diffusive species- in a 1D premixed laminar flame can be estimated as:

$$\tau_{v,H} = \frac{\Delta_x^2}{D_{eff,H}} \tag{6.77}$$

where

$$D_{eff,H} = \frac{\nu \mathcal{F}}{\rho Sc_H} \tag{6.78}$$

Or, equivalently, for a flame discretized with n points (Eq. 6.44):

$$\tau_{v,H} = \frac{\Delta_x}{\nu n} \rho Sc_H \delta_l \tag{6.79}$$

Figure 6.10 shows that this time scale can become quite competitive with the chemical timescale in the inner flame region (identified by the normalized temperature gradient in red) for usual mesh sizes and thickening factors. The comparison between Fig. 6.10 (a) and (b) tells us that employing a constant $\mathcal{F}$ in a realistic configuration with mesh sizes variations might locally lead to a switch of the limiting process (chemical or diffusive) and that this is all the more true that $\mathcal{F}$ is large. Fortunately, however, if the goal is to get 5 points in the flame front, any choice of parameters will lead to the same balance. This is shown in Fig. 6.10 (c) for two choice of parameters: $\mathcal{F} = 5$

and $\Delta_x = 10^{-4}$ (Case A), and $\mathcal{F} = 15$ and $\Delta_x = 3.10^{-4}$ (Case B), leading to the same discretization. Contrarily to the chemical time scale, AVBP will adapt the time step to the diffusive process, through the evaluation of a Fourier number.

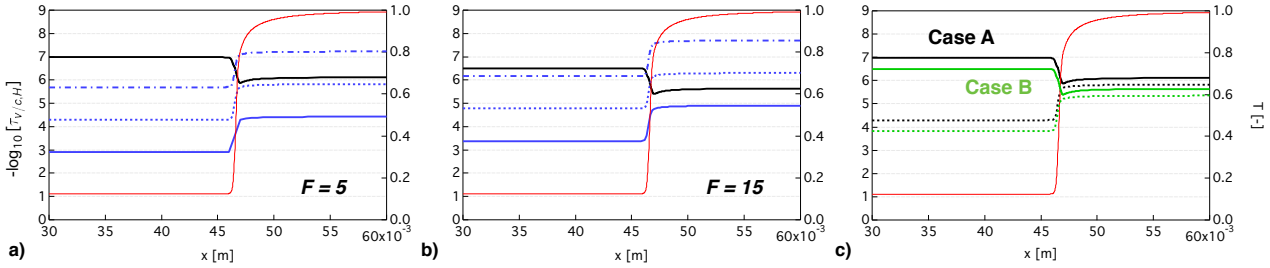

Figure 6.10: a) and b) present comparisons of τ_c (in black) and τ_v (in blue) for the H species in 1D laminar thickened premixed flames ($\mathcal{F} = 5/15$), at 3 bars, $\phi = 1$ and $T_{ini} = 300K$; computed with simplified transport in CANTERA. Various degree of resolution are evaluated: $\Delta_x = 5.10^{-4}$ (solid line), $\Delta_x = 10^{-4}$ (dotted line), $\Delta_x = 2.10^{-5}$ (dashed-dotted line). c) present the same comparisons between two computations maintaining the same number of points in the flame, $n = 5$: in black $\mathcal{F} = 5$ and $\Delta_x = 10^{-4}$ (Case A), in green $\mathcal{F} = 15$ and $\Delta_x = 3.10^{-4}$ (Case B). The kinetic scheme employed is the ARC_19_C2H4NARA. The red curve is a normalized temperature profile, marking the flame area.

6.3.4 Boundary conditions

Boundary conditions are important, especially for compressible flows. For nodes situated at the boundaries of the computational domain, it is necessary to correct the residual obtained from the convective and diffusive fluxes. To take into account acoustic waves reflected at the inlets and outlets, the residuals are modified by translating the boundary conditions in a problem of characteristic waves propagation. This method is called Navier-Stokes Characteristic Boundary Condition (NSCBC). It was originally developed by Poinsot & Lele (1992) and extended to multi-species flows by Moureau *et al.* (2005). It is implemented in AVBP and is used in all simulations presented in this work.

Part III

Applications

Chapter 7

Application to a gaseous non-premixed realistic burner

Contents

The first half of this chapter has been submitted to Combustion and Flame, and is thus self-contained. Sections 7.9 present additional results, before general conclusions are drawn.

7.1 Introduction

Recent implementation of emission control regulations has resulted in a considerable demand from industry to improve the efficiency while minimizing the consumption and pollutant emissions of the next generation of aero-engine combustors. Less expensive than Direct Numerical Simulations (DNS), Large Eddy Simulation (LES) is

an attractive tool to address those issues with high accuracy for a reasonable computing cost, and it is nowadays widely employed for the simulation of turbulent combustion in both academic and applied research (see, e. g., the reviews of Pitsch (2006) or more recently Gicquel *et al.* (2012), and references therein).

However, the computation of combustion chemistry and its coupling with turbulent flows, a recent review of which can be found in Fiorina *et al.* (2015), remains challenging in LES. One main reason is that fuel pyrolysis and oxidation proceed through complex and highly non-linear mechanisms involving hundreds of different chemical species over a wide range of characteristic length and time scales. As pointed out by Lu & Law (2009) in their extensive review on the subject, the direct integration of such detailed chemistry in CFD applications like LES is not a viable path, because of excessive computational demands and numerical stiffness. Employing overly detailed chemical schemes for a specific application may not be desirable either, as this introduces a large number of reaction parameters, which individually contribute very little to the global flame behaviour, while introducing possibly large uncertainties (Wang & Frenklach, 1991).

In practice, chemical kinetics in LES today is often taken into account through pre-tabulated laminar flame solutions based on detailed chemistry. As discussed by Peters (1984), this method assumes that thermo-chemical evolutions in the composition/temperature space can be parametrized by a reduced set of variables. Usually, these include the mixture fraction, characterizing the degree of fuel and oxidizer mixing, and the progress variable, monitoring the progress of reaction towards chemical equilibrium. Some recent techniques falling into that category include the flame-generated manifold (FGM) (Oijen *et al.*, 2001), the Flame Prolongation of ILDM (FPI) (Gicquel *et al.*, 2000) or the Flamelet Progress Variable (FPV) (Pierce & Moin, 2004) which have all been successfully coupled to various turbulence-chemistry interaction models to perform LES of complex geometries (Galpin *et al.*, 2008; Ihme & Pitsch, 2008*b*; Franzelli *et al.*, 2015*b*; Mahesh *et al.*, 2006). Simulations using tabulation are obviously very much dependent upon the type of canonical configurations chosen to build the look-up table (either premixed, partially-premixed or non-premixed) (Vreman *et al.*, 2008; Fiorina *et al.*, 2005), even if recent efforts addressing this issue should be acknowledged (Nguyen *et al.*, 2010; Knudsen & Pitsch, 2009). Another main disadvantage of this approach is that the interactions between the flame and the flow are oversimplified. As such, taking into account complex phenomena such as dilution, heat losses or slow pollutant chemistry requires additional modeling efforts that can be far from trivial. Very often, additional parametrization variables are introduced, for which transport equations must be solved (Fiorina *et al.*, 2004; Ihme & Pitsch, 2008*a*; Mueller & Pitsch, 2012), resulting in additional unclosed terms. It is especially true in the context of soot modeling. Mueller & Pitsch (2013), for example, used a statistical Method of Moments in conjunction with a tabulated gas-phase chemistry description to investigate soot production in a real aeronautical burner, and their formulation required specific treatments to account for the loss of soot precursors from the gas-phase chemistry, and to include radiation effect.

Introduced for example by Goussis & Mass (2011), another promising approach to model chemistry in LES, is to use Analytically Reduced Chemistry (ARC). ARC are directly derived from detailed kinetic mechanisms, and they aim at better describing combustion phenomena by retaining more species and reactions in a physically-oriented way. Typically, in between 10 to 30 species and up to 500 reactions are considered. By keeping only the main competing pathways, any type of combustion regime and targeted intermediate species should be captured with this approach. The use of ARC in LES is becoming more and more frequent. Jones *et al.* (2012) where amongst the first to use a sub-grid PDF method in conjunction with an Eulerian stochastic field method to investigate the flame structure in a swirled gaseous premixed burner, using an ARC based on the GRI 3.0 for methane. More recently Bulat *et al.* (2014) applied the same strategy to investigate CO and NOx formation in an industrial gas turbine combustor. Jaravel *et al.* (2016) derived a target-specific ARC for the same configuration, and, in conjunction with a DTFLES approach, they performed the LES by solving explicitly the transport equations for the considered species.

Such LES are still computationally expensive, and up until today, ARC have mainly been used for small hydrocarbons on premixed gaseous configurations. To our knowledge, no study has directly addressed the problem of partially premixing, nor soot modelling, in realistic configurations with ARC. As such, many questions are still open, and it is the objective of this work to take a step further in the aforementioned directions by considering the problem of partially premixing in a swirled gas turbine combustor burning C_2H_4. Indeed, the targeted fuel, ethylene, is commonly regarded as one of the main heavy hydrocarbon's pyrolysis products and a precursor of soot. The question of soot modeling is then partially addressed in this paper, following the work of Franzelli *et al.* (2015*b*) who investigated the predictions of an empirical soot model (Leung *et al.*, 1991) in the same configuration. Their work is extended here, by coupling the same empirical model to the previously discussed novel gas-phase chemistry approach and investigating its impact.

The paper is organized as follows: The modeling approaches used for chemistry in this study are first reviewed in Section 7.2, before being evaluated on relevant canonical one-dimensional problems in Section 7.3. Next, the soot modeling strategy is described, in Section 7.4. The experimental configuration is then introduced in Section 7.5 and the numerical strategy is presented in Section 7.6. Finally, in Section 7.7, flow-field and flame structure obtained with the two chemistry descriptions are compared and discussed with respect to the experimental results. The analysis is concluded with a discussion on soot precursors and soot predictions.

7.2 Description of the chemistry models

7.2.1 Construction of the FPI table

The first chemistry description considered in this study is the FPI-TTC tabulation method adapted to compressible solvers by Vicquelin *et al.* (2011). The look-up table is constructed from a collection of one-dimensional unstrained premixed laminar flames computed with the solver Cantera (Goodwin *et al.*, 2014), assuming unity Lewis number for all species. The detailed mechanism of Narayanaswamy *et al.* (2010) is employed, at the conditions of the target application ($T_f = 300$K and $P = 3$ bar). The flammability limit considered for the construction of the table are $0.4 < \phi < 3.0$. The two variables that allow to recover all other thermo-chemistry information are the mixture fraction Y_z based on carbon atom conservation, and the normalized progress variable $c = Y_c/Y_{c,eq}$, where Y_c is based on the mass fraction of CO and CO_2 and $Y_{c,eq}$ is the Y_c value at equilibrium. Both quantities follow classical transport equations (Vicquelin *et al.*, 2011). The look-up table is discretized by 200 x 200 points in Y_z and c, respectively; and linear interpolation is used for intermediate points. As it is constructed from premixed flamelets, the points in the Y_z direction are gathered around stoichiometry ($z_{st} = 0.063$) inside the flammability limits, as can be seen in Fig. 7.1.

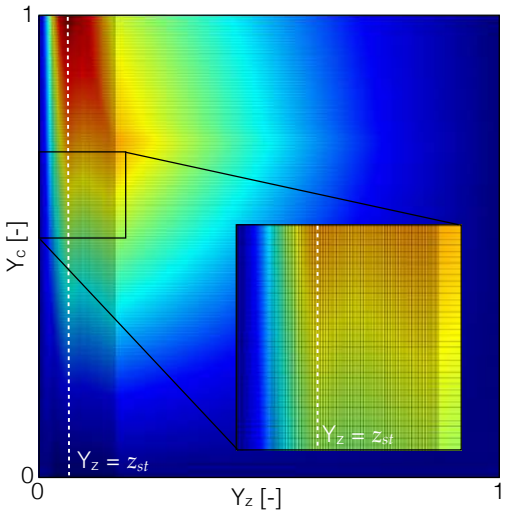

Figure 7.1: Look-up table used for the FPI computations, colored by the temperature. The dimensions are 200 x 200. $z_{st} = 0.063$.

Assuming unity Lewis number for all species can have many consequences, the least of all being an underestimation of the laminar flame speed s_l (see Section 7.3), especially for near-stoichiometric mixtures. To correct this behavior, based on simplified asymptotic analysis, a correcting factor $F_{sl,corr} = (s_l/s_{l_{Le=1}})$ is applied to the source term of the progress variable c in the look-up table. Accordingly, the same factor is also applied to the conductivity, in order to preserve the flame thickness. The impact of these corrections will be discussed further in Section 7.3.

7.2.2 Development of the ARC mechanism

As discussed in the introduction, in recent years, advanced reduction techniques have been developed to preserve the chemical information of a detailed mechanism, by retaining only relevant reaction pathways (Goussis & Mass, 2011). Such reduced schemes can be derived in three steps. First, a set of targets associated with a set

Transported species	*QSS* species
N_2 H H_2 HO_2 H_2O H_2O_2 O O_2 OH CO CO_2	S-CH_2 CH C HCO C_2H_5O HCCO
CH_2O CH_2CO CH_3 CH_4 C_2H_2 C_2H_4 C_2H_6	T-CH_2 C_2H_3 CH_2CHO C_2H_5 CH_3CHO

Table 7.1: Species contained in the ARC_18_C2H4NARA scheme.

of canonical zero- or one-dimensional configurations should be prescribed, so that the reduction can be stirred towards preserving accuracy of those targets. Next, based upon those results, a skeletal reduction is performed where, following the formalism of Turányi (1990*a*), unimportant species and reactions are removed from the original detailed mechanism. Finally, assumptions about species and/or reactions characteristic timescales should be formulated, still based upon the results of the canonical configurations, in order to implicit the stiffness of the mechanism.

Following this approach, an ARC has been derived for ethylene oxidation, based upon the detailed mechanism of Narayanaswamy *et al.* (2010), originally composed of 158 species and 1804 irreversible reactions. The reduction is based on one-dimensional laminar premixed flames and zero-dimensional auto-ignition computations, representative of the studied configuration of Geigle *et al.* (2013). Targets consist of auto-ignition time (τ_{ig}), burnt gas temperature (T_b), laminar flame speed (s_l), main species final values, and specific intermediate species profiles (OH and C_2H_2). The skeletal reduction is performed by applying the Directed Relation Graph with Error Propagation method (DRGEP), a full description of which can be found in Pepiot-Desjardins & Pitsch (2008). This results in a skeletal mechanism composed of 29 species and 334 irreversible reactions. Next, the Quasi Steady State Approximation (QSSA) is assumed for 11 species, identified by the Level of Importance (LOI) criterion described by Lovas *et al.* (2002) as being species with the shortest lifetime. The resulting ARC is labelled ARC_18_C2H4NARA in what follows, and retains 18 transported species, listed in Table 7.1. The reduction was performed with the automated tool YARC developed by Pepiot (2008).

7.3 Assessment of the chemistry models on canonical configurations

In his section, we evaluate the performances of the previously introduced chemistry descriptions in canonical configurations. The comparison is not exhaustive, and only two cases were selected to help the following discussion on LES results. The two configurations are epresentative of the combustion regimes encountered in the DLR burner. First, one-dimensional laminar unstrained premixed flames (PFU) are considered, corresponding to the canonical configuration used to derive the ARC mechanism. Second, counterflow strained diffusion flames (DFS) are investigated, because the target application operates under a partially premixed regime were the occurrence of diffusion structures is expected.

All computations are performed with the solver Cantera (Goodwin *et al.*, 2014), using the same simplified transport model as the one used in the LES solver (see section 7.6). A unity Lewis assumption is made for the transported variables involved in the FPI formulation. For the ARC scheme, no such assumption is made and the values of species Schmidt numbers and Prandtl number are taken in the flame zone of a complex transport calculation. All results will be compared to the detailed mechanism used to build both the FPI table and the ARC mechanism (Narayanaswamy *et al.*, 2010), where both a mixture averaged formulation (Mix) and a unity Lewis assumption have been employed (Le=1). The evaluation against experimental data is out of the scope of the present article. For validations of the detailed mechanism, the reader is referred to Blanquart *et al.* (2009); Narayanaswamy *et al.* (2010).

7.3.1 Unstrained Premixed Flames (PFU)

To be consistent with the operating points of interest (see Table 7.3), two sets of PFU have been computed. The pressure is either 3 bar or 5 bar, while the initial temperature is set to 300 K. Computations with the FPI look-up table and with the detailed mechanism where all species have unity Lewis numbers are reported only for P = 3 bar.

7.3.1.a Validations for P = 3 bar

Burnt gas temperature as well as laminar flame speed are plotted versus equivalence ratio, respectively, in Fig. 7.2 (a) and (b). The ARC mechanism performances are excellent. In the targeted range of equivalence ratio ($0.5 < \phi < 1.5$), the relative error on s_l never exceeds 4%, while it stays below 10% over the entire range of flammability. As expected, when a unity Lewis assumption is made we observe an under-prediction of s_l, a trend that is emphasized near-stoichiometry where the relative error can reach up to 25%. The detailed mechanism's results are better predicted with the FPI look-up table, which features the correction factor $F_{sl,corr}$.

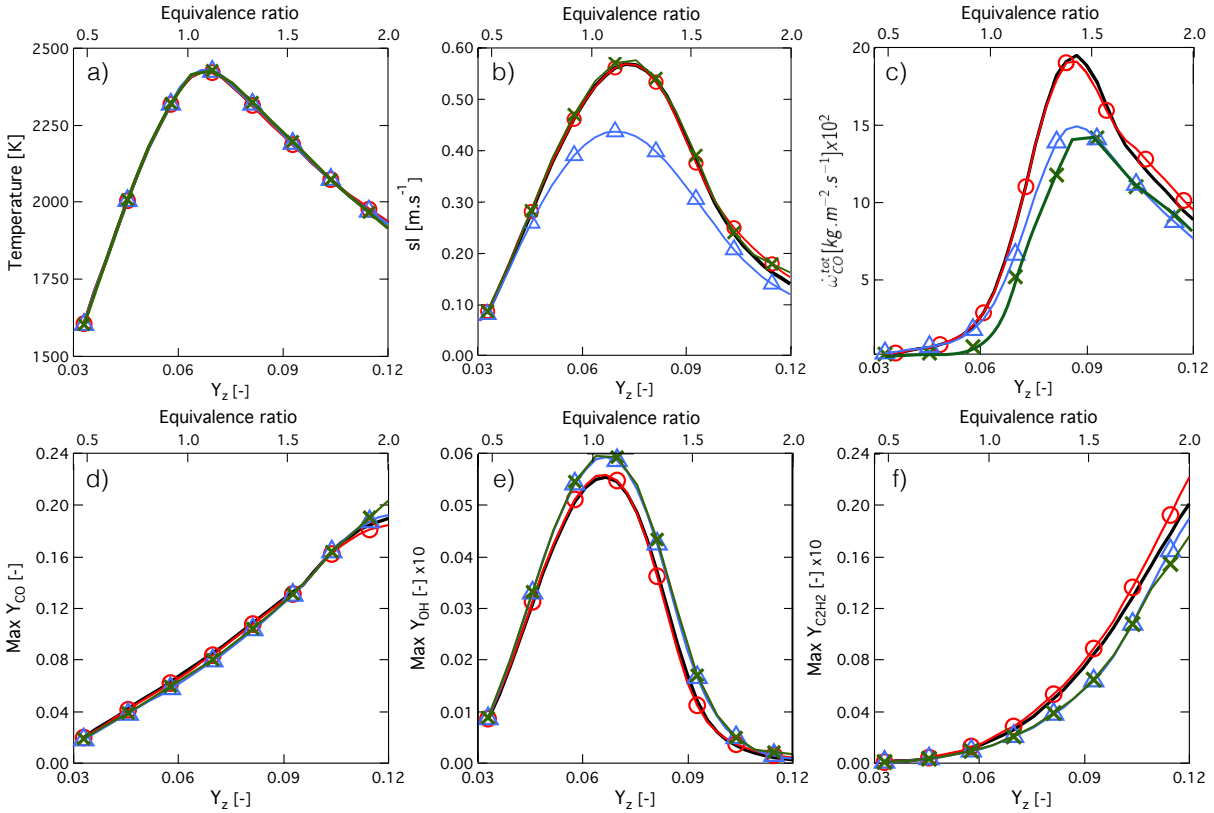

Figure 7.2: a) Burnt gas temperature b) laminar flame speed c) global CO production and maximum of d) CO e) OH and f) C2H2 reached in a series of PFU. Initial temperature is 300 K, P = 3 bar. Detailed mechanism - Mix (solid line), ARC_18_C2H4NARA (o), Detailed mechanism - Le=1 (Δ), FPI (+).

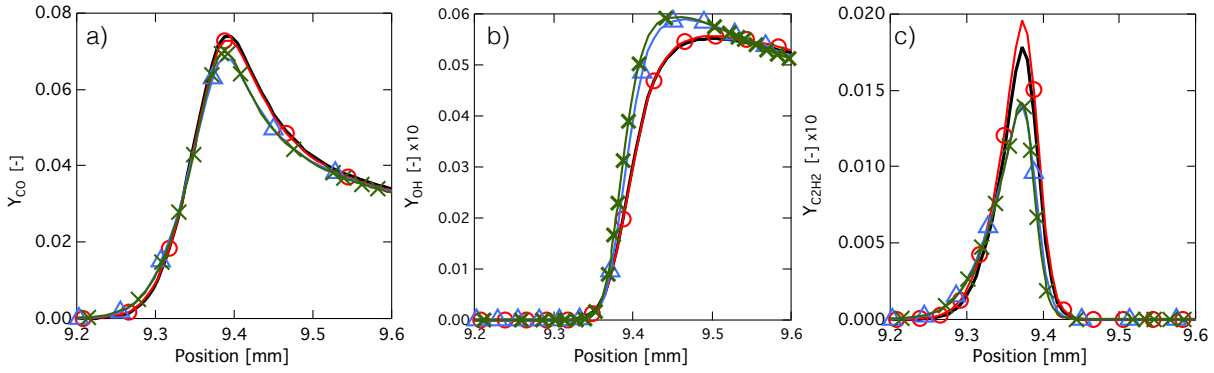

Figure 7.3: Profiles of a) CO b) OH and c) C2H2 across a *PFU*. Fresh gas temperature is 300 K, P = 3 bar and $\phi = 1$. Detailed mechanism - Mix (solid line), ARC_18_C2H4NARA (o), Detailed mechanism - Le=1 (Δ), FPI (+).

Next, we investigate CO global production through the flame, by integrating the mass production rate across the reaction front:

$$\dot{\omega}_{CO}^{tot} = \int_{c<0.98} \dot{\omega}_{CO} dx \tag{7.1}$$

In the above expression, the integration is made up to $c = 0.98$ to illustrate the kinetics. Results are presented on Fig. 7.2 (c). Here also, an excellent agreement is observed between the detailed mechanism and the ARC_18_NARAC2H4 results. The global error computed over the entire range of equivalence ratio is under 2%. The FPI results under-predict the global CO production, consistently with the $Le = 1$ detailed mechanism results. A better agreement is observed under rich conditions, where the relative error is below 20% starting from $\phi = 1.3$. We note some small differences whether we employ the FPI look-up table or a unity Lewis assumption, especially for $\phi < 1.5$.

Finally, the evolution of the species of interest -namely, CO, C_2H_2 and OH- across the flame front is investigated. For concision, maximums are plotted versus mixture fraction, in Fig. 7.2(d)-(f), while results for one flame of interest ($\phi = 1$) are presented in Fig. 7.3. The graph is focused on evolutions across the reaction front, however, it is noted that all simulations evolve towards the same burnt gas state. For the ARC mechanism in particular, the relative error on equilibrium values for the entire range of equivalence ratio is below 0.5% for the temperature, below 2% for OH, and below 4% for CO and CO_2. Overall, an excellent agreement can be observed between the detailed mechanism and the ARC mechanism. It is seen on Fig. 7.2(f) that the maximum of C_2H_2 is best predicted in moderately rich conditions ($1.1 < \phi < 1.6$). Outside of this range, the relative error can reach up to 10%, as it is the case for the flame shown in Fig. 7.3 for example. From these plots, it is also apparent that a unity Lewis assumption modifies the flame structure. In particular, the FPI approach always under-predicts peak levels of C_2H_2 by about 20%, and predicts a higher peak of heat release rate (not shown, but consistent with OH levels seen on Figures 7.2 (e) & 7.3 (b). CO and CO_2 (not shown) maximum levels are consistent with the reference computations, with a maximum relative error below 7%.

In all simulations, a small offset between FPI results and results deriving from a unity Lewis assumption can be observed. This is somewhat counter-intuitive, as the look-up table was directly constructed from premixed simulations using this assumption. There can be several explanations for these discrepancies. First of all, results are very sensitive to the refinement in the progress variable direction, especially for species with a strong gradient in the phase space, such as OH for example. Considering 200 points might not be enough. Furthermore, when the mixture is near-stoichiometric, differences can be explained by the correction factor $F_{sl,corr}$. Enabling this correction modifies the profile of the progress variable across the flame front, and equilibrium is reached faster, as can be seen on Fig. 7.3 (b). Finally, when the mixture is very rich, differences can be attributed to a lack of refinement in the mixture variable direction (see Fig. 7.2(f)). These remarks serve to emphasize the fact that a further discussion based solely on results obtained from unity Lewis assumptions, as is often done in the literature, could lead to erroneous conclusions. This will be even more true in a non-premixed context, as we will see shortly. Based on these observations, results with the detailed mechanism and a unity Lewis assumption will not systematically be presented in what follows.

7.3.1.b Validations for P = 5 bar

Results are here presented only for the detailed mechanism, and the ARC_18_C2H4NARA mechanism, as the same conclusion holds for unity Lewis assumptions as in the 3 bars case. Burnt gas temperature as well as laminar flame speed are plotted versus equivalence ratio, respectively, in Fig. 7.4 (a)-(b). The laminar flame speed is consistently lower than in the P = 3 bars case. The agreement is excellent between both mechanisms, for the entire range considered. With the ARC mechanism, the relative error on s_l never exceeds 5%, while the maximum relative error on the burnt gas temperature is under 1%.

CO global production is plotted on Fig. 7.4 (c). The evolution with the mixture fraction is comparable to that of the case P = 3 bar, but levels are about 35% higher. The accuracy of the ARC mechanism is similar to what was discussed in the case P = 3 bar.

Maximums of species of interest are plotted against mixture fraction, in Fig. 7.4(d)-(f). The curves are almost indistinguishable, except for the maximum of C_2H_2 for which the ARC mechanism exhibit about 10% of relative error over the entire equivalence ratio range. Figure 7.5 displays the evolution of the species of interest across a stoichiometric flame front. As expected, it can be seen that the flame is thinner than in the P = 3 bars case. Despite the small offset on the predicted peak of C_2H_2 that can be seen on Fig. 7.5 (c), results with the ARC scheme are considered excellent. It is noted, here also, that both mechanisms eventually converge towards the same burnt gas state.

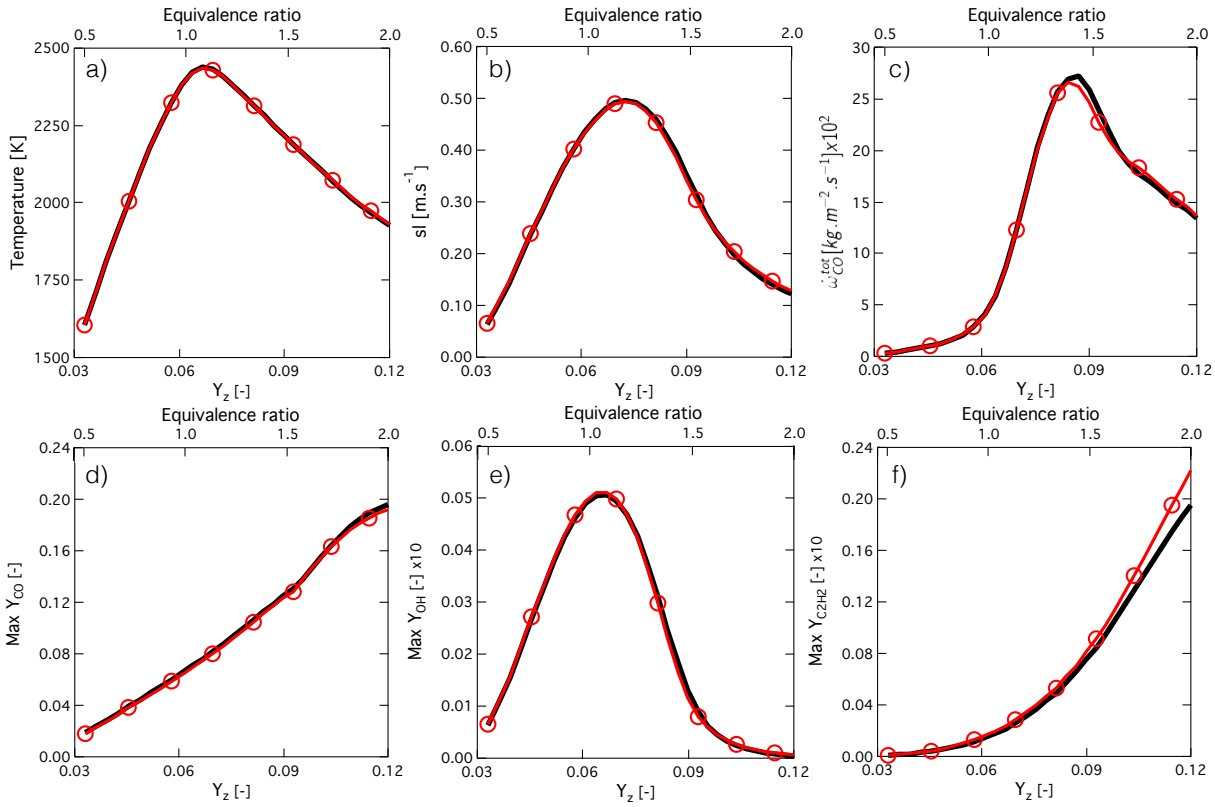

Figure 7.4: a) Burnt gas temperature b) laminar flame speed c) global CO production and maximum of d) CO e) OH and f) C2H2 reached in a series of *PFU*. Fresh gas temperature is 300 K, P = 5 bar. Detailed mechanism - Mix (solid line), ARC_18_C2H4NARA (o).

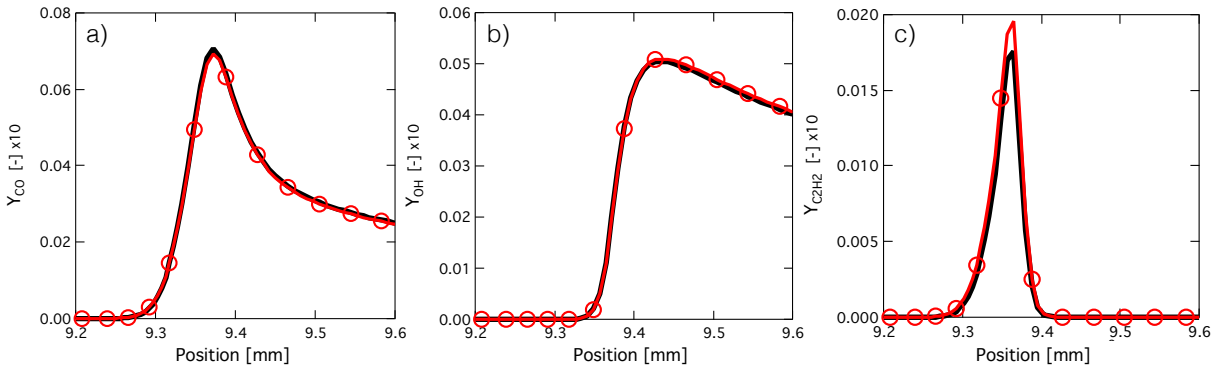

Figure 7.5: Profiles of a) CO b) OH and c) C2H2 across a *PFU*. Initial temperature is 300 K, P = 5 bar and $\phi = 1$. Detailed mechanism - Mix (solid line), ARC_18_C2H4NARA (o).

7.3.2 Strained Diffusion Flames (DFS)

The reduced mechanisms are further compared on a series of counterflow diffusion flames, for a large range of strain rates. To be consistent with the DLR combustor operating conditions of interest (see Table 7.3), the oxidizer inlet is composed of air at 300 K while the fuel inlet is composed of pure ethylene at 300 K. The pressure is either 3 bar or 5 bar.

7.3.2.a Validations for P = 3 bar

The response to strain is assessed in terms of maximum temperature reached in the flame, and global fuel and CO consumption, as shown respectively in Fig. 7.6(a)-(c). A global strain is used:

$$a = \frac{u_o + u_f}{d} \tag{7.2}$$

where u_o and u_f are the oxidizer and fuel inlet velocity, respectively, and d is the distance between the two inlets. The first observation is that the ARC mechanism's behavior is excellent, especially considering the fact that non-premixed configurations were not targeted in the reduction. The relative error on maximum temperature never exceeds 1% for all strain rates, and extinction occurs at $a_{ext} \approx 2320\ s^{-1}$, consistently with the prediction of the detailed mechanism. CO and OH maximum levels are equally well predicted, with a relative error below 5%, except for small strain rates ($a < 50\ s^{-1}$) where the relative error on the maximum of OH can reach up to 10%. Levels of C_2H_2 are less accurately predicted, with a relative error ranging from 10% everywhere to 30% for small strain rates ($a < 75\ s^{-1}$). This offset can be seen on Fig. 7.7(c) & (f), were an example of flame structure for a small strain rate ($a = 50\ s^{-1}$) in both physical and phase space is provided.

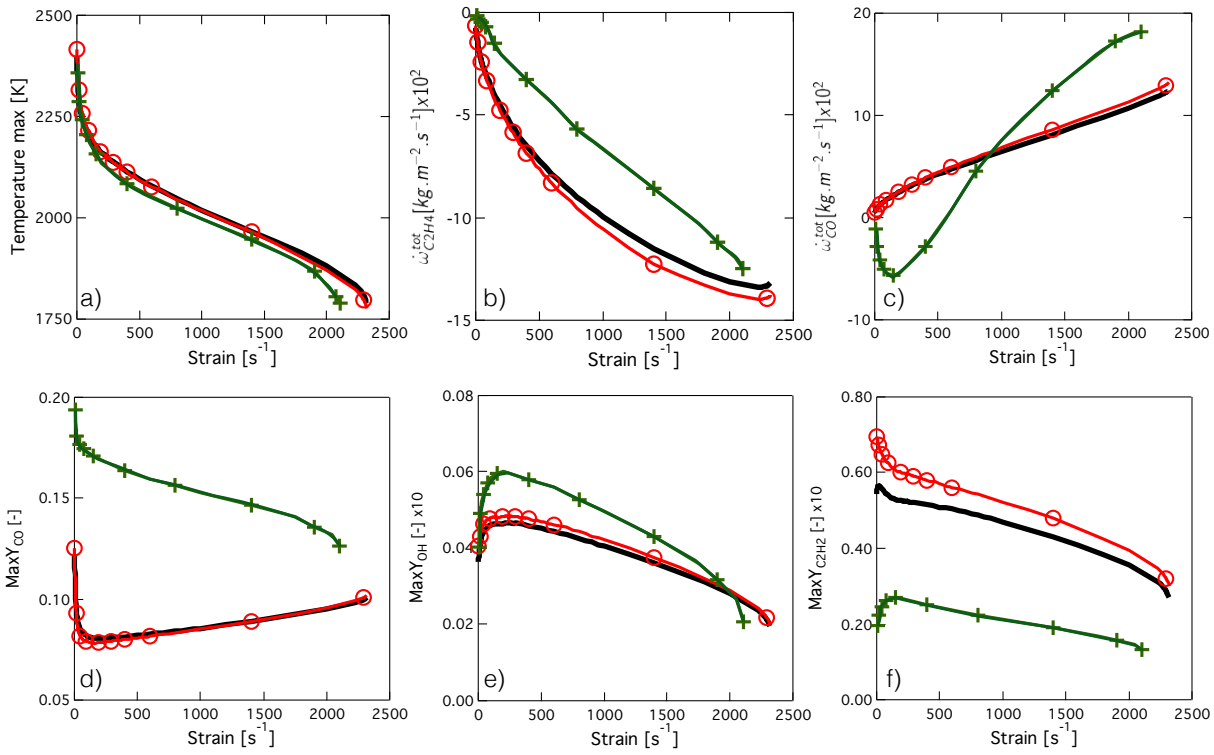

Figure 7.6: a) Maximum temperature b) global C_2H_4 and c) CO production and maximum of d) CO e) OH and f) C2H2 reached in a series of *DFS*. Fresh gas temperature is 300 K, P = 3 bar. Detailed mechanism - Mix (solid line), ARC_18_C2H4NARA (o), FPI (+).

Results with the FPI table exhibit a response to strain, as can be seen on Fig. 7.6, but with a behavior that is difficult to analyze. Figures 7.6(a)-(c) shows that global tendencies are captured: the maximum temperature decreases when the global fuel consumption increases. However, it can be seen from Fig. 7.6(d)-(f) that maximum levels of species of interest are either over or under predicted. Moreover, maximum levels of CO species seem to be decreasing with increasing strain rate, when the opposite tendency is expected. The predicted strain rate of extinction is 2105 s^{-1}, which is not that far from the expected value of $a_{ext} \approx 2320\ s^{-1}$. All those discrepancies are consistent with what has already been observed by Fiorina *et al.* (2005) in similar test cases. They concluded that the FPI tabulation was indeed valid in a small inner reaction zone close to the stoichiometric surface, where diffusive processes are dominated by chemistry. Outside of this zone, they reported big differences in CO and CO_2 mass fractions, which is also apparent from Fig. 7.7(a) & (d). The same can be said about C_2H_2, Fig. 7.7 (c) & (f), which is poorly predicted over the entire mixture fraction range. The linear interpolation outside of the flammability range ($0.03 < Y_z < 0.17$), also visible from Fig. 7.7(d)-(f), is another source of error. OH

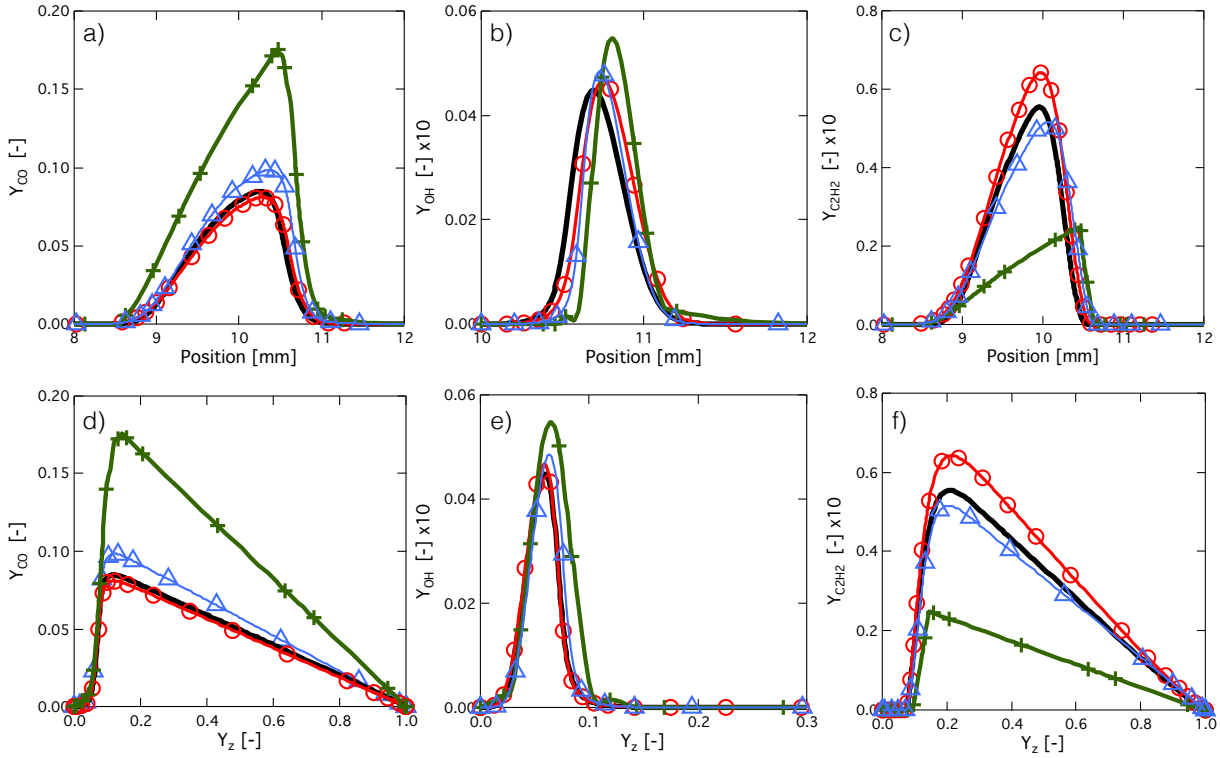

Figure 7.7: Structure of a DFS with $a = 50\ s^{-1}$. Fresh gas temperature is 300 K, P = 3 bar. Spatial evolutions of a) CO b) OH and c) C_2H_2 as well as evolutions in the phase space of c) CO d) OH and e) C_2H_2 mass fraction. Detailed mechanism - Mix (solid line), ARC_18_C2H4NARA (o), Detailed mechanism - Le=1 (Δ), FPI (+).

evolution is generally better recovered, see Fig. 7.7(b) & (e), because levels are only significant inside the premixed flammability limits, in a region near stoichiometry. These results suggest that pollutant and soot predictions in partially-premixed configurations should yield very different results with the FPI and the ARC approach. Results with the detailed mechanism and the unity Lewis assumption are also reported on the graph, to stress once more that results bear no resemblance with that of the FPI.

7.3.2.b Validations for P = 5 bar

Similar to the P=3 bars case, the response to strain of the ARC mechanism, presented in Fig. 7.8, is very good. The predicted extinction strain rate is $a_{ext} \approx 3260\ s^{-1}$ and $a_{ext} \approx 3190\ s^{-1}$ with the detailed and ARC mechanisms, respectively. Those values are significantly higher than for the P = 3 bars case. Here also, the level of C_2H_2 presents the higher offset, with very similar levels of error than what was found in the P = 3 bars case. This error in peak values of C_2H_2 is also seen on the profiles of Fig. 7.9(c), (d) & (f), featuring the structure of a diffusion flame for a very high strain rate ($a = 2600\ s^{-1}$), in both physical and phase space. CO and OH evolutions are remarkably well predicted.

Those results emphasize once more the main asset of ARC, which is that the derived mechanisms remains accurate outside of their derivation targets and operating range.

7.4 Soot modelling

7.4.1 Methodology for soot modelling

Soot formation is a highly intermittent and complex process dependent upon the flow time history, and proceeding in stages; from nucleation, which is the inception of a new soot particle from its precursors, to the various

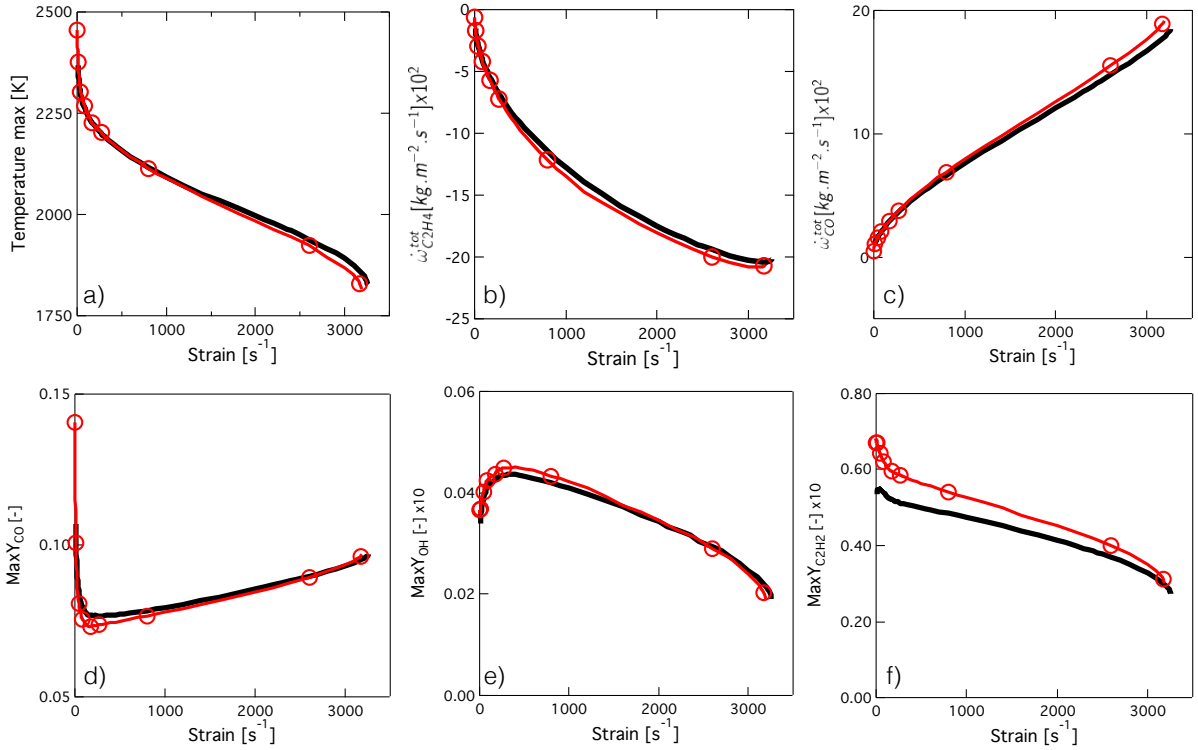

Figure 7.8: a) Maximum temperature b) global C_2H_4 and c) CO production and maximum of d) CO e) OH and f) C2H2 reached in a series of *DFS*. Fresh gas temperature is 300 K, P = 5 bar. Detailed mechanism - Mix (solid line), ARC_18_C2H4NARA (o).

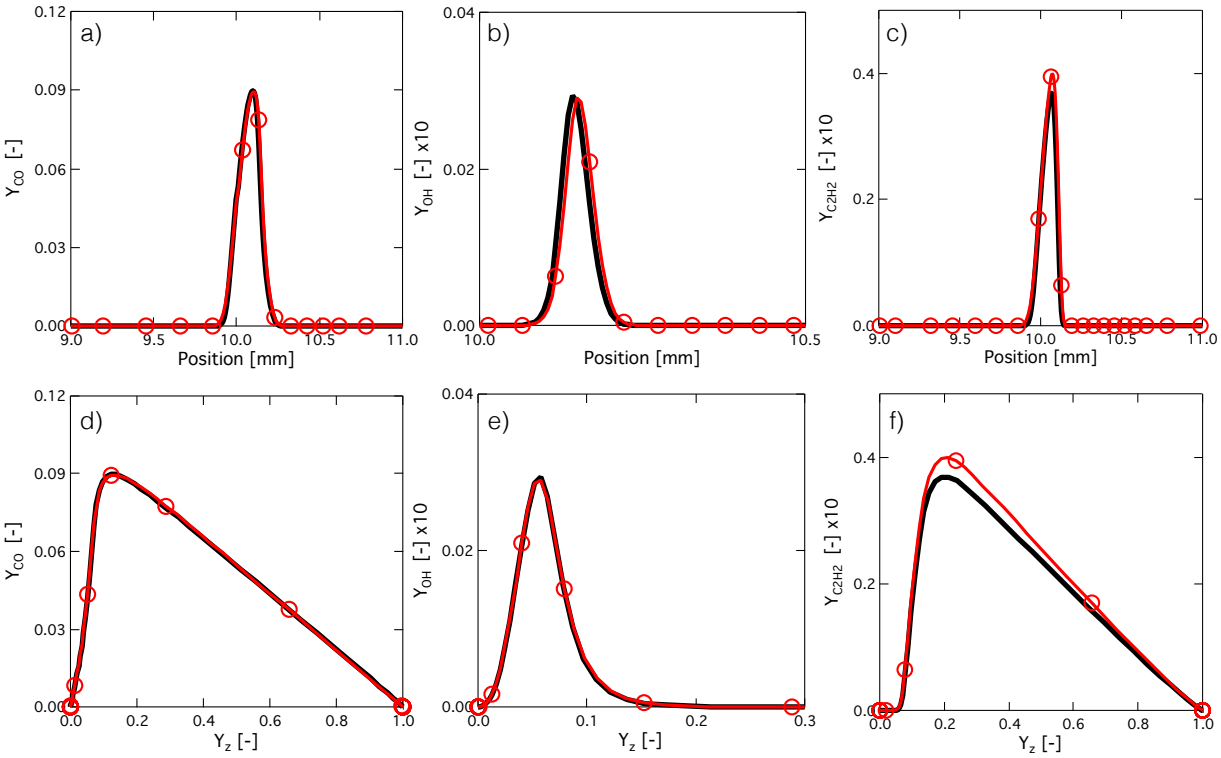

Figure 7.9: Structure of a DFS with $a = 2600\ s^{-1}$. Fresh gas temperature is 300 K, P = 5 bar. Spatial evolutions of a) CO b) OH and c) C_2H_2 as well as evolutions in the phase space of c) CO d) OH and e) C_2H_2 mass fraction. Detailed mechanism - Mix (solid line), ARC_18_C2H4NARA (o).

surface reactions and particle agglomerations increasing its size and mass (Kennedy, 1997; Frenklach, 2002). At the heart of these processes, aromatic species such as C_6H_6 and intermediate species such as C_2H_4, C_2H_2 and OH, are thought to play a key role. Obviously, an accurate gas-phase chemistry description is thus a pre-requisite to any accurate soot modeling (Frenklach, 2002). The soot modeling employed in this study is a simple two-equation empirical model proposed by Leung *et al.* (1991), providing good estimations of the soot levels at a low computational cost. The transport equations for the number density of soot particles n_s and the soot mass fraction Y_s are solved, in addition to the multi-species Navier-Stokes equations:

$$\frac{\partial \rho n_s}{\partial t} + \frac{\partial \rho u_i n_s}{\partial x_i} = k_T \frac{\partial}{\partial x_i}\left(\frac{\rho \nu n_s}{T}\frac{\partial T}{\partial x_i}\right) + \dot{\omega}_{n_s}, \tag{7.3}$$

$$\frac{\partial \rho Y_s}{\partial t} + \frac{\partial \rho u_i Y_s}{\partial x_i} = k_T \frac{\partial}{\partial x_i}\left(\frac{\rho \nu Y_s}{T}\frac{\partial T}{\partial x_i}\right) + \dot{\omega}_{Y_s} \tag{7.4}$$

where $k_T = 0.54$ is a constant of the model and ν is the kinematic viscosity. The source terms on the right-hand-side of Eqs.(7.3) & (7.4) are given by:

$$\dot{\omega}_{n_s} = \frac{2N_A k_1(T)}{C_{min}}[C_2H_2] - 2C_a\left(\frac{6M_s}{\pi\rho_s}\right)^{1/6}\left(\frac{6\kappa T}{\rho_s}\right)^{1/2}(\rho n_s)^{11/6}\left(\frac{\rho Y_s}{M_s}\right)^{1/6}, \tag{7.5}$$

$$\dot{\omega}_{Y_s} = M_s\left[k_1(T)[C_2H_2] + k_2(T)[C_2H_2]S^{1/2} - k_3(T)S[O_2]\right] \tag{7.6}$$

where $C_{min} = 100$ is the number of carbon atoms in a nascent soot particle and $C_a = 9$ is an agglomeration rate constant; N_A and κ are the Avogadro and Boltzmann constants, respectively, and [X] designs the molar concentration of species X. $M_s = 12.011$ kg.kmol^{-1} and $\rho_s = 2000$ kg.m^{-3} are the soot molar mass and density, respectively; and S is the soot volume surface per unit volume of gas, based on the evaluation of a mean particle size (see Leung *et al.* (1991)). This model postulates that the soot formation and growth occur through four main stages, translated into the different R.H.S terms. Y_s evolution is governed by nucleation, surface growth, and oxidation, while n_s evolves according to nucleation and coagulation. These stages are described by a set of reaction rates k_i of the Arrhenius type, involving each a set of 3 constants, A_i, n_i and Ti, that must be determined to reproduce the correct sooting tendencies. As pointed out by Franzelli *et al.* (2015*b*), retrieving the right tendencies in laminar configurations does not guarantee a correct prediction in the complex configuration. In their simulations, an underestimation of the instantaneous peaks of soot volume fraction by about two orders of magnitude was observed. Accordingly, the reaction rates were modified to better account for the physics in this particular configuration. The final set of parameters are reported in Table 7.2.

		A_i	n_i	T_i
k_1	(nucleation)	2.0 10^4	0	21100
k_2	(growth)	1.2 10^4	0	12100
k_3	(oxidation O_2)	1.0 10^2	0.5	19680

Table 7.2: Arrhenius constants for the empirical soot model, adapted to the present configuration from Leung *et al.* (1991).

7.4.2 Validations in canonical configurations

We now investigate the ability of the ARC_18_C2H4NARA mechanism to predict soot levels in canonical sooting configurations, when coupled to the empirical soot model described above. The solver Cantera (Goodwin *et al.*, 2014) is employed to perform the computations. Results from the FPI tabulation are reported for P = 3 bars only.

The first validation case is the experimental configuration of Tsurikov *et al.* (2005), providing both temperature and soot volume fraction profiles for two different pressures (P = 3 and 5 bars) and several equivalence ratios (ϕ = 2.3 - 2.5) in a burner premixed ethylene flame. Results are plotted in Fig. 7.10 (a), for two cases as reported on the graph. Experimentally, a strong dependency of soot volume fraction to pressure and equivalence ratio is observed. As expected, results are not perfect, since the parameters of the empirical model were adjusted following the results of Franzelli *et al.* (2015*b*) (see discussion at the end of Section 7.4.1) on the P = 3 bars case; thus explaining in part the larger discrepancies in the case P = 5 bars. Note furthermore that the offset between

the two chemistry descriptions in the case P = 3 bars is not due to the unity Lewis assumption used to construct the FPI table, but rather to a discrepancy in the prediction of C_2H_2. Indeed, the operating points of interest here ($\phi = 2.3$) lie well outside of the targeted range of reduction of the ARC mechanism. However, results are considered satisfactory since, in particular, equivalence ratio and pressure dependencies are correctly captured.

The second validation is a non-premixed case studied experimentally by Hwang & Chung (2001), where two different categories of operating points were considered: SF (soot formation) flames correspond to flame stabilizing on the oxidizer side while SFO (soot formation/oxidation) flames refer to flames stabilizing on the fuel side of a stagnation plane. SFO flames are subject to a high level of soot oxidation. It is noted that the flames are investigated under atmospheric pressure, hence they are not exactly representative of the configuration of interest in this study. However, they are interesting in that they illustrate the difference of soot levels to be expected in partially-premixed configurations where secondary oxidation is present. For this reason, only results with the ARC mechanism are reported on Fig. 7.10 (b) & (c). The legend is as in Hwang & Chung (2001). The first observation is that soot volume fraction levels can vary by more than one order of magnitude, depending on the quantity of oxidizer available. This is correctly captured by the relatively simple soot model. However, the SF flames are better predicted, which was expected: our choice of Arrhenius constants tend to slow down the oxidation since the oxidation rate parameter A_i is divided by 100 when compared to the original set of constants (Leung *et al.*, 1991) (see k_3 in Table 7.2).

Overall, results are considered satisfactory, allowing to use this model in LES.

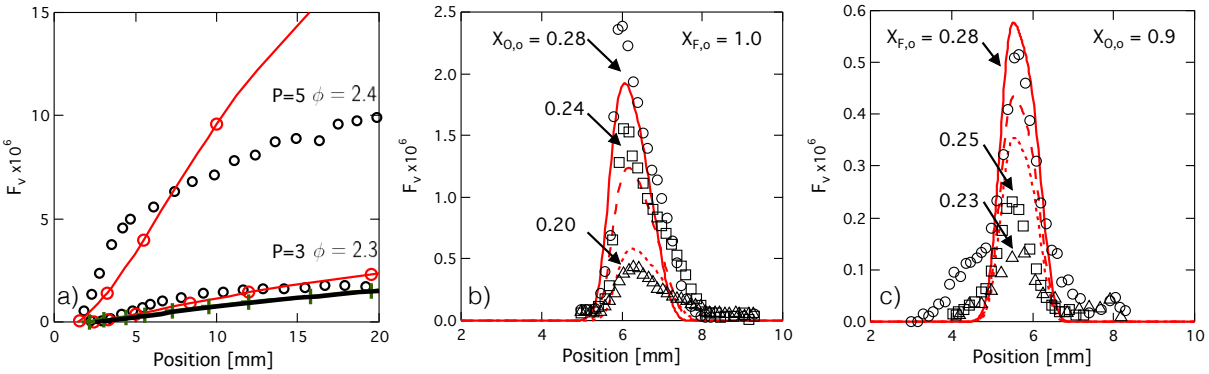

Figure 7.10: a) Soot volume fraction in premixed ethylene flames (Tsurikov *et al.*, 2005): experiment (symbols), detailed mechanism - Mix (solid line), ARC_18_C2H4NARA (o) and FPI (+). Soot volume fraction results in b) SF and c) SFO counterflow ethylene flames (Hwang & Chung, 2001): experiment (symbols), ARC_18_C2H4NARA (lines).

7.5 Experimental configuration

7.5.1 Presentation of the DLR burner

The experimental configuration studied in this work is installed at DLR and was presented and investigated in several recent publications (Geigle *et al.*, 2013, 2015*a*; Eberle *et al.*, 2014). This burner was designed to study soot formation in gas turbine combustors under elevated pressure, with or without secondary air dilution. To this end, the burner features a non-premixed swirled injection system consisting of three concentric nozzles and two radial swirlers (see Fig. 7.11a). Air at 300 K is supplied to the flame through both the central (diameter 12.3 mm) and annular (inner diameter 14.4 mm, outer diameter 19.8 mm) nozzle. The air flows are fed from separate plenums and pass radial swirlers consisting of 8 channels for the central nozzle (width 4.2 mm, height 5.4 mm, swirl number 0.82) and 12 channels for the annular nozzle (width 3.2 mm, height 4.5 mm, swirl number 0.79). Gaseous fuel (C_2H_4) is injected at 300 K between both air flows through 60 straight channels, forming a concentric ring. The fuel injection mimics the behavior of an atomizing lip observed in air-blast liquid atomizer (Lefebvre, 1998). All nozzle exit planes are located at the level of the combustion chamber dump plane. The combustion chamber measures 120 mm in height, has a square section of 68×68 mm^2, and features large optical access from all 4 sides. To enhance soot oxidation, additional air ducts (5 mm diameter) inject secondary air into the combustor 80 mm downstream the combustion chamber inlet.

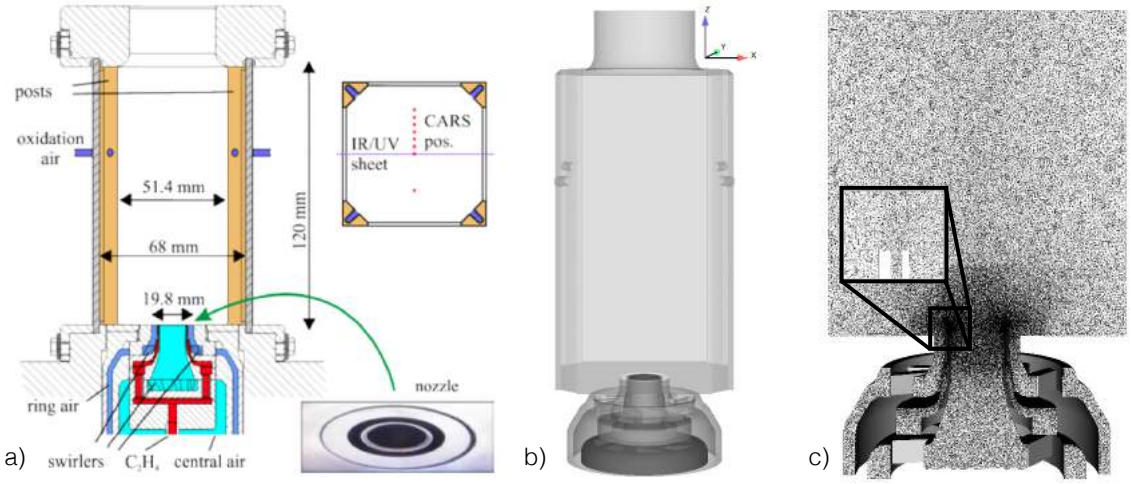

Figure 7.11: a) Sketch of the experimental configuration from Geigle et al. Geigle *et al.* (2015*a*). b) Computational domain with c) focus on the injection zone.

Amongst the various operating points experimentally studied by Geigle *et al.* (2013), the two cases chosen for the present study are summarized in Table 7.3. They differ by the operating pressure, which has been shown to have a strong effect on the soot production (Geigle *et al.*, 2013; Lammel *et al.*, 2007). The cases will be referred to as Case A and Case B in what follows. The equivalence ratio listed in Table 7.3 indicates that even though the burner is operated under overall lean conditions ($\phi = 0.86$) the primary combustion zone (PZ) is characterized by an overall rich equivalence ratio ($\phi = 1.2$).

	Pressure [Bar]	$Q_{air,central}$ [kg.s^{-1}]	$Q_{air,radial}$ [kg.s^{-1}]	$Q_{air,oxy}$ [kg.s^{-1}]	Q_{fuel} [kg.s^{-1}]	ϕ [-]	ϕ_{PZ} [-]	P_{global} [kW]
Case A	3.0	3.089×10^{-3}	7.049×10^{-3}	4.016×10^{-3}	8.191×10^{-4}	0.86	1.2	38.6
Case B	5.0	5.025×10^{-3}	1.172×10^{-2}	6.697×10^{-3}	1.364×10^{-3}	0.86	1.2	64.4

Table 7.3: Experimental operating conditions of interest.

7.5.2 Available validation data

Comprehensive validation data obtained by several laser diagnostics is available for each operating point. For the flow field validation, velocity component statistics at several positions downstream of the dump plane were obtained from Stereo - Particle Image Velocimetry (Stereo-PIV). Due to the high level of soot luminosity, two different detection schemes were employed, referred to as the Field of View (FoV) and the sum-of-correlation (SoC) (see Geigle *et al.* (2016) for definitions). These two sets of velocity data will be employed in the following analysis, although it is noted that Geigle *et al.* (2016) describe the FoV as being more reliable. For flame analysis, temperature measurements at several locations in the combustor were obtained by Coherent Anti-Stokes Raman scattering (CARS), and Laser Induced Fluorescence (LIF) was used to provide a qualitative estimate of the OH radical distribution. Finally, Planar Laser-Induced Incandescence (LII) was used to measure the soot volume fraction.

7.6 Numerical setup

7.6.1 Computational domain and numerical strategy

The computational domain is displayed in Fig. 7.11 (b). It includes the channels of both air inlets, the combustion chamber, secondary air ducts and part of the outside atmosphere (not shown). The 60 straight channels for the fuel inlet are modeled by a continuous annular nozzle. The domain is discretized into a fully unstructured mesh

using ≈ 40M tetrahedral elements, with a cell size of about 0.07 mm in the very thin (0.4 mm) fuel injection nozzle and in the primary mixing region. A picture of the mesh with focus on the fuel injection can be seen in Fig. 7.11 (c). The axial direction is referred to as the z-axis, corresponding to the main flow direction, while the x-axis and y-axis denote the transverse directions.

All simulations are performed with the LES solver AVBP (Schönfeld & Rudgyard, 1999; Gicquel *et al.*, 2011), an explicit cell-vertex massively-parallel code solving the compressible reacting Navier-Stokes equations. A third-order accurate in space and time Taylor-Galerkin finite-element scheme with low-dissipation (Colin & Rudgyard, 2000) is used for the discretization of the convective terms, while a second order Galerkin scheme is used for diffusion terms. A full description of the filtered LES equations can be found, e.g., in the review of Gicquel *et al.* (2012). The filtering operation produces unclosed sub-grid scale (SGS) turbulent fluxes that must be modeled. The Reynolds SGS stress tensor is modeled using the WALE approach (Nicoud & Ducros, 1999), while the SGS diffusive heat and species fluxes are modeled by analogy with the filtered diffusive heat and species fluxes, assuming constant turbulent Prandtl and Schmidt numbers ($Pr^t = {Sc^t}_k = 0,6$). Turbulence-chemistry interactions are detailed in Section 7.6.2. Inlet and outlet boundary conditions are treated according to the Navier-Stokes Characteristic Boundary Conditions formulation (Poinsot & Lele, 1992), and all walls are considered adiabatic non-slipping.

7.6.2 Chemistry-turbulence interaction

7.6.2.a The DTFLES approach

LES have been performed using either the FPI tabulation or the ARC_18_C2H4NARA chemical scheme. In both cases, the Dynamically Thickened Flame (DTFLES) model of Colin *et al.* (2000); Legier *et al.* (2000) was employed to ensure at least 5 points in the flame front. With this approach, a thickening factor $\mathcal{F}_{max}$ is calculated based on a theoretical flame thickness δ_l^0, by taking into consideration the local mesh size Δ_x, such that:

$$\frac{\mathcal{F}_{max}\delta_l^0}{\Delta_x} = 5 \tag{7.7}$$

A dynamic sensor $\mathcal{S}$ detects regions of high heat release where a real thickening factor $\mathcal{F} = 1 + (\mathcal{F}_{max} - 1)\mathcal{S}$ is then applied to the filtered equations. An efficiency function $\mathcal{E}(s_l)$ based on a SGS equilibrium assumption between turbulence and flame surface (Meneveau & Poinsot, 1991; Colin *et al.*, 2000) is used to account for the loss of flame-turbulence interaction resulting from flame front thickening.

In partially premixed conditions a wide range of equivalence ratios is encountered that induces significant changes of δ_l^0 and s_l (see Figs. 7.2 (b) & 7.4(b)). Furthermore, since this burner is operated under elevated pressure, the flame thickness δ_l^0 can locally be very small (≈ 0.1 mm around stoichiometry). Thus, choosing single reference values can lead to locally erroneous evaluations of $\mathcal{E}$ and to either too many or not enough points to discretize the flame front. Usually, the values of δ_l^0 and s_l are chosen at stoichiometry resulting in unnecessary high thickening factors in lean and rich regions. In the present simulations, this problem is addressed by adapting the values of δ_l^0 and s_l to local flow conditions. This results in acceptable thickening factors, ranging from 3 in the central region to 30 at the tip of the flame for case A, and from 3 to 40 for case B.

Note that although the DTFLES model was primarily designed for premixed flames, many studies have demonstrated its efficiency on partially premixed configurations (Legier *et al.*, 2000; Franzelli *et al.*, 2013*a*; Esclapez *et al.*, 2015; Jaravel *et al.*, 2016). As such, this model appears suitable for the present configuration.

7.6.2.b Building the sensor

The sensor $\mathcal{S}$ is built differently with both chemistry descriptions. It is based on the source term of fuel in the ARC simulation (following the methodology of T. Jaravel described in Section 6.2.2.c), and on the gradient of Y_c in the FPI simulation. It has been verified that the resulting sensor shape is similar in all LES, as displayed in Fig. 7.12 (top row) for Case A with both the FPI table and the ARC mechanism (grey iso-contours). $\mathcal{S}$ is seen to encompass the region of high heat release rate in all simulations.

As a result, the spatial distribution of the efficiency and thickening with respect to the flame front, as well as the maximum levels exhibited by these quantities are fairly similar in both simulations, as shown on the bottom row of Fig. 7.12 for the efficiency.

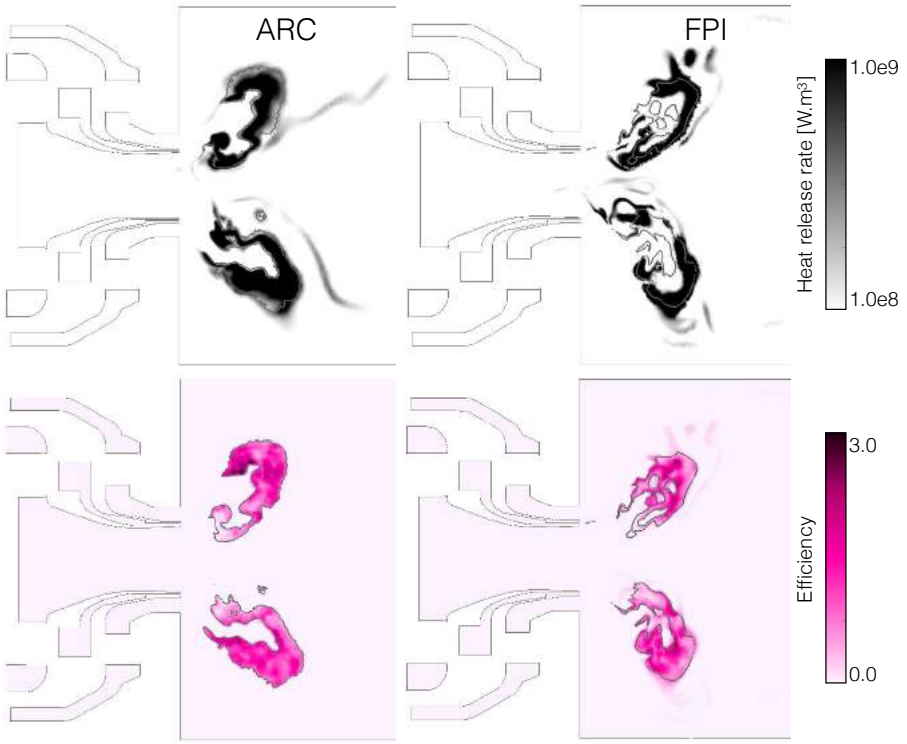

Figure 7.12: Instantaneous fields of heat release rate (top) and efficiency (bottom) with overlaid iso-contours of $\mathcal{S} = 0.5$, for both the ARC and 2S chemistry descriptions.

7.6.3 Computational requirements

The time step of the simulation is limited by the acoustic CFL number, set to 0.7 for stability reasons. This value imposes a simulation time step similar for both chemistry descriptions and operating conditions (Case A and B) and equal to $\approx 0.2 \times 10^{-7}$ s . The computation of 1 ms of physical time then requires $\approx$ 50000 iterations. A summary of CPU requirements for each LES computations is presented in table 7.4, using Intel Haswell nodes (E5-2680v3) cadenced at 2.5 GHz.

No noticeable differences were observed in terms of CPU requirements between both ARC simulations. As expected, employing an ARC mechanism requires more CPU than employing an FPI table. Note however that using the ARC mechanism requires to handle three times as much species than when using the FPI table, but that the FPI-LES simulation is only 2 times faster than the ARC-LES simulation. Indeed, in our case, no efforts were made to optimize the handling of the two-dimensional table, which can prove to be a very time consuming process.

Flow statistics have been collected during 30 ms, i.e., about 2 flow through time of the combustor, for all simulations.

	Case A - ARC	Case A - FPI	Case B - ARC
Navier-Stokes	5	5	5
Transported species	18	2	18
Soot model	2	2	2
Total transported variables	**25**	**9**	**25**
CPUh for 1 ms	**12500**	**6200**	**12500**

Table 7.4: Summary of computational requirements

7.7 Results and discussion

Due to the high operating pressure, no experimental velocity information is available for Case B. Furthermore, the flow-field features are found to be very similar to those of case A. As such, flow-field validations will mainly focus on Case A. Likewise, only Case A will be used to investigate the flame structure predicted by the ARC mechanism (ARC-LES approach) in comparison with that of the FPI tabulation (FPI-LES approach). Differences induced by increasing the operating pressure on the flame dynamic and structure will be discussed with regards to their effect on pollutant and soot predictions.

7.7.1 Reactive flow-field validations

Figure 7.13 (b) provides a comparison of mean axial velocity fields obtained with both chemistry descriptions. Similar profiles are observed. The main flow structures are characteristic of swirled stabilized burners where a large inner recirculation zone (IRZ) is located in the center of the combustion chamber, induced by the radial expansion of the swirled jets, and corner recirculation zones are observed in the outer part of the swirled jets. The IRZ extends downstream up to z = 90 mm, and its radial expansion is slightly more pronounced with the ARC mechanism. Its most upstream point is located within the central air injection nozzle in both LES, and is subjected to oscillations: as observed in the experiment, the burner is prone to instabilities and flame stabilization is difficult to reach. This is especially true in the case of the FPI, where the IRZ extends all the way up into the injector.

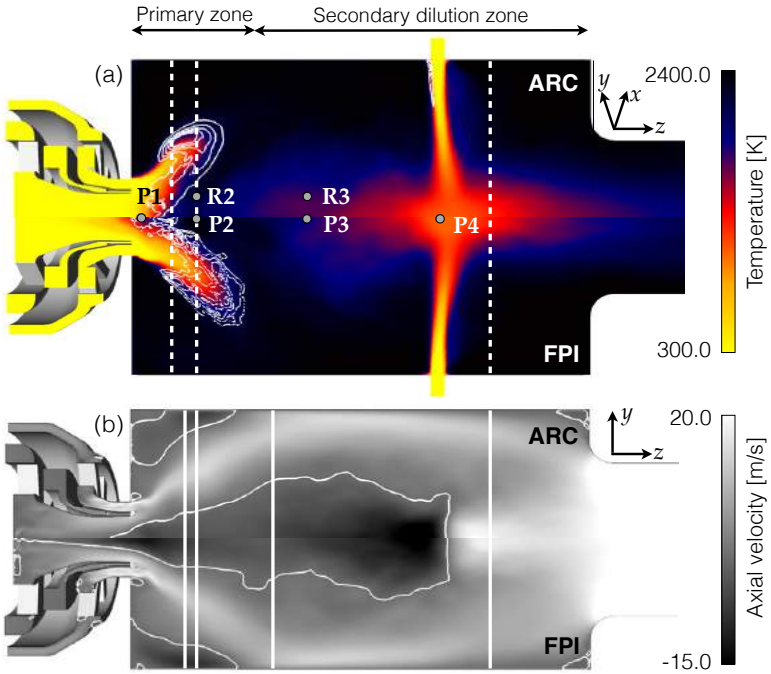

Figure 7.13: (a) Mean temperature fields, with heat release rate iso-contours in white to localize the reaction zone. ARC_18_C2H4NARA (top half) and FPI (bottom half). (b) Time-averaged axial mean velocity fields, with white iso-contours corresponding to zero axial velocity. ARC_18_C2H4NARA (top half) and FPI (bottom half).

As can be seen on the mean velocity fields, the secondary air injected at z = 80 mm interacts with the downstream end of the IRZ, inducing an intermittent variation of the recirculated gas temperature and composition, and leading to the entrainment of secondary air back into the primary combustion zone (see Fig. 7.13). These effects are visible on the mean temperature fields provided on Fig. 7.13 (a), where it is noted that the recirculated fresh gases reach further upstream with the ARC mechanism.

In Fig 7.14, numerical axial, radial and tangential velocity profiles are validated against experimental data at 4 axial positions of interest in the combustion chamber: z = 15 mm and 18 mm are located in the primary combustion zone, z = 95 mm is located near the secondary air injection while z = 38 mm sits in between. These positions are materialized by white solid lines on Fig. 7.13 (b). Note that both sets of experimental data discussed in section 7.5.2 are presented. A very reasonable agreement is reached with both chemical descriptions for the

first 3 axial positions, considering the scatter of experimental data. The width and magnitude of the IRZ near the injector, in particular, is well captured by both LES. Larger discrepancies are observed around z = 95 mm. In both simulations, the tangential velocity is under predicted, while an over prediction of axial velocity near the central axis is observed. This axial position is located just after the meeting point of the 4 dilution jets. In the LES, intermittent variations of the jets positions are observed, associated with an oscillation of the stagnation point.

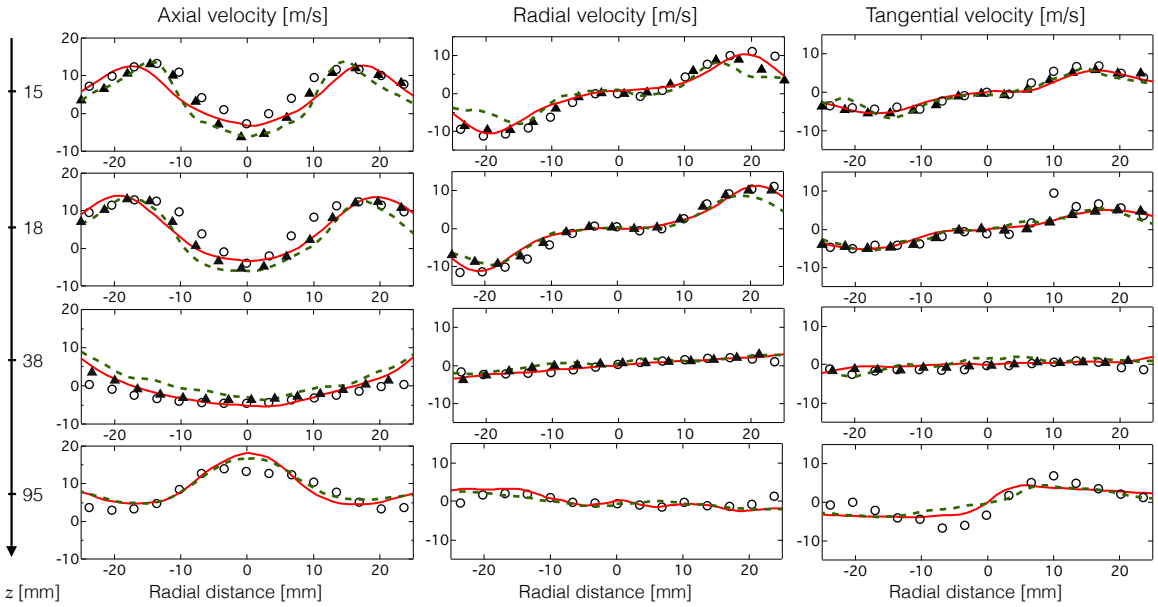

Figure 7.14: Mean axial, radial and tangential velocity profiles for both chemical mechanisms extracted in mid-plane at z = 15, 18, 38 and 95 mm, ARC_18_C2H4NARA (solid line), FPI (dotted line), experiment: FoV(▲) and SoC(o).

Figure 7.13 (a) displays the mean temperature fields in the plane of the dilution holes, with heat release rate iso-contours in white to localize the reaction zone. A "V" shape flame is observed with both mechanisms, although the mean flame opening angle is wider with the ARC mechanism, as can be seen also on the radial profiles of temperature provided in Fig. 7.15 (b) at locations materialized by dashed white lines in Fig 7.13 (a). As suggested by the longer tail of the distribution at z = 18 mm and x = 8 mm presented in Fig. 7.15 (c) (probe R2 in Fig. 7.13 (a)), differences between both LES in flame front regions can at least partially be attributed to a higher intermittency with the FPI tabulation, when the flame appears more stable with the ARC mechanism. It is also true further upstream in the central zone near the injector, where the sharp mean temperature gradient of Fig. 7.15 (a) top reveals that the flame stabilizes downstream of the tip of the recirculation zone with the ARC mechanism. On the contrary, with the FPI tabulation, a broader region of intermediate temperatures is observed. This is consistent with the longer IRZ observed in this latter case. The unstable behavior is further revealed, for instance, in the histograms of temperature for the position z = 3 mm and x = 0 mm (probe P1) which confirms the frequent occurrence of burnt gases in this central region. As a result, an over prediction of the mean temperature near the combustor main axis is observed in Fig. 7.15 (a), with FPI, in the range $0 < z < 10$ mm. With the ARC mechanism, the right tendencies are recovered.

The flame obtained with the ARC mechanism is also more compact. This shorter flame signature, with wide opening angle, is visible on the radial profiles of temperature for the positions $z = 12$ mm and $z = 18$ mm. If the flame angle seems better predicted with ARC, the apparently longer flame obtained with FPI leads to minimum temperature levels closer to experiments.

Mid chamber, the PDFs at probes P3 and R3 at $z = 45$ mm along with the radial temperature profiles (not shown) suggest that the radial extend of the recirculated fresh gases is better captured in the LES with the ARC mechanism.

Further downstream, both LES exhibit the right trends, as evidenced by the axial temperature profile, the radial profile at $z = 95$ mm and the PDFs at probe P4 at $z = 81$ mm, although it is noted that the temperature drop in the core of the secondary dilution zone is slightly over predicted with the FPI simulation.

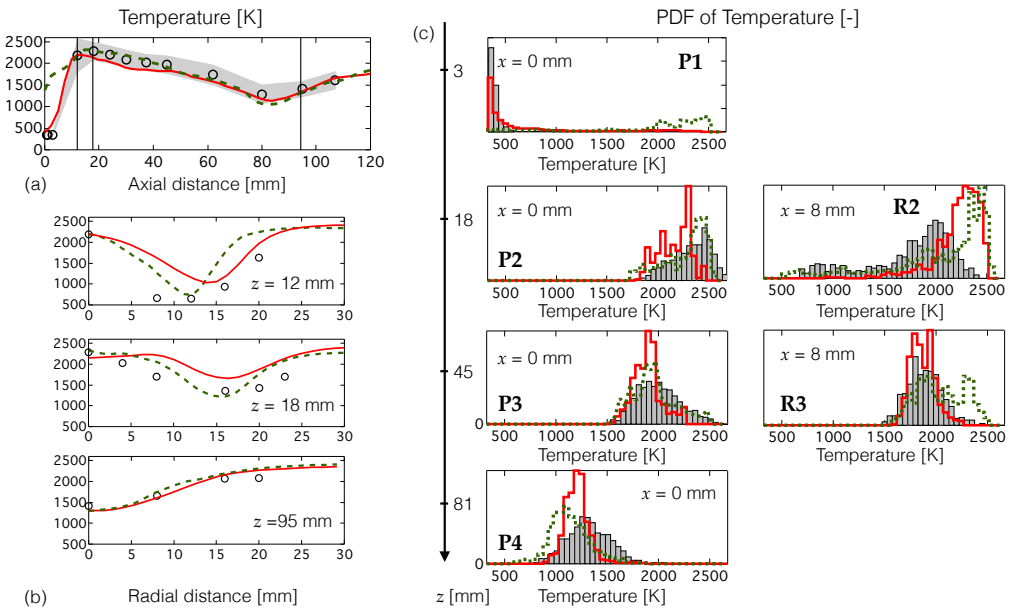

Figure 7.15: a) Mean axial temperature profiles with experimental distribution width (shaded area) and b) mean radial evolution of temperature extracted in mid-plane at z = 12, 18 and 95 mm, ARC_18_C2H4NARA (solid line), FPI (dotted line), experiment (symbols). c) Probability Density Functions of temperature in locations of interest, ARC_18_C2H4NARA (solid line), FPI (dotted line), experiment (bars).

7.7.2 Instantaneous flame structure

Figure 7.16 shows instantaneous fields of temperature as well as OH and CO mass fractions, in a central cut plane of the combustor, for both LES. The flame is highly turbulent, as can be inferred from the white heat release iso-contours on the temperature fields, Fig. 7.16 (a). It is confirmed also that the main flame extent obtained with the FPI tabulation is significantly longer. However, the flame surface, calculated as the integral of the flame surface density ($\int_V |\nabla c|\ dV$ where c is directly transported in the FPI simulation and is computed in the ARC simulation) gives a total flame surface of about 70 cm^2 with the FPI and of about 85 cm^2 with the ARC mechanism. This reveals that the longer flame extent in the FPI case is due to a more lifted and fragmented flame front. In Fig 7.16 (b), both OH fields reveal multiple reaction fronts. In particular, high levels of OH are found behind the main reaction front in the outer shear layer (OSL) of the swirled jets. Other peaks of OH are also observed in the outer part of the central recirculation zone, coincident with the grey stoichiometric iso-contours. The combustion regimes in this area appears different in both LES. Figure 7.16 (c), shows that CO is massively produced behind the primary flame front and that similar levels are found in both LES. The regions of high CO concentration coincide with rich areas with low OH levels. Note also a less homogeneous distribution of CO and OH in the ORZ with the FPI simulation.

Following these observations, the domain is divided into two zones (see Fig. 7.13 (a)): the Primary combustion Zone (PZ) and the secondary Dilution Zone (DZ), which are studied separately in order to emphasize the effect of the chemistry description on the flame structure. Flame dynamics are first discussed focused on the ARC simulation when similar features were found in both LES.

7.7.2.a Flame dynamics

In both LES, the PZ flame is found to oscillate at a given frequency corresponding to the PVC frequency (500 Hz, similar to the value measured in the experiment by Eberle *et al.* (2014)). The interaction with the PVC wrinkles the flame front located in the inner shear layer (ISL) and induces the intermittent formation of rich pockets of hot gas mixture at the tip of the V-shaped flame, which are pushed along the walls towards the exit of the combustor. This is visible on the CO fields of Fig. 7.16 (c), where regions of high CO concentration are found throughout the combustion chamber following the outer part of the recirculation zone. These dynamics are further illustrated on a series of instantaneous snapshots of CO and C_2H_2 mass fractions with overlaid iso-contours of mixture fraction in white and of C_2H_4 in black, Fig. 7.17. The snapshots follow a pocket of rich mixture identified by the black arrow. Around t = 0.0 ms, the pocket forms around rich -almost pure- pockets of C_2H_4 with peripheral reaction,

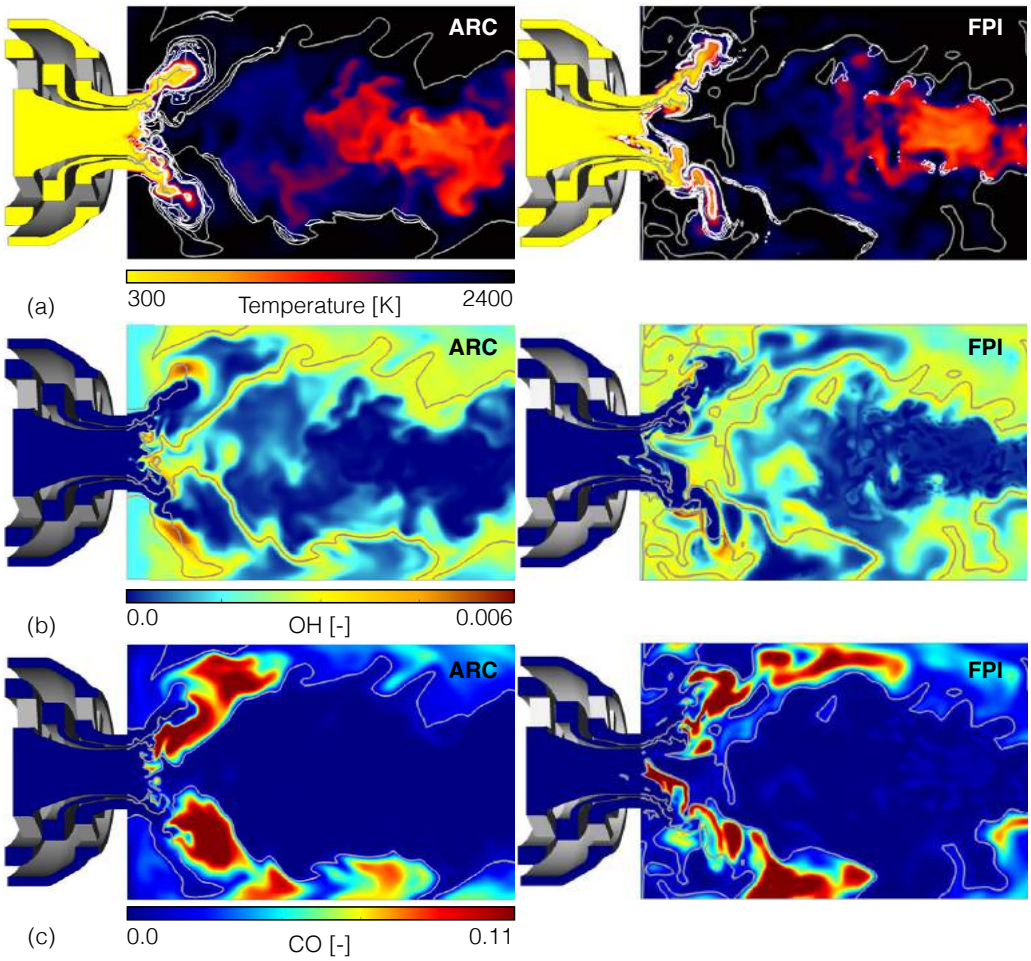

Figure 7.16: Mean fields of a) temperature b) OH mass fraction and c) CO mass fraction, with heat release rate iso-contours in white to localize the reaction zone and stoichiometric iso-contour in grey. Left: ARC mechanism, right: FPI tabulation.

and grows by diffusion. Progressively, the pocket detaches from the main flame before being convected away towards the DZ, at t = 1.0 ms. As the reaction proceeds, C_2H_4 is first converted in C_2H_2 in high heat release regions, in the flame core, as observed for instance at t = 0.5 ms in the insert depicting the temperature with white heat release iso-contours. Eventually, at t = 1.0 ms, the pocket is mainly composed of CO and combustion products such as H_2O and CO_2.

It is clear from the heat release iso-contours and the OH fields of Fig. 7.16 that air entering from the dilution jets induce secondary intermittent reaction fronts downstream of the main C_2H_4 reaction zone. They follow the stoichiometric line, have relatively low heat release levels ($\approx 10^8$ W.m^3), and are located at the meeting of the IRZ with the aforementioned hot and rich pockets. These reaction fronts are diffusion fronts between the residual CO and the O_2 entering from the dilution holes. If the heat release iso-contours following the stoichiometric line are also visible with the FPI, the correlation with OH is less clear. Additionally, in the case of FPI, we observe high heat release iso-contours in relatively low temperature regions filled with air incoming from the dilution jets (Fig. 7.16 (a)). As already mentioned, the flame structure in this area appears different in both LES, as will be discussed in section 7.7.2.c.

Another intermittent behavior of the flame is observed in the central region of the PZ, near the dump plane. As mentioned previously, air inflowing from the dilution holes induce a low frequency motion of the IRZ in the axial direction. Thus, different instantaneous flow-field configurations can be observed, as illustrated on Fig 7.18 (a). The sequence displays subsequent snapshots of temperature with superimposed white heat-release rate iso-contours, and grey stoichiometric iso-contour. At t_1 = 0.0 ms, the fresh air inflow (1) from the central air nozzle is clearly distinct from the recirculated fresh gases (2), as indicated by the two separated stoichiometric iso-contours. Between the two, the pockets of hot rich mixture previously discussed, mainly composed of CO, are found. This type of flow field configuration will be labelled type 1. Progressively, zone 2 moves upstream towards zone 1, while the burnt gases region separating the two grows thinner. They eventually merge at t_1 =

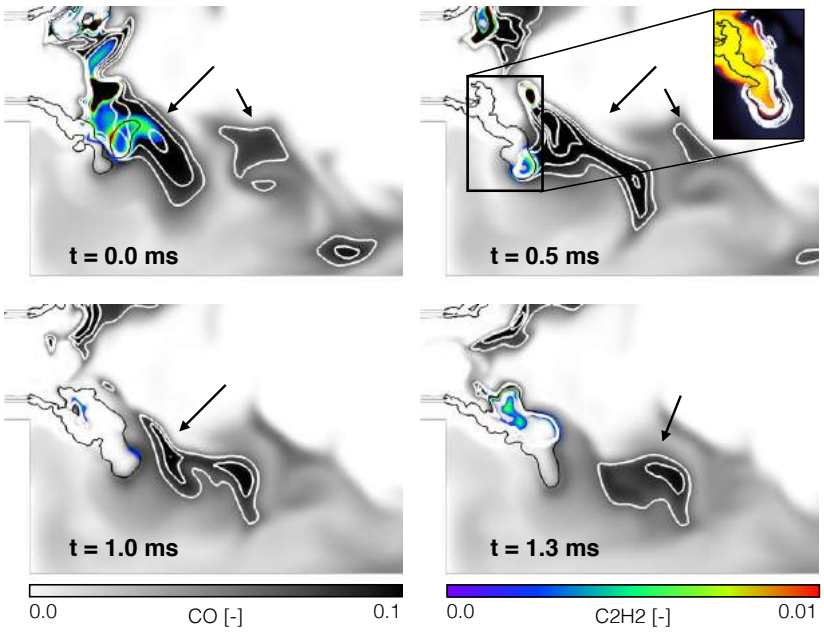

Figure 7.17: Sequence of instantaneous fields of CO and C_2H_2 mass fraction, from the LES with the ARC mechanism. White iso-contours localize pockets of rich mixture ($1.2 < \phi < 1.5$) while black iso-contours represent pockets of C_2H_4. The insert on the top right Figure is a close up coloured by temperature, with white heat release iso-contours.

1.8 ms. This leads to a flow field of type 2. This sequence also illustrates that type 1 configuration promotes reaction fronts between zone 1 and the recirculated burnt gases. These reaction fronts are CO diffusion structures similar to those observed on the stoichiometric iso-contours of Fig 7.16 (a), and they will be further studied in section 7.7.2.d.

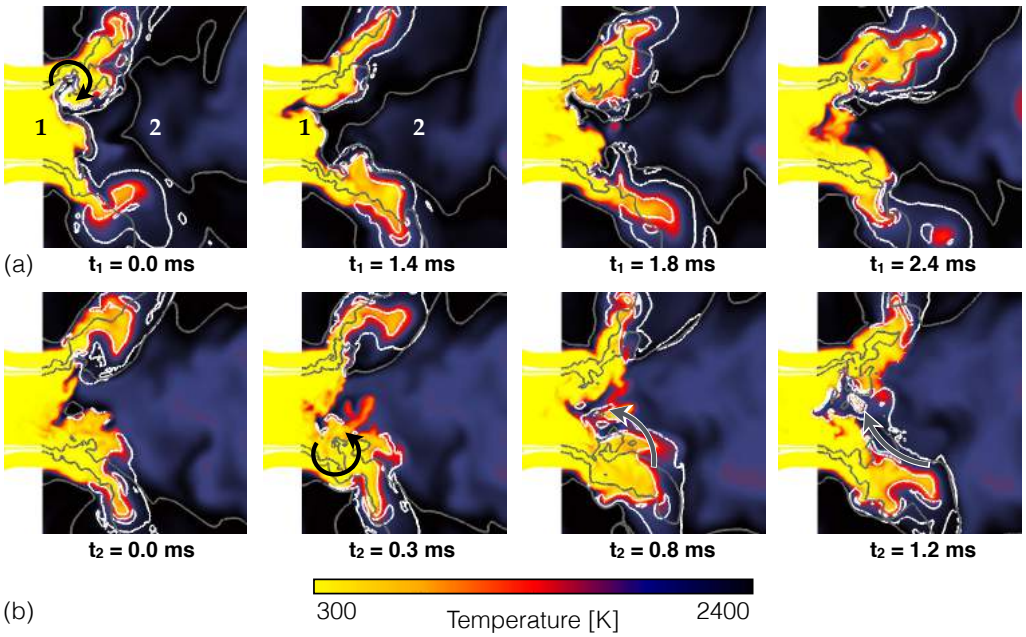

Figure 7.18: Sequence of instantaneous fields of temperature, from the LES with the ARC mechanism. Heat release rate iso-contours in white localize the reaction zone and grey iso-contours represent the stoichiometric line. (a) Intermittence of the flow fields of type 1 and 2 (see text). (b) Illustration of the reformation mechanism of a flow type 2 from a flow type 1.

When zones 1 and 2 join, the temperature eventually drops in the central region, as shown in the bottom sequence of Fig. 7.18. The recurrent interaction of the ISL with the PVC enhances the premixing of fuel and air. It further induces a swirling motion of reacting fronts, periodically forcing burning premixed pockets towards the center, reigniting locally flammable mixtures. The swirling motion effect is underlined by a black arrow at $t_2 =$

0.3 ms in Fig. 7.18 (b), but also at $t_1 = 0.0$ ms in Fig. 7.18 (a). The reaction front propagation towards the center is illustrated by a grey arrow at $t_2 = 0.8$ and 1.2 ms in Fig. 7.18 (b). A burning pocket of -rich- premixed fuel and air was detached from the right lobe of the flame (bottom part of the Figures), and pushed towards the left lobe (top part of the Figures). High heat release rate regions follow its motion. This type of event can lead to the formation of a new stable layer of burnt gases between the central air inflow and the IRZ and to the reformation of a flow field configuration of type 1.

7.7.2.b Combustion regimes

First introduced by Yamashita *et al.* (1996), the local Takeno Index (TI) is often used to distinguish premixed from non-premixed reaction fronts. The TI is based on simplified geometrical considerations, assuming a locally one-dimensional topology of the flow, where alignment of fuel (F) and oxidizer (O) gradients reveal a premixed flame front when opposite gradients indicate a diffusion front:

$$TI = \frac{\nabla Y_F \cdot \nabla Y_{O_2}}{|\nabla Y_F \cdot \nabla Y_{O_2}|} \tag{7.8}$$

Several improvements to the TI have been proposed in the literature. Fiorina *et al.* (2005) use different evaluations of the gradient of oxidizer to best distinguish diffusion driven fronts apparently premixed burning. Knudsen & Pitsch (2009) evaluate the relative contributions of premixed and non-premixed terms to the total progress variable source term budget. These author further acknowledge that, by focusing solely on the fuel, the classical formulation has limitations when complex kinetic mechanisms are employed. In particular the combustion of long hydrocarbons will proceed through smaller components, as it is the case in this work, where C_2H_4 dissociates in C_2H_2 and CO. In an attempt to differentiate between pure C_2H_4 and CO combustion fronts, two TI are employed, based either on C_2H_4 (TI_f, Figure 7.19 (a)) or CO (TI_{CO}, Figure 7.19 (b)) as a fuel, in Eq. 7.8. Note that both TI are conditioned on the source term of the fuel employed, so that when no reaction takes place, TI = 0.

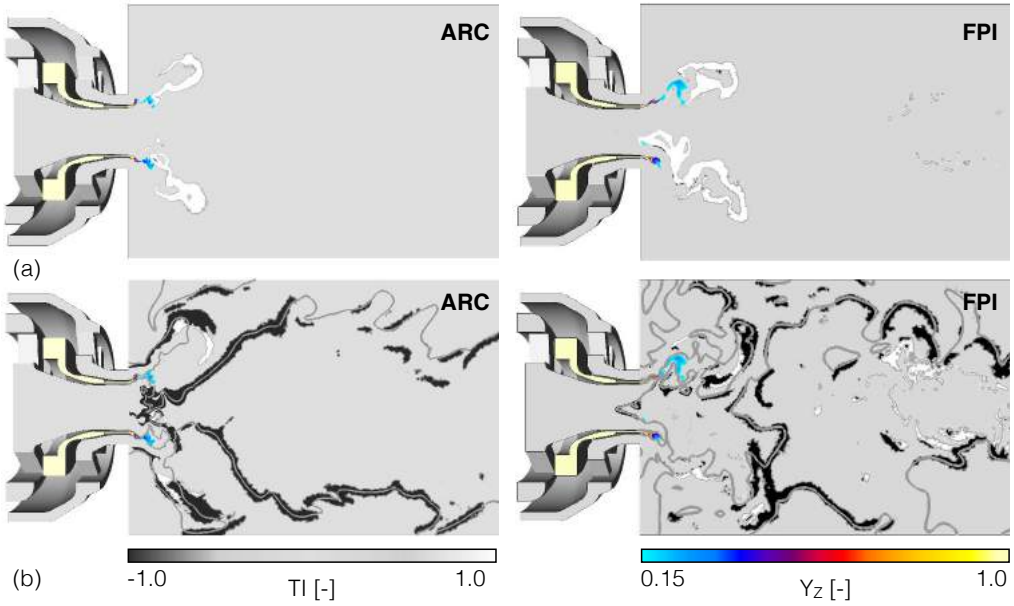

Figure 7.19: Takeno Index computed based on a) C_2H_4 as a fuel and b) CO as a fuel, with overlaid grey stoichiometric iso-contour and Y_Z iso-volume. Left: ARC mechanism, right: FPI tabulation.

With both chemical descriptions, the TI_f reveals that the PZ exhibits a premixed flame front in the wake of the swirled jets. C_2H_4 diffusion flame structures are rarely observed, contrarily to what could be expected from a non premixed injection system. In fact, the intense shear layers between the inlet streams along with the PVC interactions enable a complete premixing of the fuel jet with the incoming air. The FPI tabulation is thus expected to accurately predict the flame structure in this region.

The TI_{CO} is more complex to analyze, especially in the FPI simulation, due to the more fragmented field obtained. However, we clearly distinguish the non-premixed structures corresponding to the reaction fronts

between unburnt products from the primary rich premixed flame with air incoming from the dilution holes, already discussed in section 7.7.2.a. It is interesting to note that those combustion fronts closely follow the C_2H_4-based stoichiometric iso-contour. In fact, by making use of a two-step global reaction mechanism involving any chosen carbonate intermediates (I), it is possible to rescale the definition of the local equivalence ratio:

$$\Phi = s^{C_2H_4} \frac{Y_z \, Y_{C_2H_4,0}}{(1 - Y_z) Y_{O_2,0}} \tag{7.9}$$

to that of the intermediates:

$$\Phi_I = s^I \frac{Y_z \, Y'_{I,0}}{(1 - Y_z) Y'_{O_2,0}} \tag{7.10}$$

This rescaled definition show that the stoichiometry ($\Phi_I = 1$) of any intermediates always corresponds to $Y_z = z_{st} = 0.063$ (see Appendix A). As such, any type of diffusion front will gather around this particular Y_z value. This observation is interesting in that it allows to distinguish between "real" CO diffusion structures and diffusion structures resulting from the PZ premixed post-flame, in Fig.7.19 (b).

A few isolated premixed like structures are found in the second part of the combustion chamber, with the FPI tabulation, when none is detected in the ARC simulation. This dynamic is discussed in more depth in the next section.

7.7.2.c Dilution Zone (DZ)

To better understand the dynamics in the DZ center, Fig. 7.20 displays a close view of the area. The heat release rate, TI_{CO}, source term of CO and mass fraction of C_2H_4 are reported, for both LES.

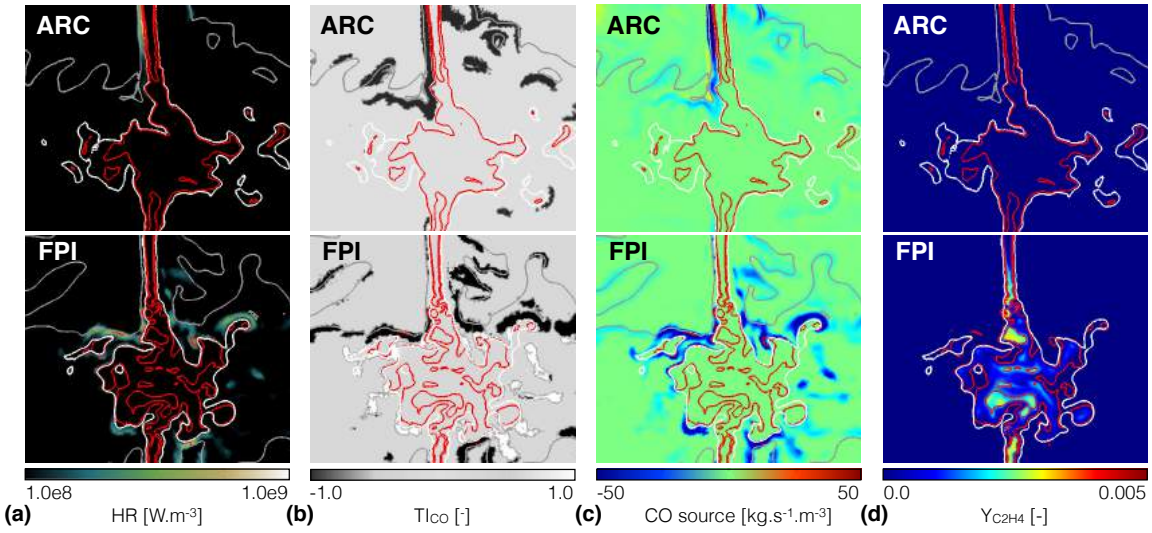

Figure 7.20: Instantaneous views in the plane of the dilution holes for (a) the heat release rate, (b) TI_{CO}, (c) the source term of CO and (d) Y_{C2H4}. The grey iso-contour marks the stoichiometry, the white iso-contour marks the lower flammability limit while inside red iso-contours are values of c smaller than 0.95. Top: ARC mechanism, bottom: FPI tabulation.

The most striking observation is that regions of high heat release rate are not localized in the same areas in both LES. ARC mainly predicts strong CO combustion fronts along the dilution jets (Fig. 7.20 (a) & (b)), where fresh air comes into contact with recirculated hot rich pockets, while the flame fronts closely follow the white flammability limit iso-contour with the FPI. An inspection of the TI_{CO} in that region in the FPI case tells us that about 50% of those structures are premixed-like, when they are all exclusively non-premixed with the ARC mechanism. Further, many amongst the non-premixed structures found in the FPI-LES do not follow the stoichiometric grey iso-contour, so that in regards with what was discussed in Section 7.7.2.b, they might not be true diffusion fronts. A careful inspection of the mass fraction of C_2H_4 in this region (Fig. 7.20 (d)), with overlaid c iso-contours in red, reveals that these structures that follow the flammability iso-contour actually result from a "virtual" post-combustion of very lean C_2H_4 premixed fronts. However, these fronts are clipped in the present simulation, since they are considered to belong to the non-flammability region. This is an artifact of

the type of canonical configurations chosen to built the look-up FPI table and of the interpolation method outside flammability limits. In particular, also due to interpolation in the table for very small c and non-negligible Y_z values, a small amount of fuel mass fraction is predicted inside the dilution jets, which is, of course, unphysical.

This regime analysis is confirmed by an inspection of the scatterplots of CO mass fraction, presented on Fig. 7.21 (a) and (c), for simulations with the ARC mechanism and FPI table, respectively. The lean mixture cut-off around $Y_Z = 0.028$ is clearly visible in the FPI scatterplot (dark grey markers). This scatterplot further shows that the aforementioned premixed CO structures are located in the vicinity of this cut-off value (black markers). It is clearly demonstrated that they are the result of an interpolation in the 2D FPI look-up table for relatively high c (> 0.75) and low Y_Z (< 0.04) values, characteristic of the secondary combustion zone. In fact, it is possible to exactly identify the region where $TI_{CO} = 0/1$ in the look-up table: it is contained in a triangle delimited by the upper c and lower Y_Z limit and by the thick solid red line trajectory shown on the insert of Fig. 7.21 (d). This trajectory is reported on all FPI-LES scatterplots of Fig. 7.21, and is seen to encompass all points with $TI_{CO} = 1$. Note that the black shaded area in the insert identifies the lean non-flammability region.

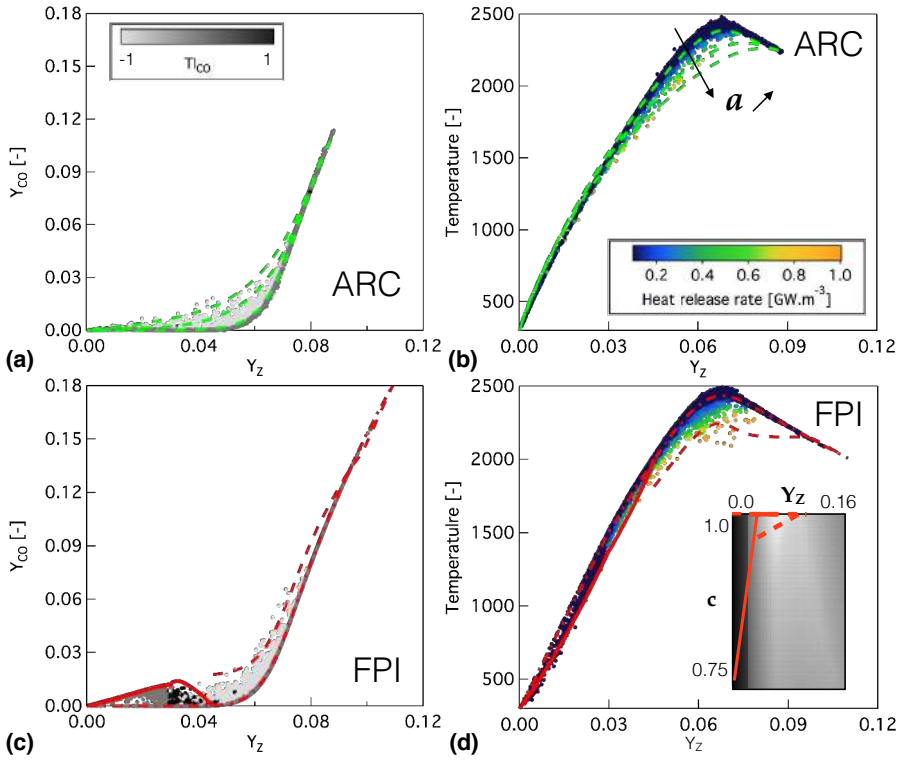

Figure 7.21: (a) and (c) present scatterplots of CO mass fraction colored by TI_{CO} while (b) and (d) present scatterplots of temperature colored by the heat release rate; for both the ARC-LES (top) and FPI-LES (bottom). ARC-LES scatterplots (a) and (b) are superimposed with laminar premixed strained CO structures in green (see text). FPI-LES scatterplots (c) and (d) are superimposed with trajectories extracted from the 2D look-up FPI table in red. The close-up in the bottom right Figure identifies the trajectories in the 2D look-up FPI table (see text).

Inside the flammability limits, the distribution of points in all the scatterplots of Fig. 7.21 appears very similar for both schemes. In particular, a large scatter is seen inside the flammability region on all plots, typical of highly strained structures. However, if strained flames are effectively present in the ARC-LES, it is not the case in the FPI-LES, which was not designed to account for strain effects nor CO structures. One-dimensional diffusion fronts between a hot, rich mixture of burnt gases ($Y_Z = 0.083$) and fresh air at 300 K are computed with CANTERA, and profiles are superimposed to the scatterplots of the ARC-LES (green dotted lines). Three representative strain rates are displayed: 50 s^{-1}, 1200 s^{-1} and 4600 s^{-1}, encompassing the data. Note that consistently with diffusion flame theory, the highest strain rate points exhibit the highest heat release rate. As expected, these points are all located on the lean side of the scatterplot and correspond, as observed on Fig. 7.20 (a), to the highly strained fronts found along the dilution jets. Note also that, again as predicted by diffusion flame theory, the heat release rate in strained CO/O_2 structures is spread over a large Y_Z range. In the FPI-LES, high heat release rate structures are seen on the rich side of the temperature scatterplot (Fig. 7.21 (d)). A closer inspection of both the LES fields and the 2D look-up table reveals that the scatter of data observed in this case is due to non homogeneous values of Y_Z and c inside the IRZ. Two bounding structures extracted from the FPI-

LES are presented on the FPI-LES scatterplots (red dotted lines), along with their trajectories in the 2D look-up table. They encompass the high heat release rate region, and explain the scatter and distribution of the data. The high heat release structures were thus erroneously identified as true CO diffusion structures in the FPI-LES.

Finally, note the higher CO levels found in the DZ with the FPI, which is linked to larger Y_Z values found in the PZ, and is discussed hereafter.

7.7.2.d Primary Zone (PZ)

Effect of partial premixing The primary reaction zone exhibits a mainly premixed flame front, characterized by a large stratification of the fuel-air mixture, due to the interaction of the pure ethylene jets with the swirled flow. In order to evaluate the mean burning equivalence ratio, the PDF of equivalence ratio in the reacting zone (i.e. source term of fuel < -10 kg.m^{-3}.s^{-1}) is computed and plotted in Fig. 7.22 (a) for both the ARC and the FPI simulations. For the ARC-LES, the PDF is found to be near gaussian, with a most probable value around

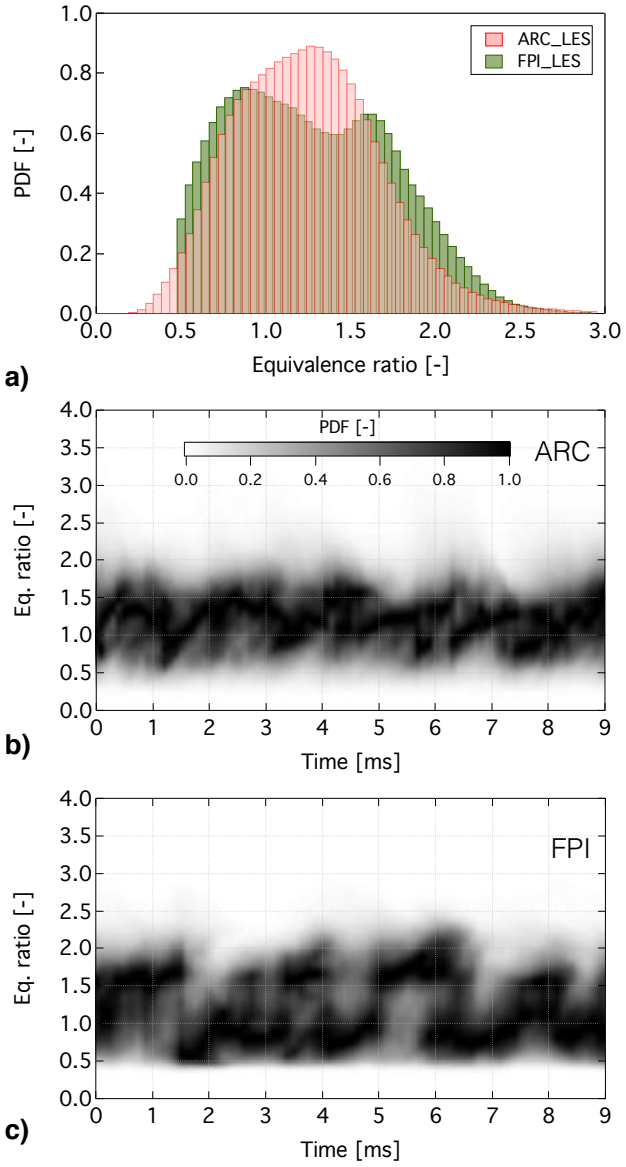

Figure 7.22: a) PDF of equivalence ratio in the reactive zone of the PZ ($\dot{\omega}_{C2H4} < -10$ kg/m^3/s) averaged over 9 ms, b) temporal evolution of the instantaneous PDF of equivalence ratio for the ARC-LES, and c) temporal evolution of the instantaneous PDF of equivalence ratio for the FPI-LES.

$\phi = 1.2$ corresponding to the global equivalence ratio of the PZ. In contrast, the FPI-LES distribution exhibits a

bi-modal shape with peaks around $\phi = 0.8$ and $\phi = 1.6$. To better explain this difference, the temporal variations of the two PDFs are plotted in Fig. 7.22 (b) & Fig. 7.22 (c) for the ARC-LES and FPI-LES, respectively. Note that for clarity, the distribution at each instant is normalized by its maximum value. The temporal evolution of the PDF shape is found to be fairly stable with the ARC mechanism, were the most probable value of the distribution oscillates between 0.9 and 1.4, around the mean value of 1.2 as in Fig. 7.22 (a). For the FPI-LES, the PDF is found to very rarely peak at the global equivalence ratio, and to change rapidly between rich and lean burning. The larger occurrence of very rich mixtures ($\phi > 1.7$) with FPI is thought to explain, at least in part, the higher CO levels found in the DZ (see Fig. 7.20).

The differences between the two computations are thought to have two main sources: mixing in the flame region and flame position, which are closely related. As was already mentioned, the flame is more lifted in the FPI-LES. The pure ethylene jet is thus enabled to penetrate further into the PZ before burning. In Section 7.7.2.a it was shown that in the ARC-LES, the interaction of the ISL with the PVC is a source of mixing, by forcing rich burning pockets to cross the central region and the fuel stream to curl. The effect of this motion is clearly visible on the bottom of Fig. 7.23 (a) & (b), where the mean and fluctuations of fuel mass fraction fields extend towards the center. The same effect, albeit with less intensity, is also visible for the FPI-LES, but further downstream. Mixing therefore therefore occurs further upstream (prior to combustion) in the ARC-LES, and as a result, flammable mixtures of global to rich equivalence ratio ($\phi \approx 1.2 - 1.6$) are more frequently observed in the flame front in this region. On the contrary, lean and rich mixtures are predominantly found in this near injection area in the FPI-LES, explaining the PDF of Fig. 7.22 (a). In addition, the lifted flame with FPI is less stable and the tip of the flame, which is situated in a globally rich region, is prone to flapping, inducing frequent detachments of growing rich burning pockets. The signature of this intermittent motion is revealed by the fluctuations of fuel mass fraction in the tip of the flame region in Fig. 7.23 (b), which are still very large with the FPI-LES. On the contrary, the ARC-LES flame being less lifted and more compact, leaner mixtures from the outer air injection in the ORZ are enabled to travel and curl towards this area, locally reducing the equivalence ratio seen by the tip of the flame.

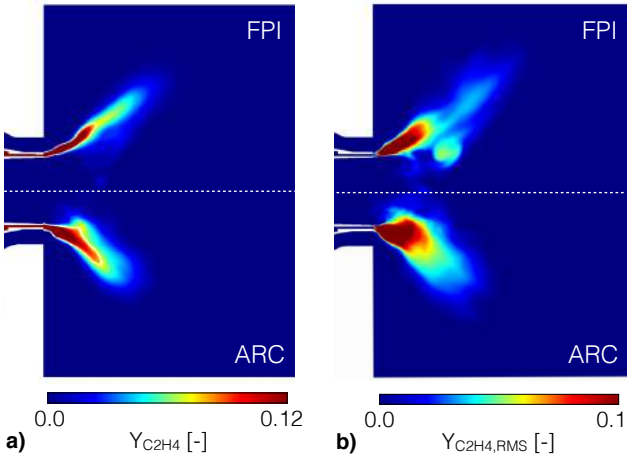

Figure 7.23: a) Time-averaged fields of fuel mass fraction and b) RMS of fuel mass fraction for both LES.

Effect of strain Another interesting difference between the two simulations arise from the interactions of the flame with the turbulent flow. The flame is wrinkled and stretched, affecting its structure and propagation speed (S_d, see Section 4.2.2). To evaluate these effects, the flame stretch is computed, defined as the sum of a tangential strain rate a_T and a curvature component $S_d\kappa$; where $\kappa = \boldsymbol{\nabla} \cdot \boldsymbol{n}$ is the flame curvature defined as the divergence of the flame surface normal $\boldsymbol{n} = -\boldsymbol{\nabla} Y_C / |\boldsymbol{\nabla} Y_C|$. Both computations exhibit the same distribution of strain and curvature in the flame front, as reported in Fig. 7.24. Scatterplots are constructed from locations where $\phi = 1.2 \pm 0.02$ and $Y_C = 0.5 \pm 0.02$. The same correlation of stretch with a_T is observed in both LES. Additionally, it is found that negative curvatures are almost always associated with positive strain rates.

In the context of LES, the density-weighted flame displacement $S_d^* = \frac{\rho}{\rho_f} S_d$ is usually preferred. S_d^* is negatively correlated with curvature, consistently with what was observed in previous DNS studies (Echekki & Chen, 1996; Hawkes & Chen, 2004). It is noted that the correlation exhibit a slightly nonlinear shape for very negative curvatures in the ARC-LES, a trend not seen in the FPI-LES nor in previous studies employing global

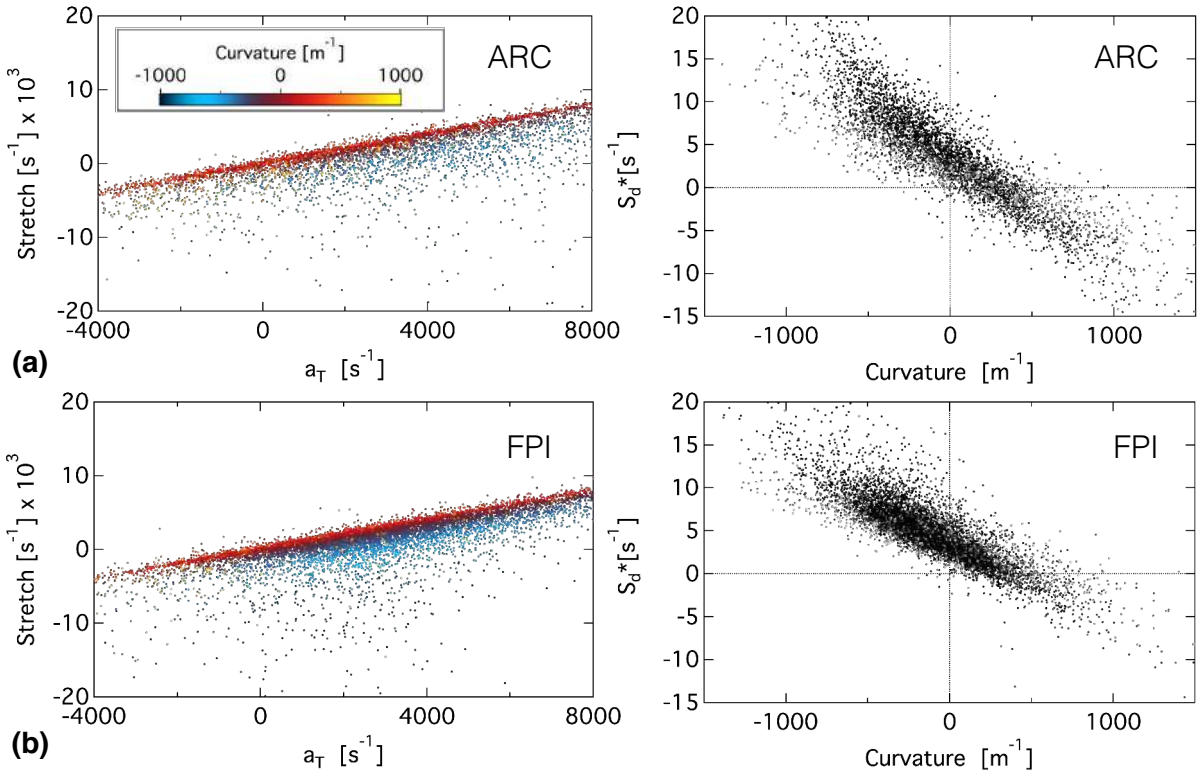

Figure 7.24: Scatterplots of stretch versus a_T and S_d^* versus κ, for (a) the ARC-LES and (b) the FPI-LES. Points are selected at $\phi = 1.2 \pm 0.02$ and $Y_C = 0.5 \pm 0.02$

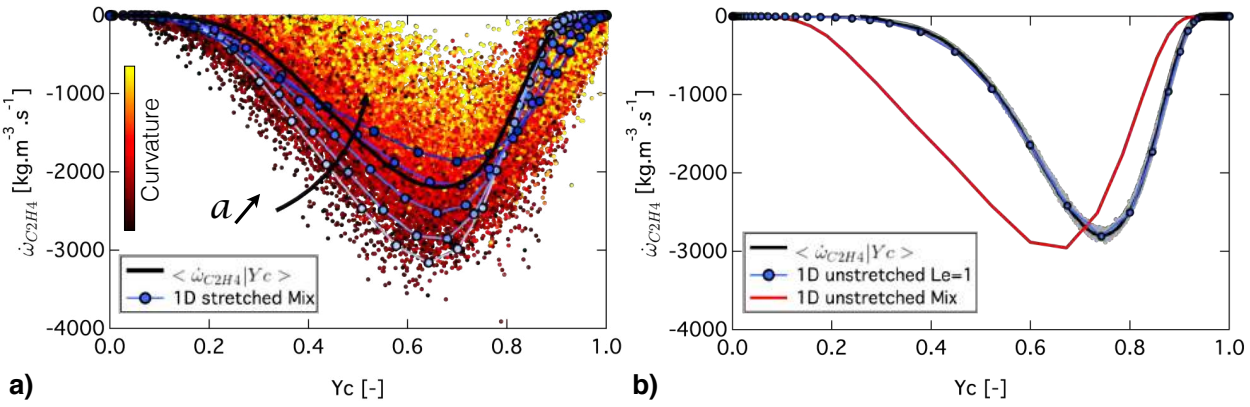

Figure 7.25: Scatterplots of fuel consumption rate vs. progress variable Y_C at $\phi = 1.2$ for (a) the ARC-LES and (b) the FPI-LES simulations. Laminar 1D flames at increasing strain rates a = 1000, 5000, 10000, 20000 and 50000 s^{-1} are overlaid on the ARC-LES scatterplots.

chemistries. This is attributed to diffusive effects of small radicals included in detailed chemistries. These differential diffusion effects, along with other strain related effects, are expected to induce large deviations from the canonical 1D unstretched flames. This is illustrated in Fig. 7.25 showing scatterplots of the fuel consumption rate in function of Y_C for both simulations. In both cases, only points within $\phi = 1.2 \pm 0.05$ are used to construct the scatterplots. The conditional mean values $< \dot{\omega}_{C2H4}|Y_C >$ are also reported in thick black lines. Note that the use of a unity Lewis assumption in the FPI-LES calculation solely induces a change in the laminar flame structure, as illustrated by the two 1D profiles plotted in Fig. 7.25 (b). A wide scatter around the conditional mean is observed in the ARC-LES, while the flame structure is frozen in the FPI-LES. This scattering is found to be strongly correlated to the local flame curvature: positive curvature results in a reduction of the consumption rate while the opposite trend is observed for negative curvature. This is consistent with trends observed in DNS simulations of methane-air flames with reduced chemistry (Echekki & Chen, 1996).

7.7.3 Species and pollutant prediction

7.7.3.a Qualitative OH comparisons

Experimental OH PLIF data allow to perform a qualitative comparison between measurements and the various computations. Looking at Figs. 7.26 and 7.27, a first comment is that no major difference can be seen in terms of instantaneous flame shape or position between Case A and Case B in the experiments, a trend that the ARC-LES reproduces. Differences arise when comparing levels, especially in and right behind the primary flame front: first, it is seen that Case B exhibits lower peak levels of OH in both experiments and computations; second, experimental data also reveal that a non-negligeable amount of OH is recirculated on the IRZ right behind the primary flame front, a trend better reproduced with the FPI-LES. However, the FPI-LES seem to predict too high OH levels in the ORZ. Overall, the major structures are retrieved with both chemistry descriptions, in particular, secondary combustion fronts are clearly visible in the DZ, responsible for maintaining significantly high OH levels throughout the combustion chamber.

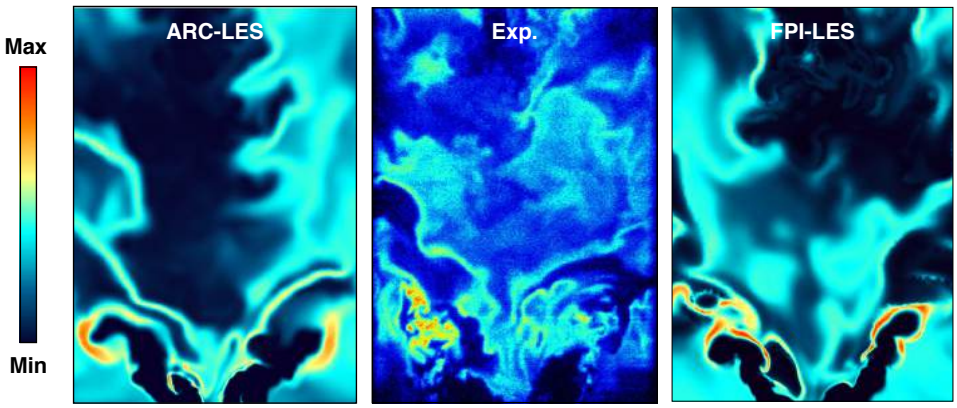

Figure 7.26: Instantaneous snapshots of OH mass fraction (LES) and OH-LIF (Experiments), for Case A.

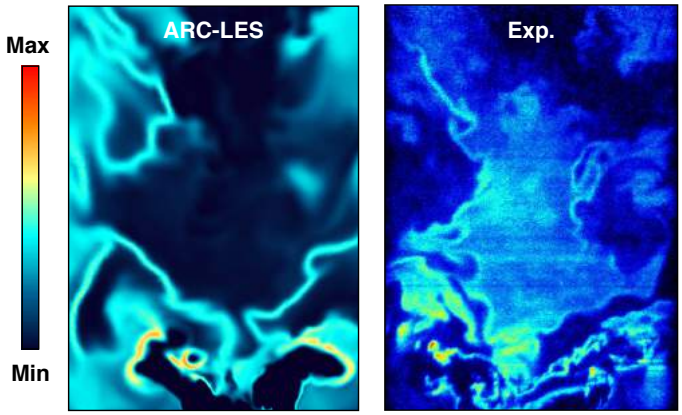

Figure 7.27: Instantaneous snapshots of OH mass fraction (LES) and OH-LIF (Experiments), for Case B.

Fig. 7.28 displays time-averaged experimental and computed fields of OH mass fraction. Computational results have been rescaled to match the minimum/maximum values of the FPI-LES (Case A) computation, to allow a direct comparison. Here also, the difference of levels between both operating pressure is striking. However, the main features remain the same: high levels are found behind the primary flame front and following the outer IRZ limit throughout the combustion chamber. All computations exhibit the right trends. From the rescaling, it is observed that the FPI-LES displays lower OH levels than the ARC-LES, except in the ORZ, where OH levels are, there, overpredicted by the FPI-LES. Note that no heat losses were considered in the computations, explaining the too high OH values near the combustor walls.

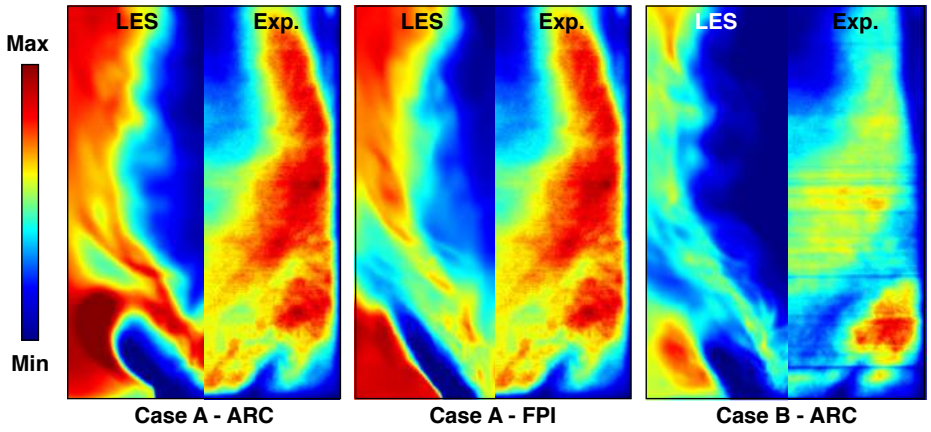

Figure 7.28: Time-averaged fields of OH mass fraction (LES) and OH-LIF (Experiments) for all cases. LES values are normalized by the maximum values found in the FPI-LES while experiments are normalized by the maximum value of Case A.

7.7.3.b CO exhaust levels investigations

As already discussed, in lean premixed or partially-premixed combustion systems, exhaust levels of CO can be non negligable and constitute an important source of pollution. As indicated in Fig. 7.2(c) & (d) and 7.4(c) & (d), the CO production in unstrained laminar premixed flames strongly depends upon the flame equivalence ratio, which is expected to have more effect than increasing the pressure from 3 to 5 bars. In fact, a laminar EICO can be estimated in these test cases, for conditions relevant to LES computations, by (Takeno & Nishioka, 1993):

$$\mathrm{EICO}^{lam} = -\frac{\dot{\omega}_{CO}^{tot}}{\dot{\omega}_{C2H4}^{tot}} \tag{7.11}$$

Results are reported in the first two columns of Table 7.5. It can be seen that all cases lead to the same emission index, but that this index is strongly dependent upon the equivalence ratio, with levels differing by about one order of magnitude from an evaluation at ϕ_g or at ϕ_{PZ}. Inhomogeneities at the combustor outlet are thus expected to have a strong impact on exhaust CO levels. In the LES, the EICO is preferably evaluated directly at the outlet, by:

$$\mathrm{EICO} = \frac{<\int_S \rho u_z Y_{CO} dS>}{<\int_S \rho u_z Y_Z dS>} \tag{7.12}$$

where $<\cdot>$ stands for temporal averaging over several instantaneous shots. The results are reported in the third column of Table 7.5, for the different computations (of course, the laminar values are the same for both Case A).

	$\mathrm{EICO}^{lam}_{\phi_g}$ [g/kg]	$\mathrm{EICO}^{lam}_{\phi_{PZ}}$ [g/kg]	EICO [g/kg]	EICO^{eq} [g/kg]	$\overline{Y_z'}$ [-]
Case A - ARC	∼50	∼800	185	172	$1.1e^{-2}$
Case A - FPI	-	-	177	168	$1.1e^{-2}$
Case B - ARC	∼50	∼800	171	177	$9.8e^{-3}$

Table 7.5: CO emission indices and mixture fraction variance in the outlet plane.

This global indication provides similar values in all simulations; with a strong departure from the value expected at ϕ_g. An estimation of the local deviation from equilibrium is provided by computing an equilibrium index EICO^{eq}:

$$\mathrm{EICO}^{eq} = \frac{<\int_S \rho u_z Y_{CO,eq} dS>}{<\int_S \rho u_z Y_Z dS>} \tag{7.13}$$

where $Y_{CO,eq}$ is the CO mass fraction expected in the burnt gases of unstretched premixed flames at the local ϕ. The values are reported in the fourth column of Table 7.5. They are fairly equivalent to the true EICO in all cases, indicating a sufficiently large residence time inside the combustor to allow equilibrium to be reached.

To illustrate these conclusions, an example of instantaneous snapshot of the combustor exit plane is provided in Fig 7.29, for Case A with the ARC mechanism. The far left image reports values of $\Delta Y_{CO} = Y_{CO} - Y_{CO,eq}$. It

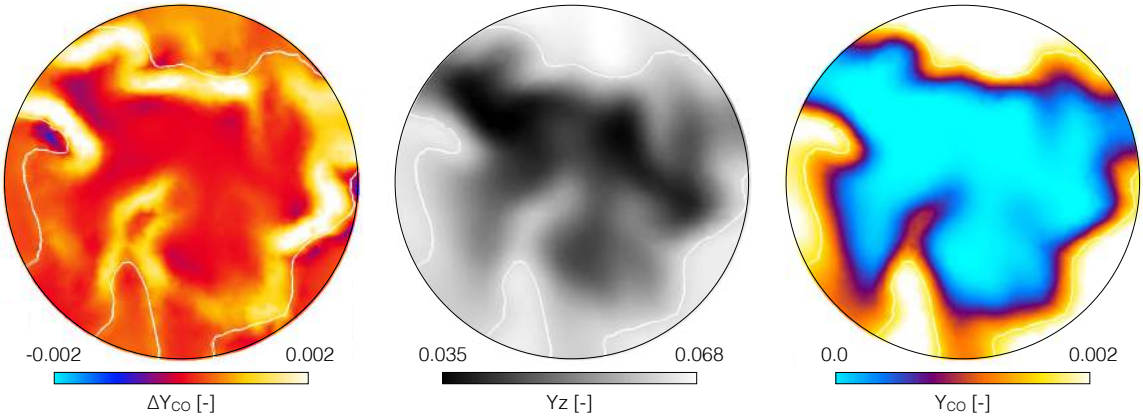

Figure 7.29: z-plane at the combustor outlet colored by ΔY_{CO} (left), Y_z (center) and Y_{CO} (right). The white iso-contour indicates the stoichiometry. From the ARC-LES computation.

is observed that the regions where equilibrium has not been reached are all located in the vicinity of $\phi = 1$, easily identified as being secondary CO oxidation fronts of the DZ pushed towards the combustor exit. A comparison with the snapshot coloured by Y_{CO} provided on the right end of Fig. 7.29 confirms that the Y_Z inhomogeneities are the leading order phenomenon in explaining the departure of the emission index from the laminar EICO at ϕ_g.

The distribution of mixture fraction and CO mass fraction are representative of what is observed in all simulations: the center is characterized by lean mixtures, while higher Y_{CO} values are found in the outer region near the walls. The RMS of Y_z reported in the last column of Table 7.5 is similar for all LES, and provides an explanation to the similar departure of EICO from the expected laminar values.

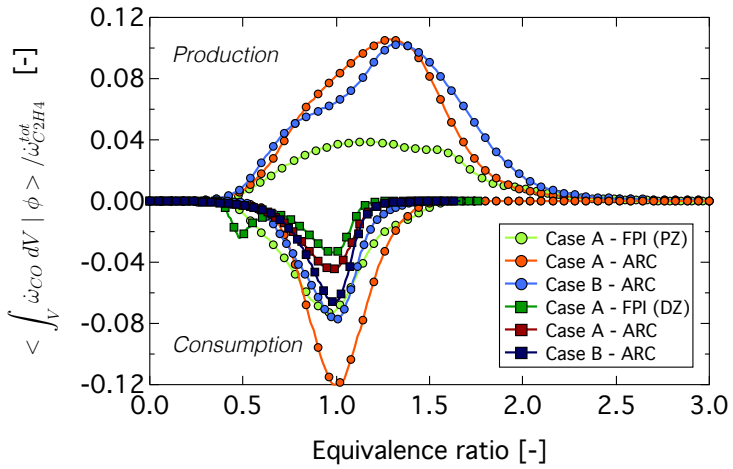

Figure 7.30: Integrated CO production and consumption rates conditioned on the equivalence ratio.

However, differences between the simulations arise when analyzing separately the CO production and consumption throughout the combustor. As indicated before, CO is massively produced in the rich premixed flame fronts of the PZ and is oxidized downstream through diffusion flames between the burnt gases and air coming from the dilution jets. The integrated production rate of CO conditioned on the equivalence ratio in the PZ $< \int_V \dot{\omega}^+_{CO}\ dV|\phi >$ and the integrated consumption rate of CO conditioned on the equivalence ratio $< \int_V \dot{\omega}^-_{CO}\ dV|\phi >$ in both the PZ and the DZ are plotted as function of the equivalence ratio, for all LES, in Fig. 7.30. Note that $\dot{\omega}^+_{CO} = max(\dot{\omega}_{CO}, 0.0)$ and $\dot{\omega}^-_{CO} = min(\dot{\omega}_{CO}, 0.0)$ are net production and consumption rates, respectively. In order to allow a comparison between all cases, values are normalized by the total fuel consumption rate. The production of CO is found to peak around ϕ_{PZ} for both ARC-LES while consumption peaks near stoichiometry, corresponding to the CO/O_2 diffusion flame fronts discussed earlier. Consistently with the PDF of equivalence ratio presented in Fig. 7.22, the production of CO is more spread out in the FPI-LES. Furthermore, both production and consumption rates are found to be about twice smaller in this case, which seems to indicate that the flame/turbulence interactions -not taken into account in the FPI simulation- result in

an increase of CO reactivity.

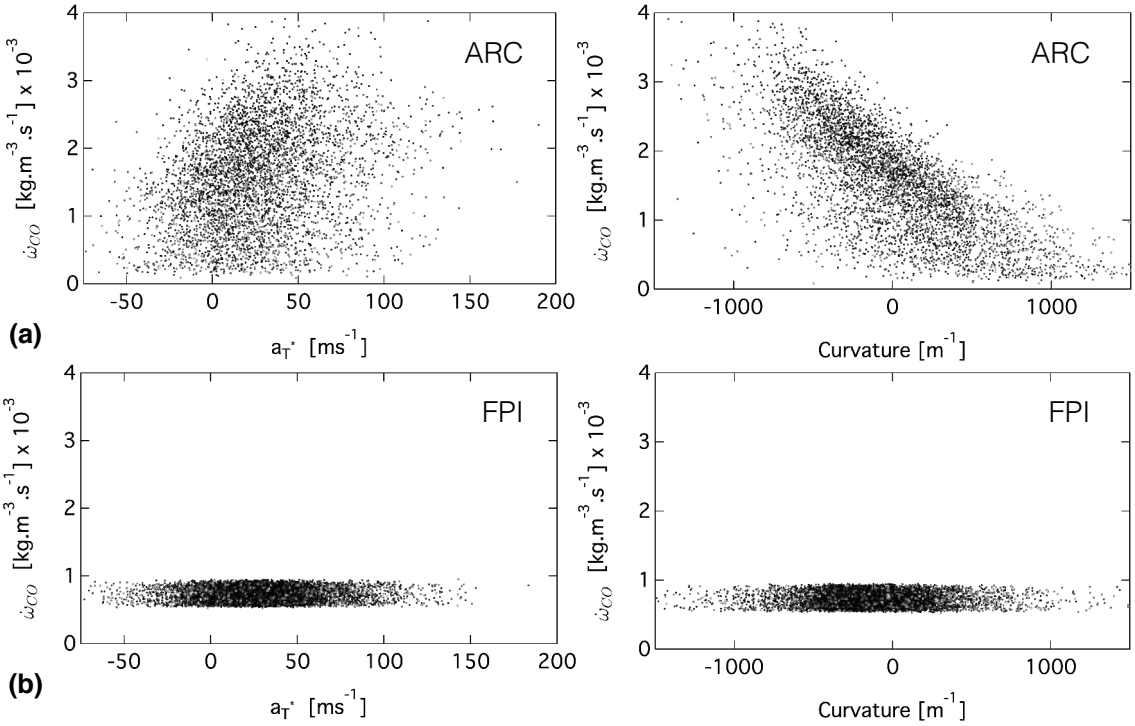

Figure 7.31: Scatterplots of CO source term versus effective strain rate a_T^* and curvature κ for (a) the ARC-LES and (b) the FPI-LES.

To analyze these differences further, Fig. 7.31 (a) and (b) displays scatterplots of CO source term against the *effective* strain a_T^* ($= a_T \mathcal{F}/\mathcal{E}$) and the curvature, for both the ARC-LES and the FPI-LES of Case A, respectively. Scatterplots are constructed from locations where $\phi = 1.2 \pm 0.02$ and $Y_C = 0.5 \pm 0.02$. Note that, for this value of the progress variable, CO is produced but not oxidized. In the ARC-LES, the CO net source term is found to strongly depend on curvature with values up to 4 times that of the FPI-LES for negative curvatures, in agreement with what was observed in Fig. 7.25.

7.7.3.c Soot predictions

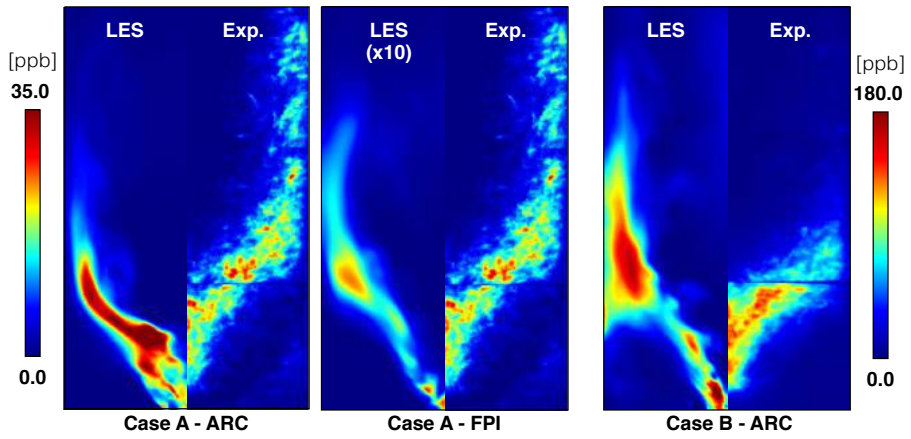

Figure 7.32: Comparison of time-averaged LII soot measurements with time-averaged soot mass fraction. Note that for comparison, the FPI-LES field has been multiplied ten times.

Figure 7.32 presents quantitative comparisons of time averaged fields of soot obtained in all LES with experimental results. Qualitatively, it is seen that soot is mostly present in the PZ. More precisely, high levels are found in the bottom part of the IRZ, right behind the post-flame of the main combustion zone, for all operating

points. The secondary oxidation trace is clearly visible, preventing any soot from surviving near the centerline in the DZ (Geigle *et al.*, 2015*b*). Overall, the shape of the region of high soot loads is correctly predicted in all computations. However, this region is slightly shifted towards the injection, in all LES. This could be an artifact of the simple model employed in this study, were acetylene is the sole soot precursor, not necessarily produced or localized in the same flame parts than heavier PAH. Another possible explanation could be the spatial discrepancies observed in the OH instantaneous and mean distributions between experiments and LES, Section 7.7.3.a. Indeed, the bottom part of the IRZ in the experiment is characterized by a drop in OH levels, propitious to the formation of soot, not recovered in the LES. Soot is also absent from the DZ in the LES of

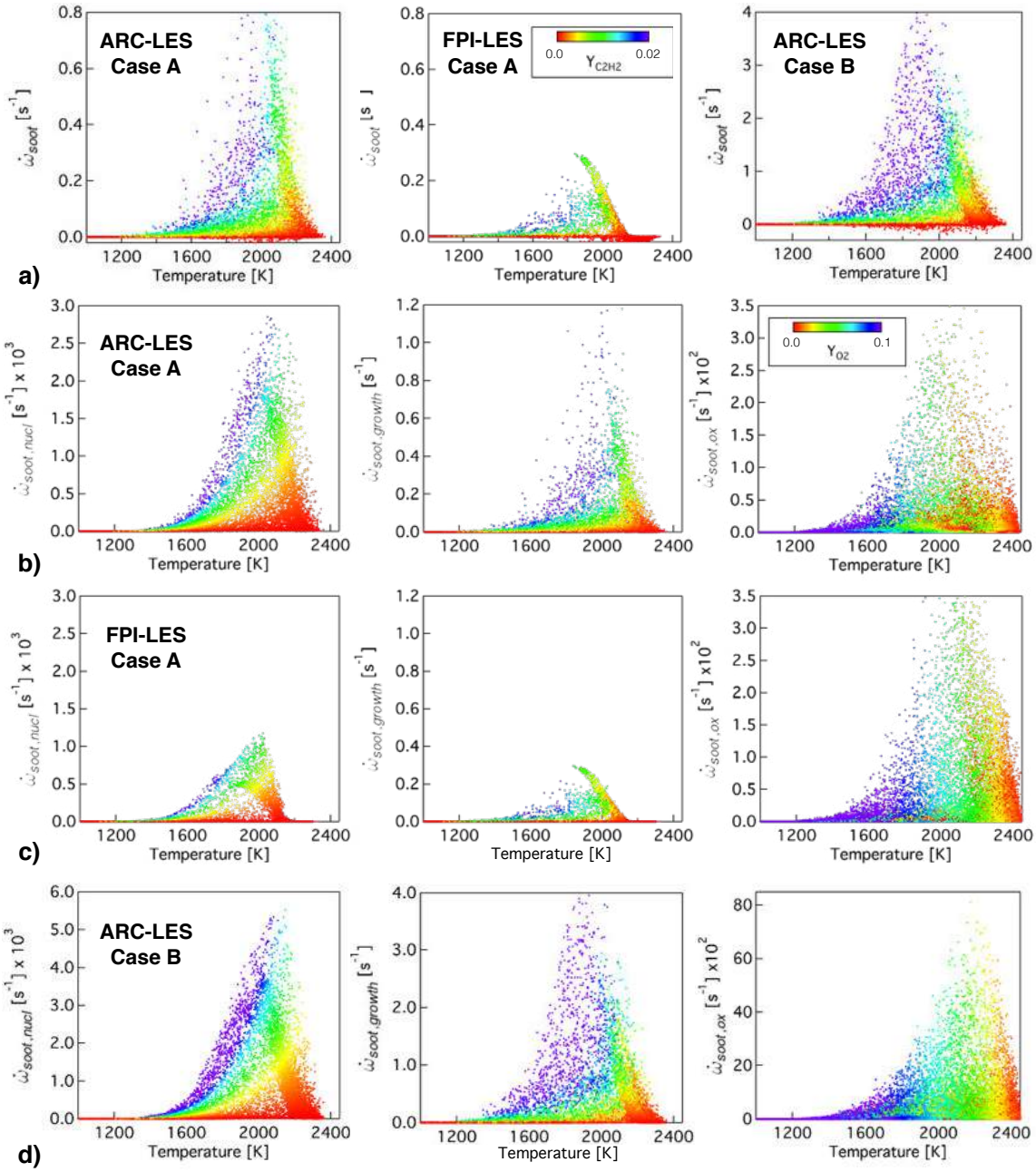

Figure 7.33: a) Scatterplots of net soot source term for all computations, coloured by C_2H_2 mass fraction. b) c) & d) Scatterplots of the different contributions to the soot source term, for each computation. From left to right: nucleation and growth -coloured by C_2H_2 mass fraction, and oxidation -coloured by O_2 mass fraction.

Case A, but this might simply be due to a too short averaging time window. Quantitatively, the FPI-LES levels seen on Fig. 7.32 (levels have been multiplied by ten on the Figure) are off by about one order of magnitude, when the ARC-LES allows to recover the right trends for both operating points. In particular the higher levels of Case B are very well predicted. Such a large difference between both approaches is surprising, since all chemistry descriptions are originally based upon the same detailed mechanism; but consistent with previous LES results on

this configuration (Franzelli *et al.*, 2015*a*).

To understand the origin of these discrepancies, the source term of the soot mass fraction Y_s is investigated in more depth in Fig. 7.33. Scatterplots of $\dot{\omega}_{Ys}$ against temperature are shown in Fig. 7.33 (a), for all computations, and they are coloured by C_2H_2 mass fraction. Consistently with previous findings, it is seen that the production of soot in Case A is about twice smaller with the FPI-LES than with the ARC-LES. The scatterplot analysis of the FPI-LES also reveals that, conversely, soot consumption appears to be slightly more important than in the ARC-LES, and that the production of soot is stopped abruptly around $T = 2200$ K. For Case B, soot production is about 4 times higher than in Case A (ARC chemistry). Finally, note that both scatterplots of computations with the ARC chemistry also reveal more frequent occurrence of higher acetylene levels, a major actor of the simple two equation soot model employed.

To identify the leading order phenomenon in the production/consumption of soot, each of the terms composing $\dot{\omega}_{Ys}$ (see Eq. 7.6) are analyzed separately. Remember that production is the sum of a nucleation and a surface growth component, both linearly dependent upon the levels of acetylene; and that consumption is the result of oxidation by O_2. An instantaneous spatial distribution of each of these contributions is provided in Fig. 7.34, for the ARC-LES of Case A. C_2H_2 iso-contours are displayed in grey in each snapshot. Accordingly with the simple soot model, both nucleation and surface growth are localized in the same flame peripheral area where acetylene levels are important, while oxidation occurs at the meeting of the burnt gases with the incoming fresh air from the dilution jets. To better apprehend the differences between simulations, scatterplots of each of these constituting components against temperature are displayed in the rows of Fig. 7.33(b)-(d), with each line corresponding to a LES computation. Investigation of these plots reveal that the leading order term throughout the temperature range is production by surface growth. The lack of points with high acetylene levels in the FPI-LES is striking, and points towards either a completely different distribution of C_2H_2 in this computation, or to lower levels throughout the combustion chamber. Additionally, note that no nucleation occurs in the post flame-zone, whenever $T > 2200$ K, contrarily to what both ARC-LES computation exhibit. This is consistent with previous observation on $\dot{\omega}_{Ys}$ (Fig. 7.33 (a)), and is attributed to the negligible C_2H_2 values returned by the FPI table in the post-flame zone. However, as seen for all LES, oxidation is still very important in this region, such that the balance between production and consumption is perturbed with the FPI, resulting in a slight overprediction of soot consumption in the post-flame zone.

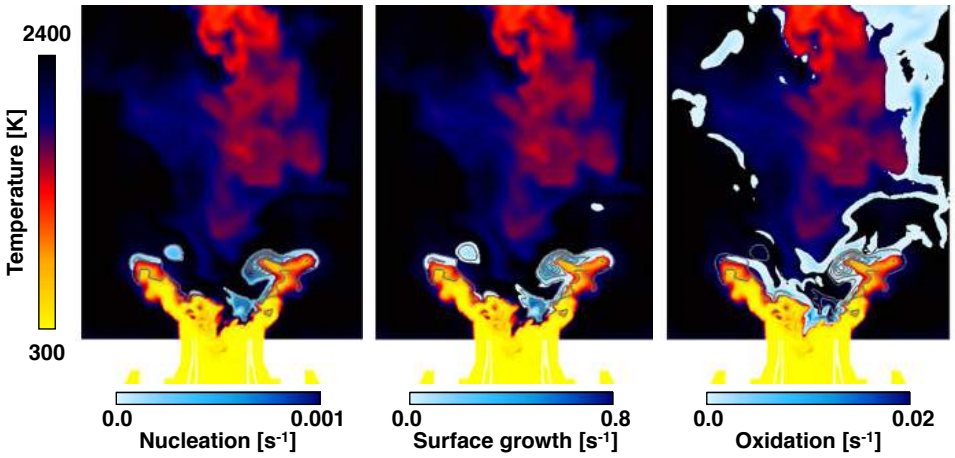

Figure 7.34: Instantaneous spatial distribution of each component of the soot source term: nucleation, surface growth and oxidation. From the ARC-LES.

Figure 7.35 confirms that the spatial distribution of acetylene is similar in all LES, but that values are significantly smaller in the FPI-LES. This Figure also reveals very high RMS values for all LES, higher than the mean values, which is the sign of a very strong skewness of the distribution. Signs of this skewed distribution is also suggested by the scatterplots of mass fraction of C_2H_2 against temperature displayed in Figs. 7.36 (a) & (b), confirming that points with $Y_{C2H2} > 10^{-2}$ are frequently observed in instantaneous snapshots, especially in the ARC-LES.

Focusing on points with $\phi = 1.2 \pm 0.01$ in Fig. 7.36 (d), with superimposed 1D laminar profiles computed with and without the unity Lewis assumption, the unity Lewis assumption is identified as being one possible reason for the lower acetylene values observed in the FPI-LES. However, comparison with the ARC-LES in Fig. 7.36 (c), advances that this is not the primary cause. Attempts to correlate the data scatter of the ARC-LES with

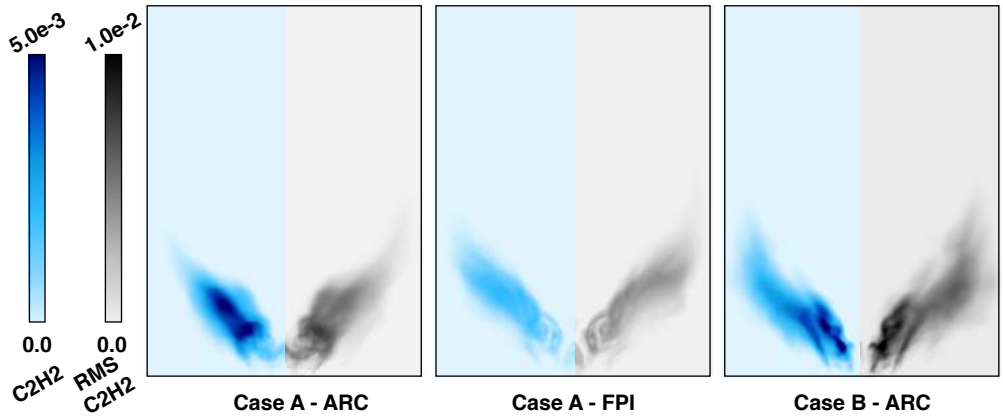

Figure 7.35: Comparison of time-averaged C_2H_2 mass fraction (left part) and RMS (right part), for each computation.

strain and curvature were unsuccessful, at least in the major part of the temperature domain, as can be seen on Fig. 7.36 (c) were points are coloured by the local curvature. Furthermore, no 1D canonical test case studied so far seems to be able to explain the phenomenon either. In fact, acetylene levels across stretched 1D premixed laminar flames tend to decrease when compared to unstretched flames, as seen on the profiles added in Fig. 7.36 (c).

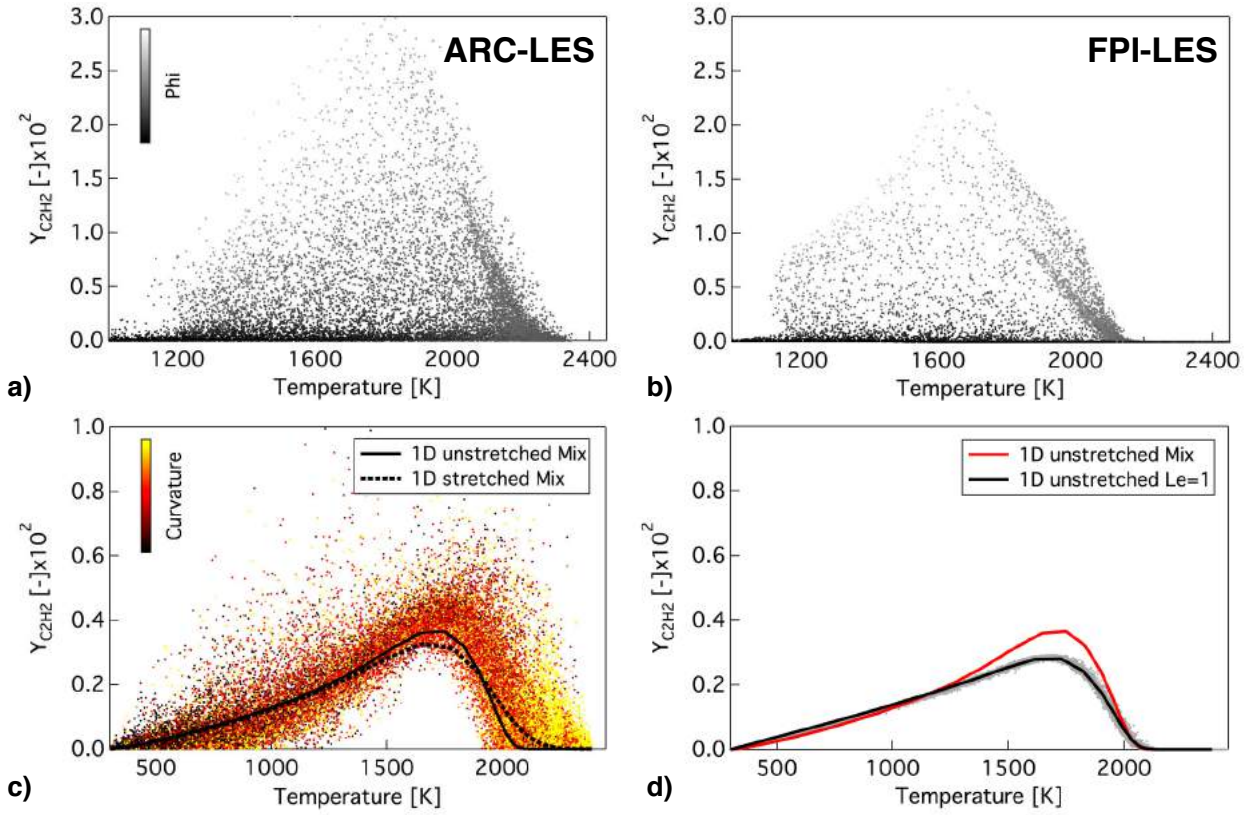

Figure 7.36: (a) and (b) are scatterplots of C_2H_2 mass fraction coloured by the equivalence ratio for both LES of Case A. (c) and (d) are scatterplots of C_2H_2 mass fraction with points chosen in the range $\phi = 1.2 \pm 0.2$, coloured by curvature, for both LES of Case A. (c) is superimposed with stretched and unstretched 1D laminar profiles, while (d) is superimposed with unstretched 1D laminar profiles computed with and without unity Lewis assumption. 1D computations are performed with the ARC_18_C2H4NARA mechanism.

To explain the discrepancies in predicted acetylene levels, another underlying mechanism is naturally suggested by partial premixing. As already said, the flame fronts exhibit a highly non-homogeneous distribution of equivalence ratio. When a flame propagate in such a stratified mixture, its inner structure is altered, leading to a modification, for example, of the turbulent flame speed and pollutant emissions. To assess the importance of this effect in the present configuration, two quantities are employed. First, the cross-scalar dissipation rate, χ_{zc}

is defined:

$$\chi_{zc} = D_z |\boldsymbol{\nabla Y_z}||\boldsymbol{\nabla c}| \tag{7.14}$$

giving an estimation of the local degree of simultaneous Y_c and Y_z evolutions across the flame, and already employed, for instance, by Domingo *et al.* (2005) to analyze both gaseous and spray turbulent-lifted flame structures in DNS. Second, the cross-scalar angle, α_u is:

$$\alpha_u = cos^{-1}\left(\frac{\boldsymbol{\nabla Y_z}\cdot\boldsymbol{\nabla c}}{|\boldsymbol{\nabla Y_z}||\boldsymbol{\nabla c}|}\right) \tag{7.15}$$

characterizing the degree of mixture stratification: whenever $\alpha_u = 90°$, reaction progresses along an iso-Y_z level. On the contrary, $\alpha_u = 180°$ means that the flame propagates towards rich mixtures, and $\alpha_u = 0°$ towards leaner mixtures. Stratification effects are expected whenever $\chi_{zc} >> 0$ and $\alpha_u \neq 90°$.

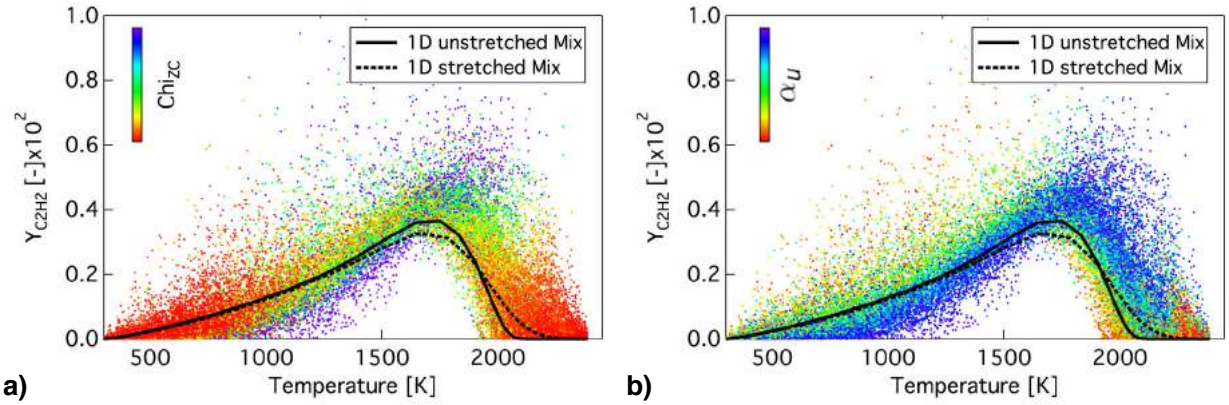

Figure 7.37: Scatterplots of C_2H_2 mass fraction in the ARC-LES (Case A), (a) coloured by χ_{ZC} and (b) coloured by the unmixedness angle α_u. Points are chosen in the range $\phi = 1.2 \pm 0.2$. Superimposed are stretched and unstretched 1D laminar profiles computed with the ARC_18_C2H4NARA mechanism.

Fig. 7.37 displays the same scatterplot than that of Fig. 7.36 (c), but coloured by χ_{zc} (a) and α_u (b). The correlation with both quantities is obvious. In particular, points straying away from the 1D laminar profiles (superimposed to the plots), and exhibiting very high acetylene levels are all identified as being points with $\alpha_u = 0°$ or more frequently 180°, also characterized by moderate to high χ_{zc} values. This proves that stratification effects are responsible, for the most part, for the higher acetylene levels observed in the ARC-LES; and in turn, for the higher predicted soot levels. This also amounts to saying that additional effects, other than classical flow related effects such as stretch and curvature, might play a crucial role under certain circumstances, and that short from being able to add this complexity into the table, an FPI simulation might provide erroneous results. Since there are no proper way to determine *a-priori* which effects might be of interest in realistic configurations, a methodology able to account for all of them without additional modeling assumptions, such as the one presented in this article, is of great interest.

7.8 Conclusions

The present study has demonstrated the efficiency of Analytically Reduced Chemistry (ARC), combined with the Dynamically Thickened Flame (DTFLES) approach to predict with high accuracy the complex flame structures encountered in realistic burners. This approach is able to account for the various flame regimes as well as targeted intermediate species without any additional modeling, something that is not possible with the more popular tabulation techniques. Additionally, the methodology employed to produce ARC from detailed mechanisms, being a fully automated procedure, allows to directly control the stiffness as well as maximum allowed error on targeted quantities, to find the best possible compromise in any specific configuration. It has therefore a very strong potential to address many issues related, for example, to pollutant predictions in practical systems, as was demonstrated here with CO and soot predictions.

7.9 Additional material

7.9.1 Summary of the different computations

Table 7.6 provides a summary of all computations performed. Case A and B still refer to the operating points summarized in Table 7.3. Runs highlighted were investigated in the first part of this Chapter. In the following,

Chemistry description	Case(s)	run time [ms]
ARC-DTFLES	**A, B**, A + heat losses	30, 22, 20
FPI-DTFLES	**A**	35
2S-DTFLES	A	20

Table 7.6: Characteristics of the performed runs.

the ability of a global 2-steps (2S) scheme in predicting the flame structure with impact on exhaust CO levels and overall soot predictions is assessed. A general conclusion providing CPU information on all runs closes the Chapter. Information about and validations of the 2S scheme for ethylene/air oxidation employed is provided in Appendix B.

7.9.2 Reactive-flow field validations

7.9.2.a Time-averaged fields

Figure 7.38 provides a comparison of mean axial velocity and temperature fields in a central cut plane, obtained with both the ARC mechanism and the 2S mechanism. As expected, the results are fairly similar, particularly for the velocity fields, where the large IRZ extending from the meeting of the dilution jets up into the central air injection nozzle is retrieved in the 2S-LES. It is noted that the IRZ extends further upstream in the 2S simulation, and that ORZ are more pronounced. This extent of the IRZ into the central air injection nozzle is consistent with the shift of flame position further upstream that can be observed on the mean temperature fields. With this chemistry description also, flame stabilization is difficult to reach and as a result, an incessant "pumping" movement is observed in this central region. This particular instability appears stronger in the 2S simulation than in the ARC simulation. Mean temperature and velocity fields are, in that regard, similar to those observed with the FPI chemistry description. This movement could be the reason why the lower temperature central region axial extend is less pronounced in both the FPI and 2S simulations.

In Fig. 7.39, numerical axial, radial and tangential velocity profiles are validated against experimental data at the same 4 axial positions of interest materialized in Fig. 7.13(b). Not much difference can be seen between all runs, all leading to a very good agreement with experiment. A better agreement with the 2S scheme is observed around z = 95 mm, just after the meeting point of the 4 dilution jets, where the tangential velocity is under predicted with all other chemistry descriptions.

Axial and radial profiles of temperature are provided in Fig. 7.40 (a) and (b), at several locations of interest spanning the entire combustion chamber. Note that results with the ARC mechanism and the heat losses (ARC+HL) are also presented. As seen on Fig. 7.40(a), adding heat losses worsen the temperature levels on the centerline of the combustor. This under-prediction of temperature on the centerline is better understood when looking at the radial temperature evolutions, Fig. 7.40(b). Obviously, as observed at z = 18 mm, the physics of the problem is not completely retrieved in the LES: where a single drop in temperature around x = 15 mm is observed in the experiment, a double drop is observed in all LES with the second one located around x = 0 mm -albeit with more or less intensity. This amounts to saying that, if radially averaged, temperature levels are the same between LES and experiments, but the distribution is clearly off. This offset is difficult to explain, since all velocity components were correctly retrieved at these near-injection locations. Concerning the main temperature drop, located in the flame front, the 2S scheme is seen to give less accurate results, with as expected a strong over-prediction of the temperature. Note, to conclude, that the ARC scheme appears as the only chemistry description enabling to retrieve the right temperature of $\approx$ 300 K at z = 0 and x = 0 (Fig. 7.40 (a), with and without HL).

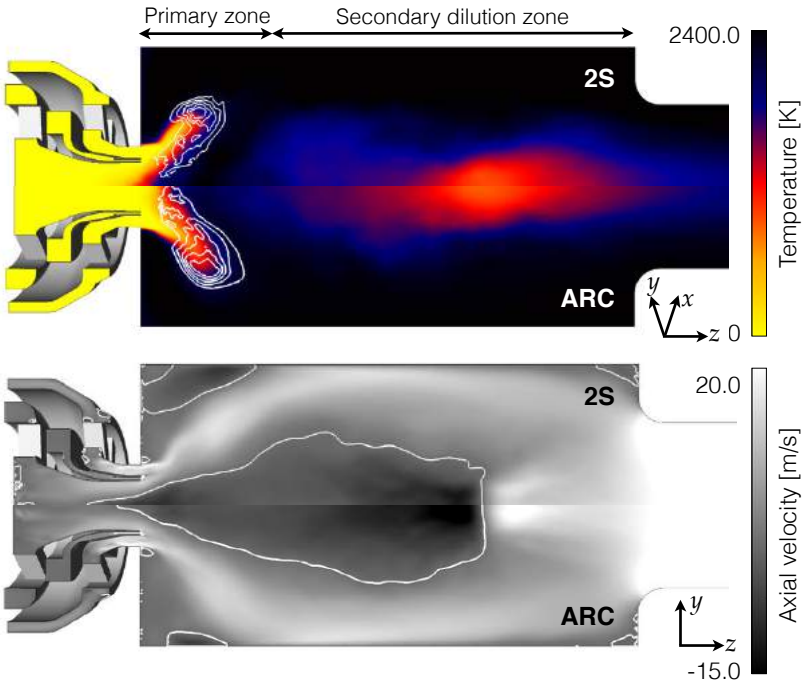

Figure 7.38: (a) Mean temperature fields, with heat release rate iso-contours in white to localize the reaction zone. (b) Time-averaged axial mean velocity fields, with white iso-contours corresponding to zero axial velocity. 2S (top halves) and ARC_18_C2H4NARA (bottom halves).

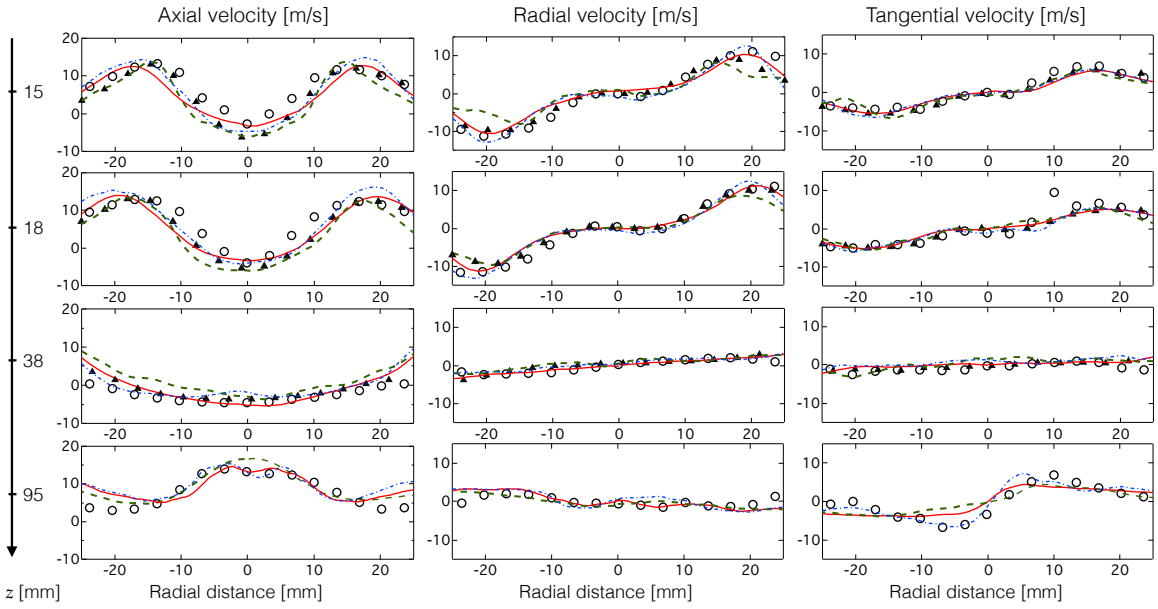

Figure 7.39: Mean axial, radial and tangential velocity profiles for several chemical mechanisms extracted in mid-plane at z = 15, 18, 38 and 95 mm, ARC_18_C2H4NARA (solid line), 2S chemical scheme (dashed-dotted line), FPI (dotted line), experiment: FoV(▲) and SoC(o).

7.9.2.b Flame structure

Dilution Zone Just as seen in the ARC-LES and FPI-LES, the DZ exhibit CO/O_2 diffusion fronts, located close to the IRZ boundary and near stoichiometric iso-contours (see Fig. 7.20). To better characterize these fronts, scatterplots of CO mass fraction are presented at the top of Fig. 7.41, for both the ARC-LES and the 2S-LES. They are coloured by the CO Takeno Index (TI_{CO}) introduced in Section 7.7.2.c. Consistently with the

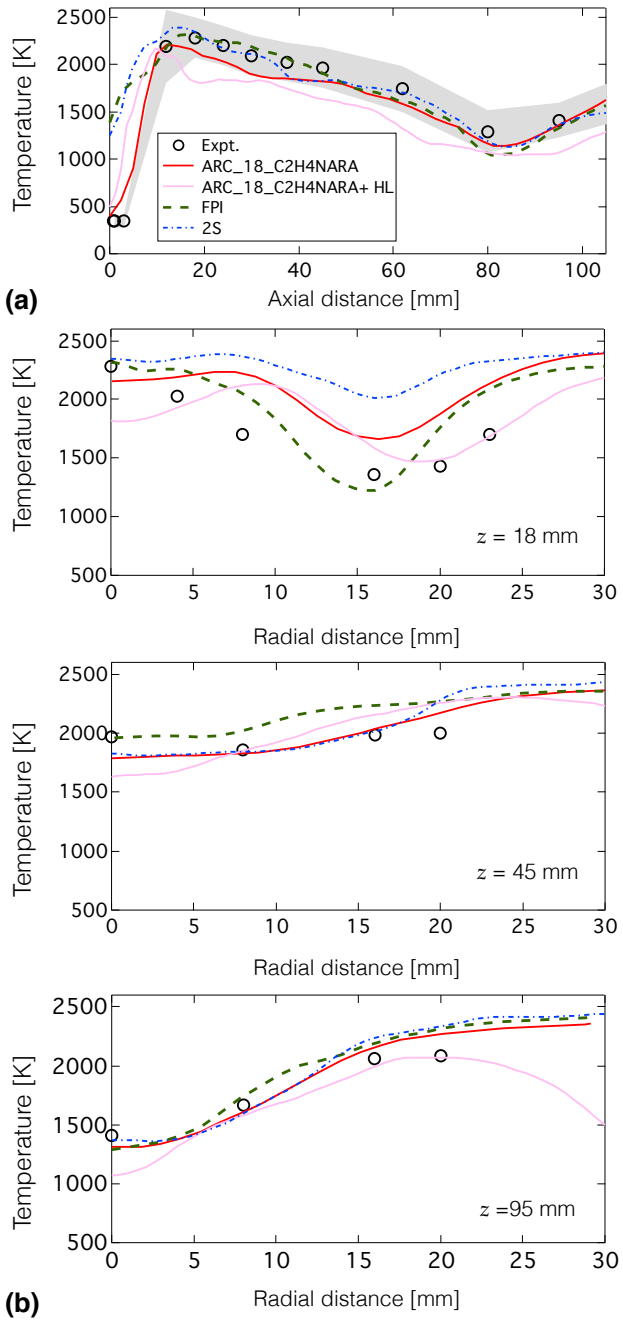

Figure 7.40: (a) Mean axial temperature profile for several chemical mechanisms and (b) mean radial temperature profiles for several chemical mechanisms extracted in mid-plane at z = 18, 45 and 95 mm, ARC_18_C2H4NARA (solid line), ARC_18_C2H4NARA with heat losses (solid line), FPI (dotted line), 2S chemical scheme (dashed-dotted line), experiment (o).

ARC-LES, no premixed-like structures are found in this region. As in Fig. 7.21, superimposed to the scatterplots of the ARC-LES are profiles extracted from 1D diffusion fronts between a hot, rich mixture of burnt gases (Y_z = 0.083) and fresh air at 300K. Likewise, superimposed to the scatterplots of the 2S-LES are profiles extracted from the same types of 1D diffusion fronts, but computed with the 2S_C2H4_BFER. Only two strain rates are displayed for the 2S-LES: 1000 s^{-1} and 4600 s^{-1}. As expected from the unity Lewis assumption made for the 2S_C2H4_BFER transport data, no response to strain is observed. Note the large scatter of data in the 2S simulation, for $Y_z > 0.8$. Around the same Y_z value, it is seen on the scatterplot of temperature that points are starting to stray from 1D profiles. This behavior is to be associated with the PEA corrections (Franzelli *et al.*, 2010) applied to each reaction rate of the 2S scheme to account for rich mixtures.

To confirm this analysis, scatterplots of CO and CO_2 mass fractions are displayed in Fig. 7.42, coloured by

the PEA factor applied to the second reaction. The PEA factor of the second reaction is almost zero in very rich mixtures (in red in the aforementioned scatterplots), indicating that the second reaction is virtually stopped and species tend to stray from their theoretical equilibrium values. This type of unphysical behavior prevents a systematic quantitative analysis of the CO species in 2S simulations; in particular, there is no *a-priori* guarantee of the accuracy of the EICO (to be investigated in the next Section).

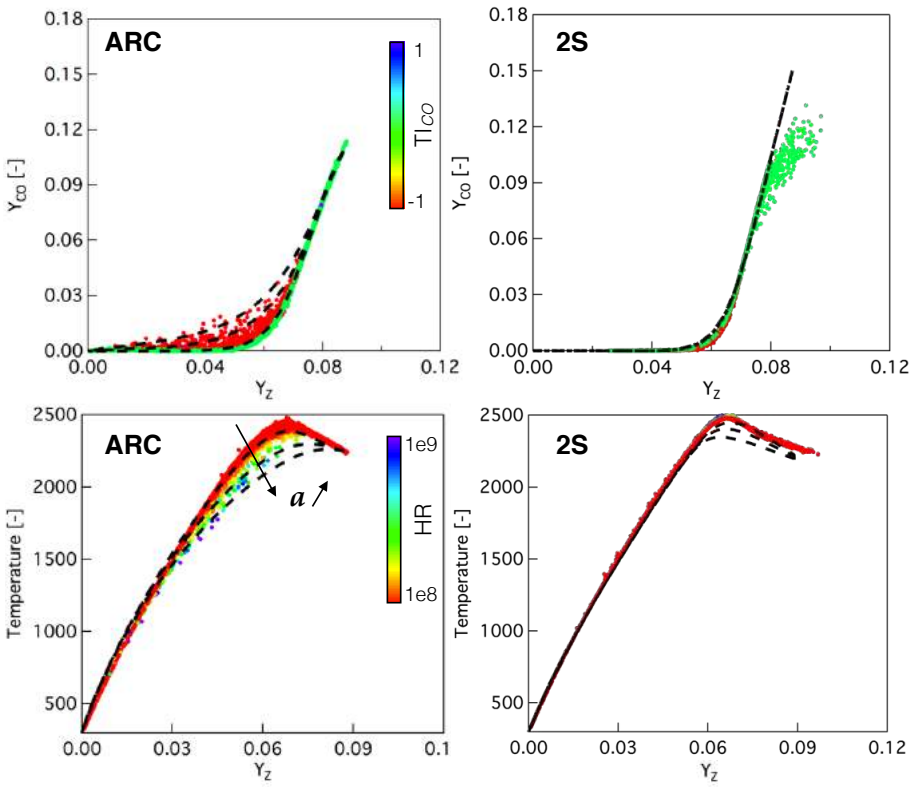

Figure 7.41: Scatterplots of CO mass fraction colored by TI_{CO} (top) and temperature colored by the heat release rate (bottom). Left row: ARC-LES, right row: 2S-LES.

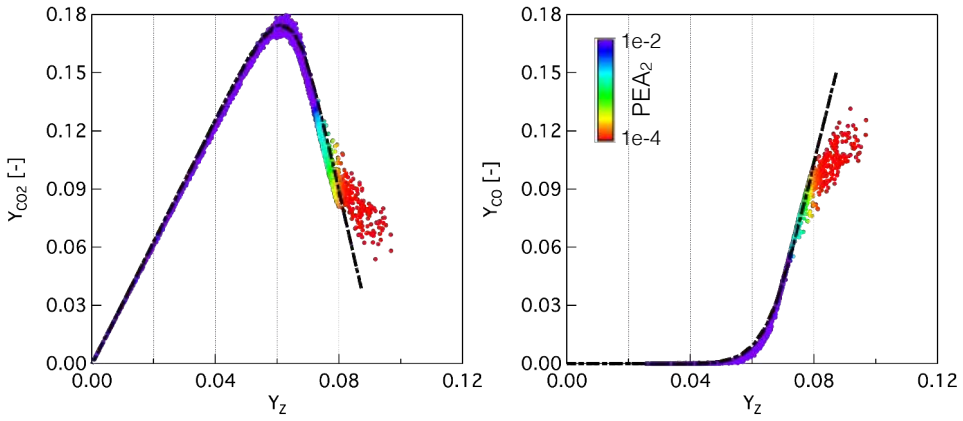

Figure 7.42: Scatterplots of CO_2 and CO mass fraction colored by the second reaction PEA factor (PEA_2).

Primary Zone To investigate the level of partial-premixing in the PZ with the 2S-LES, the PDF of equivalence ratio in the reacting zone (i.e. $\dot{\omega}_{C2H4} < -10$ kg/m3/s) is evaluated and plotted in Fig. 7.43, along that of the ARC-LES. Just as for the FPI-LES, a bi-modal shape with peaks around $\phi = 0.8$ and $\phi = 1.6$ is obtained. The explanation given in Section 7.7.2.d is thought to be, at least partially, relevant in the present case also. Indeed, remember that for the ARC-LES, the interaction of the ISL with the PVC was identified as a source of early mixing, and that traces of this motion were identified in the mean and RMS fields of fuel mass fraction, see the

bottom of Fig. 7.44 (a) and (b). These traces seemed to indicate an enhanced mixing closer to the injection system than in the FPI-LES, where such traces were also observed but further downstream. The same features are observed for the 2S-LES, see the top of Fig. 7.44 (a) and (b). This indicates the predominance of leaner flammable mixtures in this near injection area, responsible for the leaner peak found in Fig. 7.43. Additionally, it is observed that the fluctuations of fuel mass fraction in the tip of the flame region are still very large with the 2S-LES, consistently with what was found in the FPI-LES analysis. Richer mixtures are thus expected in this area, responsible for the second peak of the PDF of ϕ.

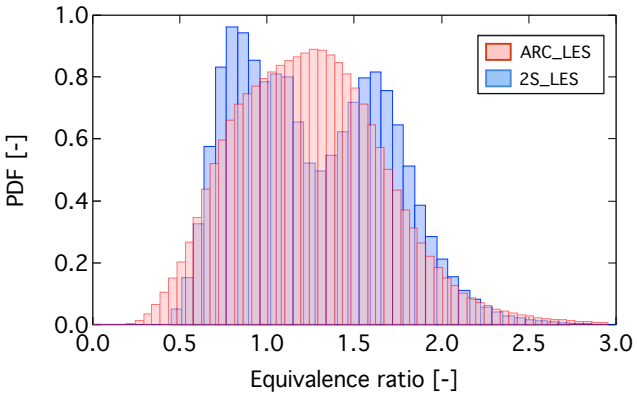

Figure 7.43: PDF of equivalence ratio in the reactive zone of the PZ ($\dot{\omega}_{C2H4} < -10$ kg/m3/s), averaged over 9 ms.

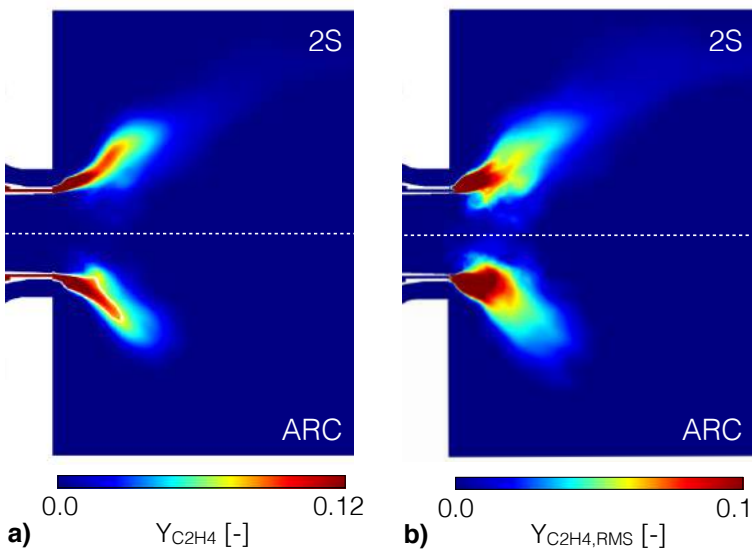

Figure 7.44: a) Time-averaged fields of Y_{C2H4} and b) RMS of C_2H_4 for both ARC-LES and 2S-LES.

7.9.3 Species and pollutant predictions

7.9.3.a Qualitative OH comparisons

Instantaneous fields of OH mass fraction are compared to experimental OH PLIF measurements in Fig. 7.45. OH is retrieved via the table provided for the soot computation, which is the same than that employed in the FPI-LES (see Appendix B). It is seen that the major structures observed in the experiment are equally well retrieved with both chemistry descriptions considered here. As in the ARC-LES, secondary combustion fronts are clearly visible in the DZ with the 2S chemistry description, and similar relatively high OH levels are observed throughout the combustion chamber. Overall, the tabulation with the modified progress variable appears to exhibit the right trends.

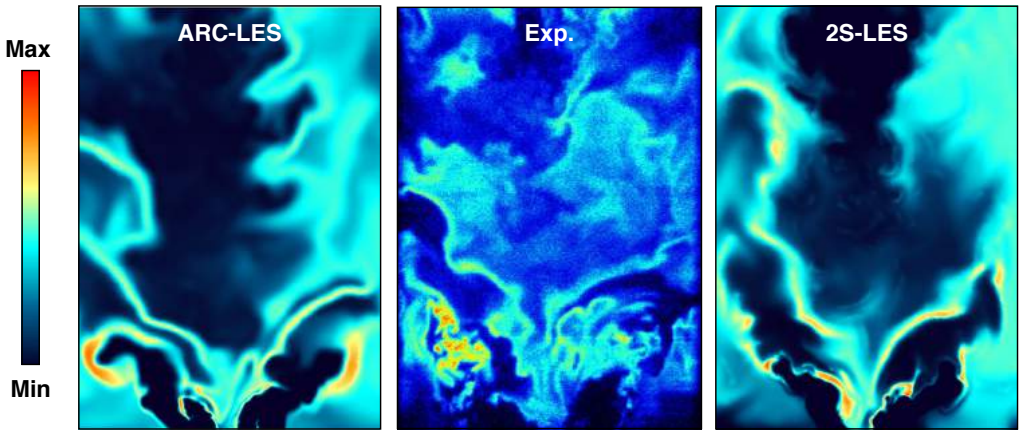

Figure 7.45: Instantaneous snapshots of OH mass fraction (ARC-LES, 2S-LES) and OH-LIF (Experiments), for Case A.

7.9.3.b CO exhaust levels investigations

As in Section 7.7.3.b exhaust CO levels are investigated by evaluating averaged EICO using either local Y_{CO} values or theoretical equilibrium values at the local equivalence ratio $Y_{CO,eq}(\phi)$. Results are reported in Table 7.7 for all computations. Not much differences are observed between all considered chemistry descriptions. Although there are no experimental data to confront those results to, this suggests that in this case, the 2S chemistry description is able to provide quantitative CO levels. This result is not that surprising, since 2S schemes are built in order to retrieve the correct burnt gas composition.

	EICO [g/kg]	EICO^{eq} [g/kg]	$\overline{Y_z'}$ [-]
Case A - ARC	185	172	$1.1e^{-2}$
Case A - FPI	177	168	$1.1e^{-2}$
Case A - 2S	179	183	$1.0e^{-2}$

Table 7.7: *CO* emission indices and mixture fraction variance in the outlet plane.

7.9.3.c Soot predictions

Figure 7.46 adds the 2S-LES results to the series of quantitative comparisons of time averaged fields of soot discussed in Section 7.7.3.c. Overall, the shape of the region of high soot loads is consistent with all other LES results, with a similar shift towards the injection system when compared to experimental results. Like in the experiments, no soot is found near the combustor's centerline, where the dilution jets meet.

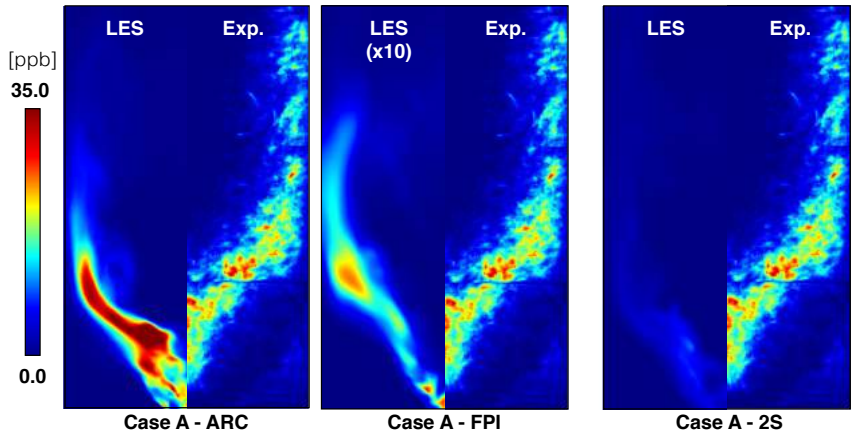

Figure 7.46: Comparison of time-averaged LII soot measurements with time-averaged soot mass fraction. Note that for comparison, the FPI-LES field has been multiplied ten times.

Interestingly, the 2S-LES levels are found to sit in between those obtained in the FPI computation (10 times too low) and those obtained with the ARC computation (consistent with experimentally observed levels): the under-prediction is only of about a factor 3. Since precursor levels, restricted to acetylene in the present case, are read in the same table than in the FPI simulation (see Appendix B), the higher soot loads cannot be imputed to higher acetylene levels. To confirm this intuition, scatterplots of C_2H_2 mass fraction are compared for all LES of Case A, in Fig. 7.47 (a). As expected, acetylene levels found in the LES with the 2S chemistry are

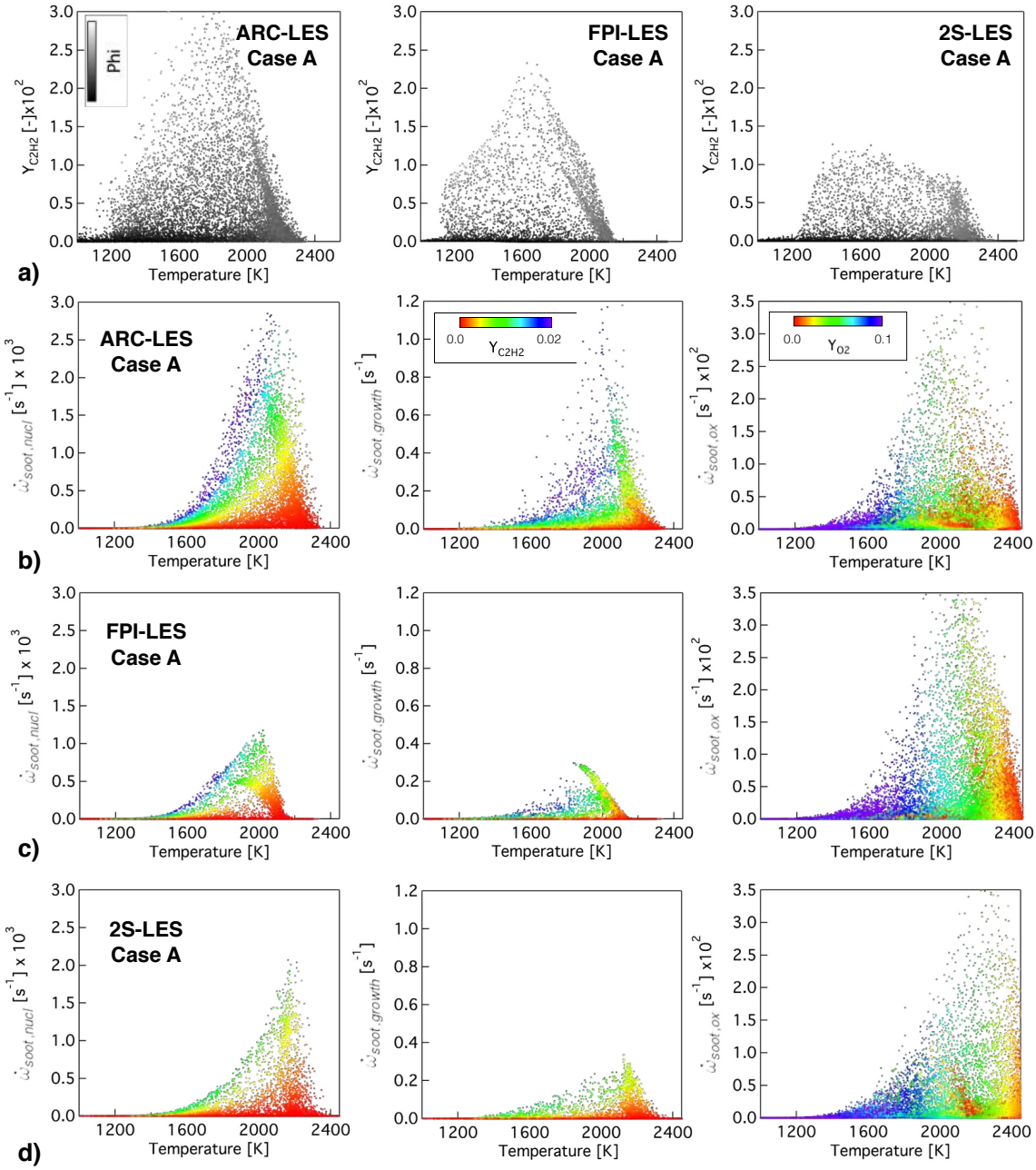

Figure 7.47: a) Scatterplots of C_2H_2 mass fraction for all Case A computations, coloured by ϕ. b) c) & d) Scatterplots of the different contributions to the soot global source term; each line corresponds to a LES simulation. From left to right: nucleation and growth -coloured by C_2H_2 mass fraction, and oxidation -coloured by O_2 mass fraction.

about twice smaller than those observed in the ARC-LES. The fact that levels appear even smaller than in the FPI-LES is just to be associated with the specific choice of instantaneous solutions employed to construct the scatterplots. Another interesting feature of these scatterplots is that, just as in the ARC-LES, relatively high acetylene levels (> 0.005) are observed for temperatures higher than 2200 K in the 2S-LES. However, as discussed in Section 7.7.3.c and observed in Fig. 7.47 (c), the FPI-LES soot production is abruptly stopped for these temperatures, where the progress variable border on 1. This points towards a completely different distribution of the progress variable in the FPI-LES and the 2S-LES, enabling in this last case to retrieve even

moderate levels of C_2H_2 in relatively high temperature regions. This acetylene/temperature distribution, in turn, enable nucleation and soot growth to occur, as can be seen on Fig. 7.47 (d). In fact, as seen in Figs. 7.47 (b) & (d) and 7.48 (a) & (b), the temperature regions and spatial locations where soot nucleation, growth and oxidation occurs are consistent between the 2S-LES and the ARC-LES (considered to be the reference).

This analysis helps quantifying the impact of the various simplifying assumptions on obtained soot loads. Following the findings of this Section and Section 7.7.3.c, two factors are identified as being leading order phenomena in the present configuration: the progress variable distribution and, through acetylene levels, the equivalence ratio stratification. Furthermore, both appear as equally important. Of course, there is no way to certify for sure that these conclusions will apply to other configurations, operating under different pressure, temperature, with a different injection system or with a different fuel etc. However, it seems reasonable to assume that ARC mechanisms, by keeping the physics of the problem and being free of any modeling assumption, will naturally adapt to the problem at hands. As such, simulations with ARC chemistry enable to perform both qualitatively and quantitatively relevant analysis. In the present case, it was the only chemistry description able to provide quantitatively accurate soot loads.

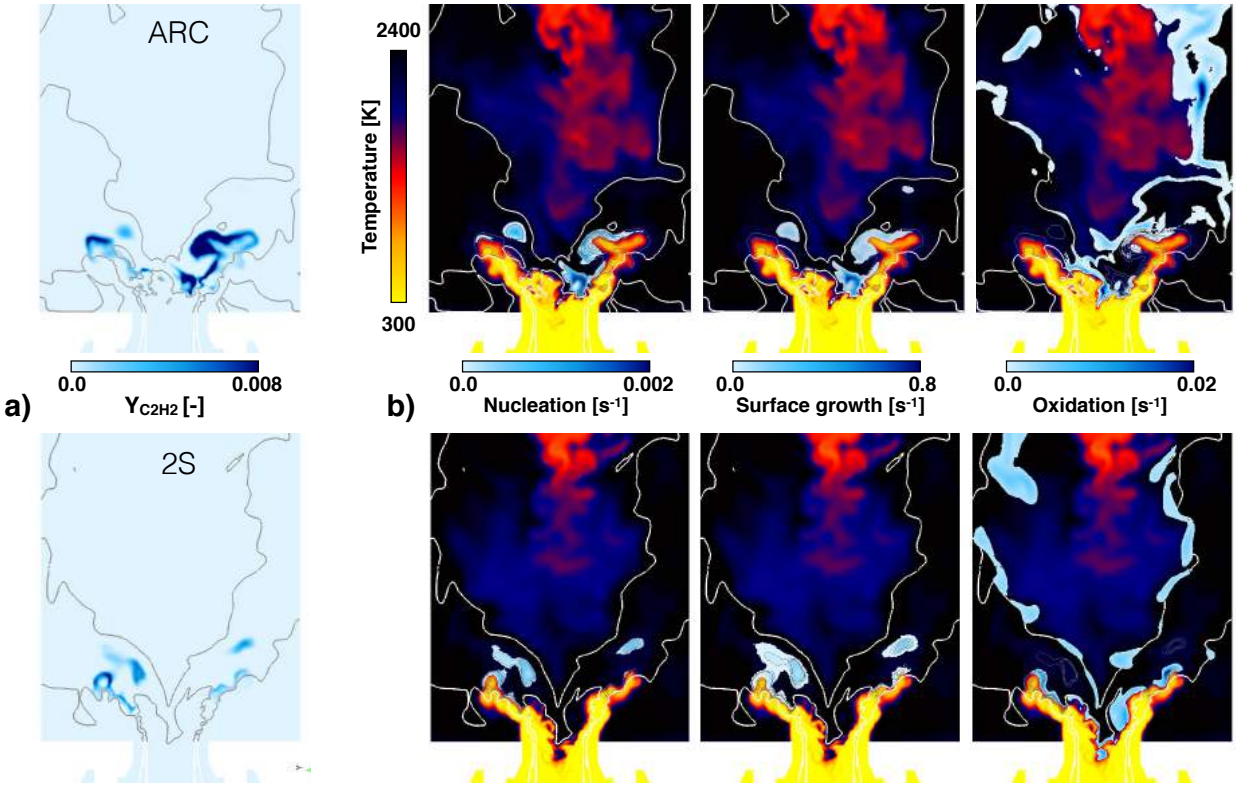

Figure 7.48: Instantaneous fields of a) C_2H_2 mass fraction and b) temperature with overlaid iso-volume of the various components of soot source term, for ARC (top) and 2S (bottom) schemes.

7.10 Overall conclusions of the chapter

In this Chapter, several LES of the gaseous FIRST configuration were performed, with the intent to investigate the impact of the chemistry description on the accuracy of various measured quantities. Emphasis was put on soot predictions. Three chemistry descriptions were investigated: a global 2 step scheme, an FPI table based on premixed canonical configurations, and an ARC mechanism. All these chemistry descriptions were complemented with a simple two-equation soot model, requiring to transport 2 additional species. Implementation in the ARC and FPI simulations was straightforward, when it required additional efforts in the 2S case lacking the main precursor, acetylene. All simulations employed the DTFLES combustion model, and it has been verified that thickening was similar in all cases, both in terms of spatial distribution and overall values.

Results show that all chemistry descriptions are able to provide satisfying predictions of average velocity and temperature fields, as expected. Noteworthy also, is the fact that in the present case, all chemistry description

agree on exhaust CO levels. This was not necessarily an expected outcome. Indeed, it has been shown that the FPI table, being constructed on ethylene/air premixed archetypes, failed to provide the correct CO/air flame structures in the secondary combustion zone. The role of chemistry was however revealed to be crucial in predicting accurate levels of soot. The FPI and 2S scheme, both relying upon a table virtually freezing the interactions between the flame and the flow, failed to provide accurate levels of soot. The under-estimation was of about one order of magnitude in the FPI case. With the 2S chemistry description, the reconstruction of the progress variable based on transported quantities (CO and CO_2) allowed for a more accurate repartition of Y_z and Y_c, such that the under-estimation was reduced to about a factor 3. The presence of Y_c values < 1 in region of high temperature was revealed to be, in particular, very important to the nucleation and growth process. Equally important is the stratification in the primary partially premixed flame fronts, leading to higher values of acetylene than expected in canonical archetypes and boosting the production of soot. In that regard, the only chemistry description able to account for all important phenomenon was the ARC chemistry description.

Finally, the impact of varying the operating point was also investigated, with an additional LES simulation at higher pressure, Case B. This computation was performed with the ARC chemistry solely. The flexibility of the ARC description is appreciated in that case, were the computational setup was easily put in place. On the contrary, the modeling of Case B with any other chemistry description considered here would have required to generate new tables, and possibly to adapt the characteristics of the global scheme to fit the new operating point. Here also, very satisfactory results were obtained in terms of soot predictions.

These results are encouraging, and demonstrate the flexibility and capability of the ARC-DTFLES methodology in predicting accurately the complex flame structures encountered in realistic burners, without the need to formulate assumptions *a-priori* on the nature of the flow.

A word about CPU requirements Table 7.8 summarizes the CPU requirements of all chemistry description, for Case A. For the purpose of comparisons, all simulations were performed on the CERFACS in-house NEMO cluster (Intel Haswell architecture). As expected, the overcost of employing the ARC mechanism is of about 50% when compared to the 2S approach, and is due to the higher number of species to transport. Note that with the 2S scheme the consideration of an additional species, the modified progress variable, is required when modeling soot (see Appendix B). Interestingly, the cost of employing an FPI table is, in the present case, similar than that of employing a 2S scheme. Indeed, handling the table throughout the simulation slows down the process considerably, due to frequent consultations and interpolations.

	Case A - ARC	Case A - FPI	Case A - 2S
Navier-Stokes	5	5	5
Transported species	18	2	6
Soot model	2	2	2 +1
Total transported variables	**25**	**9**	**14**
CPUh for 1 ms	**12500**	**6200**	**6900**

Table 7.8: Summary of computational requirements

Chapter 8

Application to a real fuel in a two-phase combustor

Contents

8.1 Introduction

In this Chapter, the HyChem approach for real fuel modeling is applied in a flow Lean Direct Injection system, burning kerosene. This Chapter directly follows Section 4.4, where the HyChem approach as well as a detailed and a reduced mechanism for a specific kerosene, the Jet A POSF10325, were discussed at length. Section 8.2 briefly summarizes the modeling procedure. Additional validations of the LES compliant reduced ARC 29_JetA2NOx mechanism are also presented. Section 8.3 then introduces the target configuration while Section 8.4 completes Section 6.1.2 by presenting the N.-S. equations for two-phase flows described in a Lagrangian framework. Finally, results are analysed, in Section 8.5.

8.2 ARC for Jet A with NO_x chemistry

8.2.1 The Jet A POSF10325 specifications

Properties of the Jet A POSF10325 were presented in Section 4.4.2 and are recalled in Table 8.1. This batch is expected to be an average Jet A fuel.

Molecular formula	Composition (mass fraction [%])					Mol. Weight
	Aromatics	*iso*-Paraffins	*n*-Paraffins	Cycloparaffins	Alkenes	[kg/mol]
$C_{11.4}H_{22.1}$	18.66	29.45	20.03	31.86	<0.001	156.0
H/C	Δh_c [MJ/kg]	DCN	T_{10} [K]	$T_{90} - T_{10}$ [K]	μ_l(300 K) [mPa s]	ρ_l(300 K) [kg/m^3]
1.91	43.1	48.3	450.0	67.8	1.37	794

Table 8.1: Properties of Jet A POSF10325

8.2.2 The detailed mechanism

The HyChem modeling strategy introduced in Section 4.4.1.a is employed here. For the Jet A (POSF10325) under consideration, the fuel breakdown is described by 6 lumped reactions, the detailed mechanism for the oxidation of the pyrolysis products is chosen to be the USCII mechanism (see Section 4.3.1), and a NO_x submechanism is added, extracted from the thesis of Luche (2003). The procedure was described in Section 4.4.4.a. The final detailed mechanism, JetA2_NOx, is comprised of a total of 129 species and 1572 irreversible reactions.

8.2.3 Derivation of the ARC mechanism

An analytically reduced chemistry (ARC) is obtained from the detailed kinetic mechanism JetA2_NOx with the tool YARC (Pepiot, 2008), following the three automated steps described at length in Chapter 4. The set of targets as well as the set of canonical configurations are representative of the studied configuration of Cai *et al.* (2005) presented in Section 8.3. The equivalence ratio range extends from $\phi = 0.5$ to $\phi = 1.5$. Targets consist of auto-ignition time (τ_{ig}), burnt gas temperature T_b, laminar flame speed s_l^0, main species final values, and specific intermediate species profiles. The full set of targets are reported in Table 8.2.

Canonical test cases	**Targeted range**	**Targeted constraints**
PF	1 atm / 300K / ϕ = 0.8-1.3	CO CO_2 C_2H_4 OH HR NO
AI	1 atm / 1300-1700 K / ϕ = 0.8-1.3	CO CO_2 C_2H_4 OH HR NO

Table 8.2: List and specifications for the reduction performed with YARC.

The resulting ARC, ARC_29_JetA2NOx, retains 29 transported species and 17 QSS. Details about the derivation were provided in Section 4.4.4.b. All species (transported+QSS) are reported on Fig. 8.1, along with a crude estimation of their lifetime (see Section 6.3.3). The size of this reduced mechanism allows a direct implementation in the LES solver AVBP, with simplified transport data, as will be described in Section 8.4.1.

8.2.4 Validation of the ARC_29_JetA2NOx

The performances of the ARC_29_JetA2NOx were evaluated against that of the detailed mechanism JetA2_NOx in zero- and one-dimensional canonical test cases with CANTERA (Goodwin *et al.*, 2014) and FlameMaster (Pitsch, 1988). A mixture averaged formulation (TranMix, see Section 5.2.2) is employed for the transport properties of the JetA2_NOx mechanism. For the ARC mechanism, the simplified transport model of AVBP is employed (see Section 5.2.3) with the constant values of species Schmidt numbers and Prandtl number taken in the flame zone of a PF computed with complex transport. These values may be found in Table 4.11.

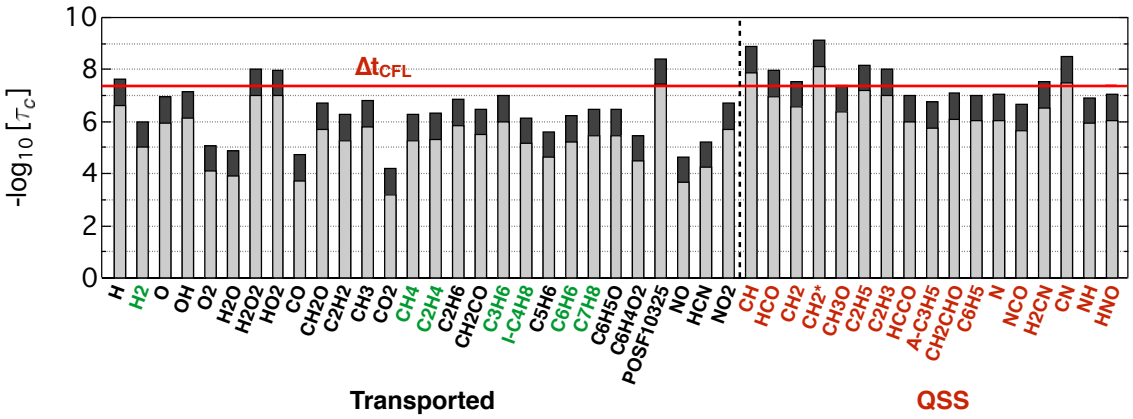

Figure 8.1: Summary of the chemical timescales of the transported and QSS species of the ARC_29_JetA2NOx. The integration time step Δ_t corresponding to the simulation with AVBP of the configuration under investigation is identified by the red line.

PF and AI test cases are first considered, corresponding to the canonical configuration used to derive the ARC mechanism. As expected, global quantities targeted by the reduction procedure, such as T_b, s_l and τ_{ig} are shown to be accurately recovered by the ARC_29_JetA2NOx, see Fig. 8.2 (a)-(c). For values of the equivalence ratio range outside the targeted range, results are still very good, as it is most often the case with this type of reduced mechanism. In the present case, the relative error on s_l is always under 3%, except in very lean conditions where it reaches a maximum of 8%. Predicted τ_{ig} are seen to be less accurate under rich conditions, but results are still well within experimental uncertainties. The pollutant predicting capabilities of both detailed and ARC mechanisms are assessed by looking at the global CO and NO production through the flame front:

$$\dot{\omega}^{tot}_{CO/NO} = \int_{c<0.98} \dot{\omega}_{CO/NO} dx \tag{8.1}$$

Results are presented on Fig. 8.2 (d)-(e). An excellent agreement is observed between the detailed mechanism and the ARC_29_JetA2NOx results for CO global production, with a relative error computed over the entire range of equivalence ratio consistently under 5%. NO global production is less accurately retrieved by the ARC mechanism, with errors ranging from 10 to 40%. In light of the uncertainties discussed in Section 4.4.4.a, however, results are considered satisfactory.

Finally, *a-posteriori* validation on laminar strained counterflow diffusion flames configurations (CF) is performed. Indeed, because the target application is a spray burner, the occurrence of diffusion flames is expected, and the validity of the ARC_29_JetA2NOx must be checked. The maximum temperature is plotted versus scalar dissipation rate at stoichiometry, χ_{st}, in Fig. 8.2(f) for both the detailed and the ARC mechanism, leading to classical S-shaped curves of. A very good agreement is observed, in particular, the extinction scalar dissipation rate χ_{ext} is perfectly matched by the ARC mechanism.

8.3 The LDI combustor

8.3.1 Experiment

To the best of our knowledge, only a handful of lab-scale experimental facilities are operated with real aeronautical fuels Cai *et al.* (2005); Lecourt *et al.* (2011); Apeloig *et al.* (2014). The configuration chosen in this work is the Lean Direct Injection (LDI) combustor operated at NASA Glenn (Cai *et al.*, 2005; Fu *et al.*, 2005; Iannetti *et al.*, 2008). This choice was mainly driven by the wealth of experimental data available in terms of temperature and chemical species, allowing an accurate validation of the proposed methodology. A picture of the experimental facility is presented in Figure 8.3(a) while details of the injection system are shown in Figure 8.3(b). The burner consists of an axial swirler composed of six helicoidal vanes inclined at 60° and a PARKER pressure-swirl atomizer located in the center. The atomizer tip is located at the throat of a converging/diverging nozzle. The outer diameter of the nozzle at the combustion chamber dump plane is $D_0 = 0.025$ m. The combustion chamber has a height of 305 mm and a square section of length 50.8 mm. Quartz windows allow optical access from all sides.

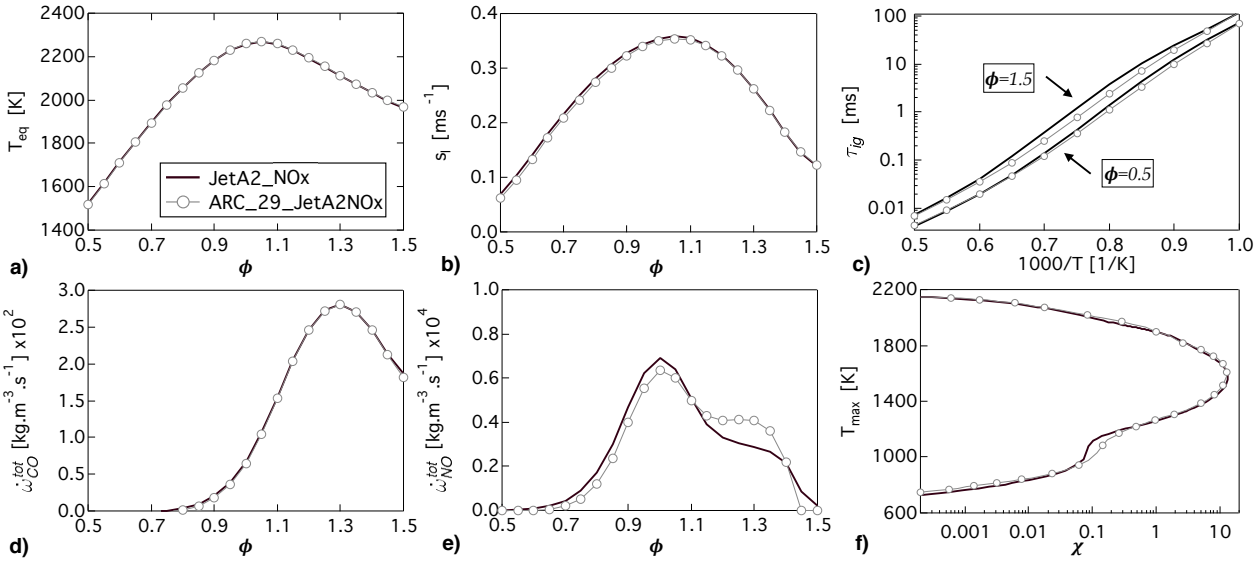

Figure 8.2: Performances of the ARC_29_JetA2NOx reduced mechanism. PF test cases: (a) T_b, (b) s_l^0, (d) global CO production and (e) global NO production for $T_i = 300$ K, P = 1 bar. AI test cases: (c) τ_{ig} for $\phi = 0.5$, 1.5, P = 1 bar. CF test cases: (f) S-curve for $T_i = 300$ K, P = 1 bar.

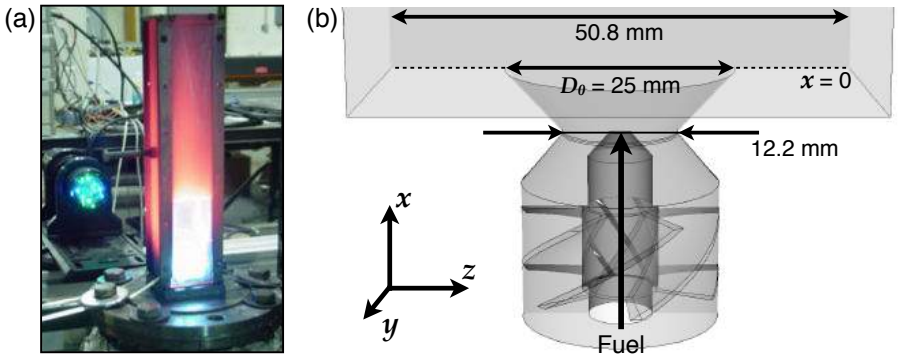

Figure 8.3: (a) Picture of the experimental test rig (Cai *et al.*, 2005). (b) Details of the injection system.

The combustor is operated at ambient conditions ($P = 1$ atm, $T = 300$ K). Air is injected with a nominal mass flow rate of 8.16 g/s through a plenum upstream of the swirler vanes while liquid Jet A fuel is injected through the atomizer with a mass flow rate of 0.415 g/s. These conditions correspond to an overall lean equivalence ratio $\phi = 0.75$. Due to the low pressure in the fuel lines, the spray is found to exhibit intermittent distribution patterns (Cai *et al.*, 2005). Laser Doppler Velocimetry is used to measure gas velocity while Phase Doppler Particle Analyzer measurements are performed for spray velocity and droplet size distribution (Cai *et al.*, 2005). Gas temperature and species profiles are obtained from thermocouple and isokinetic probes, respectively (Iannetti *et al.*, 2008).

8.3.2 Previous studies

The LDI combustor has been previously studied using LES by several groups. Patel *et al.* (2007); Patel & Menon (2008) performed LES using the Linear Eddy Model (LEM) with a 3-steps global chemical scheme accounting for fuel oxidation as well as CO and NO formation, while the Jet A was approximated by $C_{12}H_{23}$. LES predictions were found accurate for the non-reacting flow, but significant errors were observed in reacting conditions. The spray/flame interaction was then investigated and in particular, the effect of the precessing vortex core (PVC) on the droplet dispersion was highlighted. The effect of radiative heat losses on the temperature and species fields was studied by El-Asrag *et al.* (2014). This study employed the flamelet-progress variable approach modified to account for radiation and NO formation (Ihme & Pitsch, 2008*a*) where the tabulated variables were calculated from steady counterflow diffusion flamelets obtained with the detailed mechanism of a two-components Jet A surrogate (Honnet *et al.*, 2009). Comparison with experimental data indicates that taking into account radiative

heat transfer greatly improves temperature and pollutant species predictions. Finally, Knudsen *et al.* (2015) also performed LES of the LDI combustor in order to validate a multi-regime flamelet approach and investigate the LES predictions sensitivity to the spray evaporation model and boundary conditions. As in El-Asrag *et al.* (2014), the pre-calculated flamelet tables were constructed using the two-components Jet A surrogate (Honnet *et al.*, 2009). This study showed that the LES prediction are highly sensitive to both the evaporation model and the spray boundary conditions, especially the pressure-swirl cone angle. The best results were obtained using a 61° cone angle, which differs from the 90° nominal value of the pressure-swirl manufacturer.

8.4 Numerical setup

8.4.1 Governing equations

8.4.1.a Gas phase equations

In this Section, the spatially averaged compressible N.-S. equations already detailed for a reactive gaseous mixture in Section 6.1.2 are briefly recalled, with the inclusion of the source terms of exchange with the liquid phase. In the DTFLES framework (see Section 6.2.2) and assuming dilute spray regime, the conservation equations write:

$$\frac{\partial \overline{\rho}}{\partial t} + \frac{\partial \overline{\rho}\widetilde{u}_j}{\partial x_j} = \overline{\Gamma} \tag{8.2}$$

$$\frac{\partial \overline{\rho}\widetilde{u}_i}{\partial t} + \frac{\partial \overline{\rho}\widetilde{u}_i\widetilde{u}_j}{\partial x_j} = -\frac{\partial}{\partial x_j}\left[\overline{p}\delta_{ij} - \overline{\tau}_{ij} - \overline{\tau}_{ij}^{sgs}\right] + \widetilde{u}_{d,i}\overline{\Gamma} + \overline{F}_{d,i} \tag{8.3}$$

$$\frac{\partial \overline{\rho}\widetilde{E}}{\partial t} + \frac{\partial \overline{\rho}\widetilde{E}\widetilde{u}_j}{\partial x_j} = -\frac{\partial}{\partial x_j}\left[\overline{u_i(p\delta_{ij} - \tau_{ij})} + \mathcal{E}\mathcal{F}\overline{q}_j + \overline{q}_j^{sgs}\right] + \frac{\mathcal{E}\overline{\dot{\omega}}_T}{\mathcal{F}} + \overline{\Pi} + \frac{1}{2}\widetilde{u}_{d,i}^2\overline{\Gamma} - \widetilde{u}_{p,i}\overline{F}_{d,i} \tag{8.4}$$

$$\frac{\partial \overline{\rho}\widetilde{Y_k}}{\partial t} + \frac{\partial \overline{\rho}\widetilde{Y_k}\widetilde{u}_j}{\partial x_j} = -\frac{\partial}{\partial x_j}\left[\mathcal{E}\mathcal{F}\overline{J}_{k,j} + \overline{J}_{k,j}^{sgs}\right] + \frac{\mathcal{E}\overline{\dot{\omega}}_k}{\mathcal{F}} + \overline{\Gamma}\delta_{k,F} \quad \text{for } k = 1, N_s \tag{8.5}$$

where ρ is the gas density, u_j is the gas j-*th* component of velocity, E is the total non-chemical energy, p is the pressure, and Y_k is the mass fraction of species k. $\mathcal{F}$ and $\mathcal{E}$ are the thickening factor and the efficiency function, respectively, introduced by the thickened flame model (see Section 6.2.2). $\overline{\tau}_{ij}$ is the filtered stress tensor, $\overline{q}_j$ is the filtered heat diffusive flux and $\overline{J}_{k,j}$ is the filtered species diffusive flux; their evaluation is presented in Section 6.1.3. The transport coefficients are evaluated following the simplified transport model TranAVBP, presented in Section 5.2.3, with the species Sc numbers listed in Table 4.11 and a Power law for the dynamic viscosity. The superscript sgs indicates sub-grid scale contributions arising from the LES filtering, described in Section 6.1.4 and 8.4.1.c. Finally, $\overline{\Gamma}$, $\overline{F}_{d,i}$ and $\overline{\Pi}$ are the liquid phase source terms detailed in Section 8.4.1.b.

8.4.1.b Dispersed phase description

The spray is described with a Lagrangian approach where the motion of the droplets is described by the Basset-Boussinesq-Oseen equations. Under the assumption of small droplet diameter, small droplet Reynolds number and large density ratio between the liquid and the gas, the droplet motion equations write:

$$\frac{d\boldsymbol{x}_d}{dt} = \boldsymbol{u}_d \tag{8.6}$$

$$\frac{d\boldsymbol{u}_d}{dt} = \frac{1}{\tau_p}(\boldsymbol{u}_{@d} - \boldsymbol{u}_d) = \frac{\boldsymbol{F}_d}{m_d} \tag{8.7}$$

where $\boldsymbol{x}_d$ is the droplet position and $\boldsymbol{u}_d$ is the droplet velocity, $\boldsymbol{u}_{@d}$ is the gaseous velocity at the particle position and m_d is the droplet mass. τ_p is the droplet relaxation time, estimated as the Stokes characteristic time:

$$\tau_p = \frac{4}{3}\frac{\rho_l}{\rho}\frac{2r_d}{C_D|\boldsymbol{u}_{@d} - \boldsymbol{u}_d|} \tag{8.8}$$

where ρ_l is the liquid density, r_d is the droplet diameter. C_D is the drag coefficient given in terms of the droplet Reynolds number Re_p by the Schiller and Naumann correlation (Schiller & Naumann, 1935) :

$$C_D = \frac{24}{\mathrm{Re}_d}(1 + 0.15\mathrm{Re}_d^{0.687}) \tag{8.9}$$

$$\mathrm{Re}_d = \frac{|\boldsymbol{u}_{@d} - \boldsymbol{u}_d|2r_d}{\nu} < 800 \tag{8.10}$$

Droplet heating and evaporation is evaluated with an equilibrium law based on the Abramzon-Sirignano model (Abramzon & Sirignano, 1989). Under the assumption of dilute spray regime, individual droplet evaporation is considered, where droplets interactions are neglected. The droplet mass and temperature are given by:

$$\dot{m}_d = \frac{dm_d}{dt} = -2\pi r_d \frac{\mathrm{Sh}}{Sc_F}\mu_g \ln(1 + B_M)\frac{1}{\mathcal{F}} \tag{8.11}$$

$$\begin{aligned}\frac{dT_d}{dt} &= \frac{1}{c_L m_d}\left(-\phi_g + \dot{m}_d L_{h,F}\right) \\ &= \frac{1}{c_L m_d}\left(2\pi r_d \mu_g \overline{C}_p \frac{\mathrm{Nu}}{Pr}(T_{g@d} - T_p)\frac{\ln(1+B_T)}{B_T}\frac{1}{\mathcal{F}} + \dot{m}_d L_{h,F}\right)\end{aligned} \tag{8.12}$$

where T_d is the droplet temperature, $T_{g@d}$ is the gas temperature at the droplet position, c_L is the liquid heat capacity and $L_{h,F}$ is the latent heat of evaporation of the liquid species. Sh and Nu are the Sherwood number and Nusselt number, respectively, evaluated using the Ranz-Marshall empirical correlations (Ranz & Marshall, 1952):

$$\mathrm{Sh} = 2.0 + 0.55.\mathrm{Re}_p^{1/2}.\mathrm{Sc}^{1/3} \tag{8.13}$$

$$\mathrm{Nu} = 2.0 + 0.55.\mathrm{Re}_p^{1/2}.\mathrm{Pr}^{1/3} \tag{8.14}$$

Pr and Sc_F are the Prandtl number and fuel Schmidt number, respectively. μ_g and $\overline{C}_p$ are the reference condition gaseous viscosity and heat capacity estimated with the '1/3' rule between far field and droplet surface conditions. Finally, B_M and B_T are the mass and temperature Spalding number evaluated following (Abramzon & Sirignano, 1989). Note that, the thickening factor of the DTFLES model $\mathcal{F}$ appears on the right-hand side of Eqs. (8.11) and (8.12) in order to account for the thickening approach in the flame zone (Paulhiac, 2015).

Finally the Lagrangian source terms appearing in the N.-S. equations are computed using:

$$\overline{\Gamma} = \frac{1}{\Delta V}\sum_{d\in\Delta V}\Psi(\boldsymbol{x}_d)\dot{m}_d \tag{8.15}$$

$$\overline{\boldsymbol{F}_d} = \frac{1}{\Delta V}\sum_{d\in\Delta V}\Psi(\boldsymbol{x}_d)\boldsymbol{F}_d \tag{8.16}$$

$$\overline{\Pi} = \frac{1}{\Delta V}\sum_{d\in\Delta V}\Psi(\boldsymbol{x}_d)\left(\phi_g + \dot{m}_d h_{v,F}(T_d)\right) \tag{8.17}$$

where ΔV is the local control volume in which the droplet is located (usually the node cell) and $\Psi(\boldsymbol{x}_d)$ a first-order interpolation function between the particle position and the grid nodes.

8.4.1.c LES subgrid scale closures

In the present study, the SIGMA eddy-dissipation model of Nicoud *et al.* (2011) (see Section 6.1.5) is used to evaluate the subgrid Reynold stress tensor τ_{ij}^{sgs} while heat and species *sgs* transport are modeled with a gradient

assumption and a constant turbulent Pr number and turbulent Sc number, respectively ($Pr_t = Sc_t = 0.6$) (see Section 6.1.4).

The dynamic thickened flame model (DTFLES) is employed to model the turbulence/chemistry interaction (Colin *et al.*, 2000), while the efficiency function formulation of Charlette *et al.* (2002) is used to account for the subsequent loss of flame surface. The same dynamic methodology than described in Section 7.6.2.a is employed in this work, to adapt values of $\mathcal{F}$ and $\mathcal{E}$ to local flow conditions. All laminar unstrained flame characteristics appearing in this dynamic model (δ_l^0 and s_l^0) are tabulated in function of the equivalence ratio. The same methodology to build the dynamic sensor than described in Section 6.2.2.c (methodology of T. Jaravel) is employed here, in order to only apply the thickening in reacting regions. It is based upon the source term of fuel.

No sub-grid model is employed to evaluate the gas properties at the droplet position (Fede *et al.*, 2006).

8.4.2 Computational domain and boundary conditions

The computational domain comprises the entire combustion chamber and the injection system up to the annular section upstream of the swirler. The computational domain, displayed in Fig. 8.4 (a), is fully discretized using tetrahedra with size varying from 0.25 mm close to the injection system to about 3 mm in the downstream part of the combustion chamber. The final computational domain contains over 4 millions nodes and 23 millions tetrahedron. Figure 8.4 (b) displays a close-up of the mesh of the near injection.

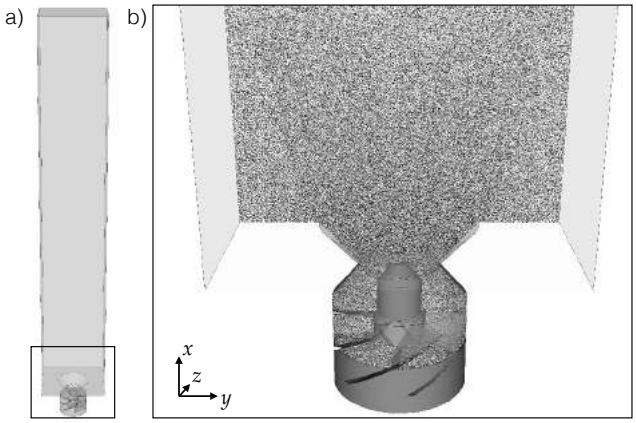

Figure 8.4: a) Entire computational domain and b) Mesh resolution at the vicinity of the injection system.

Simulations are performed with the compressible, massively-parallel LES solver AVBP. It uses an explicit time-stepping with a third order in time and space two-step Taylor-Galerkin finite element scheme for the resolution of the convective fluxes (Colin & Rudgyard, 2000) and a second order Galerkin scheme for the diffusive fluxes. Inlet and outlet boundary conditions are prescribed using the NSCBC approach while walls are considered adiabatic and non-slipping (see Section).

Lagrangian particles are advanced in time with a semi-implicit Euler scheme. The interpolation of gas properties to the particle location is performed using a first order Taylor reconstruction from the closest point. A poly-disperse spray injection boundary condition is prescribed at the pressure-swirl nozzle using the FIMUR methodology of Sanjosé *et al.* (2011). Drops are injected with a temperature of 300 K. Based on the work of Knudsen *et al.* (2015), a spray angle of 60° with a log-normal diameter distribution is employed in this work, with a mean of 17 μm and a standard deviation of 20 μm.

An analysis of the droplet/wall interactions along the chamber walls indicates that a wide range of energy of impact C_{spl} is observed. The energy of impact is defined as C_{spl} =We.Oh$^{-2/5}$, where We is the impact Weber number We=$\rho_l 2r_d|\boldsymbol{u}_d \cdot \boldsymbol{n}|/\sigma_l$ and Oh the Ohnesorge number Oh=$\mu_l/\sqrt{\rho_l \sigma_l 2r_d}$. σ_l is the liquid surface tension and $\boldsymbol{n}$ is the wall normal vector. Therefore, a splashing model is used, in which droplets either stick to the wall or are partly splashed away, depending upon a critical energy impact $C_{spl,crit}$ and a characteristic temperature T_N (Nukiyama temperature), as depicted in Fig. 8.5. The splashed droplets size distribution follow a Rosin-Rammler function, and their velocity primarily depends upon the energy of impact. More information about the splashing model can be found in (Iafrate, 2016).

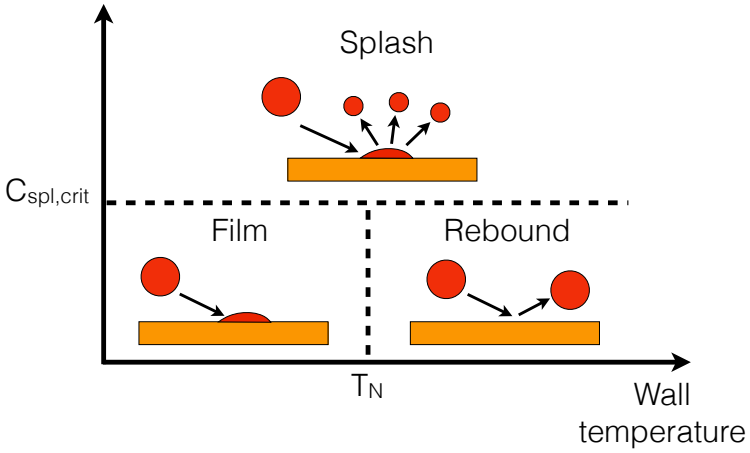

Figure 8.5: Sketch of the splashing model.

8.5 Results

8.5.1 Non-reacting single-phase flow validation

For validation purposes, the non-reacting velocity fields are compared against experimental data. Profiles are extracted at four axial positions downstream of the injector tip, marked in Fig. 8.7 (b), and are presented in Figure 8.6. LES results are in excellent agreement with experiment in terms of inner recirculation zone (IRZ) width and velocity magnitude, as well as turbulent velocity fluctuations levels. Note the large opening angle of the swirled jet, which is characteristic of high swirl number flows. Specifically, the swirl number of the injector has a value of 1.0, substantially larger than the critical swirl number of 0.6. The shear layer between the IRZ and the incoming swirled flow exhibits large fluctuations associated with a precessing vortex-core (PVC), also visible from the turbulent velocity profiles of Figure 8.6.

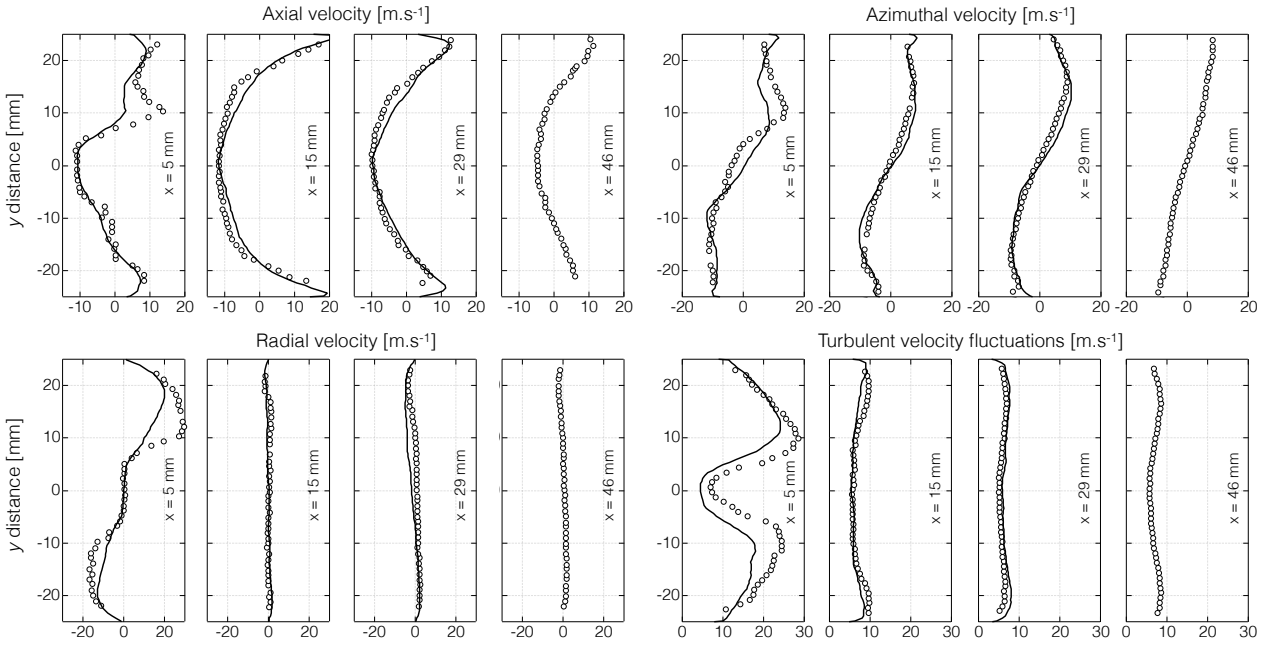

Figure 8.6: Profiles of time-averaged mean velocity and turbulent intensity at $x = 5$ mm, 15 mm, 29 mm and 46 mm in non-reacting conditions. Symbols: experiment, black line: LES.

8.5.2 Reacting two-phase flow validation

LES statistics presented in this Section were collected during 100 ms, corresponding to about 13 flow through times of the combustor.

8.5.2.a Gaseous velocity

The main flow structures are similar to that of the non-reacting case discussed in Section 8.5.1 and a comparison between LES and experiment is provided in Fig. 8.7(a). Figure 8.7(b) shows time-averaged velocity magnitude and turbulent velocity magnitude contours in a z-normal central plane, along with the zero axial velocity iso-contour. LES predictions are found to match well the experimental data, except at the vicinity of the injector where the width of the IRZ and the turbulent intensity are overestimated. Experimental results suggest that the combustion process induces a strong reduction of the turbulent intensity and a strong increase of the radial velocity component close to the injector. The IRZ is found to be narrower and shorter than in the non-reacting case, extending from just downstream of the pressure-swirl nozzle to about $x = 2\ D_0$. The magnitude of the negative axial velocity near the injection is also found to be significantly larger in the reacting case, indicating that the recirculation, playing an important role in the flame stabilization mechanism, is also impacted by the flame. The iso-contour of zero axial velocity also highlights small outer recirculation zones in the corners of the combustion chamber as well as a small recirculation in the divergent section of the injection system.

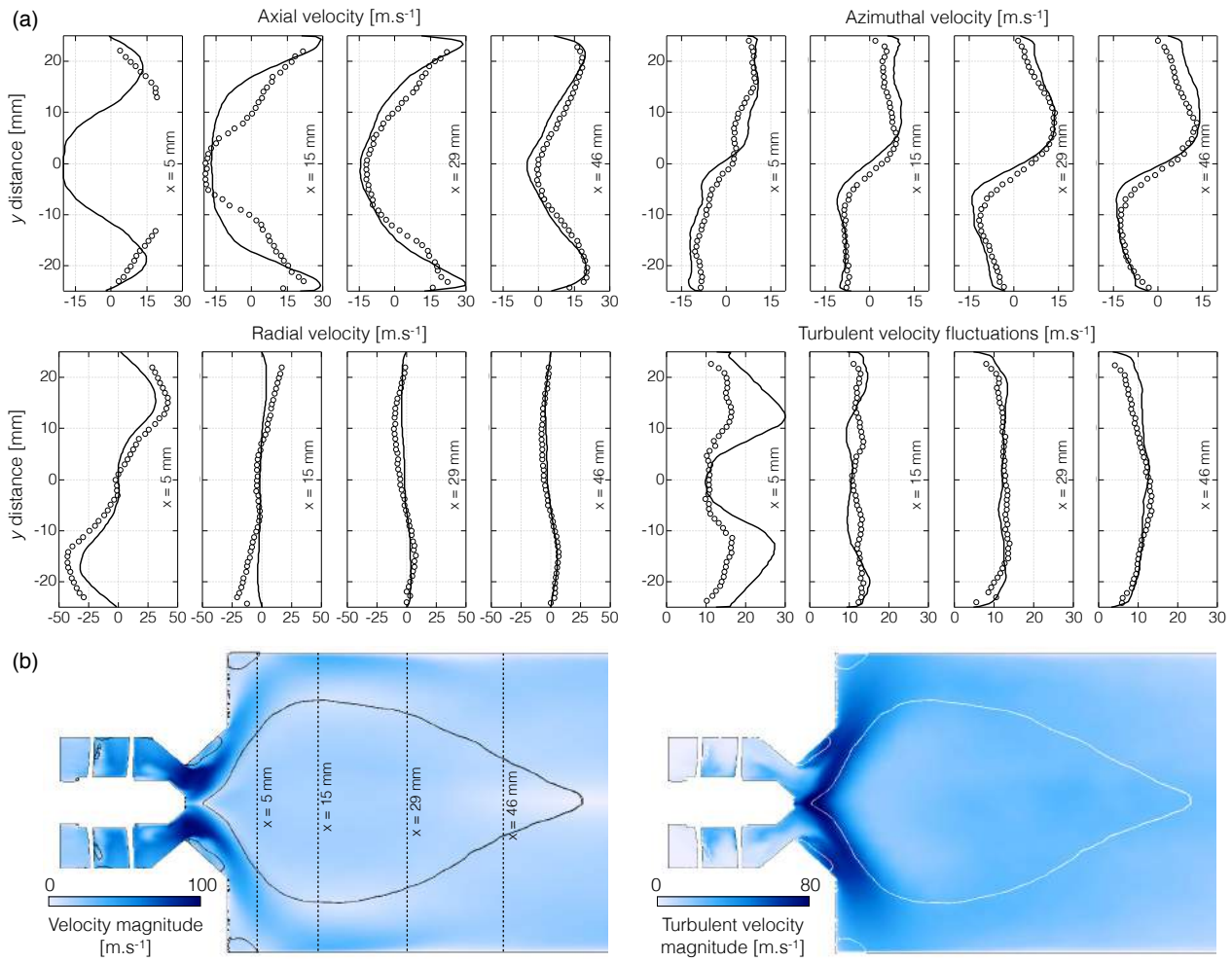

Figure 8.7: (a) Profiles of time-averaged mean velocity and turbulent intensity at $x = 5$ mm, 15 mm, 29 mm and 46 mm in reacting conditions. Symbols: experiments, black line: LES. (b) Time-averaged fields of velocity magnitude and turbulent velocity magnitude in a z-normal central cut plane from the LES. The iso-contour indicates the position of the zero axial velocity

8.5.2.b Spray statistics

Figure 8.8(a) shows a comparison of LES spray statistics against experimental data and Figure 8.8(b) shows the liquid volume fraction field in the central z-normal plane, constructed by projection of Lagrangian datasets. LES data are collected from 130 instantaneous Lagrangian solutions spanning more than 50 ms. Note that to ensure a statistical convergence, the data presented in Figure 8.8(a) are azimuthally averaged. Radial profiles of sauter mean diameter (SMD) and mean diameter (D10) are presented first. The agreement between LES and experiment is very good at all the measured positions, with only a noticeable under-prediction of the SMD along the injector axis and of the D10 at 20 mm. The good agreement on the first profile validates the selected spray boundary conditions (Knudsen *et al.*, 2015). Note the differences between the SMD and the D10 close to injector, suggesting a wide dispersion of the droplet size distribution. This is especially true close to the injector axis, where large droplets are able to penetrate the IRZ while small droplets are deflected. At increasing distance from the injector, both the SMD and the D10 increase while getting closer, indicating that small droplets are progressively vaporized and that the local droplet size distribution gets narrower. This effect is well predicted in the LES, validating the modeling approach for droplet dispersion and evaporation.

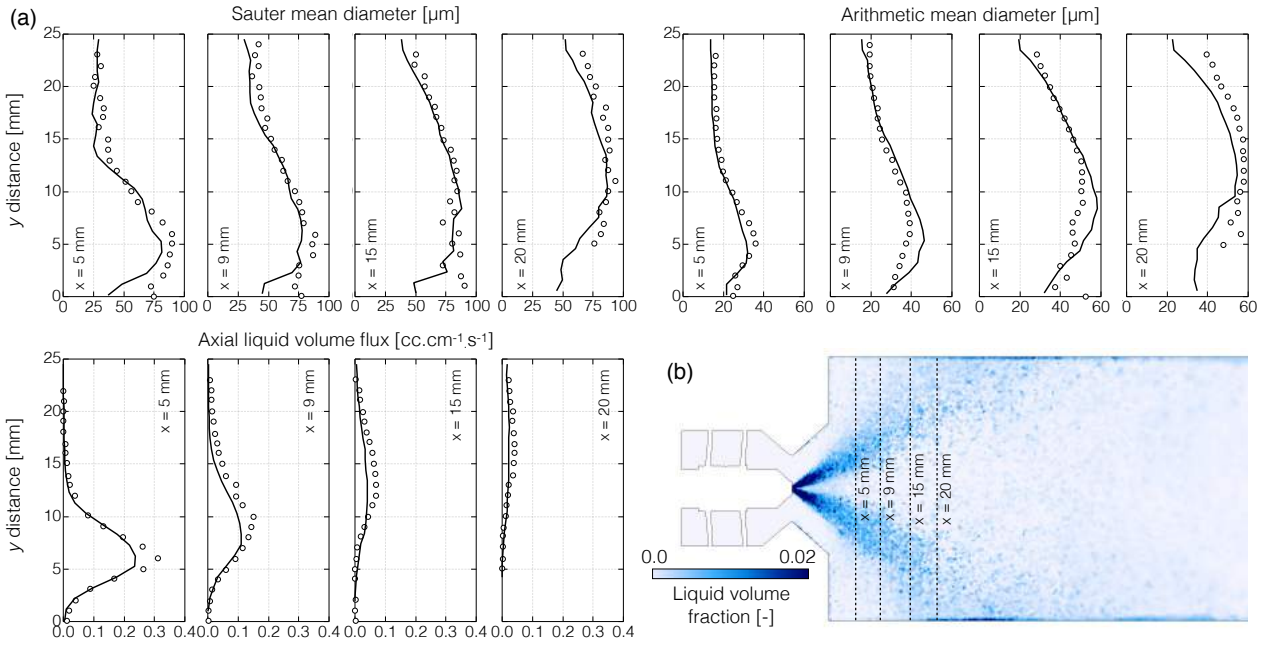

Figure 8.8: (a) Profiles of time-averaged Sauter Mean Diameter (SMD), arithmetic mean diameter (D10) and axial liquid volume flux at x = 5 mm, 15 mm, 29 mm and 46 mm in reacting conditions. Symbols: experiments, black line: LES. (b) Time-averaged fields of liquid volume fraction in a z-normal central cut plane.

Finally, the axial liquid volume flux is computed and compared to experiment, demonstrating that the spray angle and velocity are also well reproduced. Note that the flux is under-estimated, which is found to be due to a faster evaporation resulting of an upstream shift of the flame position compared to experiments. Figure 8.8(b) indicates that the spray density is rather high at the vicinity of the injector nozzle, but rapidly decreases downstream of the dump plane, validating the hypothesis of dilute spray. Finally, past 20 mm from the dump plane, high liquid volume fraction are found along the combustor walls as a result of the spray/wall interaction. It will be shown that this affects the species distribution.

8.5.2.c Temperature and species

Figure 8.9(a) compares experimental and LES radial profiles of temperature and major species, at several axial locations identified by vertical solid lines on Fig. 8.9(b), spanning the vicinity of the dump plane. H_2O and CO_2 evolutions are very well retrieved by the LES, even though with less asymmetry than in the experiments. Note that if some asymmetry is to be expected from the 6-vanes swirler, the LES results also suggest non-negligible experimental uncertainties. A less well agreement is obtained on the temperature profiles, especially at the first locations, x $<$ 20 mm. The experimental profile displays a bimodal shape at x = 20 mm, revealing the intermittent presence of a flame, apparently not seen in the LES which give a mean temperature about 200 K

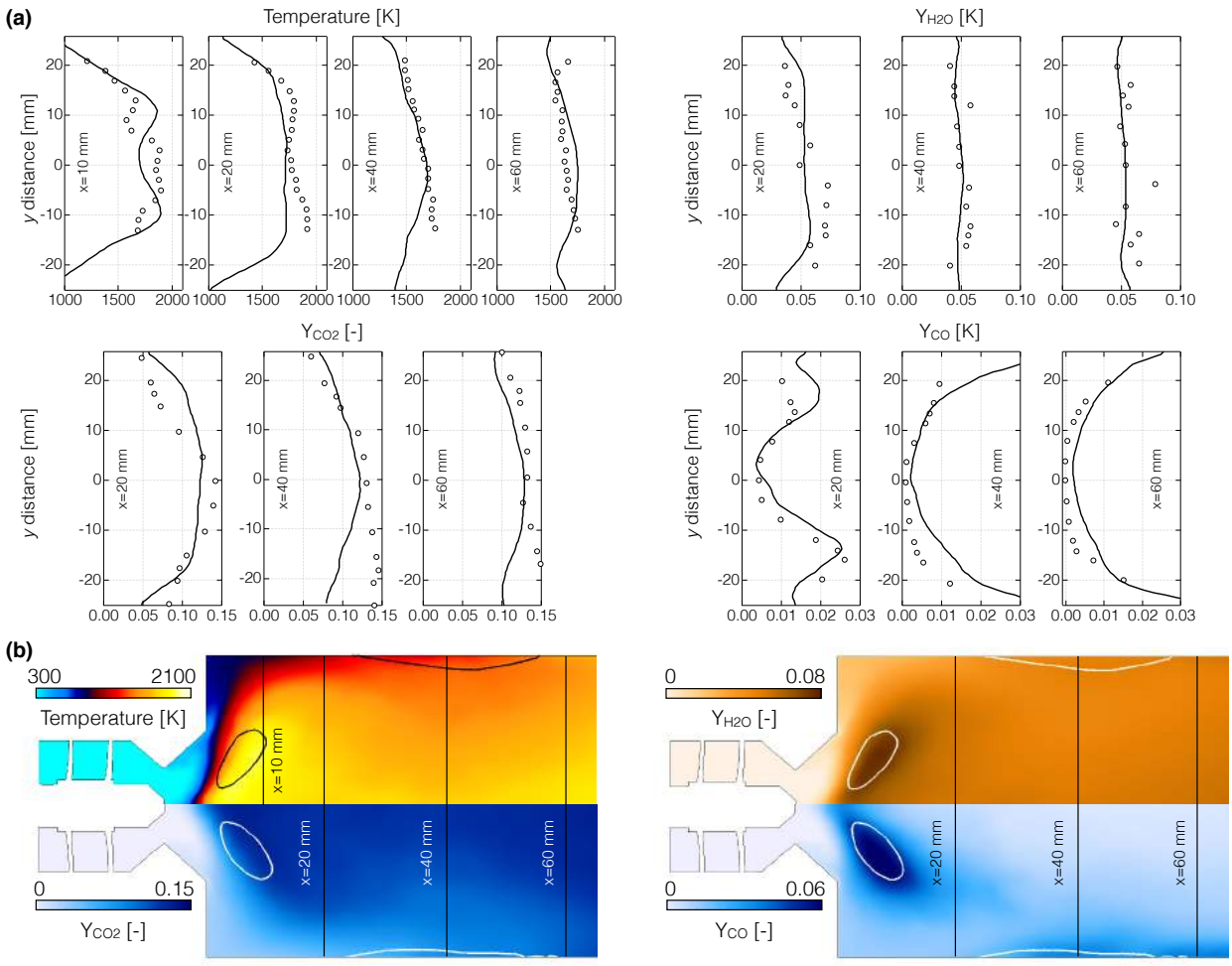

Figure 8.9: (a) Profiles of time-averaged temperature and selected species (CO_2, H_2O and CO) at x = 20 mm, 40 mm and 60 mm in reacting conditions. Symbols: experiments, black line: LES. (b) Time-averaged fields of temperature and selected species (CO_2, H_2O and CO) in a z-normal central cut plane. The iso-contour indicates the position of stoichiometry

lower in this location. The same bimodal shape is seen on the LES profiles at x = 10 mm, suggesting that the main flame front is in fact shifted further upstream than in the experiment, as previously mentioned. An inspection of the mean stoichiometric iso-contours, superimposed to the mean fields of temperature and major species mass fractions in Fig. 8.9(b), confirms that the region of highest reactivity is preferably located upstream of the first profile location. Despite this shift, however, the two peaks on the CO profile at 20 mm, representative of the early post-flame region, are very accurately predicted by the LES. It is noted that the main flame appears lifted from the LDI in both LES and experiment, in correspondence with the mean position of the tip of the IRZ seen on Fig. 8.8 (b). The flame appears mainly lifted also from the chamber's walls, which could be due to the high turbulent velocity magnitude observed in this region, see Fig. 8.7(b).

Further downstream, there seems to be an accumulation of CO along the walls, accompanied by a decrease of temperature, in both LES and experiment. It is reminded that no heat losses are included in the simulation. This phenomenon is therefore attributed to the accumulation of droplets following the jet impact on the walls, as seen on Fig. 8.8, leading to the formation of regions of very rich mixture fraction. Stoichiometric iso-contours along the walls, centered at x = 40 mm as seen on Fig. 8.9(b), confirm this analysis. For x = 60 mm, the temperature is seen to be overpredicted near the centerline. A closer examination of the experimental data indicates that the temperature at the outlet of the combustor rig is below the theoretical adiabatic value at the overall ϕ by approximately 300 K. This difference suggests heat losses (radiation, walls, etc.) and/or incomplete combustion.

NO data are presented on Figs. 8.10(a) and (b). LES results are compared to experiment at several axial positions, with the last one (x = 150 mm) at half of the combustion chamber length. NO levels are found to be highest in the core of the IRZ, in the vicinity of the main flame, and to be significantly smaller along the walls for x < 60 mm, coinciding with low temperature regions where the jet impacts. NO levels along the centerline

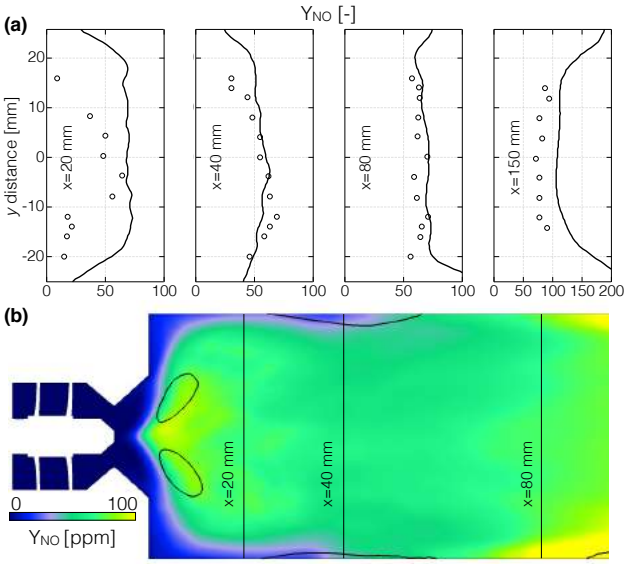

Figure 8.10: (a) Profiles of time-averaged NO species at x = 20 mm, 40 mm, 80 mm and 150 mm in reacting conditions. Symbols: experiments, black line: LES. (b) Time-averaged fields of NO species in a z-normal central cut plane. The iso-contour indicates the position of stoichiometry

are seen to slightly increase with increasing distance from the injector. Overall, the main trends and levels are found to be very well captured by the LES, validating *a-posteriori* the choice of NO_x sub-mechanism. The shape of the first profile, at x= 20 mm, is the least well retrieved by the LES, with levels that are too high in the shear layer. This is consistent with a flame front shifted towards smaller axial positions, leading to post-flame levels already reached at x = 20 mm. Consistently with increasing temperature levels observed near the chamber walls, Fig. 8.9(a), NO levels are found to increase after x = 60 mm. No data are available for these radial positions, however.

8.5.3 Flame analysis

8.5.3.a Identification of the combustion regimes

The instantaneous flame structure is depicted in Fig. 8.11 showing contours of temperature, heat release rate, velocity and several species mass fractions in a central z-normal cut plane. Iso-contours of stoichiometric mixture fraction $Y_z = 0.063$ are superimposed, where Y_z is defined following Bilger (1989). The flame presents a complex structure where three main combustion zones can be identified (Fig. 8.11(a)): (1) a flame is located close to the combustion chamber dump plane, around a torus of rich burned gases, (2) a second flame front extends downstream of the first one, along the boundary of the IRZ, (3) individual burning droplets are spread throughout the recirculation zone. The species HyChem is introduced in Fig. 8.11 (b). It is a lumped species, made up of the fuel, pyrolysis products and acetylene:

$$Y_{HyChem} = Y_{POSF10325} + \sum_{pyro.prod.} Y_{pyro.prod.} + Y_{C2H2} \tag{8.18}$$

Indeed, since the flame configuration induces a rapid pyrolysis of the gaseous Jet A, the fuel is rarely observed in the simulation. Acetylene is added to the definition of Y_{HyChem}, since an analysis of the chemical pathways indicates that this species is massively produced directly from the pyrolysis products, in regions deprived of oxidizer. From instantaneous O_2 and HyChem fields, the flame front (1) is identified as a diffusion flame. Additionally, NO, HO_2 and OH fields displayed in Figs. 8.11 (c) and (f) reveal that it is made up of a variety of structures. The nature of the two other flame structures is more complex and is further anaylzed.

In order to better understand the flame, a Takeno index $\mathcal{I}_k$ (Yamashita *et al.*, 1996) is employed, based on O_2 and the HyChem species:

$$\mathcal{I}_k = \frac{\nabla Y_{HyChem} \cdot \nabla Y_{O2}}{|\nabla Y_{HyChem}| . |\nabla Y_{O2}|} \tag{8.19}$$

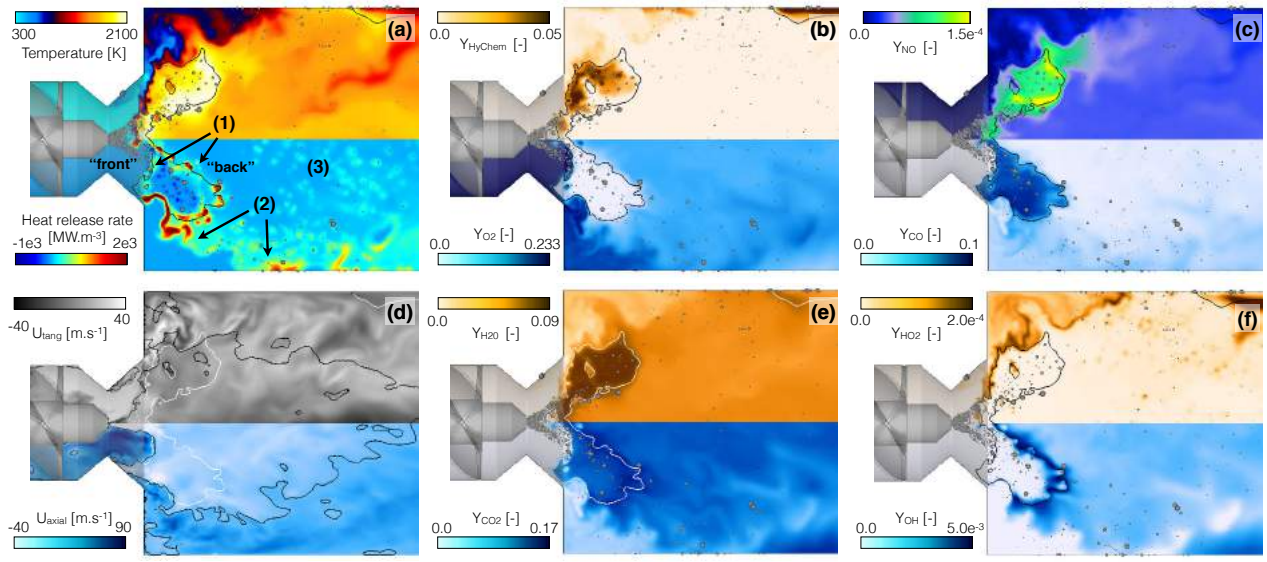

Figure 8.11: Instantaneous fields in a central z-normal cut plane. (a) Temperature (top) and heat release rate (bottom), (b) summed mass fractions of fuel and pyrolysis products (top) and O_2 mass fraction (bottom), (c) NO (top) and CO (bottom) mass fractions, (e) H_2O (top) and CO_2 (bottom) mass fractions and (f) HO_2 (top) and OH (bottom) mass fractions. The black iso-line indicates stoichiometry. (d) Tangential (top) and axial (bottom) components of velocity, black iso-contours delimit the IRZ while white iso-contours indicates stoichiometry.

It is plotted in Fig. 8.12(a). Negative values indicate a diffusion flame front, while positive values reveal a premixed flame front. The analysis of $\mathcal{I}_k$ distribution in the three aforementioned reaction zones, coupled with the species fields of Fig. 8.11, helps to shed some light on the various flame structures. The flame front (1), located around the pocket of rich burnt gases, is identified as a diffusion flame by $\mathcal{I}_k$. This front can be further divided into a front diffusion flame and a back diffusion flame, depending upon the oxidizer characteristics, as seen on Figs. 8.11(a) & (b): while the front flame oxidizer is fresh air, the back flame burns recirculated lean gases at moderate temperature (around 1600 K). The flame structure in this region bears many resemblances to that observed in the case of a spray n-heptane burner (Paulhiac *et al.*, 2017) with however a 2S global scheme. In the present case, the ARC chemistry description enables the differences in local conditions to lead to the production and consumption of different species in each flame front. Figures 8.11 (c) & (f) illustrate this fact by revealing, for instance, that NO is mainly produced in the back diffusion flame while the front diffusion flame is characterized by high HO_2 levels.

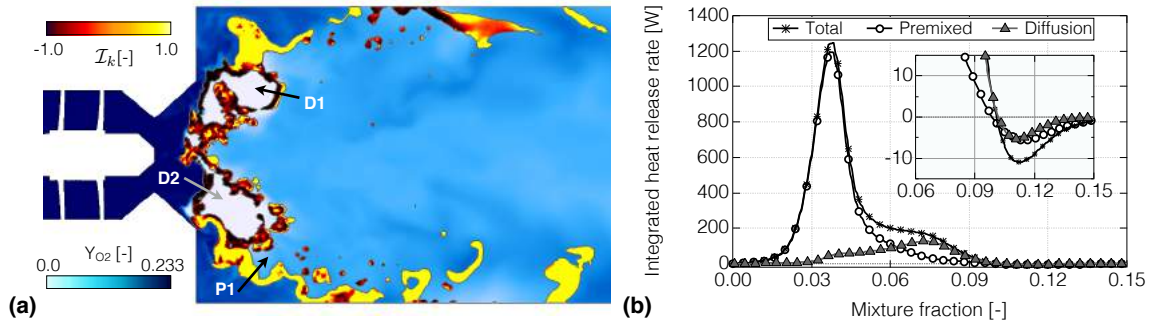

Figure 8.12: (a) O_2 mass fraction in a central z-normal cut plane with overlaid $\mathcal{I}_k$ field in regions of high heat release rate ($\dot{\omega}_T > 10^8$). Arrows indicate the position of the z-T profiles, see Fig. 8.13. (b) Integrated heat release rate conditioned on mixture fraction $< \int_V \dot{\omega}_T \, dV | z >$, with a close-up in the region $0.06 < Y_z < 0.15$.

The flame front (2) is revealed to be mainly of premixed nature. It consumes a mixture composed of fresh air diluted with burnt gases, pre-vaporized fuel and pyrolysis products in small quantities; up to an equivalence ratio of 0.3 which is below the flammability limit of the Jet A POSF10325 at the combustor inlet conditions. The local temperature is of about 900 K. Low temperature intermediate species such as HO_2 or H_2O_2 are also observed, flowing in the corners of the combustion chamber, indicating that low temperature chemistry occurs upstream of the premixed front (see Fig. 8.11 (f)). It is believed that the complex mixture feeding the premixed flames (2) forms in the vicinity of the diffusion flame (1), where local intermittent quenching allows gases from the hot torus

to leak into the fresh air stream.

Finally, the individual droplets are found to burn in a complex regime that will be described later.

8.5.3.b Heat release rate analysis

To analyze the contributions of the premixed and diffusion flame fronts to the overall heat release rate, a volumetric integration is performed, conditioned on $\mathcal{I}_k$. Results are displayed in Fig. 8.12(b). The peak of heat release occurs on the lean side, at an equivalence ratio of 0.6, lower than the global equivalence ratio of 0.75. Although both regimes appear more or less equally distributed (see Fig. 8.12(a)), the contribution from premixed flame fronts to the overall heat release is found to be largely dominant. These findings are consistent with previous DNS studies (Luo *et al.*, 2011). In the present study, these results are attributed to the large observed intermittency of the diffusion fronts, and to local mixing conditions resulting in overall rich global equivalence ratios in the back diffusion front (1).

Despite this lower contribution to the total heat release, the non-premixed reaction zone (1) is found to be crucial for flame stabilization: it is located in the wake of the spray and enables a rapid increase of the droplet temperature, promoting fast evaporation. Evaporating droplets crossing the rich and hot torus of gases induce a locally negative heat release rate, as can be seen on Fig. 8.11: the evaporating Jet A is rapidly pyrolyzed through endothermic reactions, but the lack of O_2 prevents the subsequent exothermic oxidation of the pyrolysis products. This has already been observed in DNS of spark ignition in droplet coulds (Neophytou *et al.*, 2012). The trace of this region of negative heat release rate is visible on Fig. 8.12 (b), around $\phi \approx 2.0$ ($Y_z \approx 0.1$, see the close-up). The pyrolysis products then diffuse towards the outer colder and leaner regions, directly feeding the variety of diffusion fronts (1) and maintaining the combustion. The trace of these diffusion fronts is visible around stoichiometry in Fig. 8.12 (b) (curve with triangles).

8.5.3.c Gaseous flame structure analysis

To analyze diffusion and premixed structures in more depth, scatterplots of temperature versus mixture fraction are shown in Fig. 8.13 (a). Practically all premixed flames structures, identified with dark blue markers, are found to sit on the lean side. Additionally, a high degree of mixture stratification is observed, as illustrated by the trajectory of the premixed flame P1 identified on the bottom part of Fig. 8.12 (a), and reported with red hollow triangles on the scatterplots of Fig. 8.13. The diffusion structures, identified with light blue markers on Fig. 8.13 (a), are found to cover a larger portion of the mixture fraction space. In order to identify traces of both the front and back diffusion flames discussed earlier, two representative trajectories across the diffusion flame front (1) are considered, as depicted in Fig. 8.12 (a). D1, resp. D2, is representative of the back, resp. front, diffusion flame front. The trajectory of the "back" diffusion flame D1 is reported with red hollow circles on Figs. 8.13, where it is seen to cross a region of relatively high concentration of OH species around stoichiometry on Fig. 8.13 (b), consistently with what was noted on Fig. 8.11 (f). Likewise, the trajectory of the "front" diffusion flame D2 reported with red hollow squares on Figs. 8.13 is seen to cross a region of relatively high concentration of HO_2 species, on the lean side on Fig. 8.13 (c). The three trajectories P1, D1 and D2 are seen to encompass the bulk of the data, as they are "limiting case" examples. In particular, the D1 and D2 trajectories are seen to merge on the rich mixing line in Figs. 8.11, representative of the activity inside the rich, hot torus.

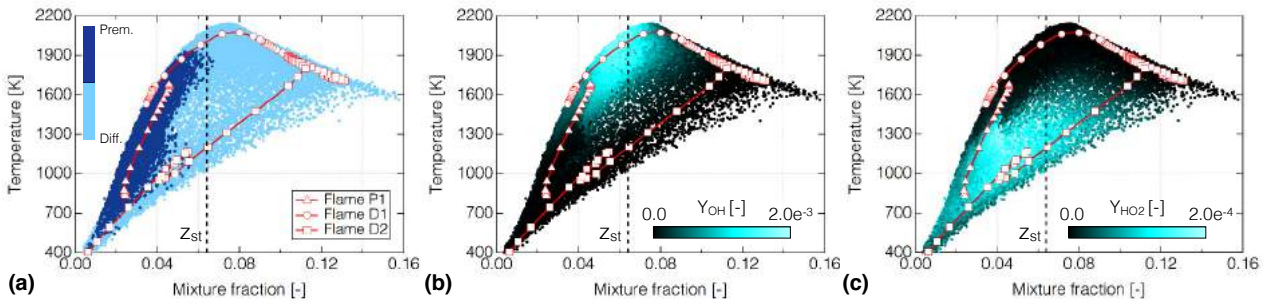

Figure 8.13: Instantaneous scatterplots of temperature versus mixture fraction coloured by $\mathcal{I}_k$ (a), OH species (b), and HO_2 species (c). Points are chosen close to the injector. Superimposed are trajectories across premixed (P1) and diffusion (D1, D2) flame fronts identified on Fig. 8.12(a).

The scatterplots of Figs. 8.13 further reveal, as was to be expected, that the front flame is highly strained. Indeed, the presence of HO_2 is usually associated with low temperature chemistry and extinction events; a fact confirmed by an inspection of the scatterplot of Fig. 8.13 (c). The strain, in a diffusion flame, can be related to the scalar dissipation rate at stoichiometry:

$$\chi_{st} = 2D|\nabla z_{st}|^2 \tag{8.20}$$

controlling the flame consumption and maximum temperature. Due to both the strong turbulence of the fresh gases and the higher Y_z limits in the oxidizer and fuel sides, the front diffusion flame is subjected to a higher dissipation rate than the back diffusion flame.

Note that the mixture fraction, in all the aforementioned scatterplots, is found to reach a maximum value of about 0.16. This value differs significantly from that reported in the previous study of Patel & Menon (2008), which was of about 0.4. The locus of this maximum value is just downstream of the front diffusion flame in the present study, which is positioned close to the location of zero axial velocity (see Fig. 8.11(d)). Small droplets crossing this first flame front are slowed by the backward velocity and rapidly evaporated. As pointed out by Knudsen *et al.* (2015), the mixture fraction field strongly depends upon the choice of evaporation model as well as upon the spray boundary conditions (both spray angle and droplet size distribution), the latter often being insufficiently characterized in both academic and industrial configurations. As such, it is difficult to draw any quantitative conclusion from these discrepancies.

8.5.3.d Evaporation and droplet dynamics

Figure 8.14 (a) displays the axial evolution of the evaporation rate, integrated over x-normal planes. Data are collected from 20 instantaneous solutions spread over 10 ms. Evaporation is found to peak around $x = 17$ mm, corresponding to the axial position of the rich torus of burnt gases, as well as to weak premixed flame fronts following the ORZ (see P1 type flames in Fig. 8.12). A plateau of evaporation is also seen in between $x = 25$ mm and $x = 50$ mm, suggesting that an important activity still takes place behind the main reaction front (1), albeit more spread out. The cumulative integrated evaporation rate as function of the axial position is also displayed, normalized by the injection rate. It indicates that 40% of the fuel is evaporated before $x = 20$ mm and confirms that more than half of the injected fuel evaporates in the premixed flame fronts alongside the walls or as isolated droplets in the IRZ. Note also that all the fuel has evaporated by $x = 100$ mm.

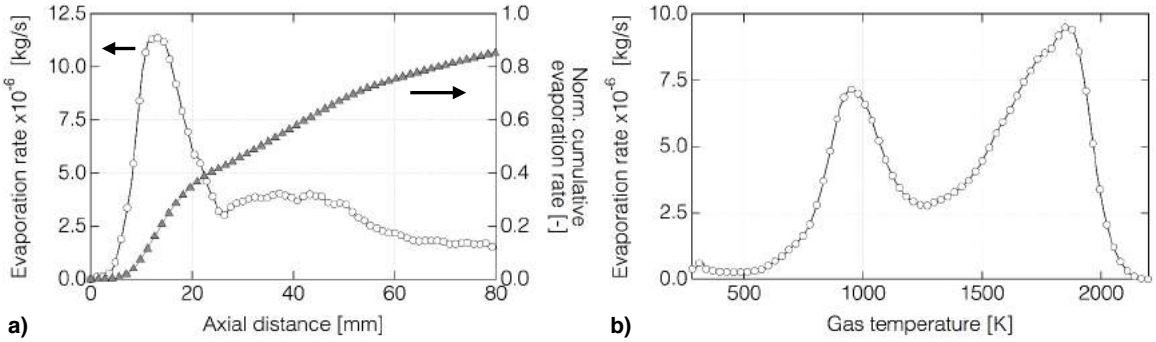

Figure 8.14: (a) Time-averaged spatial evolution of evaporation rate, integrated in x-normal planes. (b) Time-averaged total evaporation rate versus gaseous temperature, in the first half of the combustion chamber.

It was said in the previous paragraph that the reaction zone (1) plays an important role in flame stabilization by being the most important region for evaporation. In an attempt to differentiate between the role of the reaction zone (1) and the premixed fronts (2) in the first peak of Fig. 8.14 (a), Fig. 8.14 (b) shows the integrated evaporation rate conditioned on the gas temperature. Two peaks are observed, around 950 K and 1800 K, with the most important one being around 1800 K and corresponding to the diffusion front (1) (see Fig. 8.11 (a)), thus confirmed as being the preferential location for evaporation.

Figure 8.14 (b) also demonstrates that very little evaporation occurs upstream of the flame fronts near the injector. Consequently, droplets feeding the reaction zone (1) evaporate directly in the flame regions. In particular, they need to penetrate into the IRZ. To analyze the droplets dynamics in this region, Fig. 8.15 displays scatterplots of droplets axial velocity against axial gaseous velocity interpolated at the droplets position. Figure 8.15 (a) is colored by the droplets size, while Fig. 8.15 (b) is colored by the gas temperature. Both Figures indicate

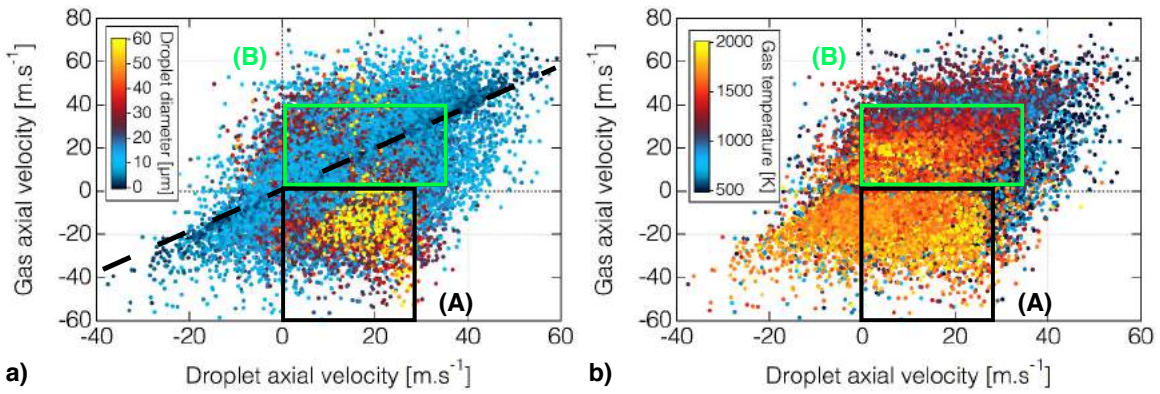

Figure 8.15: Instantaneous scatterplots of axial gas velocity versus droplets axial velocity; coloured by (a) droplets diameter and (b) gas temperature. All gas quantities are interpolated at the droplets position. Droplets are chosen such that they are located in zones were $T_{gas} > 400$ K. See text for details about the lines and frames.

that droplets penetrating the IRZ while keeping a positive axial velocity component, referred to as type (A) and framed in black in Fig. 8.15, are all sensibly large droplets ($d_p > 40$ μm). Furthermore, it is observed that a non negligible portion of these larger droplets is also situated in regions with very high temperature levels (around 2000 K), indicating that they feed the back diffusion front (2), before burning in an isolated regime in the IRZ.

Smaller droplets, on the contrary, primarily fuel the front diffusion flame (1). Indeed, their velocity is seen to rapidly equilibrate with that of the gas, as evidenced by their tendency to gather on a straight y = x line (black dashed line in Fig. 8.15 (a)). Additionally, Fig. 8.15 (b) reveals that many amongst these small droplets ($d_p \approx 10$ μm), referred to as type (B) and framed in green in Fig. 8.15, are located in gaseous regions exhibiting temperature levels characteristic of the front diffusion flame (1). Their small size allow them to rapidly evaporate in this mid-temperature region, thus directly bringing fuel to the front diffusion flame (1).

Note, to finish, that the trace of droplets flowing in the ORZ with fresh gases are also clearly identified in Fig. 8.15 (b): such droplets exhibit a high positive axial velocity and are located in regions where, as said in Section 8.5.3.a, the gaseous temperature is of about 900 K. Fig. 8.15 (a) further reveals that these droplets are of moderate size. Some bring fresh fuel to the premixed flame fronts (2).

8.5.3.e Spray-flame interaction

The first effect of the spray on the flame structure arises from the mixture fraction spatial distribution. The rapid evaporation of small droplets crossing the front diffusion flame when entering the IRZ induces a strong gradient of mixture fraction. This contributes to the higher scalar dissipation rate observed in the front diffusion flame (1) when compared to that seen in the back diffusion flame front (1), as already mentioned in Section 8.5.3.c. This is illustrated on Fig. 8.16 (b), showing an instantaneous stoichiometric iso-surface coloured with χ_{st}. On this Figures, both diffusion flames should appear but the back flame mostly masks the front one except in the outer region, in the vicinity of the divergent (where a high scalar dissipation rate is visible). In contrast, the longer evaporation time associated with larger droplets results in a more distributed addition of fuel near and past the back diffusion flame front.

Another important effect of evaporation on the Y_z field, mainly seen on the back diffusion flame (1), is the wrinkling of the stoichiometric iso-surface induced by large droplets crossing the flame. As evidenced in Figs. 8.16, the stoichiometric iso-surface is highly wrinkled, with small hills of very high negative curvature, see Fig. 8.16 (d). Isolated spheric structures are also clearly visible. The curvature is here defined as $\nabla \cdot \boldsymbol{n}_z$, where $\boldsymbol{n}_z = \nabla z/|\nabla z|$ is pointing towards rich regions. As was mentioned previously, these highly curved regions appear to have a limited correlation with the resolved scalar dissipation rate. Interestingly, the heat release rate levels, however, are significantly impacted, as can be seen on Fig. 8.16 (a). This indicates that, as opposed to what is expected from gaseous flame theory, the flame intensity is not primarily controlled by the scalar dissipation rate. In fact, the contribution from evaporation to the total fuel flux at stoichiometry can supersede that of the diffusion flux (evaluated by the level of χ_{st}), especially in low scalar dissipation rate flames. To confirm this analysis, Fig. 8.16 (c) shows that the evaporation rate is locally strong around droplets and is well correlated with the heat release rate.

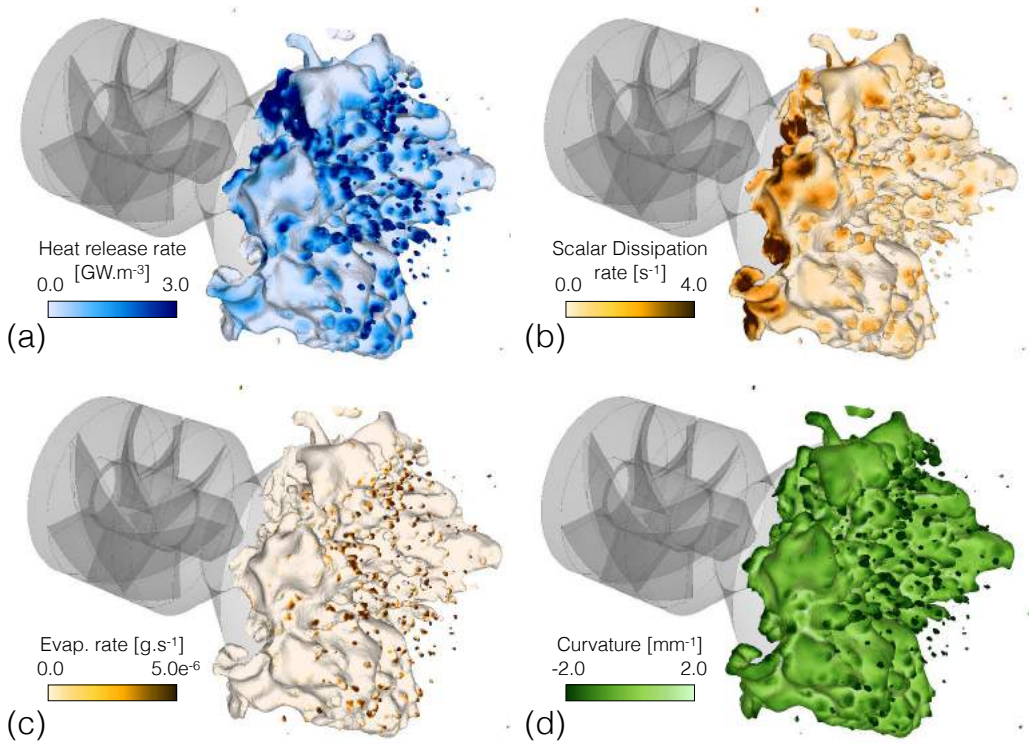

Figure 8.16: Iso-surface of stoichiometric mixture fraction, coloured by (a) heat release rate, (b) χ, (c) evaporation rate and (d) curvature.

In order to characterize in more depth the extent to which droplets and evaporation affect the flame structures, and make them deviate from purely gaseous flames, Fig. 8.17 reports scatterplots of heat release rate versus temperature, for points located on the stoichiometric iso-surface of the diffusion reaction front (1) (i. e. on iso-surfaces as depicted on Fig. 8.16). Two graphs are displayed: Fig. 8.17 (a) is composed of points where the evaporation source term is negligible, while Fig. 8.17 (b) is composed of points where it is relatively important. Both scatterplots are coloured by the source term of fuel. As expected, the regions characterized by evaporation are often associated with a strong fuel reactivity: as soon as fuel evaporates, it is pyrolyzed. More interestingly, it is observed that evaporation and subsequent pyrolysis generate a larger scatter of data. In particular, a tilted "V-like" structure is clearly visible on Fig. 8.17 (b), originating from ≈1800 K, and extending to ≈1600 K. As evidenced from the analysis of Figs. 8.18 (b) and (c), exhibiting the same scatterplots but coloured by, respectively, the fuel evaporation rate and the curvature, this V-like structure is the mark of the highly curved and spherical (around droplets) structures discussed earlier (see Fig. 8.16).

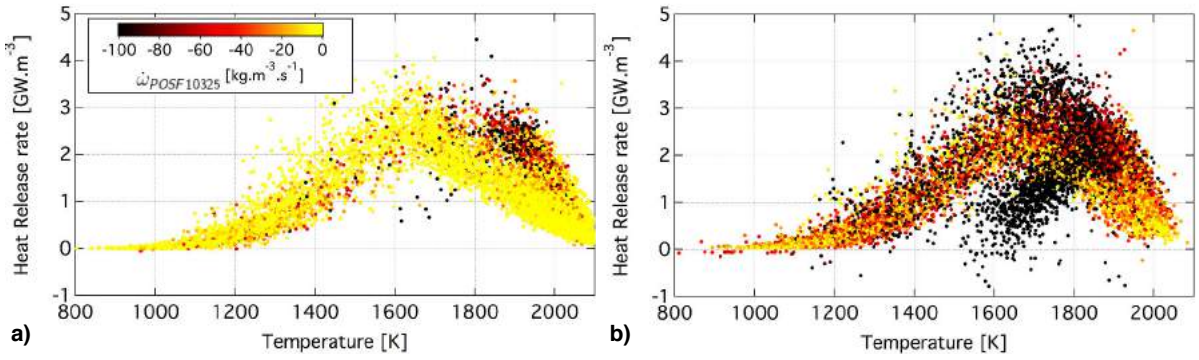

Figure 8.17: Instantaneous scatterplots of heat release rate versus temperature; coloured by the source term of fuel. Points are chosen such that $Y_z = z_{st}$, and such that the evaporation term source is (a) $< 10^{-10}$ kg.s^{-1} or (b) $> 10^{-10}$ kg.s^{-1}.

The lowest branch of this V-like shape is composed of points with relatively high concentrations of pyrolysis products, as exemplified on Fig. 8.18 (d) in the case of toluene; and lower heat release rate than that exhibited by points where the evaporation source term is almost zero. This helps identifying them as being located in regions experiencing massive evaporation. Considering also the very high values of curvature, these structures

are identified as surrounding isolated droplets. These droplets should have a sufficiently large diameter to be able to cross the hot torus of burnt gases, where most of the combustion occurs. To confirm this speculation, Fig. 8.19 exhibits the scatterplots of gas heat release rate versus gas temperature interpolated at the droplets positions, in order to colour by the droplets radii (Figure 8.19 (a)) and by the droplets positions (Figure 8.19 (b)). The same V-like structure is clearly identified, composed of droplets with large diameters located in the core of the IRZ behind the diffusion front (1). Note that in this case, droplet evaporation locally decreases both temperature and heat release rate, since pyrolysis becomes dominant over oxidation of the pyrolysis products. Interaction of a diffusion flame with an isolated droplet has been investigated experimentally, for example by Mercier *et al.* (2007), were it was found that droplets having a sufficient residence time in the flame front can ignite. In the present simulation, a diffusion flame is indeed found around large droplets crossing the back diffusion flame. However, as droplets progress further downstream in the combustion chamber, the mixture fraction in the vicinity of the droplets rapidly decreases below stoichiometry, accompanied by a switch of combustion regime from diffusion to premixed-like around the droplet.

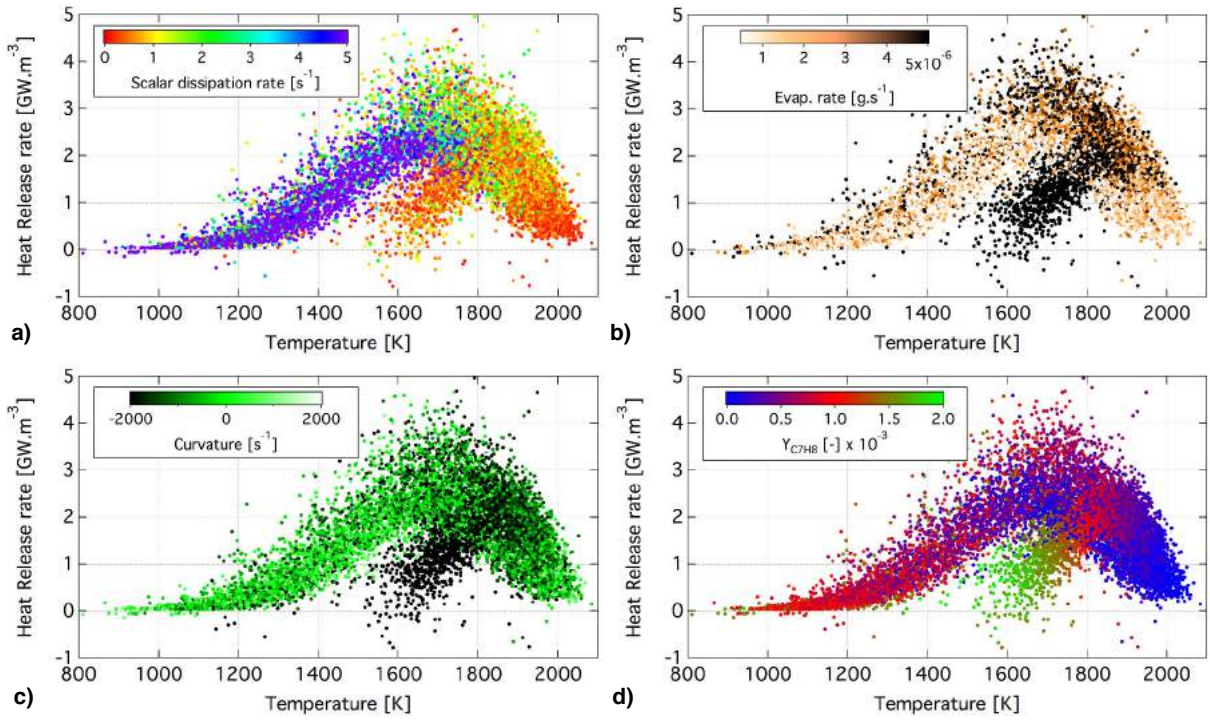

Figure 8.18: Instantaneous scatterplots of heat release rate versus temperature; coloured by (a) the scalar dissipation rate, (b) the evaporation rate, (c) the curvature and (d) the mass fraction of toluene. Points are chosen such that $Y_z = z_{st}$, and such that the evaporation term source is $> 10^{-10}$ kg.s^{-1}.

The frequent occurrence of isolated droplet combustion calls for specific models, as proposed, e.g. in (Paulhiac, 2015), which were not considered in this work. As a consequence, although the occurrence of such burning regime is well captured, the exact associated flame structures are not properly described.

The top branch of the V-like shape is composed of points with sensibly higher heat release rate. From Fig. 8.19 (b) and the analysis of the images of Fig. 8.16, the points are identified as being part of the back diffusion flame front (1), and responsible for the wrinkled structures on the stoichiometric iso-surfaces. In this case, even if evaporation has a tendency to draw energy from the gaseous phase, the addition of fuel to the already burning flame front is enough to compensate for this loss, and even to locally enhance the heat release rate. Note that droplets composing the top branch are slightly smaller than droplets burning in an isolated regime, thus preventing them from following a ballistic-like trajectory and crossing the back diffusion front.

8.5.3.f Pollutant formation: CO and NO

CO species The CO source term $\dot{\omega}_{CO}$ and CO mass fraction fields are displayed, respectively, on Fig. 8.20 (a) and (b). As expected from the locally rich conditions, CO is massively produced in the diffusion fronts (1), particularly in the back diffusion front exhibiting the highest temperature levels. Locally, CO production is also

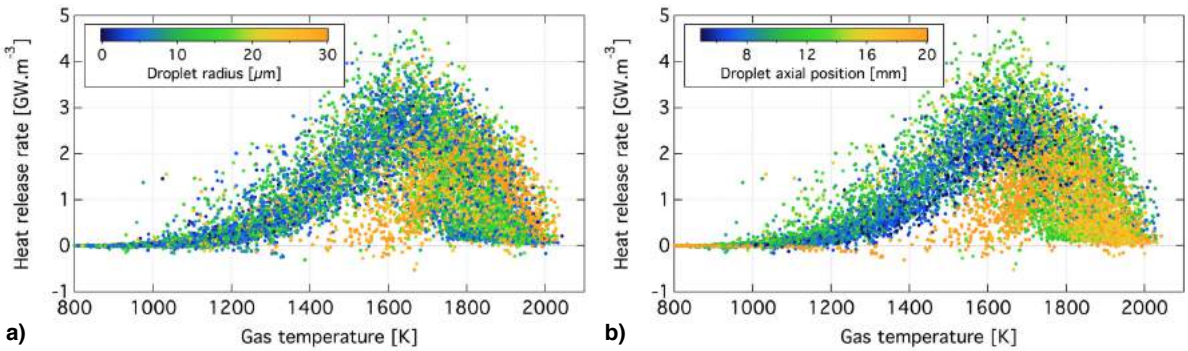

Figure 8.19: Instantaneous scatterplots of gas heat release rate versus gas temperature interpolated at droplets position; coloured by (a) the droplet radius, (b) the droplet axial position. Points are chosen such that $Y_z = z_{st}$, and such that the evaporation term source is $> 10^{-10}$ kg.s^{-1}.

boosted by the evaporation of fuel, as revealed by the clouds of CO production following evaporating isolated droplets. This is especially true of droplets located right behind the stoichiometric iso-contours: as observed for the levels of heat release rate in the previous Section, the addition of fresh fuel through evaporation is seen to strongly affect the diffusion flame structure, by enhancing the production of CO. This is best put forward on Fig. 8.21 showing a scatterplot of CO production versus mixture fraction, coloured by the evaporation source term.

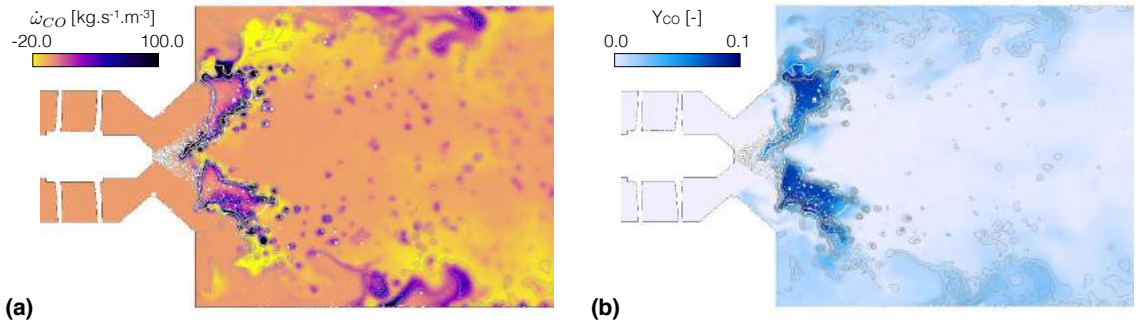

Figure 8.20: Instantaneous fields of (a) CO source term and (b) CO mass fraction in a central z-normal cut place with overlaid droplets and iso-contours of heat release rate (grey) and stoichiometry (white).

The CO produced in the diffusion front (1) is stored in the burnt gas torus, where intermittent extinctions allow pockets to leak into the cold air stream (see the combustion chamber corners on Fig. 8.20 (b)). CO mass fraction close to 0.03 can then be observed on the fresh side of the premixed flame fronts (2), explaining the relatively high CO consumption observed before $x = 50$ mm. Finally, a non negligible amount of CO production occurs also in premixed fronts located further downstream in the combustion chamber, near the walls. Indeed, impacting evaporating droplets around $x = 50$ mm allow a sufficient increase of the local equivalence ratio and feed additional pyrolysis products to the lean premixed flame fronts; locally modifying the premixed structure from CO consuming to CO producing. This is consistent with the high CO mass fraction observed close to the walls on the time-averaged profiles in both LES and experiment (see Fig. 8.9).

NO species NO emission control and overall reduction in aeronautical combustors can only be achieved through understanding of the formation and destruction mechanisms. To this end, it is interesting to differentiate and quantify the NO production related to fuel consumption and fast flame processes, which are strongly dependent upon the local conditions; from that occurring in post-flame regions, associated with slower timescales and bearing a more universal nature. This is usually done by investigating the reaction pathways involving the NO species.

As briefly reviewed in Section 2.2.4.a, several NO production pathways have been identified in the literature. They are labelled formation routes. The three major ones relevant under gas-turbine conditions are the Thermal, the Prompt and the N_2O route (Correa, 1993; Miller & Bowman, 1989). The NNH route can also become quite important in the burnt gases under relatively low temperatures (Bozzelli & Dean, 1995). Note that in

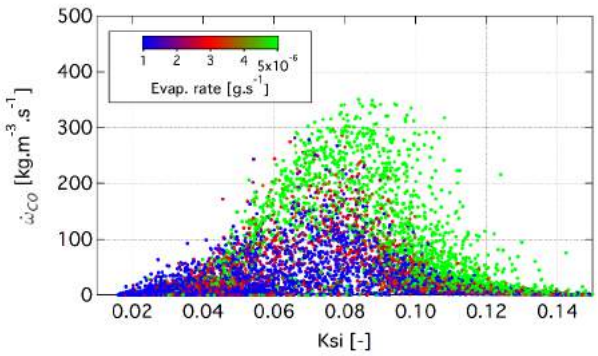

Figure 8.21: Scatterplot of CO source term versus mixture fraction, coloured by the evaporation rate. Points are chosen on the diffusion front (1) with $T > 800$ K.

the ARC_29_JetA2NOx mechanism employed in the LES, the N_2O route is not included. Indeed, it is usually argued that this route is important under fuel lean/high pressure conditions. However, the configuration under investigation operates at atmospheric pressure, which could be the reason why the reduction tool YARC identified it as being insignificant. The NNH route, on the contrary, is reduced but conserved.

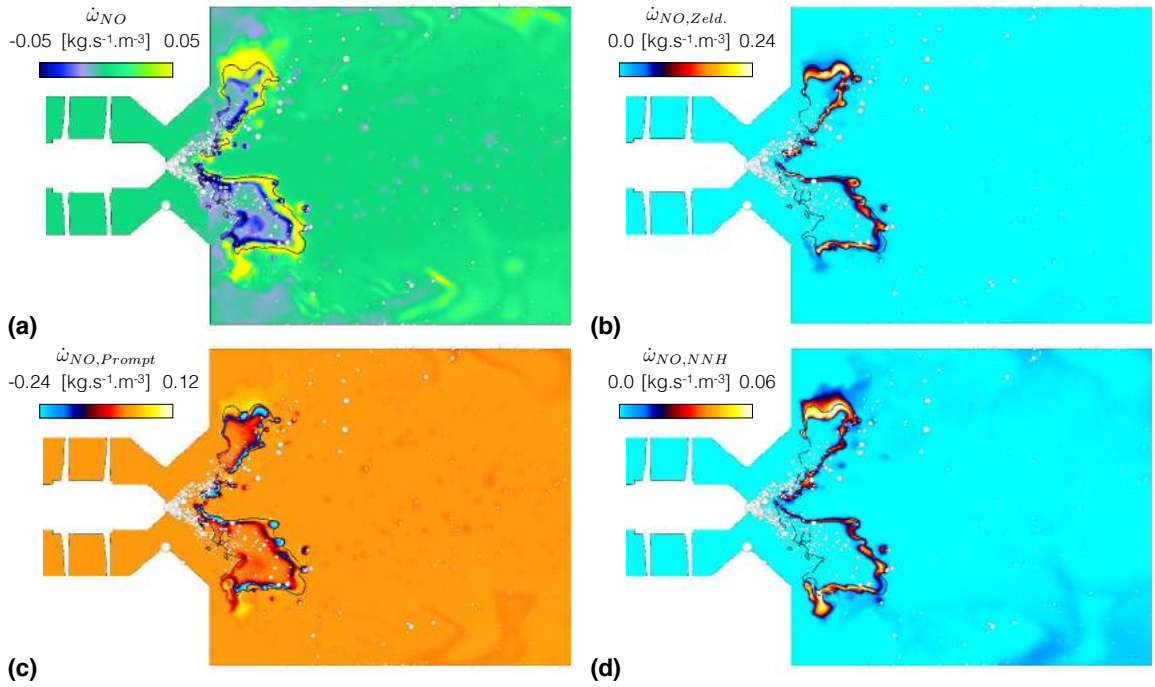

Figure 8.22: Instantaneous fields of (a) source term of NO with decomposition into (b) Zeldovich (thermal) pathway, (b) Prompt pathway ans (c) NNH pathway.

Fig. 8.22 presents the NO source term as well as the contribution from the Thermal, Prompt and NNH routes, in a z-normal central cut plane. These routes are identified based on specific reactions and associated pathways, as prescribed on the aforementionned publications (See Appendix C). It is then important to keep in mind that, in reality, all of these pathways are non-linearly coupled. For example, a direct consequence of the Prompt route is an enhanced production of N atom, which will eventually lead to an increased NO production through the Thermal route. Additionally, note that the Prompt route is here based on *net* production rates involving radicals such as HCN and CH, thus, the NO reburning is included in this route (Hill & Smoot, 2000). A better way to evaluate the impact of the various routes would be to perform several computations, by only considering one pathway at a time. However, this would be too costly in the context of LES.

As for CO, NO is seen to be mainly produced in the back diffusion flame front (1). The main contribution to net production in this high temperature region is from the Zeldovich mechanism, as expected. Interestingly, NO is massively reburnt inside the rich torus, and the pathway analysis reveals that this is primarily due to

the consumption pathways included in the Prompt mechanism. In particular, some NO is also consumed by the Prompt mechanism in the front diffusion flame (1); however no NO is produced in this flame front where the relatively high NO levels are due to diffusion. The contribution from the NNH pathway is exclusively positive (no consumption) and is not negligible, here also, in the back diffusion front (1). All three pathways contribute to the production of NO in the portion of the back diffusion front (1) that is subjected to intermittent premixing with incoming air and leaked burnt gases, thus exhibiting a complex partially premixed structure.

Note that some NO formation is seen to occur in the lean premixed flame fronts in Fig. 8.22 (a). If part of this formation is imputable to the NNH pathway, there are obviously non negligible contributions from additional pathways which are not considered in any of the aforementioned three routes. Likewise, none of the considered route is able to explain the NO reburn seen on the corner of the combustion chambers in Fig. 8.22 (a). This amounts to saying that a complete description of the NO formation, including secondary pathways, can prove to be very valuable under certain circumstances. As demonstrated here, ARC mechanisms provide a very convenient framework in such a case.

Note finally, that evaporation increases the NO reburn, as evidenced by the very negative NO consumption rate surrounding isolated droplets in Fig. 8.22 (c) and also visible in the IRZ on Fig. 8.22 (a).

8.6 Conclusions

In this Chapter, LES of the NASA-LDI configuration, a two-phase flow lean direct-injection system operated with kerosene, was performed. The main intent was to evaluate the feasibility of a new methodology, combining an analytically reduced chemistry (ARC) description and a thickened flame chemistry-interaction model with a real fuel description to improve predictive capabilities in terms of flame structure and pollutant formation. A Lagrangian framework is chosen for the spray description. The Jet-A fuel description relies on the recently proposed hybrid chemistry (HyChem) approach (Xu *et al.*, 2017*b*,*a*).

An ARC comprised of 29 transported species is easily derived, based on the HyChem model, with the tool YARC (Pepiot, 2008). This ARC is first validated in canonical archetypes representative of the configuration under consideration, before being successfully implemented in the LES solver AVBP. This is a non-trivial result, in view of the difficulties encountered when trying to reduce traditional multi-component surrogate approaches to a LES-compliant size (see Chapter 4).

The proposed methodology is then used to simulate the Jet-A fueled lab-scale burner. A very good agreement is observed between the LES results and the experimental data in terms of velocity fields and spray characteristics. Comparisons with temperature and species data further validate the methodology. Additionally, results demonstrate the improved predictive capabilities, when compared to previous studies of the same configuration. Finally, the level of description attained in this work allows a detailed analysis of the complex flame structure, including a study of the spray/flame interactions, and an investigation of the pollutant formation mechanisms.

These results confirm that the ARC-DTFLES methodology is easily adapted to any type of configuration: gaseous as well as two-phased, in an Eulerian (Jaravel, 2016; Franzelli *et al.*, 2016) as well as in a Lagrangian framework. It has also been assessed that the ARC-DTFLES approach is well suited to the novel realistic fuel description HyChem, thus opening new perspectives for LES of industrial kerosene fueled configurations.

Chapter 9

Conclusions and perspectives

The main intent of this PhD thesis was to investigate the advantages and drawbacks of employing Analytically Reduced Chemistries (ARC) in Large Eddy Simulations (LES), when compared to classical approaches such as tabulation and global schemes, still widely employed today in the community. To this end all the "steps", from the investigation of fuel-specific detailed mechanisms, to the final LES computations, including an investigation of available techniques to perform a kinetic reduction; are considered.

In the present work, ARC mechanisms are derived using the YARC multi-step reduction tool developed by Pepiot (2008). A first part is thus dedicated to the analysis of the possibilities offered by YARC, including examples of derivation on several test cases with various fuels. YARC is found to efficiently combine existing reduction techniques in order to allow very conveniently the derivation of reduced mechanisms, with minimum input from the user. The resulting ARC are tailored to specific needs but their operating range usually extend well beyond their targeted range. Additionally, YARC allows an analysis of the feasibility of employing classical multi-component surrogates for aviation kerosenes in LES, through reduction testing of a 3-components surrogate for an average Jet A fuel. In the present case, this approach does not appear to be promising, as a sufficient reduction level could not be reached. An analysis of error levels on the obtained reduced schemes allows to shed some light on the difficulties that arise; which are found to be mainly related to the intrinsic non-linearities of the kinetic pathways of the various components. A novel hybrid fuel model developed by Xu *et al.* (2017*b*,*a*) is employed instead, and successfully reduced to a LES-compliant size.

Two ARCs are retained and further combined with the Dynamically Thickened Flame model (Colin *et al.*, 2000; Legier *et al.*, 2000) extended to multi-step chemistries (Jaravel, 2016), to perform LES of realistic gas turbine configurations of increasing complexity. The first configuration is a sooting swirl-stabilized non-premixed aero-engine combustor experimentally studied at DLR, burning ethylene. LES of this burner is performed with three different chemistry descriptions, in order to assess their performance both in terms of flame structure predictions and overall CPU cost. By comparison with global chemistry and tabulated chemistry, results with the ARC mechanism highlight the importance of accurately capturing the flow-flame interactions for a good prediction of pollutants, especially soot levels. The flexibility of the method, not requiring *a-priori* assumptions about the flow, is another great advantage. In particular, the computational setup for the LES of a second operating point was very easily put in place. The second configuration is a swirled two-phase flow burner featuring a lean direct injection system and burning a specific Jet A (POSF10325). A novel methodology to real fuel modeling (HyChem approach) is employed, which allows a subsequent ARC derivation. A Lagrangian framework is chosen for the description of the spray. The excellent results in comparison with the multiple available measurements (velocity, temperature, species) constitute an additional validation of the ARC-DTFLES methodology. Results demonstrate the improved predictive capabilities, when compared to previous studies of the same configuration found in the literature. The level of description reached by the use of an ARC chemistry enables a qualitative investigation of the flame-spray interactions, with impact on the gaseous flame structure, complementing recent DNS/LES studies. Valuable insights on the pollutant formation (NO_x) in such complex flame configurations are gained through an analysis of the production pathways considered in the ARC mechanism.

To summarize, the present work has demonstrated that accurate chemistry description can now be efficiently and *directly* included in LES of complex flows, without deep knowledge of chemistry by the user, provided that a code such as YARC is employed. It has also been demonstrated that including such accurate chemistry in simulations greatly impacts the results, bringing them closer to measurements, and providing important new

insights about the flame structure in complex configurations. It was also demonstrated that the ARC-DTFLES methodology provides an adequate framework to the implementation of real aviation fuel chemistry, taking a step further towards simulations of realistic spray burners.

This work can be seen therefore as the foundation of a new stage in LES of turbulent combustion, in which the impact of chemistry can be taken into account, without prior modeling assumptions, to predict chemistry-driven phenomena such as pollutant or soot emissions, but also ignition and extinction and, more generally, all combustion-related phenomena.

Bibliography

Abramzon, B. & Sirignano, W. 1989 Droplet vaporization model for spray combustion calculations. *International journal of heat and mass transfer* **32** (9), 1605–1618. (158)

Ahmed, A., Goteng, G., Shankar, V. SB., Al-Qurashi, K., Roberts, W. L. & Sarathy, S. M. 2015 A computational methodology for formulating gasoline surrogate fuels with accurate physical and chemical kinetic properties. *Fuel* **143**, 290–300. (69)

Ahmed, S. F., Balachandran, R., Marchione, T. & Mastorakos, E. 2007 Spark ignition of turbulent nonpremixed bluff-body flames. *Combustion and Flame* **151** (1), 366–385. (9)

Apeloig, J., d'Herbigny, F.-X., Simon, F., Gajan, P., Orain, M. & Roux, S. 2014 Liquid-fuel behavior in an aeronautical injector submitted to thermoacoustic instabilities. *Journal of Propulsion and Power* **31** (1), 309–319. (155)

Auzillon, P. 2011 Modélisation de la structure et de la dynamique des flammes pour la SGE. Phd thesis, EM2C. (13)

Auzillon, P., Riber, E., Gicquel, L. Y. M., Gicquel, O., Darabiha, N., Veynante, D. & Fiorina, B. 2013 Numerical investigation of a helicopter combustion chamber using LES and tabulated chemistry. *Comptes Rendus Mécanique* **341** (1), 257–265. (7)

Avdić, A., Kuenne, G., Ketelheun, A., Sadiki, A., Jakirlić, S. & Janicka, J. 2013 High performance computing of the darmstadt stratified burner by means of Large-Eddy Simulation and a joint atf-fgm approach. *Computing and Visualization in Science* **16** (2), 77–88. (7)

Avdić, A., Kuenne, G., di Mare, F. & Janicka, J. 2017 LES combustion modeling using the eulerian stochastic field method coupled with tabulated chemistry. *Combustion and Flame* **175**, 201–219. (7)

Barlow, R. 1996 International workshop on measurement and computation of turbulent non-premixed flames. *http://www.sandia.gov/TNF/abstract.html* . (9)

Battin-Leclerc, F., Glaude, P.A., Warth, V., Fournet, R., Scacchi, G. & Coôme, G.M. 2000 Computer tools for modelling the chemical phenomena related to combustion. *Chemical Engineering Science* **55**, 2883–2893. (20, 22)

Bekdemir, C., Somers, L. M. T., Goey, L. P. H. De, Tillou, J. & Angelberger, C. 2013 Predicting diesel combustion characteristics with Large-Eddy Simulations including tabulated chemical kinetics. *Proceedings of the Combustion Institute* **34** (2), 3067–3074. (7)

Bilger, R.W. 1989 The structure of turbulent nonpremixed flames. *Proceedings of the Combustion Institute* **22** (1), 475–488. (32, 164)

Bilger, R. W. 1993 Conditional moment closure for turbulent reacting flow. *Physics of Fluids A: Fluid Dynamics (1989-1993)* **5** (2), 436–444. (10)

Blanquart, G., Pepiot-Desjardins, P. & Pitsch, H. 2009 Chemical mechanism for high temperature combustion of engine relevant fuels with emphasis on soot precursors. *Combustion and Flame* **156** (3), 588–607. (112)

Blanquart, G. & Pitsch, H. 2009 A joint volume-surface-hydrogen multi-variate model for soot formation. *Combustion Generated Fine Carbonaceous Particles* pp. 437–463. (24)

Bockhorn, H. 1994 Soot formation in combustion: mechanisms and models. *Series in Chemical Physics, Springer-Verlag* **59**. (23, 24)

Boivin, P. 2011 Reduced-kinetic mechanisms for hydrogen and syngas combustion including autoignition. PhD thesis, University CARLOS III Madrid. (17, 46)

Bolla, M., Wright, Y. M., Boulouchos, K., Borghesi, G. & Mastorakos, E. 2013 Soot formation modeling of n-heptane sprays under diesel engine conditions using the conditional moment closure approach. *Combustion Science and Technology* **185** (5), 766–793. (24)

Borghi, R. 1988 Turbulent combustion modelling. *Progress in Energy and Combustion Science* **14** (4), 245–292. (94, 95)

Boussinesq, J. 1877 Théorie de l'écoulement tourbillant. *Mém. Présentés par Divers Savants. Acad. Sci. Inst. Fr.* **23**, 46–50. (93)

Bowman, C. T., Frenklach, M., Gardiner, W. R. & Smith, G. 1999 The GRI 3.0 chemical kinetic mechanism. *University of California: Berkeley, CA* . (77)

Bowman, C. T., Hanson, R. K., Davidson, D. F., Jr, W. C. Gardiner, Lissianski, V., Smith, G. P., Golden, D. M., Frenklach, M. & Goldenberg, M. 1995 GRI-Mech 2.11. *URL: http://www.me.berkeley.edu/gri-mech* . (77)

Bozzelli, J. W. & Dean, A. M. 1995 O+ nnh: A possible new route for nox formation in flames. *International journal of chemical kinetics* **27** (11), 1097–1109. (171)

Buckmaster, J. 1979 The quenching of two-dimensional premixed flames. *Acta Astronautica* **6** (5-6), 741–769. (50)

Bulat, G., Jones, W. P. & Marquis, A. J. 2013 Large-Eddy Simulation of an industrial gas-turbine combustion chamber using the sub-grid pdf method. *Proceedings of the Combustion Institute* **34** (2), 3155–3164. (8, 9)

Bulat, G., Jones, W. P. & Marquis, A. J. 2014 No and co formation in an industrial gas-turbine combustion chamber using LES with the Eulerian sub-grid PDF method. *Combustion and Flame* **161**, 1804–1825. (9, 110)

Bushe, W. B. & Steiner, H. 1999 Conditional moment closure for Large-Eddy Simulation of nonpremixed turbulent reacting flows. *Physics of Fluids (1994-present)* **11** (7), 1896–1906. (11)

Butler, T. D. & O'Rourke, P. J. 1977 A numerical method for two dimensional unsteady reacting flows. *Symposium (International) on Combustion* **16** (1), 1503–1515. (97)

Bykov, V. & Maas, U. 2007 The extension of the ildm concept to reaction–diffusion manifolds. *Combustion Theory and Modelling* **11** (6), 839–862. (31)

Cabra, R. 2004 Turbulent jet flames into a vitiated coflow. Phd thesis, NASA CR—2004-212887. (9)

Cabra, R., Chen, J.-Y., Dibble, R. W., Karpetis, A. N. & Barlow, R. S. 2005 Lifted methane–air jet flames in a vitiated coflow. *Combustion and Flame* **143** (4), 491–506. (9)

Cai, J., Jeng, S.-M. & Tacina, R. 2005 The structure of a swirl-stabilized reacting spray issued from an axial swirler. *43 rd AIAA Aerospace Sciences Meeting and Exhibit* . (9, 154, 155, and 156)

Calcote, H. F. 1981 Mechanisms of soot nucleation in flames—a critical review. *Combustion and Flame* **42**, 215–242. (23)

Candel, S. M. & Poinsot, T. J. 1990 Flame stretch and the balance equation for the flame area. *Combustion Science and Technology* **70** (1-3), 1–15. (50)

Carr, R.W. 2007 *Modeling of Chemical Reactions*. Elsevier. (26)

Cavaliere, D. E., Kariuki, J. & Mastorakos, E. 2013 A comparison of the blow-off behaviour of swirl-stabilized premixed, non-premixed and spray flames. *Flow, turbulence and combustion* **91** (2), 347–372. (9)

Charlette, F., Veynante, D. & Meneveau, C. 2002 A power-law wrinkling model for LES of premixed turbulent combustion: Part I - non-dynamic formulation and initial tests. *Combustion and Flame* **131**, 159–180. (159)

Chen, J.Y. 1997 Development of reduced mechanisms for numerical modelling of turbulent combustion. Reno, NV. (33)

Colin, O., Ducros, F., Veynante, D. & Poinsot, T. 2000 A thickened flame model for Large-Eddy Simulations of turbulent premixed combustion. *Physics of Fluids* **12** (7), 1843–1863. (8, 13, 97, 99, 122, 159, and 1)

Colin, O. & Rudgyard, M. 2000 Development of high-order taylor-galerkin schemes for LES. *Journal of Computational Physics* **162**, 338–371. (102, 122, and 159)

Colucci, P. J., Jaberi, F. A., Givi, P. & Pope, S. B. 1998 Filtered density function for Large-Eddy Simulation of turbulent reacting flows. *Physics of Fluids (1994-present)* **10** (2), 499–515. (12)

Cornell, J. A. 2002 *Introduction, in Experiments with Mixtures: Designs, Models, and the Analysis of Mixture Data, Third Edition*. John Wiley & Sons, Inc. (72)

Correa, S. M. 1993 A review of nox formation under gas-turbine combustion conditions. *Combustion science and technology* **87** (1-6), 329–362. (22, 171)

Cuenot, B., Franzelli, B. & Riber, E. 2014 Towards the prediction of soot in aero-engine combustors with Large-Eddy Simulation. *Proceedings of the Summer Program* p. 117. (8)

Cuenot, B. & Poinsot, T. 1994 Effects of curvature and unsteadiness in diffusion flames. implications for turbulent diffusion combustion. *Symposium (International) on Combustion* **25** (1), 1383–1390. (96)

Cuoci, A., Mehl, M., Paratico, T., Faravelli, T. & Ranzi, E. 2005 Modeling of the evaporation and combustion of jet fuel droplets under microgravity conditions. (7)

Dagaut, P. & Cathonnet, M. 2006 The ignition, oxidation, and combustion of kerosene: A review of experimental and kinetic modeling. *Progress in energy and combustion science* **32** (1), 48–92. (6, 69)

Dally, B. B., Fletcher, D. F. & Masri, A. R. 1998 Flow and mixing fields of turbulent bluff-body jets and flames. *Combustion Theory and Modelling* **2** (2), 193–219. (9)

DePaola, G. 2007 Conditional moment closure for autoignition in turbulent flows. PhD thesis, University of Cambridge. (12)

Domingo, P., Vervisch, L. & Réveillon, J. 2005 Dns analysis of partially premixed combustion in spray and gaseous turbulent flame-bases stabilized in hot air. *Combustion and Flame* **140** (3), 172–195. (142)

Donea, J. & Huerta, A. 2003 *Finite element methods for flow problems*. John Wiley & Sons. (102)

Dooley, S., Heyne, J., Won, S. H., Dievart, P., Ju, Y. & Dryer, F. L. 2014 Importance of a cycloalkane functionality in the oxidation of a real fuel. *Energy & Fuels* **28** (12), 7649–7661. (72)

Dooley, S., Won, S. H., Chaos, M., Heyne, J., Ju, Y., Dryer, F. L., Kumar, K., Sung, C.-J., Wang, H., Oehlschlaeger, M. A. *et al.* 2010 A jet fuel surrogate formulated by real fuel properties. *Combustion and Flame* **157** (12), 2333–2339. (6)

Dooley, S., Won, S. H., Heyne, J., Farouk, T. I., Ju, Y., Dryer, F. L., Kumar, K., Hui, X., Sung, C.-J., Wang, H. *et al.* 2012 The experimental evaluation of a methodology for surrogate fuel formulation to emulate gas phase combustion kinetic phenomena. *Combust. Flame* **159** (4), 1444–1466. (6, 69, 71, and 72)

Dougherty, E. P. & Rabitz, H. 1979 A computational algorithm for the green's function method of sensitivity analysis in chemical kinetics. *International journal of chemical kinetics* **11** (12), 1237–1248. (34)

Dunker, A. M. 1981 Efficient calculation of sensitivity coefficients for complex atmospheric models. *Atmospheric Environment* **15**, 1155–1161. (34)

Eberle, C., Gerlinger, P., Geigle, K. P. & Aigner, M. 2014 Soot predictions in an aero-engine model combustor at elevated pressure using urans and finite-rate chemistry. *Combust. Sci. Technol* . (120, 126)

Echekki, T. & Chen, J. H. 1996 Unsteady strain rate and curvature effects in turbulent premixed methane-air flames. *Combustion and Flame* **106** (1), 184–202. (6, 133, and 134)

Echekki, T. & Chen, J. H. 1999 Analysis of the contribution of curvature to premixed flame propagation. *Combustion and Flame* **118** (1), 308–311. (49)

Edelson, D. & Allara, D. L. 1980 A computational analysis of the alkane pyrolysis mechanism: Sensitivity analysis of individual reaction steps. *International Journal of Chemical Kinetics* **12**, 605–621. (34, 37)

Edwards, J. T. 2017 Reference jet fuels for combustion testing. p. 0146. 55th AIAA Aerospace Sciences Meeting. (70, 71, and 72)

Edwards, T. 2002 Kerosene fuels for aerospace propulsion–Composition and properties. *38th AIAA/ASME/SAE/ASEE Joint Propulsion Conference & Exhibit* . (5)

Edwards, T. 2003 Liquid fuels and propellants for aerospace propulsion: 1903-2003. *Journal of propulsion and power* **19** (6), 1089–1107. (69)

Edwards, T. & Maurice, L. Q. 2001 Surrogate mixtures to represent complex aviation and rocket fuels. *Journal of propulsion and power* **12** (2). (6, 68)

El-Asrag, H., Iannetti, A. & Apte, S. 2014 Large-Eddy Simulations for radiation-spray coupling for a lean direct injector combustor. *Combustion and Flame* **161** (2), 510–524. (156, 157)

Ern, A. & Giovangigli, V. 1994 *Multicomponent transport algorithms*, , vol. 24. Springer Science & Business Media. (84)

Ern, A. & Giovangigli, V. 1995 Fast and accurate multicomponent transport property evaluation. *Journal of Computational Physics* **120** (1), 105–116. (84)

Esclapez, L., Cuenot, B. & Riber, E. 2015 Ignition probability of a partially premixed burner using LES. *Proceedings of the Combustion Institute* **35**, 3133–3141. (97, 122)

Fede, P., Simonin, O., Villedieu, P. & Squires, K. D. 2006 Stochastic modeling of the turbulent subgrid fluid velocity along inertial particle trajectories. In *Proc. of the summer program*, pp. 247–258. Center for Turbulence Research, Stanford Univ. (159)

Felden, A., Riber, E., Cuenot, B., Esclapez, L., Ihme, M. & Wang, H. 2016 Dynamically thickened flame LES model for premixed and non-premixed turbulent combustion. In *Proc. of the summer program*, pp. –. Center for Turbulence Research, Stanford Univ. (9)

Fenimore, C. P. 1971 Formation of nitric oxide in premixed hydrocarbon flames. *Symposium (International) on Combustion* **13** (1), 373–380. (23)

Fenimore, C. P. 1976 Reactions of fuel-nitrogen in rich flame gases. *Combustion and Flame* **26**, 249–256. (23)

Fiorina, B., Baron, R., Gicquel, O., Thevenin, D., Carpentier, S., Darabiha, N. *et al.* 2003 Modelling non-adiabatic partially premixed flames using flame-prolongation of ildm. *Combustion Theory and Modelling* **7** (3), 449–470. (32)

Fiorina, B., Gicquel, O., Carpentier, S. & Darabiha, N. 2004 Validation of the fpi chemistry reduction method for diluted nonadiabatic premixed flames. *Combustion science and technology* **176** (5-6), 785–797. (7, 110)

Fiorina, B., Gicquel, O., Vervisch, L., Carpentier, S. & Darabiha, N. 2005 Approximating the chemical structure of partially premixed and diffusion counterflow flames using fpi flamelet tabulation. *Combustion and flame* **140** (3), 147–160. (7, 110, 116, and 129)

Fiorina, B., Veynante, D. & Candel, S. 2015 Modeling combustion chemistry in Large-Eddy Simulation of turbulent flames. *Flow, Turbulence and Combustion* **94**, 3–42. (110)

Franzelli, B. 2011 Impact of the chemical description on DNS and LES of turbulent combustion in industrial aero-engines. Phd thesis, INPT. (30, 99)

Franzelli, B., Fiorina, B. & Darabiha, N. 2013*a* A tabulated chemistry method for spray combustion. *Proceedings of the Combustion Institute* **34** (1), 1659–1666. (7, 122)

Franzelli, B., Riber, E. & Cuenot, B. 2013*b* Impact of the chemical description on a Large-Eddy Simulation of a lean partially premixed swirled flame. *Comptes Rendus Mécanique* **341** (1), 247–256. (9, 23)

Franzelli, B., Riber, E., Cuenot, B. & Ihme, M. 2015*a* Numerical modeling of soot production in aero-engine combustors using Large-Eddy Simulation. American Society of Mechanical Engineers. (140)

Franzelli, B., Riber, E., Cuenot, B. & Ihme, M. 2015*b* Numerical modeling of soot production in aero-engine combustors using Large-Eddy Simulations. *ASME Turbo Expo 2015: Turbine Technical Conference and Exposition* . (7, 8, 110, and 119)

Franzelli, B., Riber, E., Gicquel, L. Y. M. & Poinsot, T. J. 2012 Large-Eddy Simulation of combustion instabilities in a lean partially premixed swirled flame. *Combustion and Flame* **159** (2), 621–637. (13, 97, and 23)

Franzelli, B., Riber, E., Sanjose, M. & Poinsot, T. 2010 A two-step chemical scheme for kerosene–air premixed flames. *Combustion and Flame* **157**, 1364–1373. (8, 13, 29, 145, and 23)

Franzelli, B., Vié, A., Boileau, M., Fiorina, B. & Darabiha, N. 2016 Large-Eddy Simulation of swirled spray flame using detailed and tabulated chemical descriptions. *Flow, Turbulence and Combustion* pp. 1–29. (6, 9, 10, and 173)

Frenklach, M. 2002 Reaction mechanism of soot formation in flames. *Physical Chemistry Chemical Physics* **4** (11), 2028–2037. (23, 119)

Frenklach, M. & Wang, H. 1991*a* Detailed modeling of soot particle nucleation and growth. *Symposium (International) on Combustion* **23** (1), 1559–1566. (24)

Frenklach, M. & Wang, H. 1991*b* Detailed reduction of reaction mechanisms for flame modeling. *Combustion and Flame* **87**, 365–370. (37)

Frouzakis, C. E. & Boulouchos, K. 2000 Analysis and reduction of the ch4-air mechanism at lean conditions. *Combustion Science and Technology* **159**, 281–303. (37)

Fu, Y., Jeng, S.-M. & Tacina, R. 2005 Characteristics of the swirling flow generated by an axial swirler. pp. 517–526. American Society of Mechanical Engineers. (155)

Fureby, C. 2012 A comparative study of flamelet and finite rate chemistry LES for a swirl stabilized flame. *Journal of Engineering for Gas Turbines and Power* **134** (4), 041503. (8)

Gallot-Lavallee, S & Jones, WP 2016 Large-Eddy Simulation of spray auto-ignition under egr conditions. *Flow Turbulence and Combustion* **96**, 513–534. (9)

Galpin, J., Naudin, A., Vervisch, L., Angelberger, C., Colin, O. & Domingo, P. 2008 Large-Eddy Simulation of a fuel-lean premixed turbulent swirl-burner. *Combustion and Flame* **155** (1), 247–266. (7, 110)

Gao, F. & O'Brien, E. E. 1993 A Large-Eddy Simulation scheme for turbulent reacting flows. *Physics of Fluids A: Fluid Dynamics (1989-1993)* **5** (6), 1282–1284. (12)

Garmory, A. & Mastorakos, E. 2011 Capturing localised extinction in Sandia Flame F with LES/CMC. *Proceedings of the Combustion Institute* **33** (1), 1673–1680. (9)

Geigle, K. P., Hadef, R. & Meier, W. 2013 Soot formation and flame characterization of an aero-engine model combustor burning ethylene at elevated pressure. *Journal of Engineering for Gas Turbines and Power* **136 (2)**. (9, 112, 120, and 121)

Geigle, K.-P., Hadef, R., Stöhr, M. & Meier, W. 2016 Flow field characterization of pressurized sooting swirl flames and relation to soot distributions. *Proceedings of the Combustion Institute* . (121)

Geigle, K. P., Kohler, M., O'Loughlin, W. & Meier, W. 2015*a* Investigation of soot formation in pressurized swirl flames by laser measurements of temperature, flame structures and soot concentrations. *Proceedings of the Combustion Institute* **35**, 3373–3380. (120, 121)

Geigle, K. P., O'Loughlin, W., Hadef, R. & Meier, W. 2015*b* Visualization of soot inception in turbulent pressurized flames by simultaneous measurement of laser-induced fluorescence of polycyclic aromatic hydrocarbons and laser-induced incandescence, and correlation to oh distributions. *Applied Physics B* **119** (4), 717–730. (139)

Genyuan, L. & Rabitz, H. 1989 A general analysis of exact lumping in chemical kinetics. *Chemical Engineering and Science* **44**, 1413–1430. (41)

Genyuan, L., Rabitz, H. & Toth, J. 1994 A general analysis of exact nonlinear lumping in chemical kinetics. *Chemical Engineering and Science* **49**, 343–361. (41)

Gicquel, L. Y. M., Gourdain, N., Boussuge, J.-F., Deniau, H., Staffelbach, G., Wolf, P. & Poinsot, T. 2011 High performance parallel computing of flows in complex geometries. *Comptes rendus de l'Académie des sciences* **339**, 104–124. (122)

Gicquel, L. Y. M., Staffelbach, G. & Poinsot, T. J. 2012 Large-Eddy Simualtions of gaseous flames in gas turbine combustion chambers. *Progress in Energy and Combustion Science* **38**, 782–817. (3, 110, and 122)

Gicquel, O., Darabiha, N. & Thévenin, D. 2000 Laminar premixed hydrogen/air counterflow flame simulations using flame prolongation of ildm with differential diffusion. *Proceedings of the Combustion Institute* **28**, 1901–1908. (7, 31, 32, and 110)

Gilbert, R. G., Luther, K. & Troe, J. 1983 Theory of thermal unimolecular reactions in the fall-off range. ii. weak collision rate constants. *Ber. Bunsenges. Phys. Chem.* **87**, 169–177. (26)

Giusti, A. & Mastorakos, E. 2016 Detailed chemistry LES/CMC simulation of a swirling ethanol spray flame approaching blow-off. *Proceedings of the Combustion Institute* . (9)

Glassman, I. & Yetter, R. A. 1987 *Combustion*. New York: Academic Press. (23, 25)

Godel, G., Domingo, P. & Vervisch, L. 2009 Tabulation of no x chemistry for Large-Eddy Simulation of non-premixed turbulent flames. *Proceedings of the Combustion Institute* **32** (1), 1555–1561. (32)

Goodwin, D. G., Moffat, H. K. & Speth, R. L. 2014 Cantera: An object-oriented software toolkit for chemical kinetics, thermodynamics, and transport processes. http://www.cantera.org, version 2.1.2. (32, 52, 86, 111, 112, 119, and 154)

Goussis, D. A. 2012 Quasi steady state and partial equilibrium approximations: their relation and their validity. *Combustion Theory and Modelling* **16** (5), 869–926. (44)

Goussis, D. A. & Lam, S. H. 1992 A study of homogeneous methanol oxidation kinetics using csp. *Symposium (International) on Combustion* **24** (1), 113–120. (43)

Goussis, D. A. & Mass, U. 2011 Model reduction for combustion chemistry. *In: T. Echekki, E. Mastorakos Turbulent Combustion Modeling, Fluid Mechanics and Its Applications* **95**, 193–220. (8, 110, and 111)

Gran, I., Echekki, T. & Chen, J. H. 1996 Negative flame speed in an unsteady 2-d premixed flame: a computational study. *Proceedings of the Combustion Institute* **26**, 323–329. (49)

Griffiths, J.F. 1995 Reduced kinetic models and their application to practical combustion systems. *Progress in Energy and Combustion Science* **21**, 25–107. (33, 34)

Guéret, C., Cathonnet, M., Boettner, J.-C. & Gaillard, F. 1991 Experimental study and modeling of kerosene oxidation in a jet-stirred flow reactor. *Symposium (International) on Combustion* **23** (1), 211–216. (6)

Guin, C. & Orain, M. 2016 Deliverable d3.2.5 - detailed investigation of the selected msfi configurations. *Technical report, LEMCOTEC* . (9)

Gutheil, E. & Williams, F. A. 1991 A numerical and asymptotic investigation of structures of hydrogen-air diffusion flames at pressures and temperatures of high-speed combustion. *Symposium (International) on Combustion* **23** (1), 513–521. (33)

Hamby, D. M. 1994 A review of techniques for parameter sensitivity analysis of environmental models. *Environmental Monitoring and Assessment* **32**, 135–154. (34, 36)

Hamiroune, D., Bishnu, P., Metghalchi, M. & Keck, J.C. 1998 Rate-controlled partial-equilibrium method using constraint potentials. *Combustion Theory and Modelling* **2** (1), 81–94. (30)

Hawkes, E. R. & Cant, R. S. 2000 A flame surface density approach to Large-Eddy Simulation of premixed turbulent combustion. *Proceedings of the Combustion Institute* **28** (1), 51–58. (97)

Hawkes, E. R. & Chen, J. H. 2004 Direct numerical simulation of hydrogen-enriched lean premixed methane–air flames. *Combustion and Flame* **138** (3), 242–258. (133)

Haworth, D. C. 2010 Progress in probability density function methods for turbulent reacting flows. *Progress in Energy and Combustion Science* **36** (2), 168–259. (97)

Haworth, D. C., J., T. & Poinsot 1992 Numerical simulations of lewis number effects in turbulent premixed flames. *Journal of Fluid Mechanics* **244**, 405–436. (6)

Herbinet, O., Pitz, W. J. & Westbrook, C. K. 2008 Detailed chemical kinetic oxidation mechanism for a biodiesel surrogate. *Combustion and Flame* **154** (3), 507–528. (4)

Hill, S. C. & Smoot, L. D. 2000 Modeling of nitrogen oxides formation and destruction in combustion systems. *Progress in energy and combustion science* **26** (4), 417–458. (172)

Hirschfelder, J. O., Curtiss, C. F. & Byrd, R. B. 1969 *Molecular theory of gases and liquids*. New York: John Wiley & Sons. (83, 84, and 85)

Honnet, S., Seshadri, K., Niemann, U. & Peters, N. 2009 A surrogate fuel for kerosene. *Proceedings of the Combustion Institute* **32** (1), 485–492. (156, 157)

Hu, L. Y., Zhou, L. X. & Zhang, J. 2006 Large-Eddy Simulation of a swirling diffusion flame using a som sgs combustion model. *Numerical Heat Transfer, Part B: Fundamentals* **50** (1), 41–58. (96)

Huang, H., Fairweather, M., Griffiths, J. F., Tomlin, A. S. & Brad, R. B. 2005 A systematic lumping approach for the reduction of comprehensive kinetic models. *Proceedings of the Combustion Institute* **30**, 1309–1316. (41)

Hwang, J. Y. & Chung, S. H. 2001 Growth of soot particles in counterflow diffusion flames of ethylene. *Combustion and flame* **125** (1), 752–762. (120)

Iafrate, N. 2016 Simulation aux grandes echelles diphasique dans les moteurs downsizés à allumage commandé. Phd thesis, IFPEN. (159)

Iannetti, A., Liu, N.-S. & Davoudzadeh, F. 2008 The effect of spray initial conditions on heat release and emissions in LDI CFD calculations. *NASA Glenn Research Center, Cleveland, OH, NASA Report No. NASA/TM—2008-214522* . (155, 156)

Idicheria, C. A. & Pickett, L. M. 2005 Soot formation in diesel combustion under high-egr conditions. *Tech. Rep.*. SAE Technical Paper. (9)

Ihme, M. & Pitsch, H. 2008*a* Modeling of radiation and nitric oxide formation in turbulent nonpremixed flames using a flamelet/progress variable formulation. *Physics of Fluids (1994-present)* **20** (5), 055110. (7, 110, and 156)

Ihme, M. & Pitsch, H. 2008*b* Prediction of extinction and reignition in nonpremixed turbulent flames using a flamelet/progress variable model: 2. application in LES of Sandia flames D and E. *Combustion and flame* **155** (1), 90–107. (7, 110)

Jachimowski, C. J. 1992 An analysis of combustion studies in shock expansion tunnels and reflected shock tunnels . (9)

Jaouen, N., Vervisch, L., Domingo, P. & Ribert, G. 2016 Automatic reduction and optimisation of chemistry for turbulent combustion modelling: Impact of the canonical problem. *Combustion and Flame* . (58)

Jaravel, T. 2016 Prediction of pollutants in gas turbines using Large-Eddy Simulation. Phd thesis, CERFACS. (8, 9, 10, 13, 40, 46, 77, 79, 88, 99, 100, 101, 102, 103, 104, 105, 173, and 1)

Jaravel, T., Riber, E., Cuenot, B. & Bulat, G. 2016 Large-Eddy Simulation of an industrial gas turbine combustor using reduced chemistry with accurate pollutant prediction. *Proceedings of the Combustion Institute* . (9, 40, 97, 110, and 122)

Jarrett, O., Cutler, A., Antcliff, R., Chitsomboon, T., Dancey, C. & Wang, J. 1988 Measurements of temperature, density, and velocity in supersonic reacting flow for cfd code validation. , vol. 1, pp. 357–374. (9)

Jiménez, C., Cuenot, B., Poinsot, T. & Haworth, D. 2002 Numerical simulation and modeling for lean stratified propane-air flames. *Combustion and Flame* **128** (1), 1–21. (6)

Jones, W.P. & Rigopoulos, S. 2005 Rate-controlled constrained equilibrium: Formulation and application to nonpremixed laminar flames. *Combustion and Flame* **142**, 223–234. (30)

Jones, W. P. & Lindstedt, R. P. 1988 Global reaction schemes for hydrocarbon combustion. *Combustion and flame* **73** (3), 233–249. (30)

Jones, W. P., Marquis, A. J. & Prasad, V. N. 2012 LES of a turbulent premixed swirl burner using the eulerian stochastic field method. *Combustion and Flame* **159** (10), 3079–3095. (9, 110)

Jones, W. P. & Navarro-Martinez, S. 2008 Study of hydrogen auto-ignition in a turbulent air co-flow using a Large-Eddy Simulation approach. *Computers & Fluids* **37** (7), 802–808. (9)

Jones, W. P. & Navarro-Martinez, S. 2009 Numerical study of n-heptane auto-ignition using LES/PDF methods. *Flow, turbulence and combustion* **83** (3), 407–423. (9, 12)

Jones, W. P., Navarro-Martinez, S. & Röhl, O. 2007 Large-Eddy Simulation of hydrogen auto-ignition with a probability density function method. *Proceedings of the Combustion Institute* **31** (2), 1765–1771. (9)

Jones, W. P. & Prasad, V. N. 2010 Large-Eddy Simulation of the Sandia Flame Series (D-F) using the Eulerian stochastic field method. *Combustion and Flame* **157** (9), 1621–1636. (9)

Jones, W. P. & Tyliszczack, A. 2010 Large-Eddy Simulation of spark ignition in a gas turbine combustor. *Flow, Turbulence and Combustion* **85** (3-4), 711–734. (8)

Keck, J.C. & Gillespie, D. 1971 Rate-controlled partial-equilibrium method for treating reacting gas mixtures. *Combustion and Flame* **17** (2), 237–241. (30)

Keck, J.C., Law, R. & Metghalchi, M. 1988 Rate-controlled constrained-equilibrium calculation of ignition delay times in hydrogen-oxygen mixtures. *22nd Symposium on Combustion, The Combustion Institute* pp. 1705–1713. (30)

Kee, R. J., Coltrin, M. E. & Glarborg, P. 2005 *Chemically reacting flow: theory and practice*. John Wiley & Sons. (83, 85)

Kee, R. J., Rupley, F. M., Miller, J. A., Coltrin, M. E., Grcar, J. F., Meeks, E., Moffat, H. K., Lutz, A. E., Dixon-Lewis, G., Smooke, M. D., Warnatz, J., Evans, G. H., Larson, R. S., Mitchell, R. E., Petzold, L. R., Reynolds, W. C., Caracotsios, M., Stewart, W. E., Glarborg, P., Wang, C. & Adigun, Ola 2000 The transport program and subroutine library are part of the chemkin collection. (32, 86)

Kennedy, I. M. 1997 Models of soot formation and oxidation. *Progress in Energy and Combustion Science* **23** (2), 95–132. (24, 119)

Kim, D., Martz, J. & Violi, A. 2014 A surrogate for emulating the physical and chemical properties of conventional jet fuel. *Combustion and Flame* **161** (6), 1489–1498. (69, 71)

Kim, I. S. 2005 Conditional moment closure for non-premixed turbulent combustion. PhD thesis, University of Cambridge. (11)

Klimenko, A. Y. 1990 Multicomponent diffusion of various admixtures in turbulent flow. *Fluid Dynamics* **25** (3), 327–334. (11)

Klimenko, A. Y. & Bilger, R. W. 1999 Conditional moment closure for turbulent combustion. *Progress in energy and combustion science* **25** (6), 595–687. (11)

Knudsen, E., Kim, S. H. & Pitsch, H. 2010 An analysis of premixed flamelet models for Large-Eddy Simulation of turbulent combustion. *Physics of Fluids* **22** (11), 115109. (96)

Knudsen, E. & Pitsch, H. 2009 A general flamelet transformation useful for distinguishing between premixed and non-premixed modes of combustion. *Combustion and flame* **156** (3), 678–696. (7, 110, and 129)

Knudsen, E., Shashank & Pitsch, H. 2015 Modeling partially premixed combustion behavior in multiphase LES. *Combustion and Flame* **162** (1), 159–180. (7, 96, 157, 159, 162, and 167)

Kolmogorov, A. N. 1941 The local structure of turbulence in incompressible viscous fluid for very large reynolds numbers. *Comptes rendus de l'Académie des sciences, USSR* **30**, 301. (93)

Kronenburg, A. & Bilger, R. W. 2001 Modelling differential diffusion in nonpremixed reacting turbulent flow: Model development. *Combustion Science and Technology* **166**, 195–227. (12)

Kuenne, G., Ketelheun, A. & Janicka, J. 2011 LES modeling of premixed combustion using a thickened flame approach coupled with fgm tabulated chemistry. *Combustion and Flame* **158** (9), 1750–1767. (7)

Lam, H. S. & Goussis, D. A. 1991 Conventional asymptotics and computational singular perturbation for simplified kinetics modelling. *Lecture Notes in Physics* **384**, 227–242. (43)

Lam, H. S. & Goussis, D. A. 1994 The csp method for simplifying kinetics. *International Journal of Chemical Kinetics* **26**, 461–486. (43)

Lam, S. H. 1985 Singular perturbation for stiff equations using numerical methods. In *Recent advances in the aerospace sciences*, pp. 3–19. Springer. (42)

Lamarque, N. 2007 Schémas numériques et conditions limites pour la simulation aux grandes échelles de la combustion diphasique dans les foyer d'hélicoptères. PhD thesis, INPT. (102)

Lammel, O., Geigle, K. P., Luckerath, R., Meier, W. & Aigner, M. 2007 Investigation of soot formation and oxidation in a high-pressure gas turbine model combustor by laser techniques. *ASME Turbo Expo 2007: Power for Land, Sea, and Air* pp. 703–710. (121)

Lax, P. D. & Wendroff, B. 1960 Systems of conservation laws. *Communications on Pure and Applied Mathematics* **13**, 217–237. (102)

Lecocq, G., Hernández, I., Poitou, D., Riber, E. & Cuenot, B. 2013 Soot prediction by Large-Eddy Simulation of complex geometry combustion chambers. *Comptes Rendus Mécanique* **341** (1-2), 230–237. (24)

Lecocq, G., Poitou, D., Hernández, I., Duchaine, F., Riber, E. & Cuenot, B. 2014 A methodology for soot prediction including thermal radiation in complex industrial burners. *Flow, Turbulence and Combustion* **92**, 947–970. (8)

Lecourt, R., Linassier, G. & Lavergne, G. 2011 Detailed characterisation of a swirled air/kerosene spray in reactive and non-reactive conditions downstream from an actual turbojet injection system. pp. 185–194. American Society of Mechanical Engineers. (155)

Lefebvre, A. H. 1998 *Gas Turbine Combustion*, 2nd edn. Taylor & Francis. (2, 120)

Legier, J.-P., Poinsot, T. & Veynante, D. 2000 Dynamically thickened flame LES model for premixed and non-premixed turbulent combustion. pp. 157–168. (8, 97, 98, 122, and 1)

Lemmon, E. W., Huber, M. L. & McLinden, M. O. 2002 Nist reference fluid thermodynamic and transport properties–refprop. *NIST standard reference database* **23**, v7. (68)

Lepage, V. 2000 Elaboration d'une méthode de réduction de schémas détaillés. application aux mécanismes de combustion du gaz naturel et du n-décane. Phd, Universite Paris VI. (35, 38)

Leung, K. M., Lindstedt, R. P. & Jones, W. P. 1991 A simplified reaction mechanism for soot formation in nonpremixed flames. *Combustion and flame* **87** (3), 289–305. (24, 110, 119, and 120)

Linan, A. 1974 The asymptotic structure of counterflow diffusion flames for large activation energies. *Acta Astronautica* **1**, 1007. (95)

Lindemann, F. A. 1922 *Transactions of the Faraday Society* **17**, 598–604. (26)

Lindstedt, R. P. & Meyer, M. P. 2002 A dimensionally reduced reaction mechanism for methanol oxidation. *Proceedings of the combustion institute* **29** (1), 1395–1402. (9)

Liu, S., Hewson, J. C., Chen, J. H. & Pitsch, H. 2004 Effects of strain rate on high-pressure nonpremixed n-heptane autoignition in counterflow. *Combustion and flame* **137** (3), 320–339. (9)

Lovas, T., Amnéus, P., Mauss, F. & Mastorakos, E. 2002 Comparison of automatic reduction procedures for ignition chemistry. *Proceedings of the Combustion Institute* **293**, 1387–1393. (44, 112)

Lovas, T., Navarro-Martinez, S. & Rigopoulos, S. 2011 On adaptively reduced chemistry in Large-Eddy Simulations. *Proceedings of the Combustion Institute* **33**, 1339–1346. (30)

Lovas, T., Nilsson, D. & Mauss, F. 2000 Automatic reduction procedure for chemical mechanisms applied to premixed methane/air flames. *Proceedings of the Combustion Institute* **28**, 1809–1815. (44)

Lu, T. 2008 Reduced mechanisms for combustion applications. *http://www.engr.uconn.edu/ tlu/mechs/mechs.htm* . (46)

Lu, T., Ju, Y. & Law, C.-K. 2001 Complex csp for chemistry reduction and analysis. *Combustion and Flame* **126**, 1445–1455. (43)

Lu, T. & Law, C. K. 2005 A directed relation graph method for mechanism reduction. *Proceedings of the Combustion Institute* **30**, 1333–1341. (38, 39)

Lu, T. & Law, C. K. 2006*a* Linear time reduction of large kinetic mechanisms with directed relation graph: n-heptane and iso-octane. *Combustion and Flame* **144** (1), 24–36. (39)

Lu, T. & Law, C.-K. 2006*b* Systematic approach to obtain analytic solutions of quasi steady state species in reduced mechanisms. *J. Phys. Chem.* **110**, 13202–13208. (41, 42)

Lu, T. & Law, C. K. 2008*a* A criterion based on computational singular perturbation for the identification of quasi steady state species: A reduced mechanism for methane oxidation with no chemistry. *Combustion and Flame* **154** (4), 761–774. (9, 39, 43, and 46)

Lu, T. & Law, C. K. 2008*b* Strategies for mechanism reduction for large hydrocarbons: n-heptane. *Combustion and flame* **154** (1), 153–163. (41, 46)

Lu, T. & Law, C. K. 2009 Toward accommodating realistic fuel chemistry in large-scale computations. *Progress in Energy and Combustion Science* **35** (2), 192–215. (4, 110)

Lu, T., Plomer, M., Luo, Z., Sarathy, S.M., Pitz, W.J., Som, S. & Longman, D.E. 2011 Directed relation graph with expert knowledge for skeletal mechanism reduction. (39)

Luche, J. 2003 Obtention de modeles cinétiques réduits de combustion. application à un mécanisme du kérosène. Phd thesis, Université d'Orléans. (38, 78, and 154)

Luo, K., Pitsch, H., Pai, M. G. & Desjardins, O. 2011 Direct numerical simulations and analysis of three-dimensional n-heptane spray flames in a model swirl combustor. *Proceedings of the Combustion Institute* **33** (2), 2143–2152. (166)

Ma, T., Stein, O. T., Chakraborty, N. & Kempf, A. M. 2014 A posteriori testing of the flame surface density transport equation for LES. *Combustion Theory and Modelling* **18** (1), 32–64. (97)

Maas, U. & Pope, S. B. 1992 Simplifying chemical kinetics: intrinsic low-dimensional manifolds in composition space. *Combustion and Flame* **88**, 239 – 264. (7, 31)

Magnussen, B. F. & Hjertager, B. H. 1977 On mathematical modeling of turbulent combustion with special emphasis on soot formation and combustion. *Symposium (international) on Combustion* **16** (1), 719–729. (96)

Mahesh, K., Constantinescu, G., Apte, S., Iaccarino, G., Ham, F. & Moin, P. 2006 Large-Eddy Simulation of reacting turbulent flows in complex geometries. *Journal of Applied Mechanics* **73** (3), 374–381. (7, 110)

Malik, N., Lovas, T. & Mauss, F. 2011 The effect of preferential diffusion on the soot initiation process in ethylene diffusion flames. *Flow, turbulence and combustion* **87** (2-3), 293–312. (6)

Marinov, N. M. 1999 A detailed chemical kinetic model for high temperature ethanol oxidation. *International Journal of Chemical Kinetics* **31** (3), 183–220. (9)

Markides, C. N. & Mastorakos, E. 2005 An experimental study of hydrogen autoignition in a turbulent co-flow of heated air. *Proceedings of the Combustion Institute* **30** (1), 883–891. (9)

Massias, A., Diamantis, D., Mastorakos, E. & Goussis, D. A. 1999 An algorithm for the construction of global reduced mechanisms with csp data. *Combustion and Flame* **117**, 685–708. (33, 43)

Mathur, S., Tondon, P. K. & Saxena, S. C. 1967 Thermal conductivity of binary, ternary and quaternary mixtures of rare gases. *Molecular physics* **12** (6), 569–579. (87)

McRae, G. J., Tilden, J. W. & Seinfeld, J. H. 1982 Global sensitivity analysis—a computational implementation of the fourier amplitude sensitivity test (fast). *Computers & Chemical Engineering* **6** (1), 15–25. (34)

Mehl, M., Vanhove, G., Pitz, W. J. & Ranzi, E. 2008 Oxidation and combustion of the n-hexene isomers: A wide range kinetic modeling study. *Combustion and Flame* **155**, 756–772. (20)

Meier, W., Weigand, P., Duan, X. R. & Giezendanner-Thoben, R. 2007 Detailed characterization of the dynamics of thermoacoustic pulsations in a lean premixed swirl flame. *Combustion and Flame* **150** (1), 2–26. (9)

Meneveau, C. & Poinsot, T. 1991 Stretching and quenching of flamelets in premixed turbulent combustion. *Combustion and Flame* **86** (4), 311–332. (122)

Mercier, X., Orain, M. & Grisch, F. 2007 Investigation of droplet combustion in strained counterflow diffusion flames using planar laser-induced fluorescence. *Applied Physics B: Lasers and Optics* **88** (1), 151–160. (170)

Meyer, M. P. 2001 The application of detailed and systematically reduced chemistry to transient laminar flames. PhD thesis, Imperial College London (University of London). (9)

Miller, J. A. & Bowman, C. T. 1989 Mechanism and modeling of nitrogen chemistry in combustion. *Progress in energy and combustion science* **15** (4), 287–338. (22, 23, and 171)

Miller, J. A., Pilling, M. J. & Troe, J. 2005 Unravelling combustion mechanisms through a quantitative understanding of elementary reactions. *Proceedings of the Combustion Institute* **30** (1), 43–88. (23)

Moesl, K., Schwing, J. E. & Sattelmayer, T. 2012 Modelling nox emissions of single droplet combustion. *Combustion Theory and Modelling* **16** (1), 107–141. (77)

Morganti, K. J., Foong, T. M., Brear, M. J., da Silva, G., Yang, Y. & Dryer, F. L. 2013 The research and motor octane numbers of liquefied petroleum gas (lpg). *Fuel* **108**, 797–811. (72)

Morton, K. W. & Paisley, M. F. 1989 A finite volume scheme with shock fitting for the steady euler equations. *Journal of Computational Physics* **80**, 168–203. (102)

Moskaleva, L. V. & Lin, M. C. 2000 The spin-conserved reaction ch+ n 2 h+ ncn: a major pathway to prompt no studied by quantum/statistical theory calculations and kinetic modeling of rate constant. *Proceedings of the Combustion Institute* **28** (2), 2393–2401. (23)

Moss, J. B., Stewart, C. D. & Young, K. J. 1995 Modeling soot formation and burnout in a high temperature laminar diffusion flame burning under oxygen-enriched conditions. *Combustion and Flame* **101** (4), 491–500. (24)

Moule, Y., Sabelnikov, V. & Mura, A. 2014 Highly resolved numerical simulation of combustion in supersonic hydrogen–air coflowing jets. *Combustion and Flame* **161** (10), 2647–2668. (9)

Moureau, V., B., Fiorina & Pitsch, H. 2009 A level set formulation for premixed combustion LES considering the turbulent flame structure. *Combustion and Flame* **156** (4), 801–812. (96)

Moureau, V., Lartigue, G., Sommerer, Y., Angelberger, C., Colin, O. & Poinsot, T. J. 2005 Numerical methods for unsteady compressible multi-component reacting flows on fixed and moving grids. *Journal of Computational Physics* **202** (2), 710–736. (102, 106)

Mueller, M. A., Kim, T. J., Yetter, R. A. & Dryer, F. L. 1999 Flow reactor studies and kinetic modeling of the h2/o2 reaction. *International Journal of Chemical Kinetics* **31**, 113–125. (9)

Mueller, M. E. & Pitsch, H. 2012 LES model for sooting turbulent nonpremixed flames. *Combustion and Flame* **159** (6), 2166–2180. (7, 110)

Mueller, M. E. & Pitsch, H. 2013 Large-Eddy Simulation of soot evolution in an aircraft combustor. *Physics of Fluids (1994-present)* **25** (11), 110812. (7, 110)

Narayanaswamy, K., Blanquart, G. & Pitsch, H. 2010 A consistent chemical mechanism for oxidation of substituted aromatic species. *Combustion and Flame* **157**, 1879–1898. (52, 111, and 112)

Narayanaswamy, K., Pitsch, H. & Pepiot, P. 2016 A component library framework for deriving kinetic mechanisms for multi-component fuel surrogates: Application for jet fuel surrogates. *Combust. Flame* **165**, 288–309. (68, 69, 70, 71, 72, and 73)

Navarro-Martinez, S. & Kronenburg, A. 2007 LES/CMC simulations of a turbulent bluff-body flame. *Proceedings of the Combustion Institute* **31** (2), 1721–1728. (9)

Navarro-Martinez, S. & Kronenburg, A. 2009 LES/CMC simulations of a lifted methane flame. *Proceedings of the Combustion Institute* **32** (1), 1509–1516. (9)

Navarro-Martinez, S., Kronenburg, A. & Mare, F. Di 2005 Conditional moment closure for Large-Eddy Simulations. *Flow, Turbulence and Combustion* **75** (1-4), 245–274. (9, 11)

Navarro-Martinez, S. & Rigopoulos, S. 2011 Large-Eddy Simulation of a turbulent lifted flame using conditional moment closure and rate-controlled constrained equilibrium. *Flow, turbulence and combustion* **87** (2-3), 407–423. (31)

Neophytou, A., Mastorakos, E. & Cant, R. S. 2012 The internal structure of igniting turbulent sprays as revealed by complex chemistry DNS. *Combustion and Flame* **159** (2), 641–664. (166)

Nguyen, P.-D., Vervisch, L., Subramanian, V. & Domingo, P. 2010 Multidimensional flamelet-generated manifolds for partially premixed combustion. *Combustion and Flame* **157** (1), 43–61. (7, 110)

Nicoud, F., Baya Toda, H., Cabrit, O., Bose, S. & Lee, J. 2011 Using singular values to build a subgrid-scale model for Large-Eddy Simulations. *Physics of Fluids* **23** (8), 085106. (93, 158)

Nicoud, F. & Ducros, F. 1999 Subgrid-scale stress modelling based on the square of the velocity gradient tensor. *Flow, Turbulence and Combustion* **62** (3), 183–200. (93, 122)

Niu, Y.-S., Vervisch, L. & Tao, P. D. 2013 An optimization-based approach to detailed chemistry tabulation: Automated progress variable definition. *Combustion and Flame* **160** (4), 776–785. (7)

Norris, A. T. & Pope, S. B. 1995 Modeling of extinction in turbulent diffusion flames by the velocity-dissipation-composition pdf method. *Combustion and Flame* **100** (1-2), 211–220. (7)

O'Brien, E. E. 1980 The probability density function (pdf) approach to reacting turbulent flows. In *Turbulent reacting flows*, pp. 185–218. Springer. (97)

Oijen, J. A. Van, Lammers, F. A. & Goey, L. P. H. De 2001 Modeling of complex premixed burner systems by using flamelet-generated manifolds. *Combustion and Flame* **127** (3), 2124–2134. (7, 31, and 110)

Olsson, J. O. & Andersson, L. 1987 Sensitivity analysis based on an efficient brute-force method, applied to an experimental ch4/o2 premixed laminar flame. *Combustion and Flame* **67**, 99–109. (34)

Patel, N., Kirtaş, M., Sankaran, V. & Menon, S. 2007 Simulation of spray combustion in a lean-direct injection combustor. *Proceedings of the Combustion Institute* **31** (2), 2327–2334. (156)

Patel, N. & Menon, S. 2008 Simulation of spray–turbulence–flame interactions in a lean direct injection combustor. *Combustion and Flame* **153** (1), 228–257. (156, 167)

Paulhiac, D. 2015 Modélisation de la combustion d'un spray dans un brûleur aéronautique. Phd thesis, CERFACS. (158, 170)

Paulhiac, D., Cuenot, B., Riber, E., Esclapez, L. & Richard, S. 2017 Analysis of the spray flame structure in a lab-scale burner using Large Eddy Simulation and Discrete Particle Simulation. *In preparation* . (165)

Pepiot, P. 2008 Automatic strategies to model transportation fuel surrogates. Phd thesis, Stanford University. (5, 13, 33, 40, 41, 44, 46, 112, 154, 173, and 1)

Pepiot, P. & Pitsch, H. 2008 A chemical lumping method for the reduction of large chemical kinetic mechanisms. *Combustion Theory and Modelling* **12:6**, 1089 – 1108. (40, 46)

Pepiot-Desjardins, P. & Pitsch, H. 2008 An efficient error propagation based reduction method for large chemical kinetic mechanisms. *Combustion and Flame* **154**, 67–81. (39, 40, 41, 44, 46, and 112)

Peters, N. 1984 Laminar diffusion flamelet models in non-premixed turbulent combustion. *Progress in Energy and Combustion Science* **10 (3)**, 319–339. (7, 110)

Peters, N. 1985 Numerical and asymptotic analysis of systematically reduced reaction schemes for hydrocarbon flames. In *Numerical simulation of combustion phenomena* (ed. B. Larrouturou, R. Glowinsky & R. Temam), , vol. 241, pp. 90 – 109. Berlin: Springer-Verlag. (9)

Peters, N. 1999 The turbulent burning velocity for large-scale and small-scale turbulence. *Journal of Fluid mechanics* **384**, 107–132. (94, 96)

Philip, M., Boileau, M., Vicquelin, R., Riber, E., Schmitt, T., Cuenot, B., Durox, D. & Candel, S. 2015 Large-Eddy Simulations of the ignition sequence of an annular multiple-injector combustor. *Proceedings of the Combustion Institute* **35** (3), 3159–3166. (7)

Pierce, C. D. & Moin, P. 2004 Progress-variable approach for Large-Eddy Simulation of non-premixed turbulent combustion. *Journal of Fluid Mechanics* **504**, 73–97. (7, 110)

Pitsch, H. 1988 FlameMaster v3.1. *A C++ computer program for 0D combustion and 1D laminar fame calculations* . (46, 154)

Pitsch, H. 2005 A consistent level set formulation for Large-Eddy Simulation of premixed turbulent combustion. *Combustion and Flame* **143** (4), 587–598. (96)

Pitsch, H. 2006 Large-Eddy Simulation of turbulent combustion. *Annu. Rev. Fluid Mech.* **38**, 453–482. (110)

Pitsch, H. & de Lageneste, L. Duchamp 2002 Large-Eddy Simulation of premixed turbulent combustion using a level-set approach. *Proceedings of the Combustion Institute* **29**, 2001–2008. (96)

Pitz, W. J. & Mueller, C. J. 2011 Recent progress in the development of diesel surrogate fuels. *Progress in Energy and Combustion Science* **37** (3), 330–350. (69)

Poinsot, T. & Lele, S. K. 1992 Boundary conditions for direct simulations of compressible viscous flows. *Journal of Computational Physics* **101**, 104–129. (106, 122)

Poinsot, T. & Veynante, D. 2005 *Theoretical and numerical combustion, second edition.* R.T. Edwards, out. (3, 28, 32, 48, 49, 50, 84, 91, 95, and 21)

Pope, S. B. 2000 *Turbulent Flows.* Cambridge University Press. (90)

Ranz, W. & Marshall, W. 1952 Evaporation from drops. *Chemical Engineering Progress* **48** (3), 141–146. (158)

Ranzi, E., Frassoldati, A., Grana, R., Cuoci, A., Faravelli, T., Kelley, A. P. & Law, C. K. 2012 Hierarchical and comparative kinetic modeling of laminar flame speeds of hydrocarbon and oxygenated fuels. *Progress in Energy and Combustion Science* **38** (4), 468–501. (52)

Rein, M. 1992 The partialequilibrium approximation in reacting flows. *Physics of Fluids A: Fluid Dynamics* **4**, 873. (44)

Ren, Z., Pope, S. B., Vladimirsky, A. & Guckenheimer, J. M. 2006 The invariant constrained equilibrium edge preimage curve method for the dimension reduction of chemical kinetics. *The Journal of chemical physics* **124** (11), 114111. (31)

Revel, J., Boettner, J. C., Cathonnet, M. & Bachman, J. S. 1994 Derivation of a global chemical kinetic mechanism for methane ignition and combustion. *Journal de chimie physique* **91** (4), 365–382. (37, 38)

Richardson, L. F. 1922 Weather prediction by numerical process. *Cambridge University Press* . (90)

Rigopoulos, S. & Lovas, T. 2009 A loi-rcce methodology for reducing chemical kinetics, with application to laminar premixed flames. *Proceedings of the Combustion Institute* **32**, 569–576. (30)

Roy, S. P. & Haworth, D. C. 2016 A systematic comparison of detailed soot models and gas-phase chemical mechanisms in laminar premixed flames. *Combustion Science and Technology* **188** (7), 1021–1053. (24)

Rudgyard, M. 1993 Cell vertex methods for steady inviscid flow. In *Lectures Series 1993-04* (ed. Von Karman Institute for Fluid Dynamics), , vol. 1993-04. Von Karman Institute for Fluid Dynamics. (102)

Sabel'nikov, V. & Soulard, O. 2005 Rapidly decorrelating velocity-field model as a tool for solving one-point fokker-planck equations for probability density functions of turbulent reactive scalars. *Physical Review E* **72** (1), 016301. (12)

Sanjosé, M., Senoner, J. M., Jaegle, F., Cuenot, B., Moreau, S. & Poinsot, T. 2011 Fuel injection model for Euler–Euler and Euler–Lagrange Large-Eddy Simulations of an evaporating spray inside an aeronautical combustor. *International Journal of Multiphase Flow* **37** (5), 514–529. (159)

Savard, B. & Blanquart, G. 2015 Broken reaction zone and differential diffusion effects in high karlovitz n-c 7 h 16 premixed turbulent flames. *Combustion and Flame* **162** (5), 2020–2033. (6)

Saxena, V. & Pope, S. B. 1999 Pdf simulations of turbulent combustion incorporating detailed chemistry. *Combustion and Flame* **117** (1), 340–350. (7)

Schiller, L. & Naumann, Z. 1935 A drag coefficient correlation. *Z. Ver. Deutsch. Ing* **77** (1), 318–320. (158)

Schneider, C., Dreizler, A. & Janicka, J. 2005 Fluid dynamical analysis of atmospheric reacting and isothermal swirling flows. *Flow, turbulence and combustion* **74** (1), 103–127. (9)

Schönfeld, T. & Rudgyard, M. 1999 Steady and unsteady flow simulations using the hybrid flow solver avbp. *AIAA journal* **37** (11), 1378–1385. (102, 122)

Schulz, O., Jaravel, T., Poinsot, T., Cuenot, B. & Noiray, N. 2017 A criterion to distinguish autoignition and propagation applied to a lifted methane–air jet flame. *Proceedings of the Combustion Institute* **36** (2), 1637–1644. (9, 40)

Selle, L., Lartigue, G., Poinsot, T., Koch, R., Schildmacher, K. U., Krebs, W., Prade, B., Kaufmann, P. & Veynante, D. 2004 Compressible Large-Eddy Simulation of turbulent combustion in complex geometry on unstructured meshes. *Combustion and Flame* **137**, 489–505. (8, 13)

Seshadri, K. & Peters, N. 1989 Workshop on reduced kinetic mechanism and asymptotic approximations for methane–air flames. (9)

Shum-kivan, F. 2017 Simulation des Grandes Echelles de flammes de spray et modélisation de la combustion non-prémélangée. Phd thesis, CERFACS. (97)

Smagorinsky, J. 1963 General circulation experiments with the primitive equations: I. the basic experiment. *Monthly weather review* **91** (3), 99–164. (93)

Smooke, M. D. & Giovangigli, V. 1991 Reduced kinetic mechanisms and asymptotic approximations for methane–air flames. *Lecture Notes in Physics, Springer-Verlag* **15**. (9, 33)

Spalding, D. B. 1977 Development of the eddy-break-up model of turbulent combustion. *Symposium (International) on Combustion* **16** (1), 1657–1663. (96)

Stagni, A., Esclapez, L., Govindaraju, P., Cuoci, A., Faravelli, T. & Ihme, M. 2016 The role of preferential evaporation on the ignition of multicomponent fuels in a homogeneous spray/air mixture. *Proceedings of the Combustion Institute* . (7)

Stein, O. T., Olenik, G., Kronenburg, A., Marincola, F., Franchetti, B. M., Kempf, A. M., Ghiani, M., Vascellari, M. & Hasse, C. 2013 Towards comprehensive coal combustion modelling for LES. *Flow, turbulence and combustion* **90** (4), 859–884. (96)

Stewart, P. H., Larson, C. W. & Golden, D. 1989 Pressure and temperature dependence of reactions proceeding via a bound complex. 2. application to 2ch3 -¿ c2h5 + h. *Combustion and Flame* **75**, 25–31. (26)

Stopper, U., Aigner, M., Meier, W., Sadanandan, R., Stöhr, M. & Kim, I. S. 2009 Flow field and combustion characterization of premixed gas turbine flames by planar laser techniques. *Journal of Engineering for Gas Turbines and Power* **131** (2), 021504. (9)

Strahle, W. C. 1993 *An Introduction To Combustion*. Gordon and Breach Science Publishers. (18)

Sun, W., Chen, Z., Gou, X. & Ju, Y. 2010 A path flux analysis method for the reduction of detailed chemical kinetic mechanisms. *Combustion and Flame* **157**, 1298–1307. (38)

Sung, C. J., Law, C. K. & Chen, J. Y. 2001 Augmented reduced mechanisms for no emission in methane oxidation. *Combustion and Flame* **125** (1), 906–919. (9)

Takeno, T. & Nishioka, M. 1993 Species conservation and emission indices for flames described by similarity solutions. *Combustion and Flame* **92** (4), 465–468. (136)

Tomlin, A. S., Pilling, M. J. & Turányi, T. 1992 Mechanism reduction for the oscillatory oxidation of hydrogen: Sensitivity and quasi-steady-state analyses. *Combustion and Flame* **91**, lO7–130. (35, 46)

Touchard, S., R.Fournet, Glaude, P.A., Warth, V., Battin-Leclerc, F., Vanhove, G., Ribaucour, M. & Minetti, R. 2005 Modeling of the oxidation of large alkenes at low temperature. *Proceedings of the Combustion Institute* **30**, 1073–1081. (20)

Triantafyllidis, A., Mastorakos, E. & Eggels, R.L.G.M. 2009 Large-Eddy Simulation of forced ignition of a non premixed bluff-body methane flame with conditional moment closure. *Combustion and Flame* **156**, 2328–2345. (9)

Tsurikov, M. S., Geigle, K. P., Krüger, V., Schneider-Kühnle, Y., Stricker, W., Lückerath, R., Hadef, R. & Aigner, M. 2005 Laser-based investigation of soot formation in laminar premixed flames at atmospheric and elevated pressures. *Combustion science and technology* **177** (10), 1835–1862. (119, 120)

Turányi, T. 1981 List of publications including reduced mechanisms for combustion applications. *http://garfield.chem.elte.hu/Turanyi/ttpub.html* . (46)

Turányi, T. 1990*a* Reduction of large reaction mechanisms. *New Journal of Chemistry* **14**, 795–803. (33, 35, 46, and 112)

Turányi, T. 1990*b* Sensitivity analysis of complex kinetic systems: Tools and applications. *Journal of Mathematical Chemistry* **5**, 203–248. (34, 36)

Turányi, T. 2002 Effect of the uncertainty of kinetic and thermodynamic data on methane flame simulation results. *Physical Chemistry Chemical Physics* **4**, 2568–2578. (36)

Turányi, T., Bérces, T. & Vadja, S. 1989 Reation rate analysis of complex kinetic systems. *International Journal of Chemical Kinetics* **21**, 83–99. (34)

Turányi, T., Tomlin, A.S. & Pilling, M.J. 1993 On the error of quasi-steady-state approximation. *Journal of Physical Chemistry* **97**, 163–172. (42, 46)

Turányi, T. & Tóth, J. 1992 Comments to an article of frank-kamenetskii on the quasi-steady-state approximation. *Acta Chimica Hungarica* **129**, 903–903. (33)

Turányi, T., Zalotai, L., Dobe, S. & Berces, T. 1997 Applications of sensitivity analysis to combustion chemistry. *Reliability Engineering and System Safety* **57**, 41–48. (33, 35)

Tyliszczak, A. 2015 LES/CMC study of an excited hydrogen flame. *Combustion and Flame* **162** (10), 3864–3883. (9)

Vadja, S., Valkó, P. & Turányi, T. 1985 Principal component analysis of kinetic models. *International Journal of Chemical Kinetics* **17**, 55–81. (28, 35, and 36)

Valiño, L. 1998 A field monte carlo formulation for calculating the probability density function of a single scalar in a turbulent flow. *Flow, turbulence and combustion* **60** (2), 157–172. (12)

Valko, P. & Vajda, S. 1984 An extended ode solver for sensitivity calculations. *Computers & Chemistry* **8** (4), 255–271. (34)

Valorani, M. & Paolucci., S. 2009 The g-scheme : A framework for multi-scale adaptive model reduction. *Journal of Computational Physics* **228**, 4665–4701. (33)

Vervisch, L., Bidaux, E., Bray, K. N. C. & Kollmann, W. 1995 Surface density function in premixed turbulent combustion modeling, similarities between probability density function and flame surface approaches. *Physics of Fluids* **7** (10), 2496–2503. (97)

Veynante, D. & Poinsot, T. 1997 Reynolds averaged and Large-Eddy Simulation modeling for turbulent combustion. In *New tools in turbulence modelling. Lecture 5* (ed. J. Ferziger O. Metais), pp. 105–135. Les editions de Physique, Springer. (3)

Veynante, D. & Vervisch, L. 2002 Turbulent combustion modeling. *Progress in energy and combustion science* **28** (3), 193–266. (96, 97)

Vicquelin, R. 2010 Tabulated chemistry for turbulent combustion modeling and simulation. Phd thesis, EM2C. (13)

Vicquelin, R., Fiorina, B., Payet, S., Darabiha, N. & Gicquel, O. 2011 Coupling tabulated chemistry with compressible cfd solvers. *Proceedings of the Combustion Institute* **33** (1), 1481–1488. (111)

Vié, A., Franzelli, B., Gao, Y., Lu, T., Wang, H. & Ihme, M. 2015 Analysis of segregation and bifurcation in turbulent spray flames: A 3d counterflow configuration. *Proceedings of the Combustion Institute* **35** (2), 1675–1683. (79)

Violi, A., Yan, S., Eddings, E. G., Sarofim, A. F., Granata, S., Faravelli, T. & Ranzi, E. 2002 Experimental formulation and kinetic model for jp-8 surrogate mixtures. *Combustion Science and Technology* **174** (11-12), 399–417. (69)

Vreman, A. W., Albrecht, B. A., Oijen, J.A. Van, p. H. De Goey, L. & Bastiaans, R. J. M. 2008 Premixed and nonpremixed generated manifolds in Large-Eddy Simulation of Sandia flame D and F. *Combustion and Flame* **153** (3), 394–416. (7, 110)

Wang, H., Davis, S.G. & Law, C.K. 1999*a* Propene pyrolysis and oxidation kinetics in a flow reactor and laminar flames. *Combustion and Flame* **119**, 375–399. (18)

Wang, H. & Frenklach, M. 1991 Detailed reduction of reaction mechanisms for flame modeling. *Combustion and Flame* **87** (3-4), 365–370. (110)

Wang, H. & Frenklach, M. 1997 A detailed kinetic modeling study of aromatics formation in laminar premixed acetylene and ethylene flames. *Combustion and flame* **110** (1), 173–221. (52)

Wang, H., Laskin, A., Djurisic, Z. M., Law, C. K., Davis, S. G. & Zhu, D. L. 1999*b* A comprehensive mechanism of c2hx and c3hx fuel combustion. *Fall Technical Meeting of the Eastern States Section of the Combustion Institute, Raleigh, NC, Oct* pp. 129–132. (52)

Wang, H., You, X., Joshi, A. V., Davis, S. G., Laskin, A., Egolfopoulos, F. & Law, C. K. 2007 Usc mech version ii. high-temperature combustion reaction model of h2/co/c1-c4 compounds. *http://ignis.usc.edu/USC_Mech_II.htm* . (52)

Warnatz, J. 2000 Hydrocarbon oxidation high-temperature chemistry. *Pure Applied Chemistry* **72** (11), 2101–2110. (20, 21, and 42)

Warnatz, J., Maas, U. & Dibble, R.W. 1995 Combustion: physical and chemical fundamentals, modeling and simulation, experiments, pollutant formation. (18, 24)

Wei, J. & Kuo, J. C. W. 1969 Lumping analysis in monomolecular reaction systems. *Ind. Eng. Chem. Fundamen.* **8**, 114–133. (41)

Westbrook, C. K. & Dryer, F. L. 1981 Simplified reaction mechanisms for the oxidation of hydrocarbon fuels in flames. *Combustion Science and Technology* **27**, 31–43. (8)

Wilke, C. R. 1950 A viscosity equation for gas mixtures. *The journal of chemical physics* **18** (4), 517–519. (86)

Williams, F.A. 1985*a* *Combustion theory*. Menlo Park, CA: Benjamin Cummings. (28)

Williams, F.A. 1985*b* *The mathematics of combustion*. Buckmaster, J. D. (Ed.), Society for Industrial and Applied Mathematics. (96)

Wood, C. P., McDonell, V. G., Smith, R. A. & Samuelsen, G. S. 1989 Development and application of a surrogate distillate fuel. *J. Propul. Power* **5** (4), 399–405. (69)

Xu, R., Chen, D., Wang, K., Tao, Y., Shao, J. K., Parise, T., Zhu, Y., Wang, S., Zhao, R., Lee, D. J., Egolfopoulos, F. N., Davidson, D. F., Hanson, R. K., Bowman, C. T. & Wang, H. 2017*a* Hychem model: Application to petroleum-derived jet fuels. *10th US National Meeting on Combustion, College Park, MD* . (69, 70, 77, 173, and 1)

Xu, R., Wang, H., Davidson, D. F., Hanson, R. K., Bowman, C. T. & Egolfopoulos, F. N. 2017*b* Evidence supporting a simplified approach to modeling high-temperature combustion chemistry. *10th US National Meeting on Combustion, College Park, MD* . (6, 13, 69, 173, and 1)

Yamashita, H., Shimada, M. & Takeno, T. 1996 A numerical study on flame stability at the transition point of jet diffusion flames. *Symposium (International) on Combustion* **26** (1), 27–34. (129, 164)

Yetter, R.A., Dryer, F. L. & Rabitz, H. 1991 A comprehensive reaction mechanism for carbon monoxide/hydrogen/oxygen kinetics. *Combustion Science and Technology* **79** (1-3), 97–128. (9)

You, X., Egolfopoulos, F. N. & Wang, H. 2009 Detailed and simplified kinetic models of n-dodecane oxidation: The role of fuel cracking in aliphatic hydrocarbon combustion. *Proceedings of the Combustion Institute* **32** (1), 403–410. (9)

Zador, J., Zsély, I.Gy. & Turányi, T. 2006 Local and global uncertainty analysis of complex chemical kinetic systems. *Reliability engineering and system safety* **91**, 1232–1240. (36)

Zeldovich, Y. B. 1946 The oxidation of nitrogen in combustion and explosions. *Acta Physicochim. URSS* **21** (4), 577–628. (22)

Zeppieri, S. P., Klotz, S. D. & Dryer, F. L. 2000 Modeling concepts for larger carbon number alkanes: a partially reduced skeletal mechanism for n-decane oxidation and pyrolysis. *Proceedings of the Combustion Institute* **28** (2), 1587–1595. (41)

Zhang, H. & Mastorakos, E. 2016 Prediction of global extinction conditions and dynamics in swirling non-premixed flames using LES/CMC modelling. *Flow, Turbulence and Combustion* **96** (4), 863–889. (9)

Appendix A

Stoichiometry of intermediate species

CO equivalence ratio in ethylene flame

CO is considered as an example. The global ethylene oxidation reaction reads:

$$C_2H_4 + 3\ O_2 \rightarrow 2\ CO_2 + 2\ H_2O \tag{A.1}$$

with the mass stoichiometric factor $s^{C2H4} = 3\ \mathrm{W}_{O2}\ /\ \mathrm{W}_{C2H4} = 3.42$. A two-step mechanism, including CO oxidation, reads:

$$C_2H_4 + 2\ O_2 \rightarrow 2\ CO + 2\ H_2O \tag{A.2}$$

$$CO + \frac{1}{2}\ O_2 \rightarrow CO_2 \tag{A.3}$$

where, in reaction A.3, the CO mass stoichiometric factor is $s^{CO} = 0.5\ \mathrm{W}_{O2}\ /\ \mathrm{W}_{CO} = 0.57$.

The local equivalence ratio Φ of a mixture of pure ethylene ($\mathrm{Y}^0_{C2H4} = 1$) and air ($\mathrm{Y}^0_{O2} = 0.233$), can be expressed in function of a fuel based mixture fraction Y_z as:

$$\Phi = s^{C2H4}\frac{Y^m_{C2H4}}{Y^m_{O2}} = s^{C2H4}\frac{Y^0_{C2H4}}{Y^0_{O2}}\frac{Y_z}{1-Y_z} \tag{A.4}$$

where Y^m_{C2H4} and Y^m_{O2} are the mass fractions of fuel and oxidizer if they would have mixed without burning, and therefore correspond to a *pure mixing solution* Poinsot & Veynante (2005). With this definition, the Y_z at stoichiometry (corresponding to $\Phi = 1$) is $Y_{z,st} = 0.0637$.

Likewise, the equivalence ratio Φ_{CO} can be expressed in function of a theoretical pure mixing solution, involving the available CO and O_2:

$$\Phi_{CO} = s^{CO}\frac{Y^m_{CO}}{Y^m_{O2}} \tag{A.5}$$

However, since the mixture fraction Y_z is based on ethylene, an expression for the mixing of CO with O_2 depending on it is not straightforward. Indeed, according to the global reaction Eq. A.2, the transformation of C_2H_4 into CO requires O_2. Assuming an initial mixture composed of A moles of C_2H_4, B moles of O_2 and C moles of N_2, by mass conservation, a mixture composed of 2A moles of CO, 2A moles of H_2O, (B-2A) moles of O_2 and C moles of N_2 is obtained. Since A and B are functions of Y_z, with $\mathrm{A} = Y^0_{C2H4}Y_z$ and $\mathrm{B} = Y^0_{O2}(1-Y_z)$, an expression for 2A and (B-2A) required to express the evolution of Y^m_{CO} and Y^m_{O2} in the Y_z diagram is now straightforward:

$$\Phi_{CO} = s^{CO}\frac{2\ Y_z\ Y^0_{C2H4}\ W_{CO}/W_{C2H4}}{(1-Y_z)Y^0_{O2} - 2\ Y_z\ Y^0_{C2H4}\ W_{O2}/W_{C2H4}} \tag{A.6}$$

or more conveniently:

$$\Phi_{CO} = s^{CO}\frac{Y_z\ Y^0_{CO}}{(1-Y_z)Y^0_{O2,r}} \tag{A.7}$$

with $Y^0_{CO} = 2\,Y^0_{C2H4}\,W_{CO}/W_{C2H4}$ and $Y^0_{O2,r} = Y^0_{O2} - 2\,Y_z\,Y^0_{C2H4}\,W_{O2}/(W_{C2H4}\,(1-Y_z))$.

Replacing Y_z in Eq. A.6 by

$$Y_z = \frac{\Phi}{(\Phi + s^{C2H4} Y^0_{C2H4}/Y^0_{O2})} \tag{A.8}$$

eventually reduces to:

$$\Phi_{CO} = \frac{\Phi}{(3-2\Phi)} \tag{A.9}$$

Now, obviously, if $\Phi = 1$ in Eq. A.9, then $\Phi_{CO} = 1$, and vice versa. It is thus demonstrated that CO diffusion fronts and C_2H_4 diffusion fronts will gather around the same Y_z value: $Y_{z,st} = 0.0637$.

Generalization to any intermediates

Note that this derivation can be generalized to any intermediate species I (and virtually any fuel species but we will only consider ethylene): as long as the fuel global consumption Eq. A.1 is decomposed as:

$$C_2H_4 + \alpha\,O_2 \rightarrow \beta\,I + y\,H_2O \tag{A.10}$$

$$I + \gamma\,O_2 \rightarrow x'CO_2 + y'\,H_2O \tag{A.11}$$

The rescaled local equivalence ratio reads:

$$\Phi_I = s^I \frac{Y_z\,Y^0_I}{(1-Y_z)Y^0_{O2,r}} \tag{A.12}$$

with:

$$s^I = \gamma \frac{W_{O2}}{W_I} \tag{A.13}$$

$$Y^0_I = \beta\,Y^0_{C2H4}\,\frac{W_I}{W_{C2H4}} \tag{A.14}$$

$$Y^0_{O2,0} = Y_{O2,0} - Y_z\,Y^0_{C2H4}\,\frac{\alpha}{(1-Y_z)}\frac{W_{O2}}{W_{C2H4}} \tag{A.15}$$

As in the case of CO, replacing for Y_z in Eq. A.12 and setting $\Phi = 1$ leads to:

$$\Phi_I = \frac{\gamma\beta}{3-\alpha} = 1 \tag{A.16}$$

since $\gamma\beta + \alpha = 3$. As such, diffusion fronts of any intermediate species I will also gather around $Y_{z,st} = 0.0637$.

Appendix B

A two-step oxidation scheme for Ethylene/Air oxidation

Description of the global scheme The two-step global ethylene-air chemistry called 2S_C2H4_BFER employed in this PhD thesis is based on 6 species (C_2H_4, O_2, N_2, CO, CO_2, H_2O). The forward reaction rates for reactions 1 and 2 follow the Arrhenius law:

$$k_{f,i} = A_i f_i(\phi) T^{\beta_i} e^{-\frac{E_{a,i}}{RT}} \prod_k [X_k]^{n_{k,i}} \tag{B.1}$$

where A_i, $E_{a,i}$ and β_i are the pre-exponential factor, the activation energy and the temperature exponent of the $i-th$ reaction, respectively. X_k refers to the $k-th$ species molar fraction and $n_{k,i}$ to its reaction exponent in reaction i. All reaction parameters are summarized in Table B.1. The backward reaction rate for the $CO-CO_2$ equilibrium reaction, $k_{r,i}$ is evaluated based upon the equilibrium constant $K_{eq} = k_{f,i}/k_{r,i}$ calculated from thermodynamic tables.

Following Franzelli *et al.* (2010), the Pre-Exponential Adjustement (PEA) method is applied in order to reproduce the flame speed over the whole range of flammability. With the PEA, equivalence ratio dependent functions f_i are multiplied to the reaction rates constants before evaluation of the reaction rates. The coefficients of the f_i are here specified as in Franzelli *et al.* (2012). To comply with these PEA corrections, simplified transport and thermodynamic properties are assumed, with unity Lewis number for all species ($Pr = Sc_k = 0.7$ where k is the kth species) and the same power law for the gas mixture dynamic viscosity than is employed for all other chemistry descriptions.

Global validations Burnt gas temperature as well as laminar flame speed are plotted versus equivalence ratio in Fig. B.1, for various initial temperatures likely to be encountered in the targeted configuration. The 2S_C2H4_BFER scheme exhibits a non-linear behavior, due to the PEA corrections. However, the agreement is correct, especially for $\phi < 1.4$. The CO production is only plotted for an initial temperature of 300 K. The same nonlinearities are observed, and the agreement is particularly bad around stoichiometry. It is reminded, however, that in these types of schemes, the CO species is mostly present to retrieve the correct burnt gas temperature rather than to be quantitatively analyzed.

The behavior of 2S schemes submitted to strain has been investigated by Franzelli *et al.* (2013*b*). Since the

	C_2H_4 oxidation	CO-CO_2 equilibrium
$E_{a,i}$	35500	12000
β_i	0.0	0.7
A_i	1.0×10^{10}	2.0×10^8
$n_{k,i}$	C_2H_4 0.5	CO 1.0
	O_2 0.65	O_2 0.5

Table B.1: Reaction parameters used for the 2S_C2H4_BFER mechanism. Units are mol, s, cm^3 and cal/mol.

Lewis numbers of each species is equal to one in the present case, no response to strain is expected, as observed in the aforementioned publication.

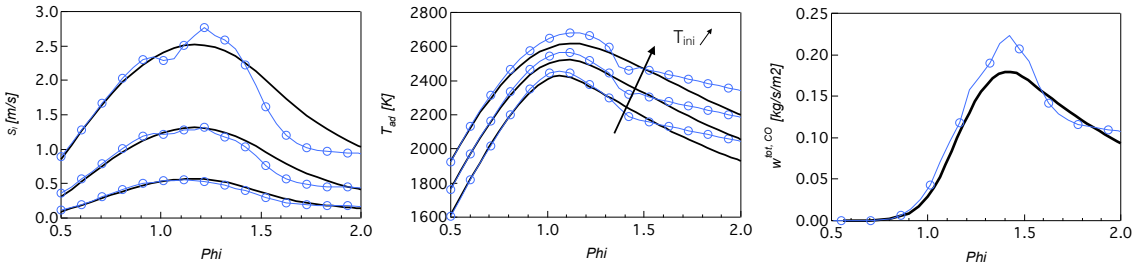

Figure B.1: Laminar flame speed, burnt gas temperature and CO total production of one-dimensional unstrained premixed ethylene-air laminar flames. Initial temperatures are 300, 500 and 700 K. Detailed mechanism (solid line), 2S_C2H4_BFER (o).

Soot model The strategy for implementing soot in 2S scheme is described in Lecocq *et al.* (2013). The basic idea is to retrieve important untransported quantities, such as OH and C_2H_2 species which are necessary to retrieve soot information, in a table build from canonical test cases. The table is built from laminar unstretched premixed flames, computed with CANTERA, just as in the FPI approach. In fact, the exact same table than that of the FPI computation is employed. In order to interpolate in the table, a progress variable Y_c and a mixture fraction Y_z need to be evaluated. One of the characteristics of a 2S scheme, however, is that the post-flame zone is quasi non existent. As such, a progress variable profile obtained from a combination of the transported CO and CO_2 species would be too stiff. To overcome this issue, Y_c is transported instead of being directly reconstructed. Its evolution follows a classical transport equation:

$$\frac{\partial \rho Y_c}{\partial t} + \frac{\partial \rho u_j Y_c}{\partial x_j} = \frac{\partial}{\partial x_j}\left(\rho D \frac{\partial Y_c}{\partial x_j}\right) + \rho \dot{\omega_{Y_c}} \tag{B.2}$$

where the source term $\dot{\omega_{Y_c}}$ is either evaluated from the 2S scheme, or interpolated in the table; depending upon the value of Y_c. In this study, $Y_{c,switch} = 0.5$.

Appendix C

List of reactions considered in the NOx pathway analysis

$N + OH \rightleftarrows NO + H$
$N_2 + O \rightleftarrows N + NO$
$N + O_2 \rightleftarrows NO + O$

Table C.1: Reactions considered in the Zeldovich route

$HCN + H2O \rightleftarrows CH_3 + NO$
$HCN + O \rightleftarrows CH + NO$
$HCN + HCO \rightleftarrows C_2H_2 + NO$
$NCO + O \rightleftarrows NO + CO$
$NCO + OH \rightleftarrows NO + HCO$
$NCO + O_2 \rightleftarrows NO + CO_2$
$NO_2 + CH \rightarrow HCO + NO$
$NO_2 + CO \rightarrow CO + 2.0\ NO$
$HCCO + NO \rightarrow HCN + CO_2$
$CH2* + NO \rightarrow HCN + OH$
$CH2 + NO \rightarrow HCN + OH$

Table C.2: Reactions considered in the Prompt route

$NH + O \rightleftarrows NO + H$
$NH + O_2 \rightleftarrows NO + OH$

Table C.3: Reactions considered in the NNH route

Abstract Recent implementation of emission control regulations has resulted in a considerable demand from industry to improve the efficiency while minimizing the consumption and pollutant emissions of the next generation of aero-engine combustors. Those phenomena are shown to strongly depend upon the underlying complex chemical pathways and their interaction with turbulence. Large Eddy Simulation (LES) is an attractive tool to address those issues with high accuracy at a reasonable computing cost. However, the computation of accurate combustion chemistry remains a challenge. Indeed, combustion proceeds through complex and highly non-linear processes that involve up to hundreds of different chemical compounds, which significantly increases the computational time and often induces stiffness in the resolved equations. As a mean to circumvent these drawbacks while retaining the necessary kinetics for the prediction of pollutants, Analytically Reduced Chemistry (ARC) has recently received high interest in the Computational Fluid Dynamics (CFD) community. ARC is a strategy for the description of combustion chemistry where only the most important species and reactions are retained, in a "physically-oriented way". ARC is on the verge of becoming affordable at a design stage, thanks to the continuously increasing available computational resources. The goal of the present work is twofold. A first objective is to test and validate efficient techniques and tools by which detailed chemistries are reduced to an LES-compliant format. To do so, the multi-step reduction tool YARC is selected and employed to derive and validate a series of ARC specifically designed to retrieve correct flame structures. A second objective is to investigate the overall feasibility and benefits of using ARC, combined to the Thickened Flame model (DTFLES), in performing LES of configurations of increasing complexity. The first configuration is a sooting swirl-stabilized non-premixed aero-engine combustor experimentally studied at DLR, burning ethylene. LES of this configuration is performed with the AVBP solver, in which ARC has been implemented. By comparison with global chemistry and tabulated chemistry, results highlight the importance of accurately capturing the flow-flame interactions for a good prediction of pollutants and soot. The second configuration is a swirled two-phase flow burner featuring a lean direct injection system and burning Jet-A2. A novel methodology to real fuel modeling (HyChem approach) is employed, which allows subsequent ARC derivation. The excellent results in comparison with measurements constitute an additional validation of the methodology, and provide valuable qualitative and quantitative insights on the flame-spray interactions and on the pollutant formation (NOx) mechanisms in complex flame configurations.

Keywords:Combustion chemistry, Reduced chemistry, Turbulent combustion, Gas turbines, Large Eddy Simulations, Pollutants

Résumé L'impact environnemental du trafic aérien fait maintenant l'objet d'une réglementation qui tend à se sévériser. Dans ce contexte, les industriels misent sur l'amélioration des technologies afin de réduire la consommation de carburant et l'émission de polluants. Ces phéomènes dépendent en grande partie des chemins réactionnels sous jacents, qui peuvent s'avérer très complexes. La Simulation aux Grandes Echelles (SGE) est un outil intéressant afin d'étudier ces phénomènes pour un coût de calcul qui reste raisonnable. Cependant, les processus chimiques, s'ils sont considérés sans simplification, font intervenir des centaines d'espèces aux temps caractéristiques très différents au sein de processus non-linéaires qui induisent une forte raideur dans le système d'équations, et un coût de calcul prohibitif. Permettant de s'absoudre de ces problèmes tout en conservant une bonne capacité de prédiction des polluants, les Chimies Analytiquements Réduites (CAR) font l'objet d'une attention grandissante au sein de la communauté. Les CAR permettent de conserver la physique du problème considéré, en conservant les espèces et voies réactionelles les plus importantes. Grâce à l'évolution toujours croissante des moyens de calculs, les CAR sont appliqués dans des configurations de plus en plus complexes. Les travaux de thèse ont principalement portés sur deux sujets. Premièrement, une étude poussée des techniques et outils permettant une réduction efficace et systématique de chimies détaillées. L'outil de réduction multi-tapes YARC est retenu et exhaustivement employé dans la dérivation et la validation d'une série de CAR préservant la description de la structure de flamme. Ensuite, une investigation de la faisabilité et des bénéfices qu'apportent l'utilisation de CAR en LES, comparé des approches plus classiques, sur des cas tests de complexité croissante. La première configuration étudiée est une chambre de combustion partiellement prémélangée brlant de l'éthylène, étudiée expérimentalement au DLR. Différentes modélisations de la chimie sont considérées, dont un CAR développé spécifiquement pour ce cas test, et les résultats démontrent qu'une prise en compte des interactions flamme-écoulement est cruciale pour une prédiction juste de la structure de la flamme et des niveaux de suies. La seconde configuration est un brûleur diphasique, avec une injection directe pauvre, brûlant du Jet-A2. Dans cette étude, une approche novatrice pour la prise en compte de la complexité du fuel réel (HyChem) est considéré, permettant la dérivation d'un CAR. Les résultats sont excellents et valident la méthodologie tout en fournissant une analyse précieuse des interactions flamme-spray et de la formation de polluants (NOx) dans des flammes la structure complexe.

Mots-clés: Chimie de la combustion, Chimies réduites, Combustion turbulente, Turbines à gas, Simulations aux Grandes Echelles, Prédiction des polluants